X-ray Imaging of Failure and Degradation Mechanisms of Lithium-ion Batteries

Donal P. Finegan

Submitted in part fulfilment of the requirements for the degree of Doctor of Philosophy at University College London

Electrochemical Innovation Lab
Department of Chemical Engineering
University College London

2016

Declaration

I, Donal P. Finegan, confirm that the work presented in this thesis is my own. Where information has been derived from other sources, I confirm that this has been indicated in the thesis.

.....

Signature

.....

Date

Acknowledgements

Interest is what largely influences our academic and professional pursuits, and often there is a critical and memorable moment where, for the first time, our interest in a particular pursuit is ignited. This moment occurred in February 2013 when, during an interview in the office of Dan Brett, a spirited and buzzing figure entered the room and immediately engaged in a presentation where through a profusion of spinning 3D images and flowing streamlines, microscopic features of battery materials were shown in a new light. This buzzing figure was Paul Shearing, for whom I reserve special thanks. Pauls unwavering enthusiasm, support, and encouragement have made the past three years a thoroughly enjoyable and interesting experience. On a similar note, I'd like to express my thanks to Dan Brett whose uplifting values shine throughout the EIL, and who is also largely responsible for setting up this PhD position. The combined values of Paul and Dan make the EIL a welcoming, open, creative and productive place.

I would not be where I am today without Gareth Hinds from the National Physical Laboratory. Gareth played a large part in setting up and arranging funding for my PhD and has always been a supporting mentor, providing valuable advice and direction whenever possible. I am also very thankful to Gareth who arranged an extension in funding to allow a comfortable completion of my PhD.

In the true spirit of engineering, my PhD involved both national and international collaborations to achieve what is described herein. I would like to express my thanks to Marco DiMichiel, Alexander Rack and Mario Scheel who were extraordinarily helpful in setting up challenging experiments at the European Synchrotron (ESRF). I would also like to thank Ian Hunt and Gregory Offer from Imperial College London, who generously gave us their time and allowed us to use their facilities to explore lithium-ion battery failures. To Steve Hall, Juanma Paz Garcia and Erika Tudisco from Lund University, who were extremely welcoming and generous with their time when we spent a week with them in Lund learning about their digital volume correlation software package. In particular, I'd like to thank Steve and Erika for inviting us to their homes for dinner and Juanma for showing us the best of the nightlife in Lund and Copenhagen. I also thank Brian

Bay, from Oregon State University, for inviting me to join him for information and training sessions on his digital volume correlation software package. And Steve Harris from Lawrence Berkeley National Labs for providing us with constructive feedback and interpretations of results over the years. More recently, we've had the privilege of working with Eric Darcy and Matt Keyser from NASA and NREL who are leading an incredibly interesting and high impact project to improve battery safety worldwide; I express my thanks to Eric and Matt, as well as Sandeep Yayathi (NASA) and Phil Partin (Boston Power) for their efforts in supplying us with advice for recent experiments.

Of course, the unique environment within the EIL would not be the same without certain individuals. The EIL has grown in size over the past three years where "quality *and* quantity" continues to hold; indeed getting to know the new generations of researchers and academics has been character defining. With the long list of wonderful persons, I fear that acknowledging each individual will come across as somewhat impersonal, but I simply must try! Thanks to my desk neighbours, Bernhard and Tom, who have kept me on my toes, both physically and mentally for the past three years. As most have found out, the 'Tjaden effect' is a very real experience, where after first meeting Bernhard you will for evermore have a niggling feeling of guilt after missing a morning gym session. An extra thanks to Bernhard, who was a wonderful host when I visited his hometown, Vienna. And to Josh, Sohrab, Dami and Xuekun, who along with Bernhard and Tom make up *the best* tomography group in the world – this corner crew have been pushing the boat out for years and there's no sign of stopping. Josh the inquisitor, for always making sure that I don't know what he doesn't know. Dami, for keeping me up-to-date with the 'pop' culture (though I am yet to understand what a Kanye is). Sohrab for unveiling the world of complex sounds and obscure electronic music. Xuekun the 'niubi', or is it 'shabi'.. I can't quite remember.. for *attempting* to teach me some mandarin. I will be forever grateful to the ever-steady Vidal, Erik, Tom and Fabiola for organising the most fun group parties I've experienced. To the resolute Dina and Chloe, who have always brought some vibrancy, fun and perspective to our office. Quentin, for all of his help with everything fuel cells and labview over the years. Francesco for his expert guidance on the CT systems and for introducing

me to limoncello :) Leon, the coffee connoisseur, for our morning chats. Vidal, Erik, James, Ana Belen and Rhod for always being up for a drink and for the numerous great dinners and late nights over the years. Toby and Jay for their unwavering support in the lab. Thanks to Tom Mason and George Mason for their help in designing and constructing my experiment rigs. And a big thanks to James, Tom, Liz, Josh and Sam Taylor for providing feedback on my thesis.

I've been on numerous beamtimes over the years, all of which have presented new challenges and left great memories. Thanks to James, Rhod, Bernhard, Tom, Josh, Romeo, Toby, Erik and Quentin for going through the highs and lows of beamtimes with me. I've been very lucky to have been part of the UCell team, so thanks to all members, old and new, for making it what it is. I've also been fortunate to have had the chance to organise the Early Career Researchers Conference (ECRC2015) with Sam Cooper, which was a wonderful experience. It was also a pleasure to work with Rhod, Harini and Tom, who organised a bigger and better ECRC2016 – may this tradition continue for the foreseeable future. Thanks to Liz Killen for getting me involved with the Pint of Science Festival last year. And Sam Taylor, Liz and Flo for pulling me away from work when I most needed it.

And finally, my family, for their continual support and care; every year, the most enjoyable moments have always been in their company.

The future is no more uncertain than the present..

- Walt Whitman

Abstract

Lithium-ion batteries are becoming increasingly energy and power dense, and are required to operate in demanding applications and under challenging conditions. Both safety and performance of lithium-ion batteries need to be improved to meet the needs of the current demand, and are inextricably linked to their microstructure and mechanical design. However, there is little understanding of the complex, multi-length scale, structural dynamics that occur inside cells during operation and failure. From the evolving particle microstructure during operation to the rapid breakdown of active materials during failure, the plethora of dynamic phenomena is not well understood.

In this thesis, both *ex-situ* and *operando* X-ray imaging, and computed tomography, in combination with image-based modelling and quantification are used to characterise battery materials and components in 3D. Degradation mechanisms are investigated across multiple length-scales, from the electrode particle to the full cell architecture, and direct comparisons between materials in their fresh and failed states are made. Rapid structural evolution that occurs during operation and failure is captured using high-speed synchrotron X-ray imaging, and quantified by correlating sequential tomograms. Consistent degradation mechanisms that occur over fractions of a second are identified and are shown to contribute significantly towards uncontrolled and catastrophic failure, and previously unexplored interplay between the mechanical design of cells and their safety and performance is described.

The experiments reported here assess the thermal and mechanical responses of cells to extreme operating and environmental conditions. The interaction between the dynamic architecture of active materials and the mechanical designs of commercial cells are revealed, highlighting the importance of the engineering design of commercial lithium-ion batteries and their efficacy to mitigate failure. These insights are expected to influence the future design of safer and more reliable lithium-ion batteries.

Table of Contents

List of Tables

List of Figures

List of Symbols and Abbreviations

Symbol	Definition
ΔG°	Change in Gibbs free energy [J mol^{-1}]
n	Number of electrons per mole of product
F	Faraday's constant [9.65 × 10^{4} C mol^{-1}]
E	Electromotive force [V]
R_m	Membrane resistance [Ω]
ρ_e	Resistivity of electrolyte [Ω m]
τ	Tortuosity factor
L	Length [m]
ε	Porosity
A	Area [m^{2}]
N_m	MacMullin number
ρ_s	Resistivity of separator soaked in electrolyte [Ω m]
Q_{tot}	Total heat output from decomposition reactions [J]
Q_{sei}	Heat output from degradation of SEI layer [J]
Q_{pe}	Heat output from reaction between the positive electrode and electrolyte [J]
Q_{ne}	Heat output from reaction between the negative electrode and electrolyte [J]
Q_e	Heat output from electrolyte decomposition [J]
Q_{bn}	Heat output from binder decomposition [J]
k	Rate constant [units depend on order of reaction]
A_r	Frequency factor [units depend on order of reaction]
E_a	Activation energy [J mol^{-1}]

Symbol	Definition
R	Ideal gas constant [J K^{-1} mol^{-1}]
T	Temperature [K]
I_0	Incident beam intensity [W m^{-2}]
I	Beam intensity [W m^{-2}]
μ	Linear attenuation coefficient [m^{-1}]
η	Distance through a material [m]
ρ	Density [kg m^{-3}]
N_A	Avogadro's constant [6.022×10^{23} mol^{-1}]
σ_{tot}	Total photon atomic cross section [m^2]
m_A	Atomic molar mass [kg mol^{-1}]
σ_{el}	Elastic scattering cross section [m^2]
σ_{comp}	Compton scattering cross section [m^2]
σ_{pe}	Photoelectric cross section [m^2]
V_v	Volume fraction
S_v	Interface density [m^2 m^{-3}]
ζ	Tortuosity
L_p	Path length [m]
L_{ec}	Euclidean distance between two points [m]
$\varkappa$	Conductivity of electrolyte [Ω^{-1} m^2]
d	Thickness [m]
Q_{CV}	Flow through a control volume [arbitrary]
Q_{pore}	Flow through a porous network [arbitrary]
$B_\lambda(T)$	Total radiant power from a blackbody [W]
h	Planck's constant [6.626×10^{-34}]
c	Speed of light in a vacuum [2.998×10^8 m s^{-1}]
λ	Wavelength of light [m]
k	Boltzmann constant [1.381×10^{-23} J K^{-1}]
w_i	Mass fraction of the element i in a compound
m_{mol}	Molar mass [g mol^{-1}]
V_{mol}	Molar volume [cm^3 mol^{-1}]

Abbreviations	Definition
ARC	Accelerating Rate Calorimetry
BMS	Battery Management System
CC	Correlation coefficient
CCD	Charge Coupled Device
CID	Current Interrupt Device
CMC	Carboxymethyl Cellulose
CMOS	Complementary Metal-Oxide-Semiconductor
c-P_oSD	Continuous Pore Size Distribution
CT	Computed Tomography
DEC	Diethyl Carbonate
DIC	Digital Image Correlation
DMC	Dimethyl Carbonate
DSC	Differential Scanning Calorimetry
DVC	Digital Volume Correlation
EC	Ethylene Carbonate
EDS	Energy Dispersive X-ray Spectroscopy
EIS	Electrochemical Impedance Spectroscopy
ESRF	European Synchrotron Radiation Facility
EV	Electric Vehicle
FBP	Filtered Back Projection
FIB	Focused Ion Beam
FOV	Field of View
FTIR	Fourier Transform Infrared Spectroscopy
GC	Gas Chromatography
HEV	Hybrid Electric Vehicles
IEC	International Electrotechnical Commission
ISC	Internal Short Circuit
LCO	Lithium Cobalt Oxide

Abbreviations	Definition
LFP	Lithium Iron Phosphate
LMO	Lithium Manganese Oxide
MD	Machine Direction
MIP	Mercury Intrusion Porosimetry
MS	Mass Spectroscopy
NaN	Not a Number
NASA	National Aeronautics Space Administration
NCA	Nickel Cobalt Aluminium
NLM	Non-Local Means
NMC	Nickel Manganese Cobalt
NREL	National Renewable Energy Laboratory
PE	Polyethylene
P_oSD	Pore Size Distribution
PP	Polypropylene
PSD	Particle Size Distribution
PTC	Positive Temperature Coefficient
PVdF	Polyvinylidene Fluoride
RV	Representative Volume
RVE	Representative Volume Element
SEI	Solid Electrolyte Interphase
SEM	Scanning Electron Microscopy
SOC	State of Charge
TD	Transverse Direction
UL	Underwriters Laboratories
UN	United Nations
WEO	World Energy Outlook
XANES	X-ray Absorption Near Edge Spectroscopy
XAS	X-ray Absorption Spectroscopy
XRD	X-ray Diffraction

Chapter 1

Introduction

1.1. Motivation

The price of oil is expected to rapidly increase long before its supply will be exhausted. This will be due to the reserves of oil beginning to dwindle and its extraction becoming a much more costly and difficult process[1]. Given the global reliance on oil as an energy source, with the United States alone consuming 18.9 M bbl/day[2], and the undeniable fact that oil is a limited resource, the world faces a severe energy crisis. In 2012, the World Energy Outlook (WEO)[3] emphasized the need for a change in the energy supply of the transport sector to accommodate for the expected shortages in oil and the concern for CO_2-related climate change. When combined with the rise in CO_2 in the atmosphere and its long-term impact on the climate, there is a major incentive to seek an alternative source of energy for the existing hydrocarbon-powered vehicles.

Lithium-ion batteries are recognised as an integral technology in the process of achieving a clean and sustainable energy future[4, 5] in particular they play a central role in achieving global CO_2 emission targets through replacing combustion engines with electric and hybrid electric vehicles[6]. Owing to their high energy and power densities, lithium-ion batteries are also ubiquitous energy storage devices in portable electronics, and other advanced systems such as those found in military, aerospace[7], and space[8] applications. Consequently, lithium-ion batteries are required to operate safely over a range of temperatures and at high charge and discharge rates[9, 10], and although the probability of failure is relatively low, batteries can and do fail[11], sometimes catastrophically. Several well-publicised incidents of battery failure have highlighted the need for improved battery safety[12, 13] which is of utmost importance, particularly with the increasing

deployment of electric and hybrid electric vehicles with high energy density batteries[14, 15].

1.2. A Brief History of Lithium-ion Batteries

In the early 1900's, lead-acid batteries presented the most promising energy source for automotive vehicles, but with a series of inventions, such as the electric starter, the internal combustion engine soon took the lead, and it wasn't until the oil crisis of 1970s (when the price of oil more than quadrupled) that the need for an alternative portable energy source was recognised.

Lithium as a metal has the most negative electrode potential of -3.04 V versus the standard hydrogen electrode, which when combined with its lightweight features (6.94 g mol^{-1} and a specific gravity of 0.53 g cm^{-3}) makes it a favourable energy storage material for high energy density batteries. While working with Exxon in 1976, Wittingham[16] began research in intercalation compounds such as $LiTiS_2$ for rechargeable lithium batteries. Despite being stable in non-aqueous electrolytes[17], the reactivity of lithium and its tendency to form dendrites while cycling, presented significant safety challenges and hindered the commercialisation of lithium batteries.

Around the same time, Goodenough[18] started working on metal-oxide electrodes that exhibited high voltage and stability capabilities. Of the metal oxides tested at the time, $LiCoO_2$ (LCO) displayed the most promising power and energy density as a positive electrode material, which when compared to $LiTiS_2$, allows almost twice as high voltages and current densities to be achieved. $LiCoO_2$ however, was expensive and unstable. Following its first investigations in Goodenough's lab, alternative intercalation materials such as iron oxide[19] and spinel manganese oxides (LMO)[20, 21] were also shown to be successful intercalation compounds and relatively less expensive and non-toxic than cobalt.

In 1989, the Sharp Corporation developed and successfully demonstrated a rechargeable lithium-ion battery composed of metal oxide as a positive electrode and a pyrolytic carbon[22] as an negative electrode[23]. However, it was Sony in 1991 who were the first to commercialise the lithium-ion battery (with a carbon

negative electrode and $LiCoO_2$ positive electrode). The advantages of the lithium-ion battery were felt across the globe and since then, billions of lithium-ion batteries have been produced for portable electronics and various other applications that require high energy density storage.

Driven by the high price of the commonly used transition metals (Cobalt and Nickel) in battery electrodes, Padhi *et al.*[24] as part of Goodenough's team developed a secondary (rechargeable) battery with an iron-based positive electrode in 1996[24]. The iron-based electrode consisted of $LiFePO_4$ (LFP) which, although cost effective, holds electrochemical disadvantages such as low capacity[25] and poor charge/discharge rates due to its inherently low ionic and electronic conductivity. However, in 2002 Chung *et al.*[26] achieved a dramatic increase in the conductivity of $LiFePO_4$ by doping it with metals that are supervalent to Li^+ ions; this positive electrode material became the product of the MIT spin-off company A123. However, $LiFePO_4$ did not achieve sufficient energy density for an electric vehicle to reach a driving distance that is competitive with the standard internal combustion engine. For this, a higher energy density and lower cost material (relative to $LiCoO_2$) was required. During the late 1990's and early 2000's [27], positive electrode materials with mixtures of Ni, Mn and Co (NMC), as well as Ni, Co and Al (NCA) entered the market with improved energy densities[25] and lower cost when compared to $LiCoO_2$ (primarily due to less Co being required).

Blends of LFP, LMO, LCO, NMC and NCA dominate the battery market today with the high energy density NMC and NCA chemistries being the predominant positive electrode material used in electric vehicles. However, considering these five electrode materials, there is a general trend of decreasing safety with increasing energy density; the onset temperature for thermal runaway tends to be lowest for the higher energy density materials, and despite the aforementioned progress, safety still hinders the success of lithium-ion batteries as an energy storage device for electric or hybrid-electric vehicles. In particular, the occurrence of thermal runaway, causing fires and explosions, receives considerable public attention, justifiably resulting in increasingly stringent safety regulations surrounding the handling and transport of lithium-ion batteries. Alongside the evolution of positive electrode materials, there has been continuous improvement in

associated battery materials and designs, such as separators, electrolytes, casings, assemblies and other safety devices, which will be discussed in the following sections.

1.3. Lithium-ion Battery Components

1.3.1. Overview

Three main components are required for an electrochemical cell to operate, a positive electrode, negative electrode and an electrolyte. Lithium-ion cells consist of positive and negative electrode materials that are capable of storing lithium. Most commonly, the positive electrode consists of a metal oxide (represented here by $LiMO_2$, where the M is a metal such as Co) and the negative electrode consists of graphitic carbon (Li_xC_6). Upon charge and discharge the lithium ions are exchanged between the electrodes via an ion-conducting electrolyte in a series of topotactic reactions where the ions are reversibly inserted and removed from the electrodes with little change to the electrodes' crystal structure. For example, during discharge lithium ions migrate from the negative electrode and intercalate into the positive electrode, whereas during charge this process is reversed. These processes are represented by the half-reactions (separately for both the positive and negative electrode) in the following set of chemical balances:

Positive electrode:

$$LiMO_2 \underset{discharge}{\overset{charge}{\rightleftharpoons}} Li_{1-x}MO_2 + xLi^+ + xe^-$$

Negative electrode:

$$C + xLi^+ + xe^- \underset{discharge}{\overset{charge}{\rightleftharpoons}} Li_xC$$

Overall:

$$LiMO_2 + C \underset{discharge}{\overset{charge}{\rightleftharpoons}} Li_xC + Li_{1-x}MO_2$$

Within a typical lithium-ion battery cell, the positive and negative electrodes are fully soaked in electrolyte to ensure that the lithium ions can travel between the electrode surfaces. To prevent short circuit, an electrically insulating, but ionically conducting, separator is placed between the electrodes. The primary components of a lithium-ion battery as described are shown in Figure 1-1.

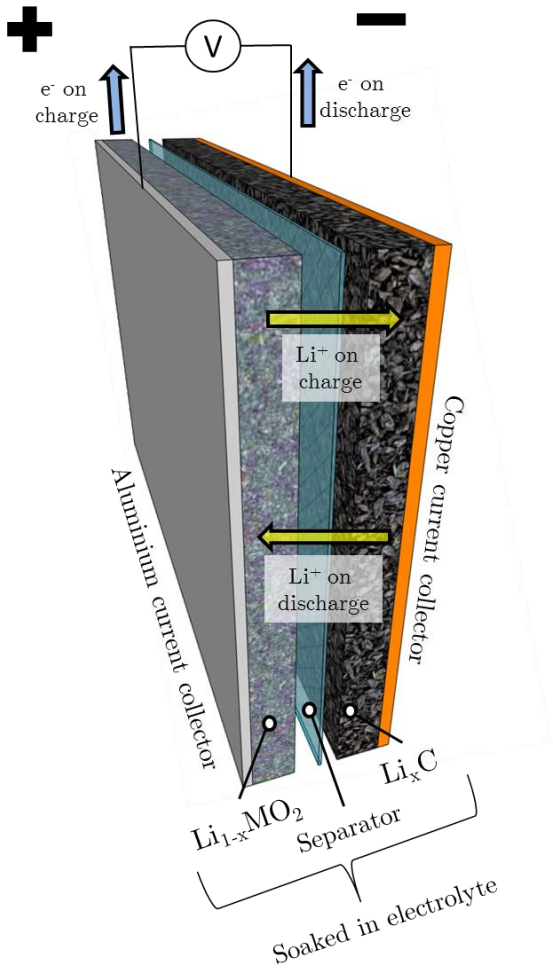

Figure 1-1: Basic components of a lithium-ion cell.

The maximum energy released and consumed during the charge and discharge processes is determined by the change in Gibbs energy (ΔG^o) of the electrochemical system, as conveyed in equation (1.1)[28].

$$\Delta G° = -nFE° \tag{1.1}$$

Where F is the Faraday constant, E^o is the standard electromotive force (volts) and n is the number of electrons per mole product. Here, the electromotive force (E) is defined by the chemical difference across the cell via the Nernst equation. However, not all of this energy can be converted to electrical energy due to polarization losses accruing from activation losses and losses through the formation of concentration gradients of reactants and products at the surface and in the bulk of the electrode material[29]. These energy losses are given off in the form of heat. However, the extent of energy loss is highly dependent on charge transfer reactions and diffusion rates through materials. Hence, the choice of cell materials and the cell design is crucial to achieve high performance.

1.3.2. Negative Electrode

Graphitic carbon is the most widely used negative electrode material. Different types of carbon materials[22] are used in commercial cells but fundamentally they consist of ordered graphene layers. Typically, graphitic carbon particles in commercial battery electrodes are < 30 µm in size (Figure 1-2a), and the extent to which the graphite structure within a particle is disordered is what determines its specific capacity, performance and electrochemical properties. For example, petroleum coke (which was used in the first commercial lithium-ion batteries in 1991)[30] displays a low specific capacity (*ca.* 180 mAh g^{-1}) when compared to the theoretical capacity of graphite (372 mAh g^{-1}) where there is one Li^+ for every six carbons (LiC_6). In a graphite structure, alternating layers of graphene are stacked as in Figure 1-2b. During lithiation, the structure of the carbon lattice changes from what is known as A-B-A-B-A (alternating layers) to A-A-A-A-A (non-alternating). However, stacking disorder[31], which can include parallel (but shifted or rotated planes) as well as non-parallel planes, can affect the intercalation of lithium ions. Petroleum coke is highly disordered and consequently it exhibits a reduced specific capacity.

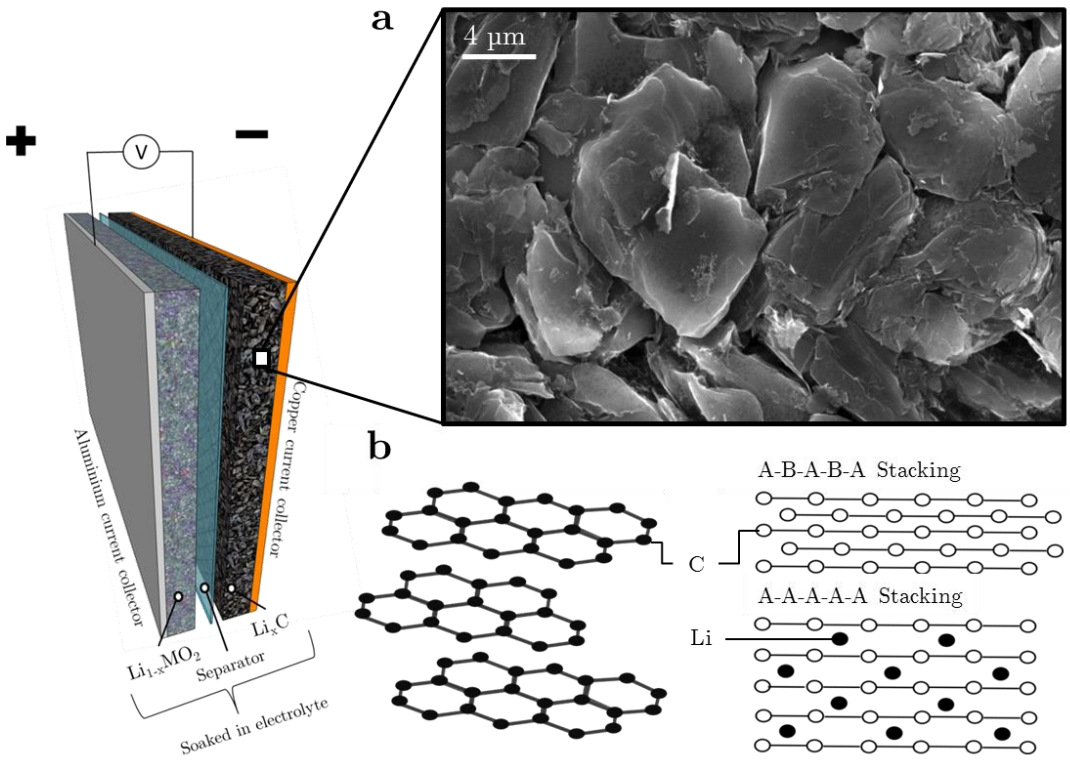

Figure 1-2: (a) Scanning electron micrograph of graphitic carbon negative electrode extracted from a commercial lithium-ion battery. (b) Graphite structure consisting of alternating layers of graphene (left) and the change in graphite structure between its non-lithiated state (right-top) and fully lithiated state (right-bottom).

The ion occupation of lattice regions is also affected by previous occupations causing hysteresis; this non-random occupation is attributed to the ions widening the Van der Waals bonded interlayer space of the graphite structure. As the structure becomes less well organised the capacity decreases. Consequently, the capacity of graphite in commercial batteries is typically *ca.* 300 to 350 mAh g^{-1} [32]. Hard carbons can achieve a higher capacity than the theoretical capacity of 372 mAh g^{-1}. As Dahn *et al.*[33] first suggested, this is due to the lithium binding to the hydrogen sites; Dahn *et al.* found that there was a correlation between the quantity of hydrogen present and the capacity of the cell[34]. Later this phenomena was put to greater use, when it was found that the theoretical capacity of graphene was double that of graphite (744 mAh g^{-1})[34], and could be used for applications requiring high energy density materials.

During the initial charge cycles, irreversible capacity loss occurs as some of the lithium ions react with the electrolyte at the surface of the graphite to form a passivation layer called the solid electrolyte interphase (SEI). The SEI layer, formed from the redox reactions at the surface of the electrode, consists of lithium salt[35] and irreversibly consumes lithium until it reaches a sufficient thickness to insulate the electrode from the reactive electrolyte (usually *ca.* 20-30 nm thick)[36]. The lost capacity of the cell shows a direct relationship to the measured surface area of the electrode[37, 38] due to the surface coverage of the SEI layer. The volumetric expansion of graphite electrodes in commercial batteries is typically *ca.* 10 % upon lithiation[39], and the mechanical stresses and strains associated with this expansion, and subsequent contraction during the de-lithiation process, can cause significant degradation of the electrode. Decrepitation, or the crumbling of the electrode material, as well as breakdown and reformation of the SEI layer (an exothermic process that will be discussed in more detail later)[40], can occur; the strains resulting from the dimensional changes can fracture the electrode structure, isolating electrode regions and degrading the cell's performance by eliminating electrical contact. In addition, breakdown and reformation of the SEI layer can result in the cell undergoing significant capacity loss as more lithium is irreversibly consumed.

1.3.3. Positive Electrode

In general, transition metal-oxides are the preferred positive electrode material for use in lithium-ion batteries due to their high reversible capacities and energy density. The metal-oxide materials can be classified depending on their reaction mechanism upon lithiation[41] where the reaction may involve alloying, insertion/extraction reactions, or conversion reactions. There is a wide range of chemical compounds that are used as positive electrodes; here, only the most common materials, LCO, LMO, NMC, and LFP are discussed in detail, and are the focus of the experiments in this thesis. The specific capacities and voltages of these metal-oxides, as well as comments on their relative safety, are presented in Table 1-1.

Table 1-1: Characteristics of common positive electrode materials[32].

Material	Specific Capacity ($mAh\ g^{-1}$)	Midpoint Voltage (V)	Comments
$LiCoO_2$ (LCO)	155	3.9	High capacity, but is expensive and thermally unstable at high states of charge.
$LiFePO_4$ (LFP)	160	3.45	High thermal stability, low cost and long life.
$LiNi_{1-x-y}Mn_xCo_yO_2$ (NMC)	140-180	3.8	Safer and less expensive than $LiCoO_2$. Can have higher or lower capacity (stoichiometry dependent).
$LiMn_2O_4$ (LMO)	100-120	4.05	Thermally stable, low cost, environmentally benign but has low capacity and is prone to capacity fade[42].

Positive electrode materials such as LCO, LFP, LMO and NMC generally have low electrical conductivities and require additional conductive carbon and binder to improve the electrical contact between the electrode particles and the current collector. Figure 1-3a shows a scanning electron micrograph of the surface of a commercial NMC positive electrode where the conductive carbon is seen to coat the NMC particles. Without conductive carbon, the electrical resistance would be much higher and the rate capabilities of the battery would significantly diminish.

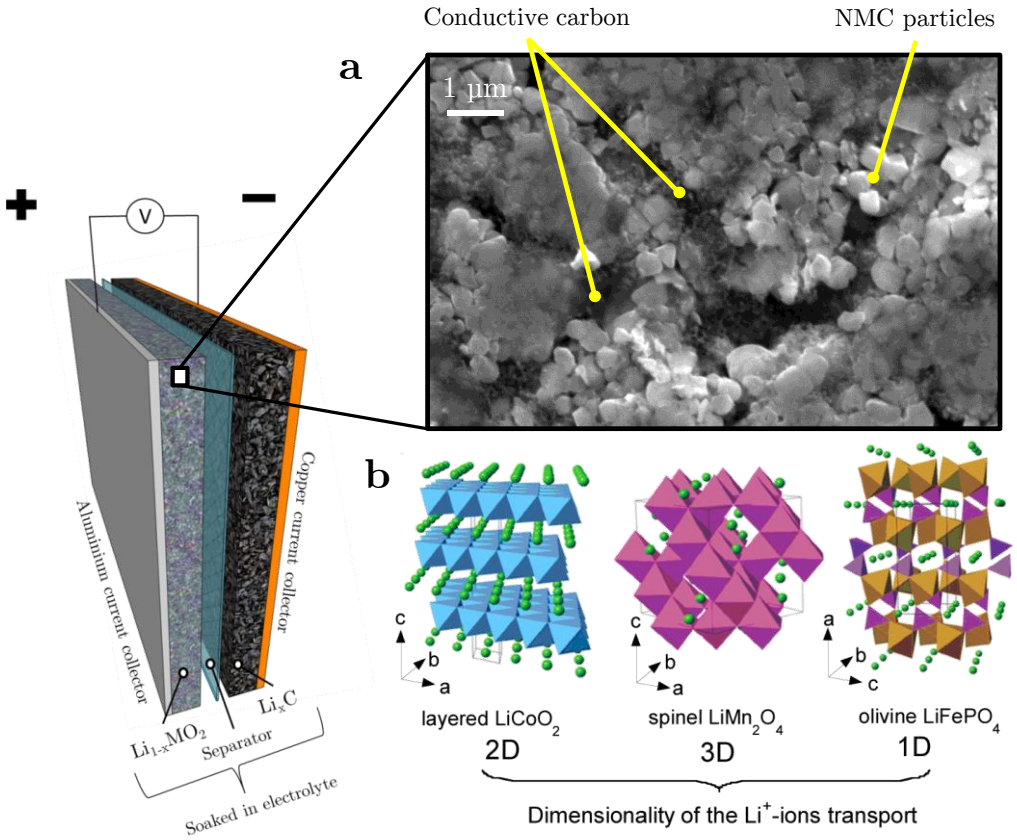

Figure 1-3: (a) Scanning electron microgram of an NMC positive electrode extracted from a commercial lithium-ion battery, showing conductive carbon coating the NMC particles. (b) Crystallographic structures of the most common positive electrode materials in lithium-ion batteries (reproduced from[43]), showing the layered structure of LCO with 2D transport (green particles are lithium, blue are octahedra of cobalt and oxygen atoms), the spinel structure of LMO with 3D transport (where Mn occupies the purple structures, the points on which are oxygen sites), and the olivine structure of LFP with 1D (or tunnel) transport (where the brown structures are occupied by Fe, the purple structures are occupied by P, and the points on the structures are oxygen atoms).

The positive electrode materials LCO, LFP, LMO and NMC, can be categorised according to their crystal structure (Figure 1-3b). LCO and NMC have a layered structure in which there are alternating layers of octahedral sites occupied by lithium, metal and oxygen atoms. LCO and NMC have a high specific energy and high voltage, but Co is expensive, toxic and thermally unstable at high

states of charge (*ca.* 4.3 V)[9]; NMC contains less Co, and presents a more cost effective and energy dense option for lithium-ion batteries. Cells with layered structures such as LCO and NMC are also hindered by capacity fade[44], and consequently have a relatively short life time and limited load capabilities (charge and discharge rates). $LiNi_{1-x-y}Mn_xCo_yO_2$ (NMC) electrodes can be tailored to high specific energies or high specific voltages depending on the composition. For example, doping $LiMn_xNi_{1-x}O_2$ with Co was first developed as a means to increase its capacity[45]. NMC materials have the same structure as $LiCoO_2$ and have similar performance. However, NMC electrodes are much more thermally stable, cost effective and also have competitive specific energies, when compared to $LiCoO_2$[9, 46].

LMO has a spinel-like structure (which allows 3 dimensional ion transport, as shown in Figure 1-3b), offers favourable kinetic properties, is low cost, has a high voltage (4 V vs. Li) and is environmentally benign. The spinel structure also has a high thermodynamic stability, giving LMO cells an inherent advantage for safety and high rate applications. However, LMO has a relatively low capacity and is prone to capacity fade; in particular, Mn undergoes dissolution in common electrolytes such as ethylene carbonate (EC) and dimethyl carbonate (DMC) due to the disproportionation of Mn(III) into Mn(II) and Mn(IV); there is ongoing research into preventing this mechanism with little effect on the material's specific capacity via surface doping but such techniques have yet to be implemented into commercial cells[47, 48]. Mn dissolution and capacity fade become particularly severe at elevated temperatures ($>$ 50 °C)[49]. Hence, LMO is less favourable for applications where there is likely to be prolonged exposure to elevated temperatures.

LFP consists of a stable olivine structure (Figure 1-3b) where lithium-ions move along in one-dimensional tunnels. LFP does not tend to react or lose oxygen to organic solvents, even at elevated temperatures. Although cost-effective and environmentally benign, LFP holds electrochemical disadvantages such as low capacity and poor charge/discharge rates due to its inherently low ionic and electronic conductivity. Due to the one-dimensional lithium transport through the structure, the rate capability of $LiFePO_4$ is greatly dependent on the quality of the

lattice, where defects and imperfections in the lattice can hinder ion transport[32]. A recent study by Lim *et al.*[50] showed that there is a skewed relationship between the exchange current density and the state of charge (SOC) of the cell (for $0 < x < 1$, in Li_xFePO_4) which amplifies the effect of domain heterogeneities within the electrode particles on rate capability. Accordingly, high-rate discharge and low-rate charge of LFP cells was found to be the most favourable operation mode for prolonged battery life. Considering these factors, LFP is used primarily for applications where safety is imperative, high rate discharge is preferred, and a high specific capacity is not essential, such as for grid storage or for large automotive vehicles such as electric buses.

Common to all of the aforementioned positive electrode materials, the crystallographic structure of the lattice and the concentration of ions in neighbouring sites has an influence on the conversion reactions taking place in the material and hence the potential and capacity of the cell. The electrostatic charge of the intercalated lithium ions changes the oxidation state of the other redox ions contained in the materials structure affecting reaction potential. For example, $LiCoO_2$ has a close-packed face-centred cubic arrangement of oxide ions with octahedral occupied regions of Li^+ and Co^{3+}. The cation positions are arranged such that lithium ions and metallic ions occupy alternating layers as shown in Figure 1-3b. If the crystallographic structure were to degrade during decrepitation, the capacity of the positive electrode material would significantly reduce and could result in the release of oxide ions which can exothermically react with the electrolyte materials causing a serious safety risk[51].

1.3.4. Electrolyte

The electrolyte acts as an ion-conducting medium between the positive and negative electrode while preventing the transfer of electrons. Typically, the electrolyte is composed of a solvent medium with dissolved lithium salts. In lithium-ion batteries the electrolytes are mostly non-aqueous (this is due to the narrow electrochemical stability window of aqueous electrolytes; although recently aqueous electrolytes that have high concentrations of salt have started to show

promise for more broad (3 V) voltage windows[52]) and come in either liquid, inorganic (glass) or organic (polymer) solid, or gel form. Solid and gel electrolytes are potential candidates for improving the safety, cyclability and design flexibility of cells but they still suffer from one or more of the following drawbacks: poor diffusion coefficients, low mechanical, chemical or thermal stability, or low conductivity[53-55]. Consequently, most commercial lithium-ion batteries include liquid electrolytes, which have superior performance when considering the combination of conductivity, thermal and chemical stability, cyclability, cost and safety. Liquid electrolytes are the focus of this review and are the only type of electrolyte used in the results section of this thesis.

Liquid electrolytes are absorbed into the porous electrode and separator materials of lithium-ion batteries (Figure 1-1). Common electrolyte constituents in commercial lithium-ion batteries are $LiPF_6$ salt and a mixture of alkyl carbonates such as ethylene carbonate (EC), diethyl carbonate (DEC) and dimethyl carbonate (DMC). Such electrolytes containing $LiPF_6$ have a high ionic conductivity and an acceptable safety; however, it should be noted that the aforementioned organic solvents are volatile and flammable, and play a key role in the catastrophic failure of lithium-ion batteries[56] (which will be discussed in more detail in the following chapters).

The safety of electrolyte solutions in lithium-ion batteries has been a prime factor of concern since their conception[57]. All common electrolyte solutions become reactive and decompose at high voltages and temperatures; for example, alkyl carbonate electrolytes with $LiPF_6$ become unstable at high voltages causing them to react with the intercalating lithium ions in the graphite[36]. Electrolytes based on the alkyl carbonate and lithium salt mixtures become unstable at high and low voltages (below 0 V and above *ca.* 4.4 V, vs. Li). During the first few charge-discharge cycles (formation cycles) of a lithium-ion cell the lithium salts in the electrolyte react at the surface of the negative graphitic-carbon electrode to form the SEI layer. The passivating SEI layer continues to grow until the electrolyte is no further net reduction from the electrode potential. At high temperatures the SEI layer decomposes, causing the electrode to be exposed and susceptible to reaction with the electrolyte.

Alternative electrolyte compositions such as lithium bis(oxalate)borate (LiBOB) exhibit superior stability with the negative electrode but inferior stability with the positive electrode when compared to the conventional $LiPF_6$[58]. Although LiBOB is not entirely advantageous relative to $LiPF_6$ for every lithium-ion battery chemistry, it may prove beneficial when incorporated into cells that are known to have positive electrodes with low reactivity, such as $LiFePO_4$. Additives are also commonly included in the electrolyte mixture to improve the performance of the cell by enhancing SEI formation and stability, increasing safety by reducing flammability, protecting electrodes from overcharge, and improving ionic conductivity[59].

The resistance to ion transport from electrode to electrode, as well as the safety and stability of a cell, is not solely dependent on the electrolyte. The positive and negative electrodes are separated by an electrically insulating separator layer. The electrolyte occupies the microstructure of the separator, thus making the separator ionically conducting (but not electrically conducting). However, the composition and microstructure of the separator also play significant roles in the safety and rate capability of lithium-ion batteries.

1.3.5. Separator

The separator layer is placed between the positive and negative electrodes of lithium-ion batteries to prevent electrical contact between the electrodes while allowing transport of lithium ions during operation. The performance and safety of lithium-ion cells greatly depend on the properties of the separator layer. Typically, separators consist of a thin (typically between 10 and 30 µm) microporous polymeric or non-woven fabric. The most common separator type in commercial lithium-ion cells is the microporous polymeric membrane[60] consisting of either polyethylene (PE) or polypropylene (PP), or an amalgamation of both (Figure 1-4a). The polymer membranes are mainly manufactured via one of two methods; dry processing or wet processing. Dry processing involves melting a polyolefin resin, extruding it as a sheet of lamellae, drawing it in the transverse direction (see direction relative to cell assembly in Figure 1-4b) and annealing; whereas in wet

processing, the polymer is mixed with a hydrocarbon liquid, is drawn in both the machine and transverse direction, followed by evaporation of the hydrocarbon. To uphold the high safety and performance standards of lithium-ion batteries, separator materials must satisfy the following requirements[61]:

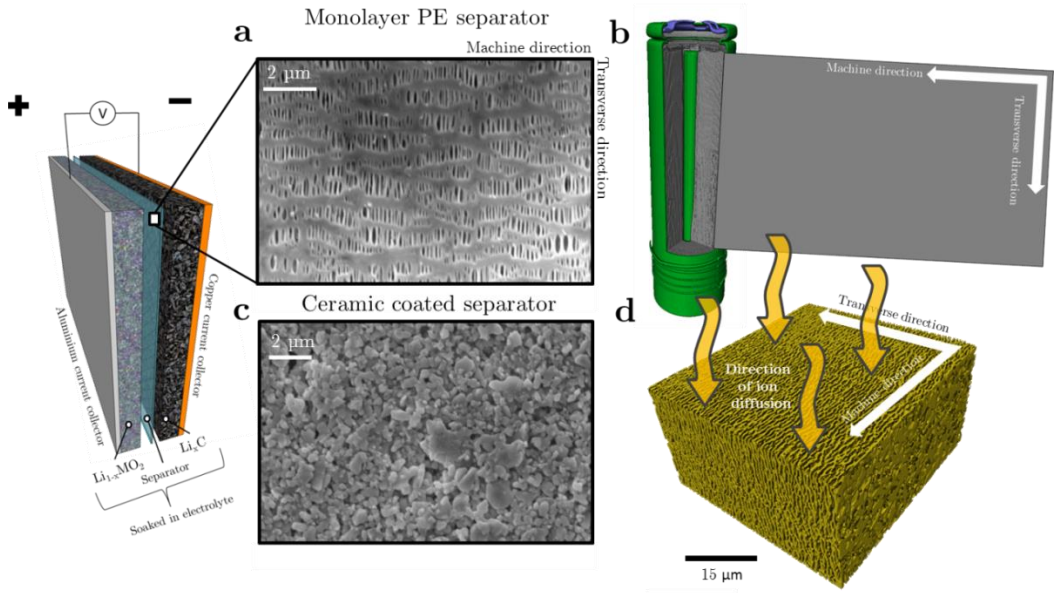

Figure 1-4: Schematic showing the placement of the separator layer with (a) scanning electron micrograph of a PE separator manufactured via the dry process, (b) illustration showing the orientation of the machine and transverse directions of separators within an 18650 cell where the grey is the separator and green is the cell casing, (c) scanning electron micrograph of the surface of a commercial ceramic coated separator and (d) 3D reconstruction showing the microstructure of a monolayer PE membrane and the direction of ion transport.

Chemical Stability: The separator must be stable in the chemical and electrochemical environment of lithium-ion batteries, i.e. compatible with electrode and electrolyte materials. The most commonly used polyethylene and polypropylene separators are stable in moderate voltages ($<$ 4.2 V vs. Li) but have been shown to degrade and cause capacity loss in higher voltage (*ca.* 4.5 V vs. Li) cells[62].

Mechanical Stability: The separator material is responsible for electrically isolating the positive and negative electrodes, preventing short circuits; therefore, the separator must be mechanically stable and able to withstand tension associated with manufacturing and displacement of the electrode assembly during operation[63, 64]. The separator should also resist puncture from lithium dendrites, internal structural collapse and any shrapnel present in the cell from manufacturing. The puncture strength of a commercial 25 µm thick membrane is typically *ca.* 350 grams[65]. The tensile strength of polymer separators is dependent on the manufacturing process; dry processing involves uniaxial stretching that results in slit-like pores (Figure 1-4a), causing a higher tensile strength in the machine direction than the transverse direction. Wet processing involves biaxial stretching which results in minimal anisotropy in tensile strength.

Thermal Stability and Shutdown: The internal contents of commercial lithium-ion cells are expected to effectively operate over a range of temperatures from near 0 °C to *ca.* 60 °C. The shrinkage and degradation of the separator material over this range should be minimal to maximise the cell's cyclability. Some separators consist of a tri-layer polypropylene, polyethylene and polypropylene (PP-PE-PP). PE and PP have melting temperatures of *ca.* 135 °C and 165 °C respectively, hence in the common tri-layer of PP-PE-PP such as Celgards 2325, the inner PE layer melts and fills the pores of the outer PP layers, cutting off ion transport in a process known as separator shutdown. However, it has previously been reported that the shrinkage associated with the melting of PE and PP may result in pin-hole formation causing soft short circuiting within cells and an increased risk of thermal runaway[66]. Uneven or incomplete separator shutdown can occur when only parts of the pores are blocked during the separator melting. Partial separator shutdown can cause increased current density in the regions that remain open to charge transfer, resulting in local heating and degradation as well as additional strain on the polymer material[66]. Ceramic coatings (Figure 1-4c) can also be applied to the surface of polymer separators to improve their thermal stability and resistance to shrinkage and tearing[67, 68].

Wettability: The uptake of electrolyte by a separator and complete wetting of the internal microstructure is essential for low ionic resistance. If a separator does not take up electrolyte then pockets of gas will occupy the pores, rendering those regions useless for ion transport. Some separators are coated with a surfactant to improve the separator's uptake and wettability[60].

Permeability: The separator must also be thin and sufficiently porous to allow liquid electrolytes to occupy the material and provide ion-conducting paths between the electrodes (Figure 1-4d); this property is critical to the performance of the cell. However, if the porosity of the separator material is too high the shutdown mechanism and the safety of the cell can be compromised. Typically, tri-layer separators have a porosity between 30 % and 40 %[65]. A uniform pore size below the size of electrode particles prevents the penetration of the separator by particles, and an even distribution of pores helps maintain a homogeneous current through the separator. The tortuosity of the separator also plays an important role in its safety; highly tortuous porous paths help mitigate the growth of lithium dendrites, reducing the risk of short circuiting.

1.4. Ion Transport in Electrodes and Separators

The microstructure of the electrodes and separators must satisfy certain transport requirements to allow the cell to function effectively. Optimising and predicting the performance of electrodes is invaluable while tailoring electrodes to specific applications. Newman[69-72] developed a highly successful macro-homogeneous model for the optimization of electrode porosity and thickness for applications requiring balances of power density and capacity. For example, porous electrodes with high active surface areas are favourable for high rate applications. Electrodes used in hybrid electric vehicles (HEVs) are tailored to maximise power density to cater for the high power associated with regenerative breaking; these electrodes may be thin and highly porous to maximise active surface area and minimise

transport resistance to allow for the large flux of lithium ions. Maximising surface area can be achieved by changing the particle's topology or by decreasing the particle size[73]; however, this can come at the expense of accelerated capacity fade due to more area being available for SEI formation. The SEI layer can also increase in thickness for smaller particle sizes causing an eventual decline in rate capability for decreasing particle size[73]. Conversely, electric vehicle (EV) manufacturers might aim to maximise a vehicle's range by tailoring the electrodes to be relatively thick and have low porosity, providing high specific energy densities at the expense of less power[74].

In addition to the requirement of a high surface area for high rate applications, the electrodes and separators must exhibit a low charge transport resistance through their microstructure. The resistance to ion transport (R_m) is described by equation 1.2., where ρ_e is the electrolyte resistivity, τ is the tortuosity factor, l is the thickness of the membrane, ε is the porosity, and A is the membrane area.

$$R_m = \rho_e \frac{\tau l}{\varepsilon A} \tag{1.2}$$

The tortuosity factor (τ) is defined as the square of tortuosity, which is the ratio of the length of the actual path that an ion would take between two points, to the shortest path[75]. Figure 1-5 shows an example of a tortuous path that an ion could experience whilst travelling between the positive and negative electrodes. The particle shape, size, orientation as well as packing, is what largely determines the effective tortuosity of electrode materials, which opens scope for optimisation of particle microstructure for high rate capabilities; for example, a recent study by Billaud *et al.*[76] showed that by selectively orienting electrode particles in a way that reduces the electrode tortuosity, the rate performance of cells can be significantly improved.

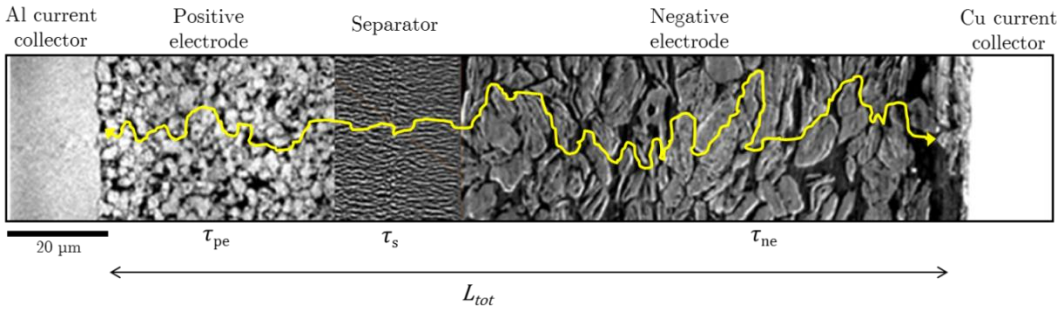

Figure 1-5: 2D slices from reconstructed tomograms showing the microstructure of commercial battery electrode and separator materials. The yellow trail highlights one possible path that a Li^+ ion could follow between the positive and negative current collector, where the tortuosity is defined as the ratio of the length of the yellow path to the shortest distance (L_{tot}). Each of the three layers (positive electrode, separator and negative electrode) has their own tortuosity factor (τ).

The tortuosity factor of electrodes and separators is most commonly determined via electrical conductivity measurements. A frequently used metric that reflects the transport resistance, hence the porosity and tortuosity factor of electrode materials, is the MacMullin number (N_m)[60, 77], which is defined as the ratio of the specific resistivity of the electrolyte (ρ_e) to the specific resistivity of the separator soaked in electrolyte (ρ_s):

$$N_m = \frac{\rho_s}{\rho_e} \tag{1.3}$$

For separator materials, manufacturers more frequently provide a different metric called the Gurley number, which is a measure of the time required for a specific volume of air to pass through a separator under a certain pressure (former standard test ASTM-D726). Relying on electrochemical measurements, the MacMullin number is a better indication of how the separator will affect the performance of the cell; whereas the Gurley number is based on a pressure driven (rather than diffusion driven) transport mechanism and does not correlate directly with cell performance. Yet, it is the Gurley number that is the most frequently provided metric by manufactures. The disconnect between the Gurley number and the performance of the cell is discussed in more detail in Chapter 4.

Quantifying microstructural parameters such as tortuosity, porosity, particle size and volume specific surface area is essential for optimisation of battery electrodes. X-ray CT can be used to characterise the structural properties of materials in 3D, which will be discussed further in Chapter 3. Lithium-ion battery electrode materials undergo volumetric expansion and contraction upon lithiation and delithiation, respectively, which can affect the microstructural properties over both short-term (from charged state to discharged state) and long-term (as the electro-mechanical forces from the evolving electrodes degrade the integrity of the cell's architecture); this change in microstructural properties over the lifetime of a battery is not yet well understood.

1.5. Electro-mechanical Degradation

Many functional electrode materials undergo a significant volume change during the insertion of Li^+ ions[78, 79] that can induce high local strains and severe mechanical degradation[80, 81] leading to capacity fade and reduced performance. Eastwood *et al.* [82] used time resolved X-ray CT imaging to track the evolution of Mn_2O_4 electrode particles during operation of a complete lithium-ion button cell. This study elucidated lithiation and the swelling behaviour of electrode materials during operation; Eastwood demonstrated that the tested button cell was electrically limited by showing that particles furthest from the current collector showed the least swelling and therefore lithiation. The occurrence of limited lithiation presented in Eastwood's work can be used to improve the accuracy of thermal and mechanical electrode models by including such heterogeneities, particularly for cells with relatively thick electrodes, where at high rates a significant potential drop can occur between the surface of the electrode and the current collector, due to lithium concentration gradients.

Various *in-situ* characterisation techniques have been used to track lithium insertion and morphological changes of electrode materials during operation[83]. Techniques such as soft X-ray absorption spectroscopy[84] (XAS) and neutron imaging[85] have previously been used to track the lithiation of electrode materials during operation, but both are restricted to two-dimensional (2D) measurements

for fast dynamic processes due to their low temporal resolution and consequent high acquisition times for three-dimensional (3D) images. *In-situ* X-ray diffraction (XRD) has also been used to monitor the progress of lithiation/delithiation of active materials inside operating lithium-ion batteries by studying their structural changes[86, 87]. Additionally, coherent XRD imaging has been shown to be a powerful tool for characterisation of strain evolution in the crystal lattices of individual electrode particles on the nanoscale[88, 89]. Whilst XRD measurements are useful for tracking reaction mechanisms, they provide no information on the impact of the resulting structural changes on the morphology of the bulk material.

Understanding the interaction between electrochemically active materials and the mechanical design of commercial batteries is becoming increasingly important particularly with the introduction of new generation electrode materials[90, 91] with high specific capacities and a large degree of motion and morphological evolution during lithiation[92-94]. This displacement of active materials can lead to contact loss between the current collector and electrode material, which is thought to be one of the primary mechanisms for increased cell impedance during cycling[95, 96]. Numerous studies have been performed to tackle the issue of high strain and mechanical degradation on both the micro- and macro-scale, including the development of strain models to determine the particle fracture conditions[94, 97, 98] and the reduction of contact losses by increased applied pressure[99]. However, the degradation associated with electro-mechanical phenomena within a cell is not well understood; this interplay between evolving electrode materials and the mechanical design of commercial batteries is the focus of Chapter 5.

1.6. Summary

In this chapter the basic operating principle and components of lithium-ion batteries, as well as the primary degradation mechanisms and factors affecting rate performance, have been described. Mechanical degradation of electrode microstructures and their crystal lattices are the primary modes of degradation while operating within the recommended voltage and temperature windows. The mass transport as well as solid-state diffusion mechanics influences the charge and

discharge rate capabilities of cells, once the cell is mass-transport limited (rather than electrically limited). However, outside the recommended operating windows, such as at high temperatures and voltages, degradation accelerates and the risk of cell failure starts to rise as unfavourable side-reactions occur. Furthermore, the engineering design of cells and their mechanical integrity, also play a crucial role in their performance and safety.

1.7. Objectives of this Thesis

There is still limited understanding of the thermal and structural behaviour of the active materials within lithium-ion batteries during operation and failure, which is the impetus for the research described in this thesis. Battery degradation and failure occurs across multiple time and length scales with unique circumstances for each combination of materials used. For example, common electrode materials undergo swelling and contraction during operation as lithium enters and exits their structure which can result in strain and crack evolution, leading to severe capacity loss over multiple charge and discharge cycles. Furthermore, when a critical temperature is reached, electrode materials can undergo rapid exothermic degradation causing an entire cell to change from being intact to being completely destroyed in a matter of seconds. The aim of this thesis is to understand and link the phenomena that occur across multiple time and length scales, predominantly through the use of *in-situ* and *operando* X-ray computed tomography (CT). The insights achieved from examining the dynamic internal architecture of lithium-ion batteries when exposed to extreme conditions could guide the design of safer and more reliable commercial battery designs.

1.8. Thesis Overview

This thesis starts with an introduction to the essential components of lithium-ion batteries and a description of their principle of operation. The influence of microstructure on the transport properties of battery materials is introduced,

followed by a discussion of the importance of being able to relate the microstructural properties of materials to the performance of the cell.

In Chapter 2, thermal runaway and the occurrences that contribute to battery failure are introduced. The sources of gas and heat generation during thermal runaway are outlined. This is followed by descriptions of various safety strategies and devices that are used by battery manufacturers to contain and manage the generated heat and gas, with the aim of mitigating the magnitude of battery failure. A description of methods that are used to test the efficacy of commercial battery designs under extreme operating conditions is presented, and how these methods are used as standard tests to set minimum safety thresholds of commercial designs is outlined.

Chapter 3 introduces X-ray CT, and describes its application to capturing the architecture of battery materials across multiple length scales. A detailed description of the types of X-ray systems along with their strengths and drawbacks is provided, and particular attention is paid to characteristics of X-ray CT systems that can capture 3D images (tomograms) over very short time periods. Thereafter, several image processing and quantification techniques for extracting microstructural information from tomograms are explained, including pore and particle size distributions, tortuosity, and tracking the displacement of features in 3D via digital volume correlation. This chapter closes with a description of the *in situ* rig designs used for high-speed synchrotron X-ray imaging experiments, as well as a background on associated characterisation techniques.

Chapter 4 is the first of the results chapters, and describes the application of X-ray phase contrast nano-CT to capture the microstructure of three different commercial polymer separators. Several image quantification methods are applied to the reconstructed tomograms and microstructural properties such as porosity, pore size distribution, and tortuosity, are characterised and related to the performance and safety of operating cells.

Chapter 5 examines the effect of microstructural evolution (swelling) on the architecture of lithium-ion batteries during operation. In this study, a commercial CR2 Li|MnO_2 battery is discharged while performing high-speed *operando* X-ray CT. The displacement of active materials in 3D within the cell is quantified by

correlating sequential tomograms by application of digital volume correlation software packages. Significant displacement of the MnO_2 electrode layer is observed and linked to delamination of the electrode layer and displacement of the current collector.

In chapter 6, high-speed X-ray CT is applied to examine the interaction between the active electrode materials and the rigid mechanical design of two different commercial rechargeable 18650 batteries. The cause of electrode layer collapse leading up to thermal runaway is identified, highlighting a key role of a core mandrel in the behaviour, failure mechanism, and overall safety of cells. High-speed radiography at 1250 fps elucidates the propagation of thermal runaway in both cells leading to the hypothesis that cell bursting (or ejection of the electrode assembly) is caused by vent clogging.

Chapter 7 describes a set of experiments that use synchrotron and lab-based X-ray CT systems to examine the failure mechanisms of a commercial $LiCoO_2$ pouch cell over multiple time and length scales. Through *pre-* and *post-mortem* CT examinations as well as particle size distribution analyses, the process of thermal runaway accruing from overcharge abuse is described from the particle level up to the cell level, linking features that occur on the nano-scale to the macroscopic thermal and structural phenomena.

Chapter 8 is the final results chapter, and explores the initiation and propagation of thermal runaway within commercial 18650 cells. The initiation of thermal runaway is captured through the use of an internal short circuiting device, developed by collaborators at NASA and the National Renewable Energy Laboratory (NREL) that consistently and reliably initiates thermal runaway at a known location within a cell. The failure mechanisms associated with the internal short circuiting device are compared to those associated with a nail penetration test, which is often used as a means to examine how lithium-ion batteries behave during an internal short. The cause of cell bursting and rupture is subsequently examined through the use of ultra-high-speed X-ray radiography of the vent region of several popular commercial 18650 cell designs.

The final chapter (Chapter 9) contains a summary of the work presented in this thesis. Considerations for the design of safer and more reliable lithium-ion

batteries are outlined based on the presented results. This chapter closes with a description of ongoing and future work.

Chapter 2

Literature Review: Batteries and Safety

2.1. What is Thermal Runaway?

The thermal response of a cell is one of the most important characteristics to understand when assessing the safety of a cell design. Undesirable temperature rises can occur within the cell as a result of electrical or mechanical abuse, or due to the presence of an external heat source, e.g. failure of a neighbouring cell. Depending on the cell design there is a range of critical temperatures which, when reached, will result in exothermic breakdown of the cell's constituents [100, 101]. Once the rate of heat generation exceeds the rate of heat dissipation into the environment the temperature of the cell starts to rise; thereafter, a sequence of detrimental events propagate in a process known as thermal runaway[102].

When thermal runaway does occur, the magnitude of failure is dependent on the cell materials and design. For example, pouch cells that are not contained within a rigid shell tend to swell and catch fire, whereas 18650 cylindrical cells that consist of a spiral-wound electrode assembly within a rigid steel container, can fail via violent rupture or explosion, due to the container acting as a pressure vessel. When placed in a large module of batteries, the heat generated during a single failure can also spread to neighbouring cells causing propagation of thermal runaway, often with catastrophic outcomes[7, 12, 13]; there is a clear need to further reduce the risk associated with battery packs and modules[103, 104]. In recent year's research into making batteries more reliable and safe has included developing safer materials, as well as innovative battery designs and safety devices to help mitigate and avoid catastrophic failure. Standard test methods are also

continuously evolving to keep up with the increasing market requirements and new energy materials being used.

In this chapter, a background to the causes of thermal runaway, as well as ways to prevent or mitigate the consequences of failure is provided. The role of, and information extracted from, testing standards and certain abuse conditions such as electrical, mechanical or thermal, are also discussed.

2.2. Heat Production and Hazards

2.2.1. Exothermic Reactions and Cell Heating

A higher rate of heat generation than heat dissipation is a primary characteristic of thermal runaway; this is of particular interest to manufacturers who wish to avoid such an instance. For example, by reducing the rate of heat generation or by increasing the rate of heat dissipation, conditions in which battery materials become unstable can be avoided.

There are five primary sources of heat that can lead to the occurrence of thermal runaway; heat released during decomposition of the SEI layer (Q_{sei}), reaction between the positive electrode and electrolyte (Q_{pe}), reaction between the negative electrode and electrolyte (Q_{ne}), electrolyte decomposition reactions (Q_e), and reaction between the binder material and the negative electrode (Q_{bn}). Therefore the total heat output accruing from decomposition reactions during thermal runaway (Q_{tot}) is described by[105, 106]:

$$Q_{tot} = Q_{sei} + Q_{pe} + Q_{ne} + Q_e + Q_{bn} \tag{2.1}$$

It should be noted that equation 2.1 only considers heat generated from decomposition reactions and not heat output from processes related to operation, such as Joule heating, which would have a significant contribution for failures involving high rates, overcharging, or undercharging. Each heat of reaction defined above can be described by the Arrhenius equation where the kinetic parameters are unique for each reaction [102, 106]:

$$k = Ae^{-\frac{E_a}{RT}} \tag{2.2}$$

Where k is the rate constant, A is the frequency factor, E_a is the activation energy, R is the universal gas constant and T is the absolute temperature. For a summary of experimentally determined kinetic parameters for equation 2.2 associated with each of the decomposition reactions mentioned above, the reader is referred to a study by Spotnitz and Franklin[102]. The kinetic parameters determine the 'onset' temperature, or the temperature at which significant degradation occurs. The five heat sources contributing to Q_{tot} have different onset temperatures and subsequent rates and quantities of heat generation, thereby contributing to the magnitude and rate of thermal runaway to different extents. The thermal behaviour of cells during thermal runaway is frequently analysed using differential scanning calorimetry (DSC)[107] or accelerating rate calorimetry (ARC)[107, 108].

Between 90 °C and 120 °C heat generation and gas evolution at the negative electrode occurs due to breakdown of the solid electrolyte interphase (Q_{sei}) and reaction between the lithiated carbon and the electrolyte (Q_{ne})[102, 109, 110]. Continuous exothermic decomposition and reformation of the SEI layer is believed to occur up to the highly exothermic breakdown of the graphite phase (*ca.* 220 °C) when the graphite begins to exfoliate and expose lithium ions that reduce common alkyl carbonate electrolytes[108, 111]. Using a combination of DSC and Gas Chromatography / Mass Spectroscopy (GC/MS) Gachot *et al.*[112] followed the heat and gas output of the degradation reactions between Li_xC_6, and EC-DMC electrolyte during heating. Gachot developed a comprehensive description of the reaction mechanisms that occur between organic solvent electrolyte and graphite electrodes for increasing temperature and different states of lithiation. Since most of the electrolyte is exothermically reduced by exposed lithium ions, the reaction processes are highly dependent on the degree of lithiation of the graphite. Additionally, commonly used lithium salts such as $LiPF_6$ start to exothermically break down at *ca.* 150 °C – 200 °C[56, 58].

At the positive electrode, it is the transition metal oxide (NMC, NCO, LMO) itself that decomposes (Q_{pe}). In general, transition metal oxide positive electrodes are exothermically reduced by the electrolyte between *ca.* 220 °C and *ca.* 300 °C, releasing oxygen[108]. For example, the $LiCoO_2$ positive electrode undergoes exothermic decomposition at elevated temperatures through a series of reduction steps in the presence of electrolyte [113, 114]. As with the negative electrode, the reaction process and onset temperatures are highly dependent on the stoichiometry and composition of the electrode and electrolyte. Generally, the organic electrolytes act as an electron source for the reduction process of the transition metal oxides. The various crystal structures and compositions of common positive electrodes (outlined in Chapter 1) have different thermodynamic stabilities and absolute potentials; hence they undergo exothermic reduction at different temperatures. Using ARC and GC, Golubkov *et al.*[115] recorded the distinctive thermal behaviour of LCO, NMC and LFP (Figure 2-1). The more energy dense materials showed the highest heating rates, heat output, and maximum temperatures; from highest to lowest: LCO, NMC and LFP.

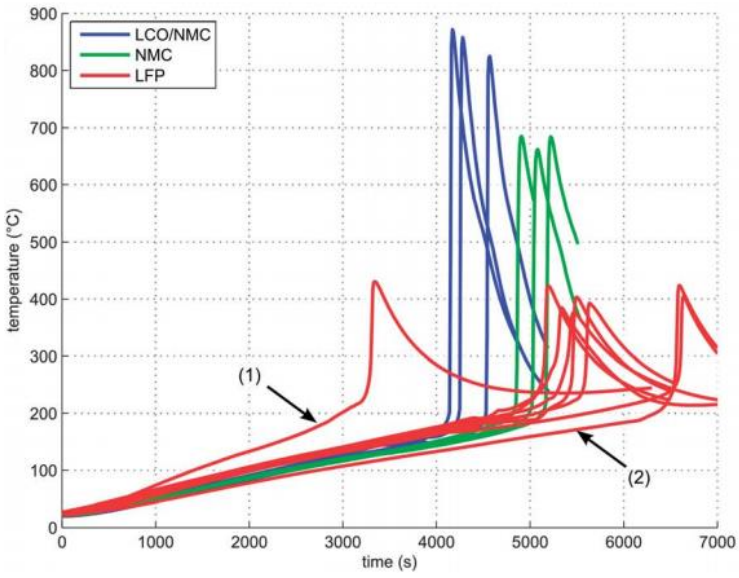

Figure 2-1: Temperature profiles of three different cell chemistries, LCO/NMC (blue), NMC (green) and LFP (red), during heating tests. For completeness, the tests labelled 1 and 2 had slightly different heating rates. Reproduced from[115].

The onset temperature, maximum temperatures reached, and rate of heat generation from the positive electrode are also highly dependent on the state of charge of the lithium-ion cell[116]. With lower lithium content, the absolute potential (hence the oxidation potential) of the transition metal oxide electrode increases, making it more reactive with organic solvent electrolytes. For example, Jhu *et al.*[116] tested commercial LCO 18650 cells at 3.7 V (nominal) and 4.2 V (fully charged), and showed a significantly lower onset temperature (as much as 20 ^{o}C) as well as a higher maximum temperature reached for the fully charged cell (from 402 ^{o}C at 3.7 V to 517 ^{o}C at 4.2 V) during thermal runaway[116]. Charging beyond the full state of charge involves extremely low lithium content in the transition metal oxide resulting in an increased resistance to lithium removal, and increased Joule heating, as Ohsaki *et al.*[117] demonstrated. Entering a state of overcharge can also result in oxidation of the electrolyte, generating gases, and lead to thermal runaway at lower onset temperatures (Figure 2-2)[118].

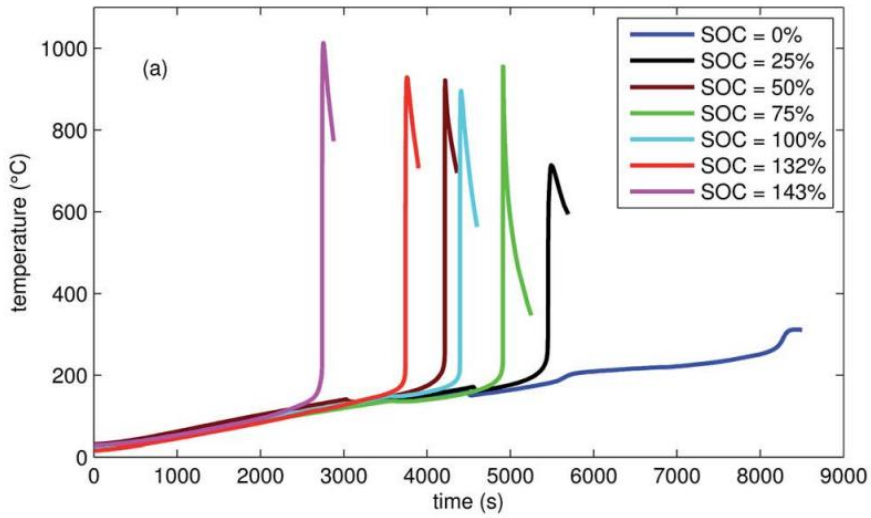

Figure 2-2: Temperature profiles from NCA 18650 cells at different states of charge during a thermal ramp test. Reproduced from[118].

In addition to the positive electrode chemistry, the composition of the electrolyte can also influence the thermal behaviour of a cell (Q_e)[119]. For example, Lin *et al.*[100] demonstrated that the onset temperature for the decomposition of an NMC electrode varied by over 100 °C depending on whether

the electrode was electrolyte-starved or not. In this instance, the concentration of $LiPF_6$ salt also played a significant role in the thermal stability of the electrode assembly. Wang *et al.*[120] also showed that the process of electrolyte degradation is accelerated when exposed to oxygen or moisture. Small impurities of H_2O in the electrolyte, or the release of O_2 from the transition metal oxide can increase the risk of thermal runaway. However, the amount of oxygen evolved from the positive electrode is limited[108], and further supply of oxygen from the surroundings is required for complete combustion of cell contents to occur[56]. Consequently, when commercial cells vent as a result of gas generation during thermal and electrical abuse, the rate of internal degradation reactions is increased and thermal runaway is accelerated.

There have been numerous studies focusing on the reaction pathways of positive electrode materials during failure[114, 121-123], but a spatial and temporal understanding of the reaction processes and their effects on particle microstructure, rate of reaction, and critical temperatures reached during failure, is yet to be achieved. The rate of reaction between the electrolyte and the positive electrode is surface dependent; the specific surface area of the electrode material determines the rate of heat generation during failure. MacNeil *et al.*[124] were the first to perform a comprehensive study on the impact of the surface area of electrode material on the rate of temperature rise during failure, showing a positive relationship. Similarly, Jiang and Dahn[125] used accelerated rate calorimetry to show the effect of particle size on the onset temperature of thermal runaway, demonstrating that a larger particle size is more thermally stable. More recently Geder *et al.*[126] conducted an investigation into the effect of particle size on the thermal stability of electrodes finding a linear relationship between mass decomposition and surface area. A higher mass loss corresponds to increased heat generation during failure, and increased gas (including O_2) evolution, further fuelling decomposition of the electrolyte[127]; smaller particles were shown to release more oxygen and have an oxygen deficiency at their surface. To date, the role of particle shape and size on the thermal stability and behaviour of electrodes during failure is not well understood; this is the focus of Chapter 7 of this thesis, where the change in particle microstructure during failure is examined and the associated consequences

of such changes at the cell level are discussed. Furthermore, the rate of cell heating is also unique for particular cell chemistries and designs; this is discussed further in the following sections.

Common separator materials such as those based on polyethylene and polypropylene start to melt above *ca.* 130 °C, exposing the battery to the risk of local short circuiting and consequent rapid local heating and temperature rise[60, 108]. The occurrence of an internal short circuit is an example of what can instigate the aforementioned exothermic decomposition reactions. Without external intervention the temperature of the cell will continue to increase as exothermic reactions propagate, until complete depletion of reactants. As well as the rate of heat generation, the rate of temperature rise is dependent on the heat dissipation capabilities of the electrodes and cell assemblies; for example, in a comprehensive study performed by Orendorf *et al.*[128] published as a report from Sandia National Labs, a scale dependence of the rate (but not quantity) of heat generation per amp-hour with increasing battery size was observed, which is primarily related to the battery geometry and its heat dissipation capability.

The occurrence of thermal runaway frequently results in catastrophic failures of commercial cells, such as fires and explosions, often with the release of flammable and toxic gases[109, 115, 129]. The evolution of gases from decomposition reactions causes internal pressure build-up (the main cause of explosions), cell bulging and other unfavourable occurrences such as breaking of the SEI layer, and delamination of the electrodes[109, 117]. Gas evolution and its effects on the cell will be discussed in more detail in the following section.

2.2.2. Gas Generation

In a recent report released from Sandia National Labs[128], individual cells and modules of NCA and LFP chemistries were brought to thermal runaway while at 100 % state of charge (SOC) via thermal abuse. Based on the results in this report, approximately 1.5 to 1.8 litres of gas are generated per amp-hour of capacity (L/Ah) of the cells, where the higher values are associated with the lower energy density LFP modules. Currently, the leading (in terms of capacity) 18650 lithium-

ion batteries are > 3 Ah which would correspond to > 4.5 L of gas per cell being generated during thermal runaway. For most combinations of electrodes and electrolytes within commercial lithium-ion batteries, the generated gas contains toxic and flammable components[129]. For example, Golubkov *et al.*[115] measured the gas compositions from LCO, NMC and LFP cells during thermal runaway which are shown in Figure 2-3.

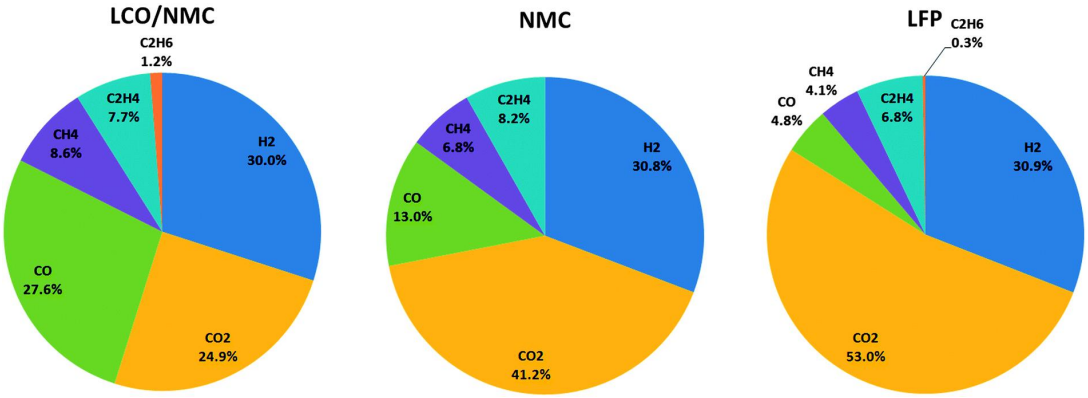

Figure 2-3: Composition of gases generated from thermal runaway of commercial graphite-based 18650 cells at 100 % SOC. For each cell, the electrolyte consisted of a mixture of dimethyl carbonate (DMC), ethylene carbonate (EC), ethyl methyl carbonate (EMC) and propylene carbonate (PC). Reproduced from[115].

The gas evolved from graphite-based 18650 cells follows a similar trend for NMC, LCO, LMO, NCA and LFP positive electrodes[115, 128-130], that being, the majority of the gaseous volume produced during thermal runaway consists of H_2, CO_2, and CO, relatively small amounts of alkanes and alkenes, and trace amounts of fluorides such as HF that stem from decomposition of lithium salts. However, significant differences between the proportions of gases between electrode chemistries occur[130, 131]; de-lithiated CoO_2 showed the greatest oxidation potential whereas Mn_2O_4 was relatively weak. $FePO_4$ was shown to react the least, even at high levels of overcharge due to the strength of the phosphorus-oxygen bond. Gas evolution highly depends on the electrode chemistries and their respective activation energies. The reaction pathways that lead to the volume and composition of generated gases are highly complex, and to date no single study has

determined with certainty, the proportion of gases that stem from individual reactions. However, some of the most likely sources of each gas component are highlighted here.

Production of H_2: A possible source of hydrogen gas during thermal runaway is from the reaction between liberated lithium ions and binder material[115]. As Haik *et al.*[110] demonstrated, when lithiated graphite reaches high temperatures ($> 230\ ^{o}C$) it can start to exfoliate and expose lithium ions. Common binder materials such as polyvinylidene fluoride (PVdF) and carboxymethyl cellulose (CMC)[132] can react with lithium with the release of hydrogen gas:

$$(\text{-}CH_2\text{-}CF_2\text{-})+Li \xrightarrow{\Delta H} LiF+(\text{-}CH{=}CF\text{-})+0.5H_2 \tag{2.3}$$

$$(CMC\text{-}OH)+Li \xrightarrow{\Delta H} (CMC\text{-}OLi)+0.5H_2 \tag{2.4}$$

Production of CO_2: There are several reactions that result in the production of CO_2. For example, thermally-induced decomposition of the SEI layer can produce CO_2, as well as C_2H_4 and O_2:

$$(CH_2OCO_2Li)_2 \xrightarrow{\Delta H} Li_2CO_3+C_2H_4+CO_2+0.5O_2 \tag{2.5}$$

During the break-down and reformation of the SEI layer, the electrolyte solvent can be reduced if it comes into contact with the exposed positive electrode material, releasing CO_2; this becomes particularly prevalent in a state of overcharge[117, 133]. Reactions between the SEI layer and decomposition products or impurities such as HF or H_2O, also produce CO_2:

$$2ROCO_2Li+H_2O \xrightarrow{\Delta H} 2ROH+Li_2CO_3+CO_2 \tag{2.6}$$

$$ROCO_2Li+HF \xrightarrow{\Delta H} ROH+CO_2+LiF \tag{2.7}$$

H_2O can also react with organic solvents and $LiPF_6$, producing more CO_2 and HF[134]. Onuki *et al.*[135] showed that the extent of CO_2 evolution from this mechanism is highly dependent on the solvent used; for example, EC produces

significantly more CO_2 than DEC[135]. In addition, in the presence of O_2, organic solvents such as EC can combust at high temperatures to produce CO_2[102, 136], where oxygen may be present from impurities in the cell, through venting or rupture of the cell, or as products of the decomposition of positive electrode materials[137].

$$C_3H_4O_3(EC)+2.5O_2 \xrightarrow{\Delta H} 3CO_2+2H_2O \tag{2.8}$$

Kong *et al.*[130] observed a significant increase in the quantity of CO_2 generated during states of overcharge, which is thought to be caused by the increased O_2 evolution at higher states of charge.

Production of CO: It is thought that the main source of CO is the partial oxidation of EC[133, 135]. Sloop *et al.*[138] and Onuki *et al.*[135] highlight that another possible mechanism for CO production is the reduction of CO_2 by exposed Li^+ ions at the negative electrode:

$$2CO_2+2Li^++2e^- \xrightarrow{\Delta H} Li_2CO_3+CO \tag{2.9}$$

Production of CH_4, C_2H_4 and C_2H_6: The alkane and alkene constituents mostly arise from the reduction of the organic solvent by lithium to form lithium carbonate. For example, CH_4 is produced during the reduction of DMC in the presence of hydrogen:

$$C_3H_6O_3(DMC)+2Li^++2e^-+H_2 \xrightarrow{\Delta H} Li_2CO_3+2CH_4 \tag{2.10}$$

C_2H_4 is produced from the reaction between EC and lithium[115, 133, 135]:

$$2Li+C_3H_4O_3(EC) \xrightarrow{\Delta H} Li_2CO_3+C_2H_4 \tag{2.10}$$

Similarly, C_2H_6 is generated from the reaction between DEC and lithium[115, 133, 135]:

$$2Li+C_3H_6O_3(DMC) \xrightarrow{\Delta H} Li_2CO_3+C_2H_6 \tag{2.11}$$

Given the quantity and compositions of generated gas outlined before, certain precautions are required before thermal runaway can be safely contained. This is particularly important for applications that require a large capacity of lithium-ion batteries such as electric vehicles, but also in the design of experiments and risk assessments for experimental testing. As Ribiere *et al.*[129] discuss, along with the primary toxic component CO, there are also trace amounts of other toxic components that together, typically make up < 0.5 % of the generated gas. These can include highly toxic constituents such as HCl, HF and NO. The exposure limits of these components are very low and sufficient containment or ventilation strategies should be in place to cater for thermal runaway of cells and not exceed exposure limits, which can become particularly challenging for large modules. Furthermore, an inherent risk associated with the generation of gases in commercial cell designs is the build-up of pressure, particularly in the steel cylindrical cases of commercial 18650 batteries that can explode if too much pressure builds up inside[116]. As seen in a study by Yufit *et al.*[139], swelling of lithium-ion prismatic or pouch cells occurs as a result of internal gas generation, this can be highly unpredictable due to the wide range of commercial cell designs, compositions, states of charge, operating conditions and failure mechanisms[140]. Consequently, abuse testing is performed on commercial battery designs under a range of conditions to test their overall safety and reliability. Commercial battery designs incorporate a number of safety mechanisms that help mitigate or avoid the risks associated with gas generation and pressure build-up, which will be discussed further in the following sections.

2.3. Mitigation Methods and Safety

2.3.1. Commercial Battery Designs

The most common designs of rechargeable lithium-ion batteries are the cylindrical cells and pouch cells. During manufacturing, the positive and negative electrode materials are mixed with binder, conductive carbon and solvent to generate a paste[141]. The paste is spread onto both sides of a current collecting material

(typically graphite paste onto Cu foil and positive electrode paste onto the Al foil). The preparation of the electrode materials then differs depending on the design of the cell. For example, the material can be wound up into a spiral for cylindrical cells, or cut and placed in layers for pouch cells.

Cylindrical cell: There are a range of dimensions of cylindrical cells, the most common, and the predominant type that is examined in this thesis, is the 18650 cylindrical cell which has a diameter of 18 mm and height of 65 mm (Figure 2-4a). The popularity of cylindrical cells stems from their high mechanical strength, safety and cost effectiveness. 18650 cells have been used since lithium-ion batteries were first commercialised[142] and are still used today for advanced applications such as for robotics and space applications, as described by Yayathi *et al.*[8]. The cells are manufactured by winding the positive and negative electrode materials separated by an electrolyte-soaked separator into a spiral (Figure 2-4b,c). The positive electrode current collector material (typically Al) is connected to the cap (positive terminal) of the battery while the negative electrode current collector (typically Cu) is connected to the steel or aluminium casing, which is isolated from the cap by an insulating ring.

Insulators, pressure relief disks, and safety devices are crimped onto the end of the casing (Figure 2-4a). The steel or aluminium casing can withstand high internal pressures, the relief vent directs built up gases in a known direction out of the cell, and the presence of thermal and electrical safety devices help prevent and mitigate thermal runaway and unfavourable states of charge. Consequently, 18650 batteries are relatively safe, however under extreme conditions rapid gas generation and pressure build-up can occur, leading to violent ruptures and explosions, due to the cylinder turning into a pressurised vessel[116, 143]. The additional safety devices and components within 18650 cells also reduce their volumetric and gravimetric energy density.

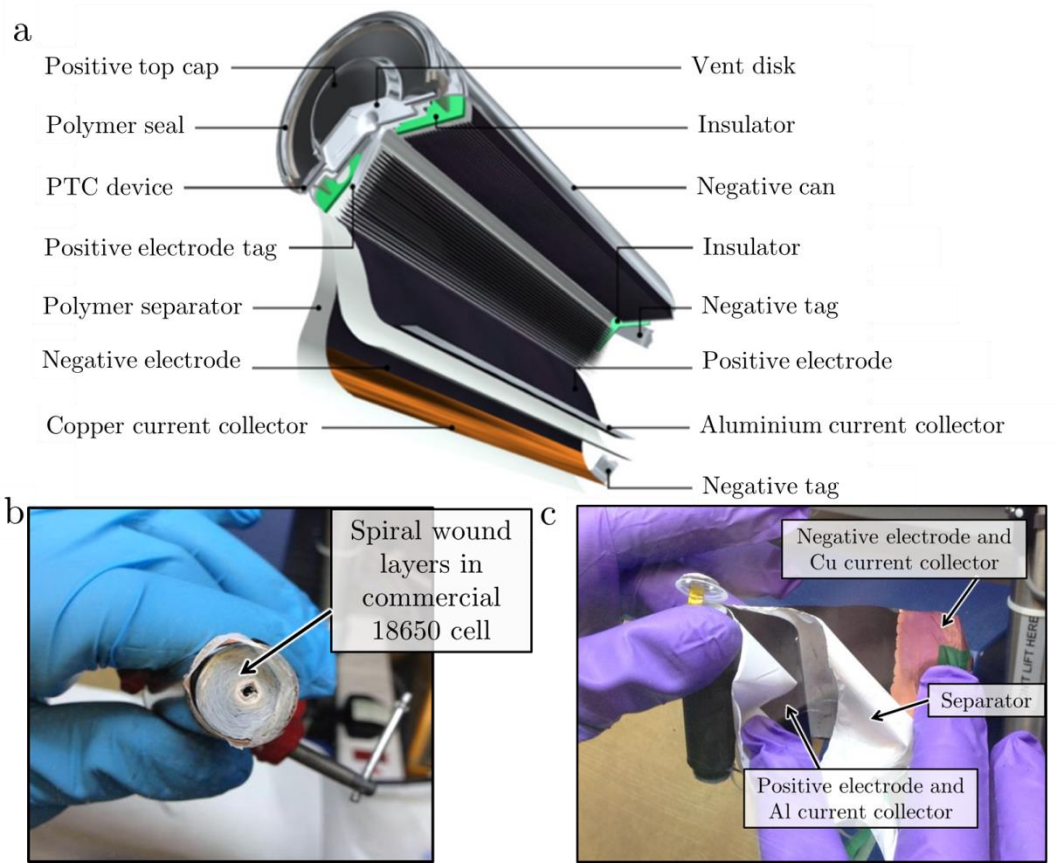

Figure 2-4: (a) Cylindrical 18650 cell with labelled components. Image is courtesy of E. Darcy, NASA. (b) Internal structure of cylindrical 18650 cell showing spiral wound layers and (c) unravelled spiral wound layers showing the Cu current collector coated with negative electrode graphite material, the Al current collector coated with positive electrode material, and the electrolyte saturated separator material.

Pouch cell: Pouch cells are enclosed by a heat-sealed multilayer foil (Figure 2-5a). The positive and negative electrodes are layered as alternating lamellae (Figure 2-5b,c) and the current collecting layers are welded to the outer positive and negative terminals. The pouch cell is compact, light-weight and flexible which gives it inherent advantages for packing, cooling and volumetric energy density. An inherent disadvantage of this design is its lack of structural support; pouch cells can be easily crushed, punctured and physically damaged due to their thin and flexible housing. However, the safety of these cells can be improved in systems by designing appropriate containment and fitting safety devices on the module or

pack. Pouch cells are unconstrained and swell when gas forms inside the cell[139, 144]. Consequently, operating outside the recommended conditions can result in significant distortions in the cell's architecture.

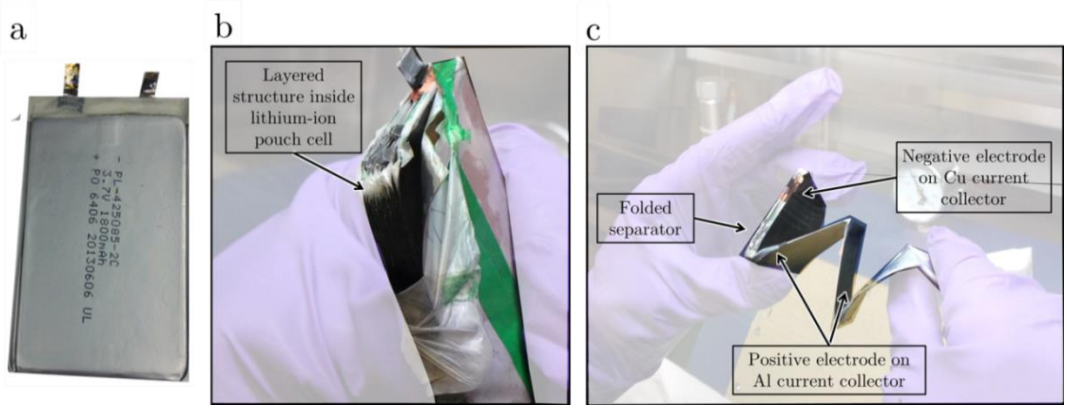

Figure 2-5: (a) Commercial lithium-ion pouch cell, (b) internal layered structure and (c) unfolded layered structure showing the Al and Cu current collectors coated on both sides with electrode material.

2.3.2. Safety Mechanisms

Since their commercialisation, safety has always been a huge concern for battery manufacturers with safety devices being incorporated into the very first commercial lithium-ion cells[142]. Today, lithium-ion batteries must pass several safety tests before being certified for commercialisation. Separately or combined, heat and gas production are the two primary factors that determine the hazardous nature of battery failure[9]. The safety of a battery system can be improved by first avoiding the conditions leading to heat and gas production, and secondly by managing the heat and gas production to mitigate the consequences of failure. Commercial lithium-ion cells have adopted several safety devices to help avoid conditions that are likely to lead to failure, in particular overheating, high current flows, and states of over- or undercharge. Consequences of failure are mitigated by pressure release, controlled ejection of contents, and heat dissipation. As Balakrishnan *et al.*[145] discuss, the following safety features are commonly found in commercial lithium-ion batteries and help prevent against and ease the consequences of thermal runaway:

Safety Vents and Current Interrupt Device: Vents allow the safe release of gas if there is a significant build-up of pressure within the cell. The bursting disk usually takes the form of a domed aluminium plate (see vent in Figure 2-6a-d). In most modern 18650 cells, the safety vent has a secondary role of acting as a current interrupt device (CID) where the aluminium plate is part of the circuit to the positive terminal; when gas builds up within the cell, the domed aluminium plate displaces away from the positive terminal, breaking the circuit and preventing any further current from flowing. Thereafter, if gas continues to build up, the dome bursts in a controlled direction, avoiding what would otherwise be a dangerous rupture of the metallic cylindrical casing. Recently, Coman *et al.*[146] developed a model of the venting process of an 18650 cell, showing that the release of pressure and gas significantly contributes to the heat dissipation and cooling of the cell, thereby reducing the risk of subsequent thermal runaway. The activation of the safety vent can result in the release of flammable and toxic organics; hence, this device is used as a back-up safety device (after the current is cut off). Other reversible devices such as the positive temperature coefficient (PTC) device are designed to activate long before venting occurs. As shown in Figure 2-6, there are numerous designs of vents and CIDs. It is well known that 18650 batteries sometimes burst (explode) during thermal runaway, where the CID and other components within the crimp detach and the electrode assembly ejects. This process is not well understood, however it is likely to arise from the vent region becoming clogged during failure[115]. To uncover the cause and occurrence of vent clogging and cell bursting, it is necessary to non-invasively see inside the cell at the moments leading up to and during failure. In Chapter 7 of this thesis, the effectiveness of various vent designs in improving the safety of 18650 cells is examined via high speed X-ray imaging.

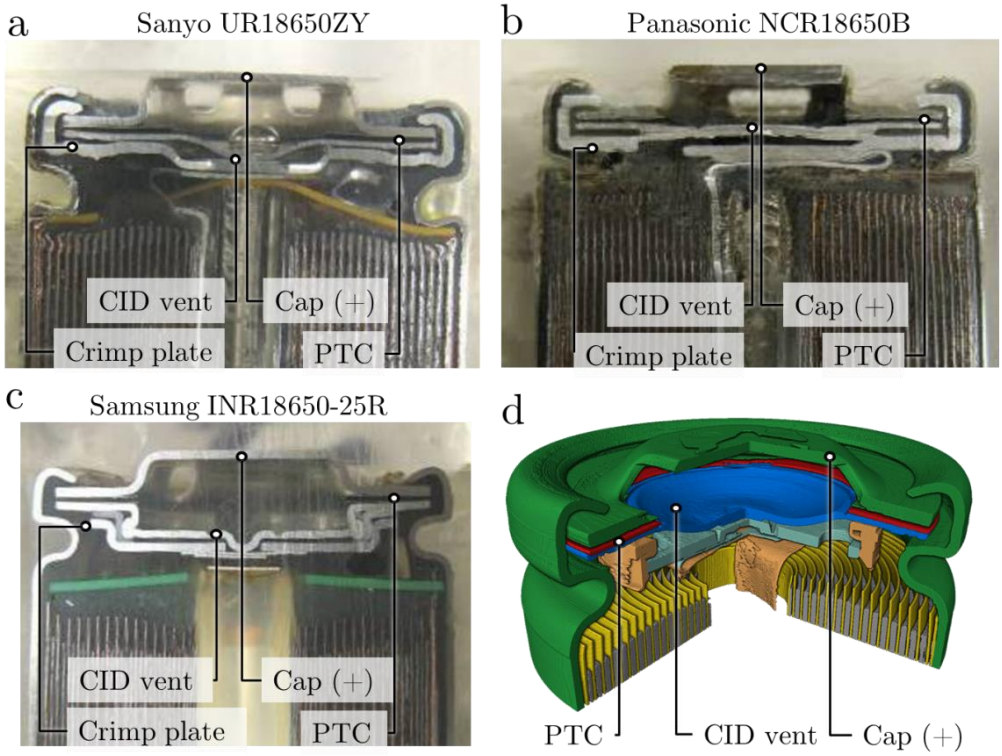

Figure 2-6: (a-d) Cross sectioned views of three commercial 18650 lithium-ion batteries showing the placement of the vent and current interrupt device (CID) and the positive temperature coefficient (PTC) device. Images are courtesy of E. Darcy, NASA. (d) Reconstructed tomogram of the cap of a commercial 18650 battery giving a 3D perspective of the integrated safety devices.

Positive Temperature Coefficient Device: A positive temperature coefficient (PTC) current limiting material is integrated into the batteries' internal circuit to protect against unwanted high currents, such as those that would occur as a result of an external short circuit[9, 145]. Within 18650 cells, the PTC usually consists of a conductive polymer annulus laminated on both sides with a metal (Figure 2-6d). The conductive polymer (polyethylene) contains embedded conductive particles that complete a conducting path (Figure 2-7). At elevated temperature the polymer changes state when it begins to melt (typically *ca.* 125 ^{o}C). The accompanying expansion results in a breakage of the conductive pathway (Figure 2-7) and rapidly increases the resistance of the material. Joule heating plays a large role in activating the device; for this reason, PTCs are not often found in high-rate

lithium-ion batteries. For example, Robinson *et al.*[147] showed that large temperature rises can occur at the PTC while operating at high rates due to Joule heating.

PTC devices are either crimped into the shell casing of 18650 cells or attached to a terminal in pouch cells, both of which risk a delayed response to a temperature rise of the active material. For example, at high charge and discharge rates, the core of the battery consisting of active electrode material will rapidly rise in temperature with a delayed thermal response of the battery casing. This can result in local pin-holes and uneven shutdown in the separator causing internal short circuits. The PTC may activate soon after this, but the internal short circuit will continue to generate heat and can lead to thermal runaway. Feng *et al.*[148] incorporated an epoxy carbon PTC material between the $LiCoO_2$ electrode and current collector, providing a more instant and local response to electrical abuse. However, incorporating PTC material into active material reduces the energy density of the cell, an important feature for commercialisation.

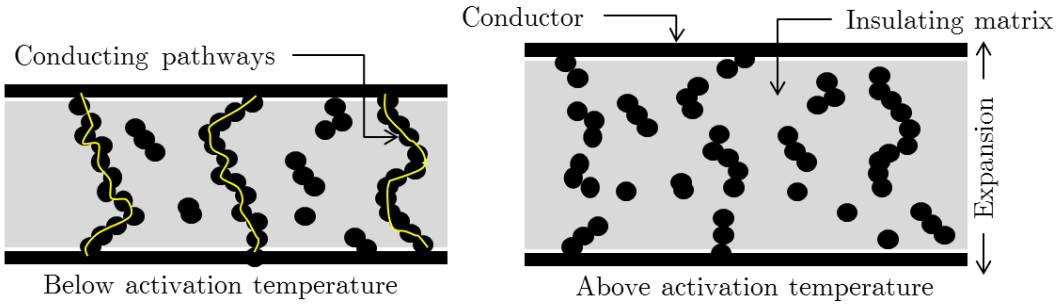

Figure 2-7: Illustration demonstrating the principle of a conductive polymer positive temperature coefficient (PTC) device.

Shutdown Separator: As outlined in Chapter 1, at elevated temperatures (*ca.* 130 °C) the separator between the positive and negative electrode softens and the pores close, preventing the flow of ions and thus ceasing the current flow. However, there can also be a delayed response from the separator and uneven shutdown, causing increased local current flow. The separator can also distort and fully melt at higher temperatures (*ca.* 160 °C for the most common separators) resulting in internal short circuits. The melting-induced shutdown mechanism has also been

applied in a different way by Baginska *et al.*[149] who incorporated thermo-responsive polymer microspheres in electrode materials; the polymer microspheres melt at a certain temperature and coat the electrode surface with a non-ionic conducting polymer layer.

Battery Management System: As highlighted, lithium-ion batteries are stable within certain voltage and temperature ranges, where the safety and performance of the cell can be compromised if either condition is exceeded. An external battery management system (BMS) is often incorporated into battery modules and devices to monitor the state of the battery pack and its environment, and counteract any unfavourable parameters to keep the battery operating within its window of stability. However, a BMS can have one or more functions[150]; the overall aim of a BMS is to maintain favourable operating conditions, which may include measurement and control of one or more of the following: temperature, rates, voltages, capacities, or states of health (SOH). Control of such parameters in modules may also involve individual cell measurements and equalisation strategies through sophisticated modelling algorithms (that are beyond the scope of this review)[150].

When combined, the separator, PTC, CID and BMS significantly improve the safety of battery systems. For example, Figure 2-8 shows an event tree that demonstrates how, up to a critical temperature, the safety devices can help avoid and mitigate the consequences of thermal runaway. In particular, these devices are very effective in protecting the cell against external thermal or electrical abuse, that are the primary causes of battery failures. However, despite the efficacy of these devices in protecting against external phenomena, the occurrence of internal short circuits, which can be caused by the presence of contaminated or defective cells[151], remains a risk. In addition, the aforementioned safety devices are not present in all cells; for example, pouch and prismatic cells tend not to contain a CID or vent, start to swell during gas generation and eventually burst[152].

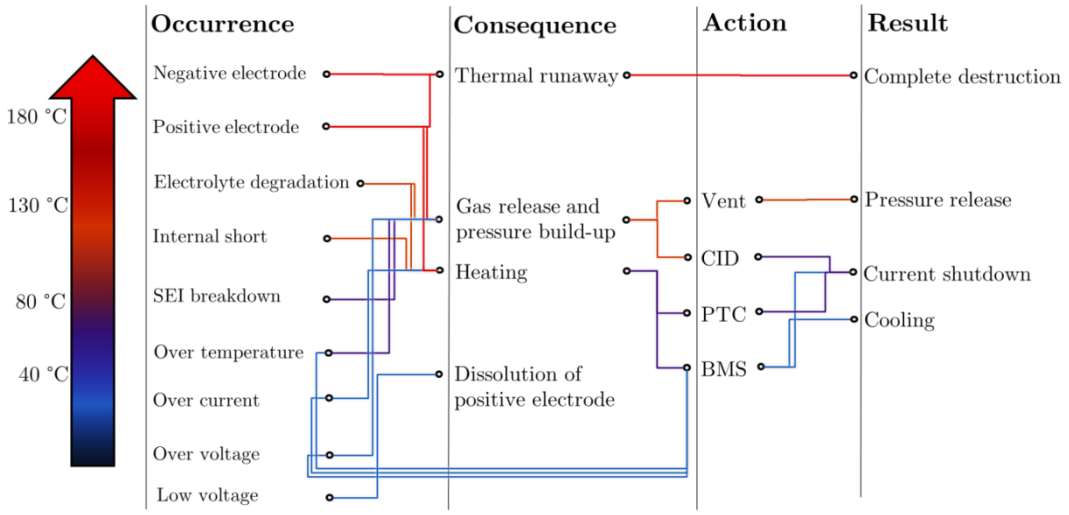

Figure 2-8: Event tree connecting occurrences within an 18650 lithium-ion battery to the activation of safety devices, and ultimate outcome.

2.4. Internal Short Circuits

Internal short circuits occur when a negative component (electrode or current collector) makes contact with a positive component[151]. This typically results in a rapid discharge of the cell with rapid local heat generation. The magnitude of the internal short circuit and the associated risk of thermal runaway depends on the electronic and heat conduction properties of the materials that make contact[153, 154]; if two materials with high electronic conductivities (e.g. positive and negative metallic current collectors) make contact, the rate of discharge and Ohmic heating is high. In contrast, if the positive electrode material (which is often a relatively poor electronic conductor) connects with the negative electrode material, the rate of discharge and local heating is relatively low. The thermal conductivity of the materials involved in the short circuit also play a crucial role in determining the likelihood of thermal runaway; if heat dissipates quickly, then the risk of ignition is lowered.

Internal short circuits are challenging to replicate since their occurrence is unpredictable and does not require any external influence (mechanical, thermal or electrical). Until recently, most attempts to reproduce an internal short circuit involved mechanical force. For example, Maleki *et al.*[155] induced internal short

circuits by pinching, blunt crushing and nail penetration of commercial pouch cells. However, none of these methods provides any control over the type of internal short circuit that occurs (the combination of materials that make contact), and inherently involve distortion of the cell's architecture as well as introducing additional heat sinks. More recently, Orendorff *et al.*[156] incorporated a low melting point alloy (Sn/Bi/In alloy that melts at 70 °C) between the positive electrode and the separator, inducing a local internal short circuit by melting the metal and allowing it to connect the electrodes via the separator. However, at the time, this method did not yet yield reproducible results. In Chapter 7, efforts to replicate and capture the occurrence of an internal short are presented. A novel integrated short circuiting device, developed by Keyser *et al.*[157] is described and utilised.

2.5. The Role of Failure Characterisation

If stored and operated within safe limits, the failure rate of lithium-ion batteries is estimated to be *ca.* 1 in 40 million[9]. However, unforeseen circumstances such as accidental short circuiting, overcharging and mechanical abuse can still result in catastrophic battery failure. Despite the variety of safety mechanisms included in commercial lithium-ion batteries[145], there have been numerous high-profile battery failure incidents, many of which have caused significant set-backs for commercial products and enterprises. Such occurrences, although statistically improbable, have had a profoundly negative effect on public perception of battery-powered vehicles and devices. Table 2-1 lists some of the recent high-profile occurrences.

Table 2-1: High profile lithium-ion battery failures in recent years.

Date	Incident	Cause
3 Sep 2010	Boeing cargo plane crashed due to lithium-ion battery cargo catching fire, Dubai	Overheating and combustion of packaged lithium-ion batteries
18 July 2011	EV bus catches fire, Shanghai, China	Overheat and thermal runaway of $LiFePO_4$ batteries
2011-2012	Numerous Galaxy S and IPhone4 smartphones catch fire	Overheating
7 Jan 2013	Fire on-board Boeing 787 Dreamliner[158], Boston, USA	Short circuiting and thermal runaway
1 Oct 2013	Tesla Model S electric car catches fire, Washington State, USA	Short circuiting after debris punctured the battery pack
6 Nov 2013	Tesla Model S electric car catches fire, Tennessee State, USA	Short circuiting after a tow hitch punctured the battery pack
20 Mar 2014	Lenovo recalls laptop batteries	Manufacturing error caused the batteries to overheat
1 Sept 2016	Samsung Note 7 smartphones catching fire	Yet to be confirmed

For a more detailed overview of incidents involving lithium-ion batteries failing, the reader is referred to a review by Lisbona *et al.*[159]. Following the numerous dangerous incidents that stem from lithium-ion battery failures, regulations for transport and storage of lithium-ion batteries have been revised. Effective from the 1st of April 2016, the International Civil Aviation Organisation (ICAO) prohibited the shipment of lithium-ion batteries as cargo on passenger airplanes. When batteries are shipped on "cargo-only" aircrafts they must be in a state of less than 30 % state of charge (SOC). A list of the recent amendments can be found on the International Air Transport Association (IATA) website[160]. The

profoundly damaging effects that battery failures can have on commercial products has also made private enterprises revise their product designs to further reduce the risk of battery failure. For example, improved containment of the battery failure on the Boeing Dreamliners could have eliminated the immediate danger, and possibly avoided grounding the entire fleet of aircraft[7]. Each individual cell needs to be thoroughly tested and its failure mechanisms characterised to engineer suitable containment systems. Standard tests provide the minimum safety threshold of lithium-ion batteries, both for individual cells and for specific applications. However, further understanding of the risks associated with battery failure is needed to engineer appropriate safety systems such as containment, venting and fire suppression systems. This involves rigorous abuse testing of cells, understanding how and why specific designs behave under extreme conditions, and acting to mitigate the consequences.

2.6. Abuse Testing and Standards

Safety test standards for lithium-ion batteries define criteria outside the safe operating limits to determine the response of particular types of lithium-ion cells. The cell is accepted for use if its response satisfies the safety criteria defined by the standard. Testing standard criteria aim to recreate realistic conditions which lithium-ion batteries could experience during their life-time in order to provide manufactures with information on their behaviour under well-defined abuse conditions. The most well-known and widely used international testing standards for lithium-ion batteries are:

- UN/DOT 38.3, which defines standard tests for transport of lithium-ion batteries[161].
- IEC 62133, which defines standard tests for IEC-devices[162].
- UL 2054 and UL 1642, which define standard tests for electronic devices[163, 164].

In addition to the three testing standards above, the FreedomCAR, SAND99-0497 and EUCAR abuse test manuals are also often used for failure

characterisation. The FreedomCAR[165] and SAND99-0497[166] testing criteria are not strict standards, but are intended to provide information on cell's behaviour under extreme conditions, with the aim of engineering safer systems and modules[167]. The UN, IEC and UL standards are based on pass/fail tests and do not provide as much information about the cell's behaviour. Each test standard breaks down into three categories; thermal abuse, electrical abuse and mechanical abuse.

2.6.1. Thermal Abuse

Across the different standards, thermal abuse tests range from moderate to extreme. For example, the UN test standard requires a cell (at 100 % SOC) to be stored at 72 °C and -40 °C for 6 hours, where the pass criteria requires no leakage, maintaining mechanical integrity, and staying above 90 % of the original voltage. In a similar temperature range, the FreedomCAR and SAND99 suggest elevated storage at temperature from 40 °C to 80 °C for a period of two months whilst monitoring voltage, gas release, and resistance.

At intermediate temperatures, the UL and IEC tests require a cell to maintain its mechanical integrity (not venting or undergoing thermal runaway) while being stored at 100 % SOC for 10 minutes at 130 °C. SAND99 suggest ramping the temperature of the cell at increments of 5 °C per 30 minutes until thermal runaway, while continuously monitoring voltage, temperature, resistance and associated times where gases are released. This is similar to the procedure carried out by most ARC tests[115, 118].

The FreedomCAR testing manual suggests recording the voltage and temperature of the cell during a simulated fire (890 °C for 10 minutes), as well as post-failure gas composition analyses and video recording for comprehensive characterisation of the cell's behaviour. The simulated fire approach was adopted by Huang *et al.*[168] and Ribiere *et al.*[129] for testing lithium-ion cells and modules, while monitoring onset temperatures, gas compositions, heat release, and mass loss. The thermal and gas analyses gave valuable information for the design of safe large-scale storage systems. The UL standards have a similarly extreme

temperature test where a cell is exposed to a flame, and projectiles from the cell during thermal runaway must not puncture a surrounding mesh. In Chapters 6 and 8, 18650 lithium-ion batteries are subject to extreme temperatures which would be similar to those experienced by the cell during a simulated fire test. Given that projectiles are a major risk and determine whether a cell passes UL test standards, particular attention is paid to identifying the root cause of projectiles in Chapters 6 and 8.

2.6.2. Electrical Abuse

Electrical abuse tests for lithium-ion batteries include high-rate charge and discharge, as well as entering states of overcharge or undercharge. The high-rate discharge tests involve external short circuiting. The severity of the short circuit differs between standards; the IEC and UL test standards specify a short on a circuit with 20 mΩ resistance until the cell reaches < 0.2 V, whereas the UN standards specify a resistance of 500 mΩ. In each case, the cell must not rupture, catch fire, explode, disassemble or reach over 170 °C. The FreedomCAR and SAND99 manuals suggest monitoring gas compositions, voltages, resistance and temperature during these tests, as well as taking pre- and post-test photographs.

Overcharge abuse tests greatly vary between standards. For example, the IEC standard has the most lenient overcharge, requiring 4.2 V cells to be charged to 5 V and held for 7 days. As Ohsaki *et al.*[117] demonstrated, a delayed thermal runaway response can occur when a cell is left in a state of overcharge due to the rapid increase in reaction rate as the positive electrode begins to break down at elevated temperatures. The UN test specifies charging to twice the maximum voltage recommended by manufacturers, whereas the most extreme test, which can be found within the UL standards, requires cells to be charged at three times their maximum recommended rate for 7 hours or until failure; the cells must not rupture, catch fire or explode during this test. In Chapter 7, an overcharge abuse test similar to that specified by the UL standards is carried out on a commercial prismatic cell.

The FreedomCAR and IEC tests also describe reversing voltages of cells, and testing cell's behaviour when they undergo an external short circuit as part of a module. The IEC have also introduced an internal short circuiting test which, to date, has only been used in Korea, Switzerland, France and Japan. This test involves removing the electrode assembly from its casing, inserting an L-shaped nickel particle between the positive electrode and separator one layer deep into the assembly, placing the assembly in a sealed bag to be stored in an oven for 45 minutes at 45 °C, removing the assembly and compressing the assembly until the voltage drops by more than 50 mV or 800 N (for cylindrical cells) or 400 N (prismatic cells) is applied. To pass, the assembly must not catch fire or explode. This method does not provide information about the actual cell's behaviour during an internal short, which would be determined by the cell design and integrated safety devices. Orendorff *et al.*[156] attempted to replicate an internal short circuit by placing a low melting point metal tab between the surface of the positive electrode and the separator, which when melted would penetrate through the pore structure of the separator and connect the positive and negative electrodes, causing a short circuit. This approach allowed full cell assemblies to be tested, but has not yet proven to be reliable. In Chapter 8 of this thesis, an internal short circuiting device that consistently short circuits cells is incorporated into commercial cell designs and the failure mechanisms are examined.

2.6.3. Mechanical Abuse

Mechanical abuse tests aim to replicate scenarios where commercial cells are subject to extreme mechanical force or shock, and typically involve the cells being crushed, impacted, shocked, vibrated or penetrated. The mechanical abuse tests are similar between the standards. For example, the UL, UN and IEC tests each specify applying a force of 13 kN using a flat plate to crush a cell, either until it fails, the flat plate applies a force of 13 kN, or the cell deforms by 10 - 15 %. The impact test between the UL and UN standards both specify a mass of 9.1 kg being dropped onto a 15 mm diameter cylindrical bar placed on top of the cell, from a height of 0.6 m. Rigid rod indentation and compression between flat plates were

performed by Sahraei *et al.*[169] who used the experimental data to verify that their failure model could accurately predict when a short circuit would occur.

The UL and UN standards specify shock tests that range from subjecting the cell to 75 g (where 'g' is a multiple of the acceleration of standard gravity, 9.81 N per kilogram) to 175 g with varying numbers of repeats, where the cell should not catch fire or explode. The UN and UL standards also require vibration tests where individual cells are vibrated up to 50 Hz (UN) - 55 Hz (UL) with amplitude of 0.8 mm for 18 repeats of 15 minutes (UN) or continuously for 90 minutes (UL). The IEC standards require a free-fall test from a height of 1 m, where the cell should not catch fire, leak or explode.

The FreedomCAR and SAND99 testing manuals also include a nail penetration test, however this is not included in the IEC, UN or UL standards due to the high variability in test results and its vague relation to specific field failures. The nail penetration test is also not representative of how a cell would behave when undergoing an internal short, but as suggested by the FreedomCAR manual, by gathering information on the gas compositions, temperatures reached, the mechanical behaviour of the cell (via high-speed imaging and photography), and voltages, manufactures can gain an understanding of how a specific cell would behave when punctured. Lamb and Orendorff[170] compared blunt rod and nail penetration tests to examine the types of failure that can occur in 18650 and pouch cells when punctured. In addition to the external measurements of temperature and heat release, Hatchard *et al.*[171] developed a "smart nail" that had a fast response thermocouple situated beneath the surface of the nail tip. This allows internal temperature measurement during nail penetration tests, which can differ from surface temperatures by over 100 °C.

2.7. X-ray Imaging of Internal Events

The fast reaction kinetics between the electrolyte and the positive electrode lead to generation of heat at a very high rate, which can result in internal temperatures of commercial cells reaching in excess of 1000 °C[63], damaging and by-passing integrated safety devices[145, 172], and posing a great risk to modular systems

where cell-to-cell propagation of failure is a major concern[173]. Sprays and hot projectiles are among the primary risks associated with lithium-ion battery failure, as well as toxic/flammable gases from reactions, high temperatures, and high quantities and rates of heat generation. As outlined in this chapter, most published research has involved 'external' measurements to characterise battery failure; for example, calorimetry has mostly been used to quantify overall heat output, temperature measurements are typically point measurements using thermocouples, and gas analyses are performed *ex-situ*. These experiments do not provide any information on the heterogeneous heat or temperature distribution within a cell during failure[8]. However, the occurrences within the cell play a large role in determining the hazardous nature of the battery failure; vent clogging can lead to rapid build-up of heat and pressure[146], leading to battery rupture and ejection of contents [63, 143]; furthermore, side-wall ruptures can spray hot material onto neighbouring cells causing propagation of thermal runaway. Heat generation as well as projectiles and sprays, are inherently linked to internal phenomena e.g. the cell may not burst if the vent does not clog, and may not undergo side-wall rupture if heat generation is not localised next to the surface of the battery casing. The reliability and safety of lithium-ion batteries is considered a function of the entirety of the cell or modular system. Understanding the link between behaviour on the microscale and the catastrophic effects observed for full cells and modular systems is imperative to progress towards safer battery designs. It is therefore essential to characterise the structural dynamics inside commercial lithium-ion batteries, across multiple length scales, to further understand failure mechanisms and the influence of safety devices on the outcomes of battery failure.

X-ray radiography and tomography have proven to be effective non-destructive diagnostic tools for inspecting the internal architecture of materials and devices[174]. X-ray CT has previously been used to explore the microstructural properties of electrode materials in lithium-ion batteries[74, 175-178] across multiple length scales, achieving down to sub-micron resolutions[176]. For example, Shearing *et al.*[177] used a lab-based X-ray CT system to capture and quantify the microstructural properties of a graphite electrode; this X-ray CT scan took over 4 hours and was performed *ex-situ*. Similarly, Ebner *et al.*[179] used X-ray CT to

capture in 3D the microstructure of an NMC electrode, creating a particle size distribution and identifying subsurface cracks. In this study, Ebner *et al.* used a synchrotron source to capture tomograms over a much shorter time period than what is achievable using a lab-based system, where the image acquisition took only 20 minutes. In a following study, Ebner *et al.*[81] then used synchrotron CT to capture tomograms of SnO particles every 15 minutes during a 12-hour lithiation process followed by a 5-hour delithiation process. From the change in the X-ray attenuation of the particles, the local lithium content could be estimated, and consecutive tomograms allowed 3D visualisation of crack propagation and degradation (Figure 2-9). Similarly, Chen-Wiegart[180] used *operando* tomography to capture the structural degradation of $LiVO_2$ when exposed to air.

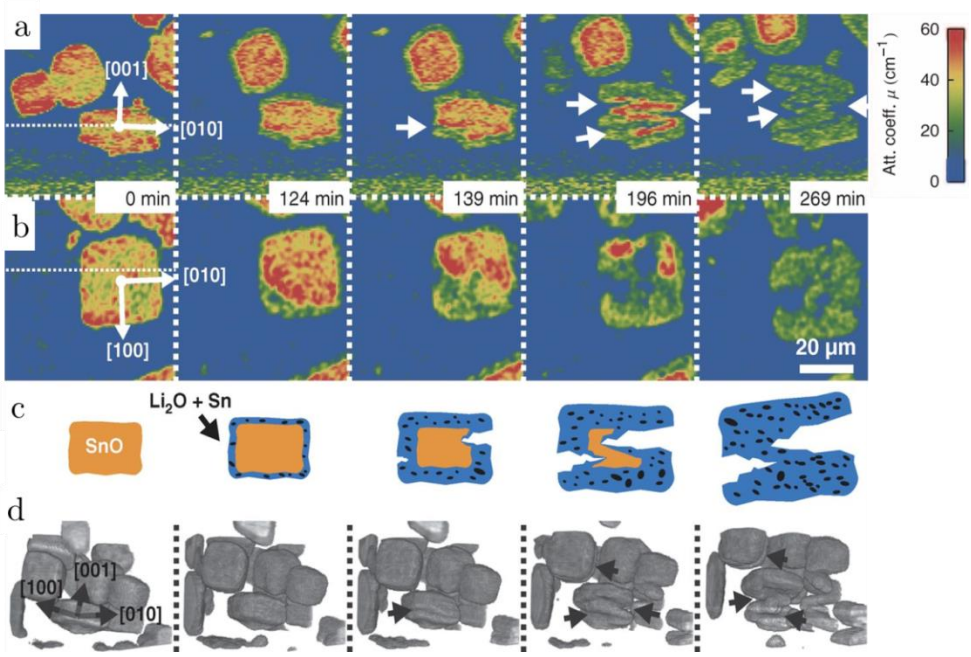

Figure 2-9: (a,b) Cross sections of SnO particles during lithiation, where the horizontal dotted lines at 0 min indicate the cutting planes and the white arrows point out crack locations. (c) Illustrations showing the process of crack growth in a zig-zag pattern. (d) 3D reconstructions of the SnO particles showing the zig-zag crack growth progression (indicated by the black arrows). From [81], reprinted with permission from AAAS.

Until recently, X-ray CT of weakly attenuating materials such as lithium metal, graphite, and polymer separators remained challenging. However, in a recent pair of publications by Eastwood *et al.*[175, 181] and another by Taiwo *et al.*[182], the application of advanced X-ray imaging techniques for enhancing structural features and improving the contrast of weakly attenuating materials has been demonstrated. In these three studies, the architectures of graphite electrodes and lithium dendrites were characterised, presenting scope for further application of contrast enhancement techniques to *operando* studies and to other challenging materials such as characterisation of polymer separator microstructures; this is the focus of Chapter 4.

With regard to battery failure, most applications of X-ray tomography to date were for *post-mortem* analyses [139, 170]. Some *in-situ* or *operando* X-ray imaging experiments have been performed to characterise battery degradation, but were carried out using bespoke cells [81, 183] which do not capture the degradation and failure scenarios that occur inside commercial cells. The rapid structural evolution that occurs leading up to and during failure of lithium-ion batteries requires high-speed imaging capabilities; some synchrotron X-ray imaging facilities have shown that ultra-high-speed imaging of failure mechanisms can be achieved, for example, Rack *et al.*[184] at the European Synchrotron (ESRF) captured, in detail, the breaking of a fuse using X-ray radiography at 36,000 frames per second, where the high frequency imaging was limited by the capability of the detector (a high-speed camera) rather than the flux of photons. The high-speed capability of synchrotron sources provides a platform for imaging rapid dynamic events and quantifying the change in material architectures over time. At the Diamond Light Source synchrotron, Dobson *et al.*[185] recently achieved tomogram acquisition rates of up to 20 Hz (20 3D images per second), allowing real-time monitoring of fluid transport through a porous network in 3D.

High-speed X-ray radiography and tomography could capture the internal structural dynamics of a cell during failure, and elucidate the influence of cell design and safety devices on the failure process. Degradation phenomena that occur during extreme operating conditions, such as delamination and collapse of electrode assemblies arising from gas generation, could be seen without altering the design of

the cell. Furthermore, coupling 4D imaging (3D with time) with image correlation and quantification techniques presents a promising means through which the evolution of material architectures could be further understood. Tracking the local displacement of materials in 3D has previously been demonstrated for geological samples subject to compression, where regions experiencing the highest strain could be identified by correlating consecutive tomograms taken at different stages of compression[186-188]. As Eastwood *et al.*[189] demonstrated, when applied to lithium-ion batteries, image correlation techniques can reveal heterogeneities in morphological evolution and lithium concentrations during operation. Creating a 4D map of displacement during operation is an effective way of identifying inactive regions and causes of performance loss within lithium-ion batteries; this is the focus of Chapter 5.

The structural evolution of active materials during initiation and failure of lithium-ion batteries occurs over fractions of a second, which even at a tomogram acquisition rate of 20 Hz (as demonstrated at Diamond Light Source[185]), is still too rapid to be captured in 3D. However, the stages of failure initiation and the propagation of the thermal runaway reactions could be captured via high-speed radiography, which would provide valuable insight into internal phenomena, providing a more comprehensive description of battery failure when combined with external temperature, gas and heat measurements. By combining these techniques the cause of degradation as well as rupture and projectiles could be better understood. The current high-speed X-ray radiography and tomography capabilities, as well as the potential application to capture the rapid failure dynamics of lithium-ion batteries, are discussed in Chapter 3.

2.8. Conclusions

The primary risks associated with thermal runaway stem from the inherent generation of heat and gas. In this chapter, the reaction processes that contribute to heat and gas generation, along with the conditions (temperature and voltage) under which they are most likely to occur, were described. The thermal runaway process and the rate of heat and gas generation occur in stages, where different

reaction processes initiate at different critical temperatures; starting with the mildly exothermic breakdown of the SEI layer at *ca.* 80 °C and ending with the highly exothermic breakdown of positive electrode materials at > 200 °C. Integrated safety devices such as the PTC, CID and BMS, help prevent the cell from reaching unfavourable conditions but are not entirely effective in preventing thermal runaway. For this reason, rigorous abuse testing of commercial lithium-ion cells is not only required by international standards, but additional procedures for comprehensive analyses of battery behaviour during failure are recommended by national laboratories, Sandia National Labs and the National Renewable Energy Labs.

However, an extensive review of literature has revealed that despite the rigour of thermal and gas composition analyses, there remains a lack of understanding surrounding the local occurrences, both structurally and thermally, within the failing cells. As outlined, the major risks associated with battery failure are determined by the behaviour of the active materials and components as the process of thermal runaway initiates and propagates throughout the cell. It is therefore concluded, that the use of non-destructive imaging techniques, such as X-ray radiography and tomography, should be combined with the conventional external measurements to progress towards a more in-depth understanding of catastrophic battery failure. In this thesis, the application of *in-situ* and *operando* X-ray imaging across multiple length scales is carried out to present a comprehensive description of battery degradation and failure. Visualisation of the dynamic internal architecture of commercial cells allows examination of the efficacy of integrated safety devices such as PTCs and CIDs in preventing or mitigating the consequences of thermal runaway. Furthermore, the influence of mechanical design features on failure mechanisms is explored, providing light on favourable and unfavourable attributes for enhanced battery safety and performance.

Chapter 3

Methodology

3.1. X-ray Imaging: Theory and Application

Since Röntgen first described X-rays in his 1898 publication series entitled "Ueber eine neue Art von Strahlen", or "On a new kind of ray"[190], the application of X-ray imaging as a non-destructive diagnostic tool became widespread. This has resulted in enormous technological advancements; in particular, X-ray radiography and computed tomography (CT) have undergone rapid improvements over the past two decades. Most notably, the spatial resolution of X-ray images has increased (now being able to achieve pixel resolutions of < 20 nm in laboratories), and image acquisition times have greatly decreased. When combined with rapid reconstruction times for 3D X-ray CT, the possibility of facile imaging of the microstructure of materials in 3D over very short time periods is now a reality. For lithium-ion batteries, this has resulted in significant advancements in our understanding of failure, degradation, and transport mechanisms; for example, previous X-ray CT studies have included visualising microstructural degradation and identifying potential shortfalls of electrode material architectures[81], determining the transport properties of electrodes[176, 177, 191], quantifying the structural dynamics associated with active materials[183, 189], and presenting empirical data to validate models[192].

In this chapter, X-ray characteristics, X-ray sources, and X-ray interaction with matter are discussed. As a large portion of this thesis is focused on high-speed imaging, the requirements for X-ray facilities as well as peripheral technologies for high-speed radiography and tomography are also described. To optimally perform image-based quantification, it is sometimes necessary to carry out post-processing

of the data sets; the post-processing and segmentation methods used in this thesis are outlined, and a detailed account of the image-based quantification techniques used here is provided.

3.1.1. X-ray Sources

3.1.1.1. Overview

There is a wide variety of X-ray system designs, and a range of X-ray spectra, properties and system capabilities to choose from[193]. The selection of X-ray source should suit the particular application; for example, synchrotron radiation sources can provide the high photon flux and brilliance necessary to achieve high resolution 3D images over short periods of time[174], presenting the possibility for tracking rapid structural evolution processes of active materials in 3D and in real time[63]; however, synchrotron imaging is expensive and typically involves a competitive application process for a short amount of usable time. In contrast, laboratory sources have a much lower flux and can be several orders of magnitude slower than synchrotron sources when capturing a tomogram[174], but can achieve comparably high spatial resolution, are more readily available, and cost much less to operate. Figure 3-1 shows a plot of the spatial and temporal capabilities of a wide range of X-ray sources; from this figure, it is seen that synchrotron sources are necessary to capture structural evolutions occurring over short time scales (seconds to minutes). For example, The European Synchrotron (ESRF) emphasizes high spatial and temporal resolutions with near real-time micro-CT, down to almost 0.01 s per series of projections for a 3D reconstruction. However, if high temporal resolution is not required then laboratory sources can achieve competitive spatial resolutions to synchrotrons (see Xradia Ultra in Figure 3-1). Figure 3-1 is a simplified demonstration that synchrotron and lab-based CT systems facilitate different requirements.

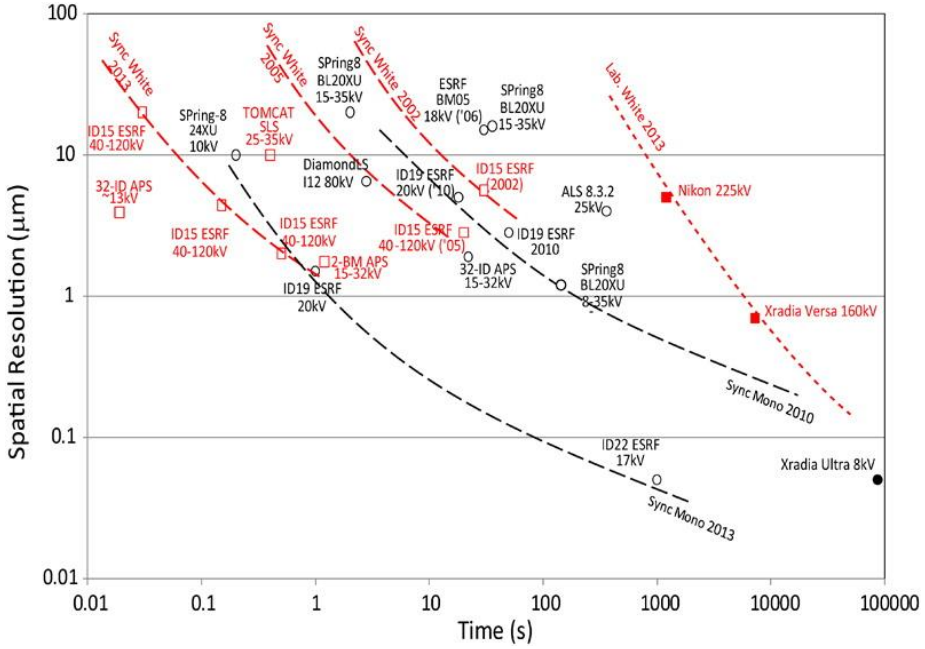

Figure 3-1: Plot comparing the spatial resolution and scan-frequency of various X-ray CT facilities. Open symbols represent synchrotron sources, filled symbols represent laboratory sources, red squares denote white beam and black circles monochromatic beam scanners. Reproduced from [174].

3.1.1.1. Synchrotron Radiation

Within synchrotrons, electrons are accelerated to close to the speed of light, typically having energies in the GeV range, before being released into a primary storage ring where the electrons are directed in a closed polygonal path through the use of magnet arrays. The polygonal shape of the storage ring contains bending magnets at each angled section of the storage ring that accelerate the electrons and changes their direction of travel. The kinetic energy lost by the electrons during deceleration in the magnetic field is in the form of radiation (Bremsstrahlung), producing extremely high intensity X-rays[194].

In third generation synchrotrons such as the The European Synchrotron (ESRF) and Diamond Light Source, an array of magnets in the straight sections of the storage ring undulate the electrons to provide much higher flux and more brilliant radiation with minimal spot size, where brilliance B, is defined by equation 3.1.

$$B = \frac{photons/second}{(mrad)^2(mm^2 source\ area)(0.1\%\ bandwidth)} \quad (3.1)$$

The brilliance within third generation synchrotrons is about 10 orders of magnitude higher than lab-based (rotating target) systems[195]. The photon spectrum and flux can determine the suitability of a beamline for a particular application. The energy of the electrons travelling in the storage ring influences the X-ray spectrum emitted to each beamline, and the current determines the X-ray flux.

The Bremsstrahlung from the storage ring then enters the "front end" of the beamline where the beam is collimated and low energy X-rays are filtered out. The next stage is the optics hutch, where the beam is refined to the needs of the user. For example, through a series of monochromators, mirrors, slits and filters, synchrotron sources can provide parallel polychromatic or monochromatic X-ray beams. For X-ray radiography or tomography, the problem of beam hardening (where low energy X-rays are attenuated more than high energy X-rays) is avoided by monochromatising the X-ray beam. By refining the beam to narrow band-widths, the X-rays can also be used for a range of other wavelength sensitive techniques such as X-ray absorption near edge spectroscopy (XANES). For a more detailed description of the physics and mechanics behind synchrotron sources, readers are referred to Willmott's book on synchrotron radiation[196].

3.1.1.2. X-ray Tubes (Lab-based)

In most cases, the source of X-rays from lab-based CT systems involves accelerating electrons from a hot filament (generated via thermionic emission) into a metal target (Figure 3-2). The interaction of the electrons with the metal target involves two different types of emissions: continuous Bremsstrahlung from negative acceleration of electrons within the magnetic field of the atoms, and characteristic fluorescence radiation.

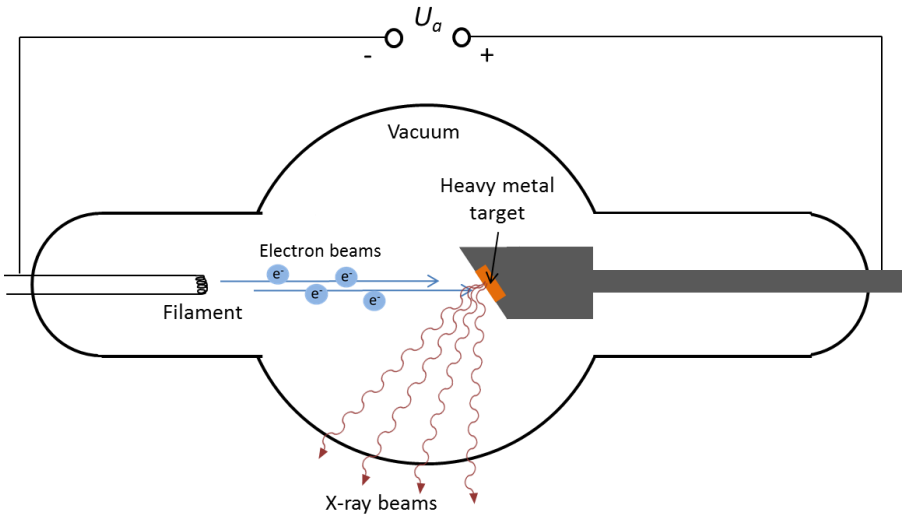

Figure 3-2: Illustration showing the basic components and operation of an X-ray tube system, where U_a is the accelerating voltage.

The energy interval of the Bremsstrahlung spectrum is dependent on the accelerating voltage of the cathode ray tube; the higher the voltage the greater the kinetic energy changed to radiation. The emission spectrum from an electron target also contains characteristic emission peaks that stem from the interaction between the incoming electrons with the inner shell electrons of the target material (Figure 3-3). When the energy of accelerating electrons is higher than a certain threshold, they can collide with and eject inner orbital electrons. When an electron from an inner orbital such as the K orbital, is ejected by collision with an incoming electron, an electron from a higher shell then falls to fill the now vacant K-shell position. The energy of the emitted photon is representative of the difference in energy between the inner shells. An example of characteristic emission spectrum from a Tungsten target for two operating voltages is presented in Figure 3-3. The radiation spectrum in Figure 3-3 includes Bremsstrahlung, which is usually bell-shaped, and is overlaid with the characteristic emission peaks where K_a and K_β represent the emission from the electron transitioning from the L and M shell respectively, to the innermost K shell.

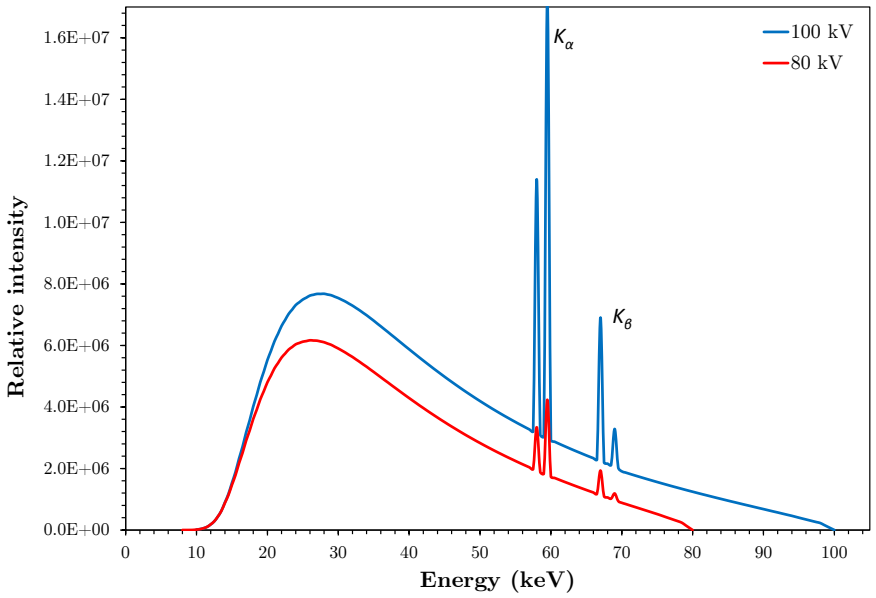

Figure 3-3. X-ray tube spectrum emission from a Tungsten target for two different operating voltages calculated using *SpekCalc* software program[197]. The characteristic emission spectrum is at a distance of 1 m through air from the target and after 1 mm of Al.

Hence, in lab systems based on the X-ray tube design, the spectrum will contain characteristic emission peaks from the target electrode overlaid on the Bremsstrahlung. Some quasi-monochromatic lab-based systems make use of the additional flux at the characteristic peaks, such as the Zeiss Xradia Ultra 810 (Carl Zeiss Microscopy, Pleasanton, CA, USA), which uses a quasi-monochromatic (via zone-plate focusing) beam of around 5.4 keV, the characteristic K_a emission from its Chromium target. The emission spectrums from the specific lab-based systems used in this thesis are described in more detail in a later section.

The basic operation and principles behind 'X-ray tube' based laboratory CT systems has been discussed here. Further detail concerning the engineering of X-ray systems and the associated physics is beyond the scope of this thesis, but can be found in Torsten Buzug's book on computed tomography[198].

3.1.2. X-ray Interaction with Matter

In this section, particular focus will be paid to interactions that are most relevant to standard absorption contrast radiography. X-ray intensity (number of photons) decreases exponentially while passing through a material due to absorption and scattering of the incident beam. The extent to which the radiation intensity decreases with distance into a material is typically conveyed through a single material-specific value, known as the linear attenuation coefficient (μ). For an incident monochromatic X-ray beam of intensity I_0, the expected intensity I at a distance η in the incident direction into a material is given by:

$$I(\eta) = I_0 e^{-\mu\eta} \tag{3.2}$$

This relationship is known as Beer's law of attenuation, and holds for a monochromatic X-ray (the polychromatic equivalent would involve an integral across multiple energies) and for a non-diverging beam (pencil beam) where scattered radiation is completely removed[199]. Generally the linear attenuation coefficient (μ) is given by:

$$\mu = \frac{\rho N_A}{m_A}\sigma_{tot} \tag{3.3}$$

Where ρ is the density, N_A is Avogadro's constant, m_A is the atomic molar mass and σ_{tot} is the total photon atomic cross section. Attenuation coefficients of materials across a broad range of wavelengths can be gathered from the National Institute of Standards and Technology (NIST) website[200, 201], which is a particularly useful source of information for prospective users of X-ray systems to estimate the suitability of a systems' emission spectrum for imaging a particular sample.

The total photon cross-section (σ_{tot}) and thus the attenuation coefficient (μ) are determined by the extent to which elastic and inelastic interactions, as well as pair production and photoelectric emissions occur upon interaction with incoming

photons. The most significant contributions to attenuation in the keV range are elastic, inelastic (Compton), and photoelectron emission.

$$\sigma_{tot} \approx \sigma_{el} + \sigma_{comp} + \sigma_{pe} \tag{3.4}$$

Where σ_{el} is the elastic scattering cross-section, σ_{comp} is the inelastic or Compton scattering cross-section, and σ_{pe} is the photoelectric cross-section. Elastic scattering involves interaction between oscillating electric fields, either through Rayleigh or Thomson scattering depending on whether the electron is tightly bound to an atom or is free, respectively[202]. Upon interaction, the incident photon wave changes direction but conserves its wavelength, and the atom remains in its ground state. Inelastic (Compton) scattering involves a transfer of kinetic energy from the incident photon to an electron where a photon of lower energy is emitted. Finally, the photoelectric effect is associated with the ejection of an electron with energy equal to the energy of the photon with which it interacted, minus its binding energy, leaving a hole. Either characteristic radiation or emitting Auger electrons occurs when another electron falls to fill the remaining hole.

In summary, the primary contributions to the total absorption coefficient are elastic and inelastic interactions, as well as the photoelectric effect. The extent to which each mechanism affects the total absorption coefficient is highly dependent on the wavelength(s) of the incident radiation as well as the atomic number of the materials involved. With the information provided, it's clear that material properties as well as compositions can be extracted based on the intensity of the transmitted radiation. Detecting the transmitted radiation in the form of relative intensity is thus vital for phase identification within a sample.

3.1.3. X-ray Computed Tomography

Tomography is the name given to a group of methods that are used to image objects in three dimensions. Using a penetrative probe, multiple transmission projections are taken at different angles to precisely identify the position of species. In X-ray CT, these projections are radiographs, and the species are identified based

on their attenuation coefficient and hence their intensity in the resulting image. Prior to reconstruction, each projection undergoes a flat-field correction to remove any artefacts or spatial variations between detector pixels or beam intensity. To illustrate the principle, Figure 3-4 shows the original intensity of the vent region of an 18650 battery, taken at ID19 at the ESRF using monochromatic 76 keV beam. The sample was removed from the field of view and the reference (flat field) image was captured using the same beam and exposure time. Inspection of the reference image shows significant spatial variation in beam intensity as well as white (possibly defective) pixels, that are also seen on the original intensity image. Upon correction, the spatial variations are mitigated, and the corrected image is then used in reconstruction.

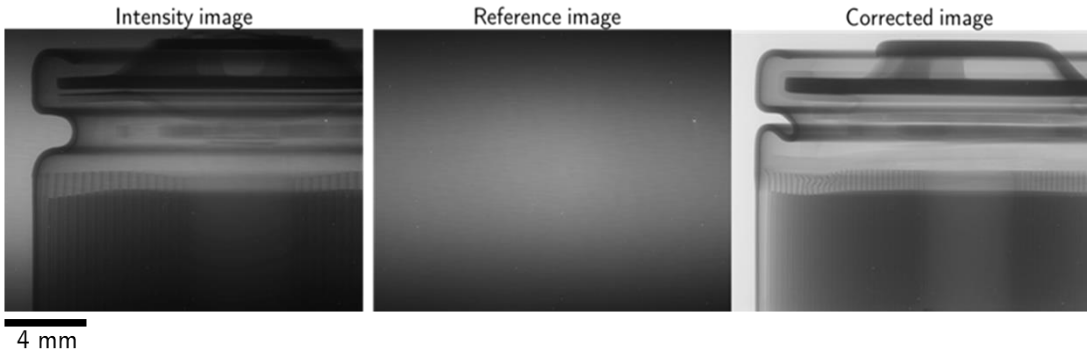

Figure 3-4: Radiographs of the top of an 18650 battery showing the differences between the original intensity images and the corrected image after flat field correction. The difference in beam intensity across the detector plane are clearly seen in the reference image.

The corrected projections are used to form a 3D image of the material through a mathematical procedure known as tomographic reconstruction. Multiple images are usually taken at equal angular increments to precisely identify the position and shape of features within a sample. For example, for a spherical object in Figure 3-5 the two perpendicular projection angles are necessary to extract its location. Additional projection angles are needed to more accurately capture the shape of the object, and to identify the location of more complex and overlapping

geometries. Otherwise, the number of angular increments at which the projections are taken may not be sufficient to capture fine geometric details.

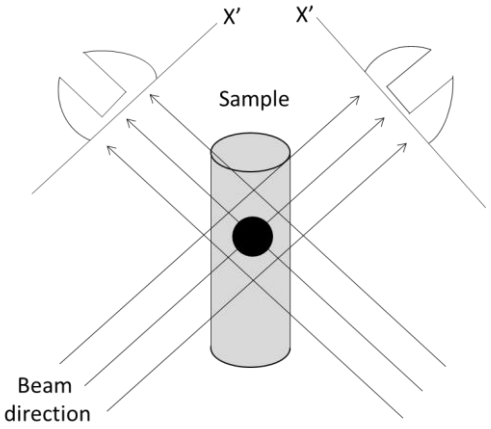

Figure 3-5: Illustration showing how the location of objects can be determined from different projection angles.

By increasing the number of projection angles, artefacts caused by overlapping transmitted X-rays can be identified and resolved. Typically, several hundred projections are gathered during a single scan[203], depending on the detector size (number of pixels in the horizontal direction). There are numerous methods used to reconstruct the 3D geometry from a series of projections[194, 204]. The reconstruction methods used in this work are based on the Filtered Back-Projection (FBP) approach[194, 204]. The basic FBP method consists of a standard back-projection step, where radiographs (integrated images representing X-ray attenuation) are reconstructed into a 3D image based on the Euclidean coordinates associated with each image taken at known angular increments. The second step in FBP is applying a filter to remove low frequency blurring. A high number of images are required to ensure sufficient resolve of features. To demonstrate the effect of the number of projections used for reconstruction, a complex microstructure of a NMC electrode was imaged and reconstructed using FBP with a range of projections at equal angular increments (Figure 3-6).

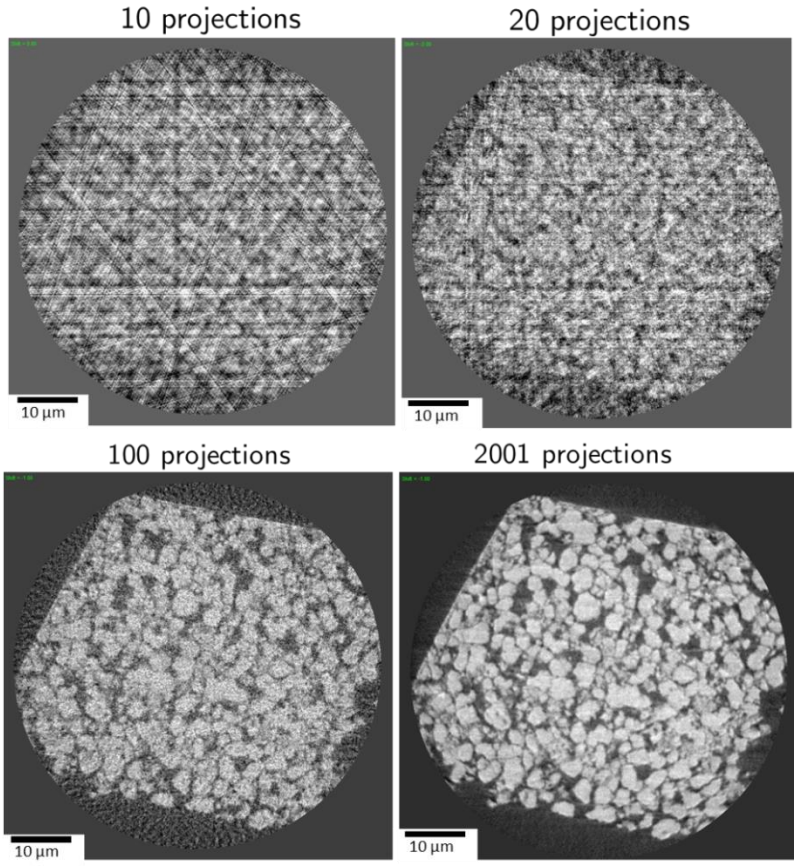

Figure 3-6: Single slice from tomographic reconstructions of NMC electrode particles showing the significant improvement in image definition with increasing number of projections used for reconstruction. The intensity images used during reconstruction were 1024 × 1024 pixels, with a pixel size of 64 nm.

3.1.4. X-ray Phase and Absorption Contrast Imaging

The variation of attenuation coefficient between materials allows visualisation and identification of different materials through the use of polychromatic or monochromatic beams. Monochromatic beams can also be used for absorption contrast tomography, where samples are imaged above or below the K-edge of a specific component to highlight its presence. However, monochromaticity inherently involves reducing the overall flux of the beam. For high-speed imaging applications that may be flux-limited, a wide range of wavelengths (pink or white beam) is preferred.

Phase contrast imaging can also be used to highlight features that may otherwise be invisible by converting phase differences into intensity differences. The image output by the detector is a phase distribution rather than an absorption distribution; hence more information on the refractive index of the sample is gathered. There are three main ways in which phase-information in transferred to intensity: Interferometry, diffraction-enhanced imaging, and propagation-based contrast. Of most relevance to this thesis is an interferometric technique known as Zernike phase contrast, however it is useful to know that propagation-based contrast is commonly used and easily implemented in synchrotron as well as lab-based sources to enhance image features.

Zernike phase contrast emphasizes material edges by using phase shifts across the incident X-ray beam[205]. Figure 3-7a shows an illustration of the principle behind the Zernike phase contrast technique employed here. Following transmission through the sample, the cone beam is focused using a zone plate. A phase ring then induces a known phase shift and amplitude reduction of the non-diffracted light. The diffracted and non-diffracted light are now of similar intensity but different phase, and so interact to form a high contrast image on the detector plane. The use of monochromatic light and the inherent reduction in intensity of the non-diffracted light to emphasize the diffracted light results in large exposure times being required per image. Figure 3-7b shows the greyscale histograms and 2D slices from both Zernike phase contrast and absorption contrast tomograms of graphite electrode particles; the phase contrast image clearly enhances edge features but lacks absorption information causing the interior of the particles to have similar greyscale values as the exterior. This phase contrast technique is particularly useful for weakly attenuating materials such as polymers and for identifying cracks in weakly attenuating solids such as graphite, and can be performed in both lab-based[206] and synchrotron[207] sources. However, due to the high exposure times required for imaging, its applicability to dynamic architectures *operando* or *in-situ* studies is limited.

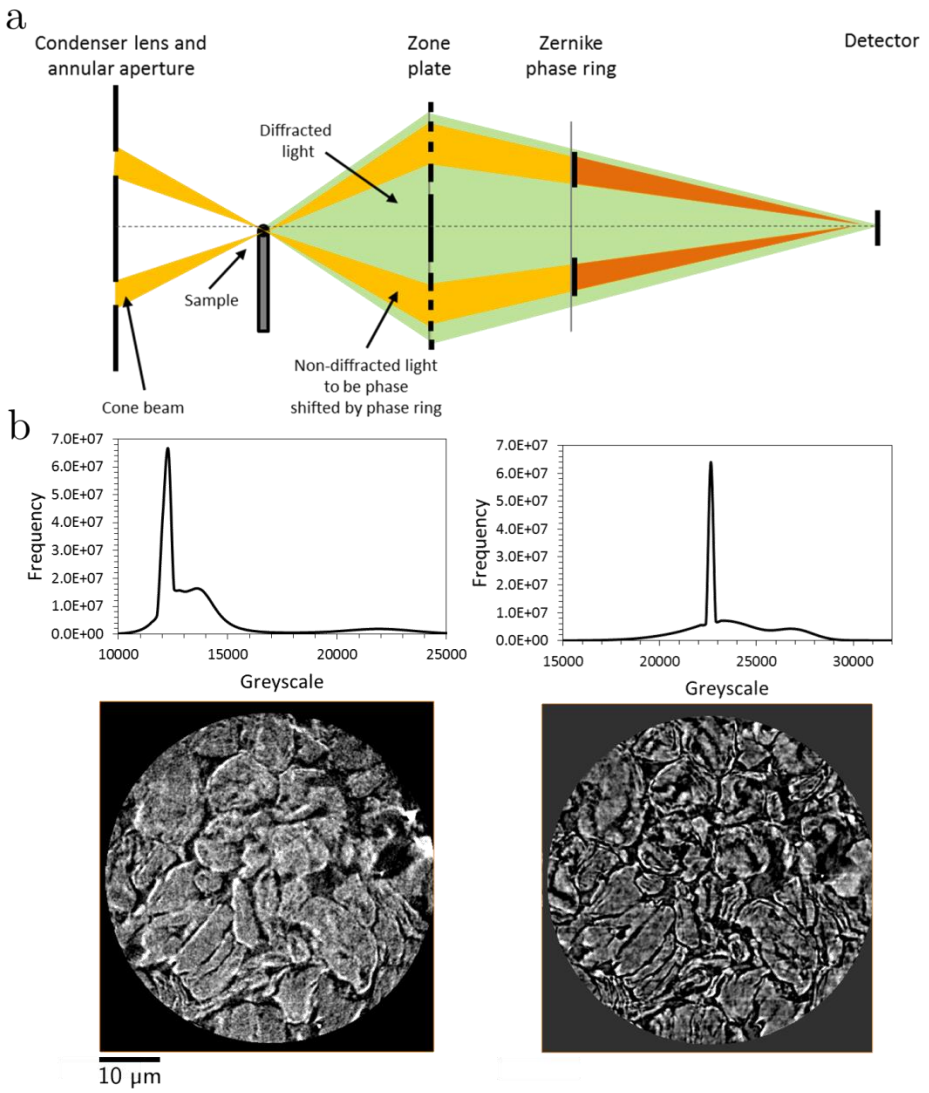

Figure 3-7: (a) Schematic showing the principle of the employed Zernike phase contrast technique. (b) Greyscale histograms (top) and 2D slices (bottom) from absorption (left) and Zernike phase (right) contrast tomograms.

3.1.5. X-ray Detection and Image Generation

There is a multitude of ways to detect transmitted radiation from a sample, the most common of which are 2D detectors that are either exposed to the radiation directly (direct detection) or indirectly (indirect detection) via conversion of the X-ray radiation to visible light.

In this thesis, only indirect detection was used for high-speed X-ray radiography. Most high-speed commercial detectors use charge coupled devices (CCD) or complementary metal-oxide-semiconductors (CMOS) that operate in the visible light range. For high-speed radiography, a scintillator is used to convert the X-ray beam into visible light through luminescence. The scintillator material must be able to achieve high spatial resolutions, have low decay times (afterglow), high detective quantum efficiency (conversion yield) and emit light within the sensitivity range of CCD or CMOS detectors. Furthermore, to assess local differences in intensity from the transmitted beam the luminescence of the scintillator material should be linear with incident intensity. If these conditions are met, then commercial high-speed visual light CCD or CMOS detectors can be used to capture the intensity images.

One of the major differences between CCD and CMOS cameras is the way in which the build-up of charge on the photosensitive pixels is processed and read as a signal. In CCD cameras, the pixel charge is shifted along other pixels to a side-line register. The charge from the individual pixels is then read by a very small number of nodes. In contrast, each pixel in a CMOS detector has a transistor, converting the charge from the photosensitive pixel material into a voltage signal which is recorded from the multiplex of pixels by an array of digital-to-analogue converters giving it an inherent advantage for high-speed recording. The superior high-speed capability of CMOS detectors stems from the greater extent to which output channels are parallelised. The lower number of output channels in CCD detectors results in each channel having a higher frequency of data to process, therefore for high-speed applications CCD detectors can have higher noise. For this reason, and others, CMOS detectors are the preferred technology for high-speed imaging.

To avail of the full high-speed imaging capability of commercial CMOS cameras such as the PCO Dimax, upload of data to central servers during imaging should be avoided. Instead, the data can be stored on the camera's on-board memory. However, commercial cameras have limited on-board memory which can hinder the quantity of data that can be gathered; for example, at full frame high-speed imaging, users may be limited to recording 1-2 seconds of events, before filling the on-board memory. This has been a limiting factor for continuous high-

speed imaging in this thesis (the specifics of which will be discussed in more detail in the results sections). Efforts to avoid this limitation at synchrotrons are underway, an example of which is the giga-FROST project at the TOMCAT beamline at the Swiss Light Source (SLS), where high speed detectors have been connected to central servers via numerous optical fibres allowing upload speeds of 8 GB/s, which for continuous imaging can result in 1 TB of data per two minutes.

3.2. X-ray CT Systems

3.2.1. Lab-based CT

In this thesis, two lab-based CT systems were used. The Zeiss Xradia 810 Ultra (Carl Zeiss Microscopy, Pleasanton, CA, USA) was used for nano-CT imaging, and the Zeiss Xradia Versa 520 (Carl Zeiss Microscopy, Pleasanton, CA, USA) was used for micro-CT imaging. Descriptions of both systems are provided here but the specific imaging parameters used for individual scans are provided in the associated results chapters.

Nano-CT Imaging: The Zeiss Xradia Ultra 810 uses a quasi-monochromatic beam around the K-edge of its chromium target (5.4 keV), operates at a tube voltage of 35 kV and a tube current of 25 mA. The quasi-monochromatic beam is achieved by energy selective optics. A capillary condenser is placed between the source and the sample to focus as much light as possible onto the sample. The efficiency of the capillary condenser is dependent on photon energy and designed to have maximum efficiency around 5.4 keV. Furthermore, a Fresnel zone plate which consists of a circular grating of radially varying pitch is designed to focus a single photon energy (5.4 keV) to a point. The Fresnel zone plate is located between the sample and the scintillated CCD detector.

The Ultra 810 also operates in two imaging modes, standard absorption contrast and Zernike phase contrast. As shown in Figure 3-7, an annular phase ring is placed between the zone plate and detector, that amplifies phase shifted light and presents an image with edge enhancement. Zernike phase imaging is most

useful for feature enhacement of weakly attenuating materials, but because the photon flux is decreased the required exposure time for a good signal to noise ratio is significantly higher. The Ultra 810 has two magnifications: Large Field of View (LFoV) that achieves a pixel size of 64 nm and High Resolution (HRes) that can achieve a pixel size of 16 nm.

Samples are prepared by cutting the material of interest into a triangular shape and mounting onto a pin using a quick setting epoxy with a tip of the triangle facing up. The pin is secured in a chuck on a sample platform that was manufactured by Zeiss, and placed on the rotation stage in the Ultra 810 system. Reconstructions are carried out using the Zeiss XMReconstructor software package where a centre shift corrections is user defined and applied in the reconstruction process. Reconstruction is based on the filtered-back-projection algorithm.

Micro-CT imaging: The Versa 520 utilises a tungsten target, the tube voltage can be varied from 30 kV to 120 kV depending on how absorbing the sample is to low energy X-rays (see example of emission spectrum in Figure 3-3). The Versa 520 has multiple objective lenses for optical magnifications of 4×, 10× and 20×, providing pixel resolutions down to *ca.* 0.2 μm. The 1× setting utilises a direct scintillator without any optical magnifications. The Versa operates with a cone beam directly illuminating the sample onto a scintillator and thereafter reaching the detector, therefore for each objective lens, the magnification can also be adjusted by changing the source-to-sample and sample-to-detector distances (geometric magnification). The Versa 520 has a reel of filter materials between the source and the sample, which can be adjusted to filter out low energy photons for highly attenuating materials and help reduce artefacts caused by beam hardening.

Samples are mounted onto a platform consisting of a stub or clip that were manufactured by Zeiss. Either a quick setting epoxy or blu-tack is used to secure the samples to the platform. The platform is then mounted on the rotation stage within the Versa 520 system. Reconstructions are carried out using the Zeiss XMReconstructor software package where centre shift and beam hardening corrections are user defined and applied in the reconstruction process. Reconstruction is based on the filtered-back-projection algorithm.

3.2.2. Synchrotron CT

The synchrotron studies in this thesis were performed at beamlines ID15A and ID19 at the ESRF which has exceptionally high flux at high energies[184, 208]. The specific beam energies, imaging parameters, and *in-situ* rig designs are discussed in later sections. The beamlines have a high brilliance beam that provides large working distances between the source and the detector in the experimental hutch, which allows *in-situ* rig designs (described in Section 3.8) to be easily installed and utilised during imaging experiments. Synchrotron imaging can be carried out using the full spectrum of wavelengths from the electron ring (known as 'white' beam), a filtered spectrum (where low energy photons are filtered out), or a monochromatic beam. Beam refining (focusing, filtering and monochromatizing) is carried out in an optics hutch upstream of the experimental hutch.

All synchrotron experiments described in this thesis utilise a scintillator and CMOS detector. Standard filtered-back-projection with ring removal, beam hardening and centre shift corrections, is used for reconstructions.

3.3. Filtering and Segmentation

The reconstructed dataset from X-ray CT consists of a 3D volume of voxels (the volume equivalent of a pixel) where each voxel is assigned a value that represents the attenuation of the signal due to the material at that location. Figure 3-8a shows a reconstructed dataset from an absorption contrast tomography of the body of an 18650 battery. The highly attenuating materials are displayed as white and the weakly attenuating materials as black. The segmentation of materials is largely based on the differences between their greyscale value. For example, in Figure 3-8a there are three distinct phases that differ greatly in greyscale value. The three materials appear as three distinct peaks in the associated histogram of voxel greyscale values shown in Figure 3-8b, and can be segmented by using threshold segmentation.

There are clear sources of error surrounding the segmentation process: the peaks associated with particular phases tend not to appear as steps in the greyscale

histogram, but as 'bell-shaped' peaks, that often overlap. Defining the minimum and maximum value for threshold segmentation can therefore be a significant source of error. The resolution of the scan can also be a significant source of error; the intensity value at a given pixel represents an amalgamation of the material attenuation coefficients within that region. For example, if a material contains pores that are smaller than the resolution of the scan, its attenuation coefficient approaches that of its pore occupant with increasing porosity. Additionally, a layer of pixels on the surface of a solid phase whose greyscale value lies somewhere between that of the solid, and that of the neighbouring phase, is typically observed; this is due to the pixel containing attenuation information from both phases since the resolution is not fine enough to distinguish the exact boundary location.

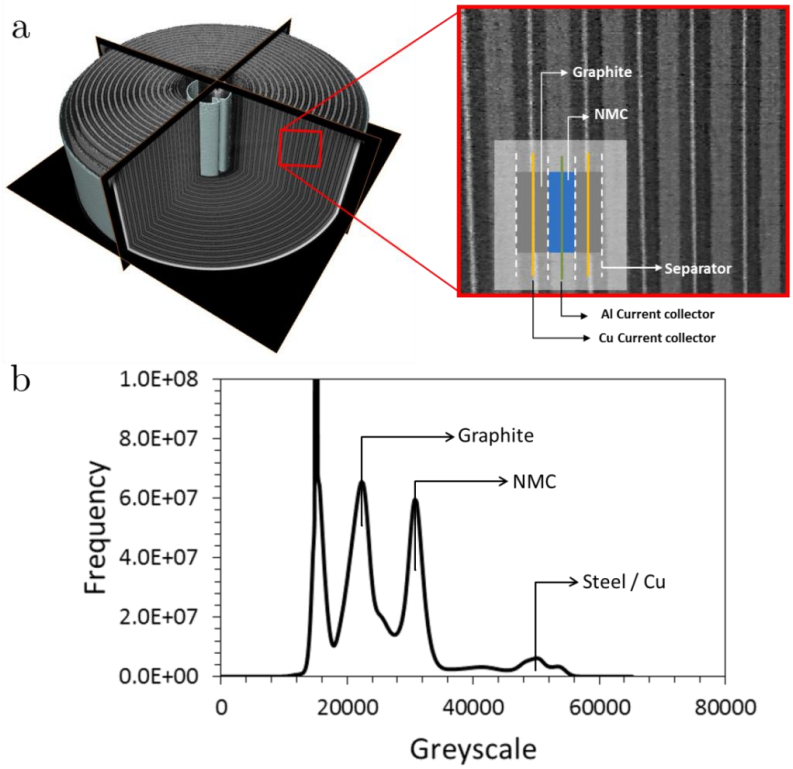

Figure 3-8: (a) Orthoslices from an absorption contrast tomogram of the body of a commercial 18650 cell, showing the greyscale differences between the materials within the electrode assembly. In this image the greyscale is inverted, where white materials are highly attenuating and dark materials are weakly attenuating. (b) Greyscale histogram of the tomogram showing three distinct peaks corresponding to the three highlighted phases.

Image artefacts can also present erroneous greyscale values[209]; among others, these include noise, beam hardening, and ring artefacts. There are a wide range of filters and image processing techniques that can be used to mitigate the effect of artefacts, improve the ease of segmentation, and enhance the quality of the segmented image. One such filter that is used in this thesis to reduce noise in images is the non-local means (NLM) filter[210]. The NLM filter operates similar to a mean filter which gives a target pixel an averaged value from a group of pixels in the target pixels neighbourhood, but applies a weight to the contribution of neighbouring pixels depending on their similarity to the target pixel. The weighting strategy is preferred to the standard mean filter due to it helping to preserve edges, and image texture. However, as with all filters, caution should be taken to ensure that the applied filter and filter settings preserve important details, in particular for applications where further image processing and quantification techniques will be applied.

3.4. Image-based Quantification

3.4.1. Overview

For a particular set of materials, it is well known that the performance of lithium-ion batteries is largely determined by the microstructural properties of the electrodes and separator. Starting with Newman's porous electrode theory[72, 211], the importance of optimising battery performance (balancing power and energy density) through manipulation of the electrode microstructural properties has become clear, and the relationship between reaction distribution and the porosity and tortuosity of electrodes is now well developed[69, 70, 212-214]. For example, for an electrode or separator soaked in electrolyte, geometric factors such as porosity (ε) and tortuosity factor (τ) determine the resistance to ion transport (R_m) from one electrode to another:

$$R_m = \rho_e \frac{\tau l}{\varepsilon A} \tag{3.5}$$

where (l) is the thickness of the membrane of area (A), and (ρ_e) is the conductivity of the electrolyte. However, quantitative assessments of the electrode microstructures are required to fully understand the link between performance and microstructure in real-world scenarios.

X-ray CT presents the possibility of non-destructively imaging battery materials in 3D and with sub-micron resolution. It is only recently that the influence of local heterogeneities and temporal dynamics within operating microstructures could be assessed through a range of *in-situ* and *operando* X-ray CT studies[81, 177, 178, 183, 191, 215-219]. With this, numerous methods to quantify microstructural and transport properties of electrode materials were developed; both open-source and commercial software packages that include methods to quantify porosity, pore size distribution, particle size distribution, tortuosity and specific surface area are now widely available. However, there remains some debate over which quantification methods most accurately capture the contribution of microstructural properties to the ionic transport through porous electrodes and hence the performance of cells. For example, Taiwo *et al.*[220] present a comprehensive comparison between 2D (stereology) and 3D quantification methods; although 2D methods tend to be less computationally intensive, they inherently fail to capture the detail required for accurately measuring the mass transport of ions through a network due to the inability to identify the influence of dead-end and interconnecting pores. Furthermore, within the realm of 3D quantification techniques, there remains uncertainty as to how best the transport resistance within a porous network can be quantified[221, 222]. An example of this can be seen in a comparative analysis of tortuosity techniques, performed by Tjaden *et al.*[223], applied to 3D reconstructions of the complex porous networks of oxygen transport membranes. Tjaden showed that not only do the different techniques output different values of tortuosity for the same segmented microstructure, but that all techniques deviate significantly from empirical measurements.

To avoid ambiguity, the methods used for quantification of microstructural properties in this thesis, as well as their strengths and limitations, are discussed in the following sections; in particular, porosity, pore size distribution, particle size distribution, tortuosity and volume specific surface area. It is also important to note that a representative volume (RV) analysis should be performed for each of these measurements in order to be confident that the parameter of interest is representative of the bulk material. However, it is acknowledged here that although an RV may be achieved for a particular sample (which is typically < 1 mm^3), there may still exist larger undetected heterogeneities and manufacturing defects within the bulk material, therefore the 'representative volume' may not always be representative.

3.4.2. Porosity

The porosity of a material is defined as the ratio of void volume to apparent geometric volume. For a binary segmentation of a 3D reconstruction this translates into the ratio of the number of voxels representing the pore phase volume, to the total number of voxels covering the sample volume within the image. Calculating the porosity is easily implemented into MATLAB, and is available as an option in most image processing software packages.

3.4.3. Pore Size Distribution

In this work, two methods were used to determine the pore size distribution (P_oSD): the first was a continuous P_oSD (c-P_oSD) 3D method developed by Munch and Holzer[222], the principle of which is based on expanding spheres from points along calculated centroid paths. Munch and Holzer provide the algorithm as an open-source plugin for the Fiji image processing software package[222]. In this method, a distance map is determined whereby voxels are assigned a value corresponding to the shortest distance to the phase boundary, from which the volume fraction of the pore phase that can be filled with spheres of a certain radius may be calculated. A 2D slice taken from the 3D plot of spheres occupying the pore

network of a 3D reconstruction of a commercial lithium-ion electrode is shown in Figure 3-9a. The voxels within the 3D plot of pore sizes are colour coded with the size of the largest sphere that is capable of occupying that region. The c-P_oSD algorithm then plots the radii of spheres (increasing in radius by steps defined by the user) against the corresponding filled volumes, outputting a cumulative P_oSD plot of pore size as a function of volume fraction of the total pores (Figure 3-9b).

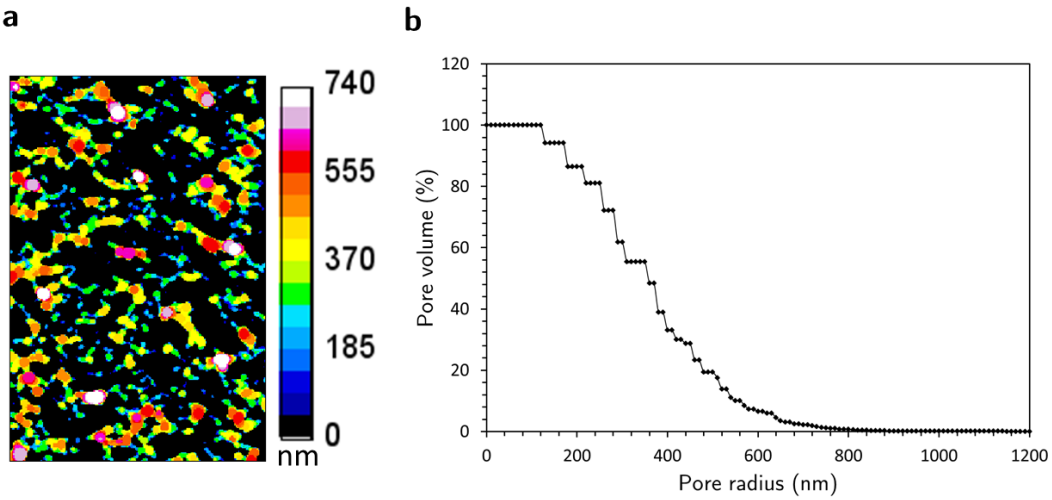

Figure 3-9: (a) Slice from 3D image of pore size colour coded with the largest sphere to fit locally, and (b) a pore size distribution plot of the pore network of a commercial lithium-ion battery electrode.

The second method is based on a stereological approach where the mean pore radius, L, within individual slices in the X, Y and Z directions, is determined by calculating the mean volume to surface ratio according to equation 3.6, where V_v is the volume fraction of the pore, and S_v is the interface density[224, 225].

$$L = 2\frac{V_v}{S_v} \tag{3.6}$$

This approach is implemented in MATLAB on a slice-by-slice basis, where the interfacial area is calculated by first identifying solid phase pixels that are connected to the pore phase, and then labelling each pixel with the number of neighbours of the opposite phase (i.e. 1-4). The boundary length is determined by

summing the values of the labelled boundary pixels. The quantification of surface length (or area) varies between software packages, and can have a significant impact on the results. For example, rather than the basic neighbour counting method described before, Avizo (version 9, FEI, France) uses a chordal approximation for calculation of both boundary length and surface area; this is one reason why any parameter that depends on the calculation of surface area or boundary length can differ between software packages.

When compared to 3D quantification techniques, stereological methods tend not to be as accurate for measuring bulk parameters[220], but are useful for identifying deviations in porosity and pore size between, and along, different axial directions.

3.4.4. Particle Size Distribution

The performance, rate capability and thermal stability of lithium-ion batteries are highly dependent on the particle size distribution of the battery electrode materials[126, 226, 227]. Inherently, an increase in specific surface area of the electrode can improve the rate capability of a cell by providing more sites for lithiation to occur. Similarly, the rate of exothermic degradation during thermal runaway increases with increased surface area, since one of the main contributors to heat generation is the reaction of the positive electrode with the electrolyte (a surface based reaction).

Particle size distributions are calculated by identifying isolated objects in a segmented image, and quantifying the volume within their boundaries. If the particles are somewhat spherical then 'equivalent diameter' (the diameter of a sphere of equal volume to the isolated phase) is used as a metric for the particle size distribution. The boundaries of the segmented particle phase are frequently difficult to distinguish, requiring additional image processing to help distinguish the boundaries of individual particles. One such tool to help distinguish individual particles is the 'separate objects' function in the Avizo Fire software package. Avizo's' 'separate objects' function combines a watershed algorithm, with a distance map and an algorithm that identifies the maximum greyscale values

within a volume, to identify regions that are likely to be boundaries between particles. For example, two touching particles may be perceived as one in a reconstructed tomogram, but might show a boundary convergence and slight gradient in greyscale at their interface (see original image in Figure 3-10); the 'separate objects' algorithm identifies these features and draws a boundary between the particles. The extent to which the algorithm separates objects is user defined, and the quality of the separation is inspected by visual comparison between the resulting image and the original greyscale image. An example of the application of Avizo's' 'separate objects' function is shown in Figure 3-10.

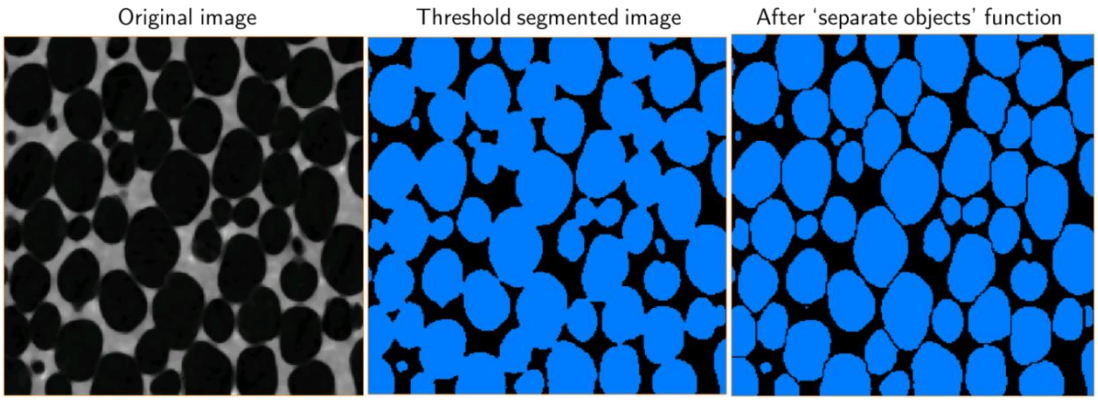

Figure 3-10: Application of Avizo's 'separate objects' function to an Avizo tutorial dataset. Most of the volume in the original threshold image is connected and would be considered as one particle upon quantification. The 'separate objects' function identifies the most likely boundary areas of the particles and separates them by a single voxel layer.

3.4.5. Tortuosity Factor

The tortuosity factor (τ) is the extent to which the resistance to ionic transport through porous materials is increased by the convoluted transport pathways. Tortuosity (ζ) however is distinct from the tortuosity factor and is defined as the ratio of the path length (L_p) to the Euclidean distance between two points (L_{ec})[75]:

$$\zeta = \frac{L_p}{L_{ec}} \tag{3.7}$$

In a communication article by Epstein[75] the tortuosity is related to the tortuosity factor through:

$$\tau = \left(\frac{L_p}{L_{ec}}\right)^2 = \zeta^2 \tag{3.8}$$

The tortuosity factor of electrode and separator materials is most frequently determined by electrochemical means such as electrochemical impedance spectroscopy (EIS) by measuring the resistance to charge transport[228, 229] where the pore volume of the material is assumed to be filled with an electrolyte of known conductivity (κ):

$$\tau = R_{ion}\,\frac{\varepsilon\, A\, \kappa}{d} \tag{3.9}$$

Using X-ray nano-CT quantification methods can be applied to the segmented image of the complex electrode and separator pore structures to elucidate contributions to the aforementioned ionic resistance. There are several methods to quantify tortuosity, and there remains some debate over which method best predicts the effect of the structure on ion transport. Among the range of methods are the random walk method[230], fast marching method[231], pore centroid methods[191] as well as image-based simulations of a scalar diffusion parameter[191, 223].

In this thesis, the tortuosity factors were calculated by simulating the steady-state diffusive flow through the pore network of a segmented volume. Although it's more computationally expensive when compared to other approaches, it best represents the diffusive behaviour of ions through the porous network. The code, *TauFactor*, developed by Cooper[232], was implemented in MATLAB and is freely available online. A finite difference simulation was run in MATLAB, where the segmented voxel data were directly used as the simulation grid to avoid any potential smoothing effects from re-meshing. The steady-state scalar diffusion equation is solved with a fixed potential difference applied at two opposite faces of the volume (in the direction of the Z axis), similar to the approach described by Cooper *et al.*[191]. By comparing the simulated flow rate through the pore network,

Q_{pore}, to that calculated for a fully porous control volume with the same outer dimensions, Q_{CV}, the tortuosity factor in a specific direction can be determined from the following expression:

$$\tau = \varepsilon \frac{Q_{CV}}{Q_{pore}} \tag{3.10}$$

3.4.6. Digital Volume Correlation

Many functional electrode materials undergo a significant volume change during the insertion of Li^+ ions[78, 79] that can induce high local strains and severe mechanical degradation[80, 81] leading to capacity fade and reduced performance. *Operando* X-ray CT can capture the evolution of particle microstructures[81] as well as the displacement of bulk electrode materials during operation[189]. The coupling of image correlation techniques with time lapse X-ray CT presents a powerful diagnostic tool in materials research, providing a picture of the material structure and quantifying its evolution over time[39, 187-189].

Digital volume correlation (DVC) is a 3D extension of the 2D digital image correlation (DIC) which can map the deformation of materials by tracking the displacement of identifiable features. The extension of 2D DIC to 3D DVC, and its subsequent application to *in-situ* tomography of deforming trabecular bone is described by Bay[233]. The technique involves the segmentation of a volume into voxels (with locally distinct patterns) which are then tracked for displacement between consecutive images in three dimensions. The resulting 3D displacement maps can then be used to develop strain fields and vector fields for deforming materials.

Until recently, DVC has mostly been applied to strain measurement during compression of bone structures (particularly trabecular bone which has distinct features to track during deformation)[234-236], geological materials[187, 188, 237], and metallic alloys[238]. One of the first studies to quantify the evolution of damage was by Buffiere *et al.*[239], where a sequence of 3D reconstructions of an Al alloy material under compression were correlated. Recently, DVC has extended

into other fields of materials research[174], including evolving architectures of lithium-ion battery electrodes[189].

The continuum DVC in this work uses TomoWarp2 code developed between the Universities of Lund and Grenoble, building on the previously developed code, TomoWarp of Hall *et al.*[187, 188, 237]. A code developed by Bay[233, 240] is also used, which operates on a similar principle. In the current context, continuum DVC refers to the displacement calculation over a 3D grid of node points that are then used to determine 3D tensor strain fields following continuum mechanics. The DVC approach can be described briefly as having the following main steps[233, 240, 241]:

- A regular 3D grid of nodes is defined over the CT image volume, and a "correlation window" is centered on each node for the correlation analysis (Figure 3-11).
- The displacement for each node is derived by identifying the 3D translation vector (u) (Figure 3-11) that maximizes the cross-correlation of the grey-level data within the correlation window in the non-deformed image and the translated correlation window in the deformed image.
- Sub-voxel resolved translation vectors are then determined based on the maximum of the interpolated correlation coefficient for a range of displacements around the initial integer voxel value.
- For continuum DVC, calculation of the strain tensor is based on the gradient of the displacements over a [pre-defined number]-point cubic elements of neighboring nodes.

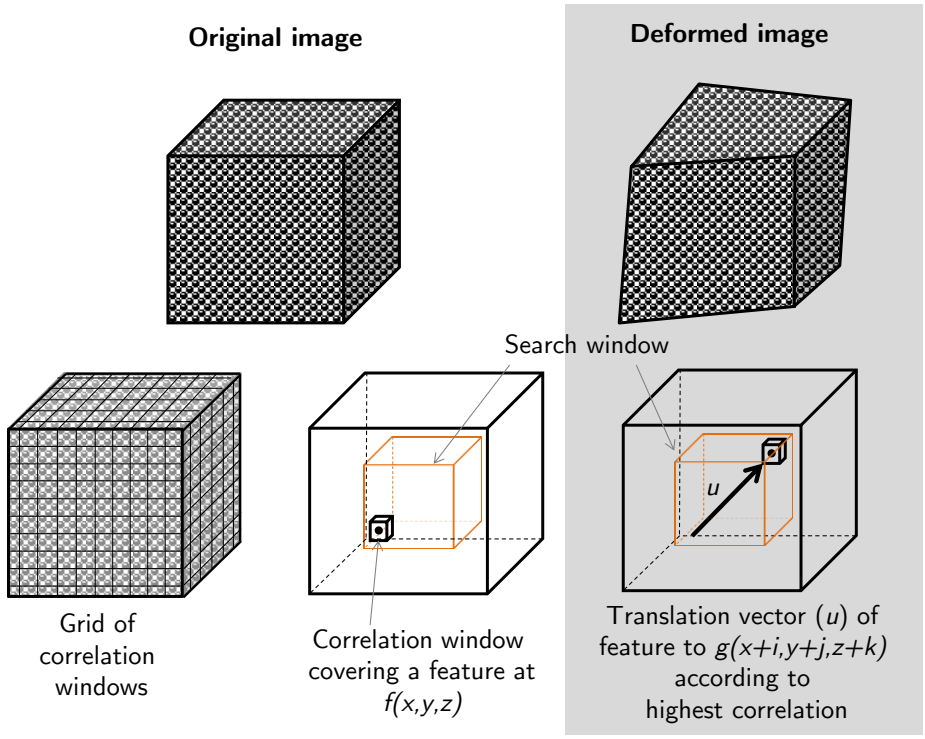

Figure 3-11: DVC correlation process showing segmentation of volume into correlation windows (subvolumes), followed by an example of a single subvolume being correlated (within a search window) between the original and deformed image. A displacement vector (u) corresponding to the region of highest correlation is assigned.

As shown in Figure 3-11, a sub-volume (correlation window) containing a locally discrete pattern or group of voxels, centred at the point of measurement is identified in the reference volume. The sub-volume, $f(x,y,z)$, is defined by a set of coordinates centred at the point of measurement (origin). The equivalent sub-volume, $g(x+i,y+j,z+k)$, is found in the deformed sample volume and a translation vector (u) is estimated to quantify its displacement. Typically a shape function is assigned at this step, which allows for some deformation of the sub-volume while searching for a high correlation. The degree of match between f and g, is defined by an appropriate correlation coefficient (CC) such as the sum of squares correlation coefficient or the cross correlation coefficient[233, 240]. An iterative process such as the Newton-Rhapson or Levenberg-Marquardt methods is used to maximise the CC and extract the best fit parameters for the volume correlation. Translation is the

main transformation of interest and provides an estimate for the translation vector u in Figure 3-11. Other transformations include rotation, normal strain and shear strain. For a more in-depth discussion on the techniques applied in DVC, readers are referred to descriptions given by Bay[240] and Bing Pan[241].

The choice of sub-volume as well as the search window size can affect the accuracy of the technique and determine how computationally intensive the algorithm will be. The sub-volume should be sufficiently large to contain a distinctive intensity pattern. However, if the sub-volume is too large such that there is significant deformation within the sub-volume, then the shape function will no longer yield a high correlation and the accuracy of the technique will decline. Therefore, a small sub-volume size is preferable, and a small search window is also favoured to minimise computation. Currently, refinement of sub-volume and search window sizes is largely based on visual inspection and trial and error, though automation methods for such refinement can easily be imagined and may be implemented in the near future. For further discussion on balancing sub-volume size with image texture readers are referred to a review by Bing Pan *et al.*[241], as well as discussions by Quinta *et al.*[235] and Liu and Morgan[234].

3.5. Thermal Imaging

One of the most important factors to consider when assessing the safety of lithium-ion batteries is their thermal response to a stimulus, where the stimulus may be applied in thermal, electrical or mechanical form. A thorough understanding of the batteries' thermal response during operation[242, 243] and failure[63, 105, 244] is needed to ensure the optimum performance and high safety standard of battery systems through appropriate design of heat dissipation mechanisms. Measurement of the thermal response of a cell also allows direct comparison between battery and system designs, including the efficacy of safety devices as well as assessing the safety of different chemistries[57, 58, 108, 137], materials[149, 245], and devices[246].

The most commonly used methods for determining the temperature of lithium-ion batteries are through the use of thermocouples and infrared (thermal) imaging.

Thermocouples measure temperature by measuring the voltage difference between two thermoelements where the ends of the thermoelements, tail end and reference end, are at the temperature of the environment to be measured and a reference temperature such as ambient, respectively. The design of a thermocouple inherently involves a point mesurement, lacking spatial resolution. The response time of thermocouples is also hindered by the thermal properties of the materials involved as well as relying on good contact with the material of interest, making them particularly susceptiable to error while measuring rapidly changing surface temperatures.

However, thermal imaging measures the temperature of surfaces by detecting the emission of infrared radiation from the target object (radiance) on a detector plane, giving it a higher temporal and spatial resolution. CCD detectors are also common for thermal imaging cameras, but are cooled to very low temperatures to minimise noise caused by thermally excited charge carries. Above 0 K every object emits thermal radiation, the quantity of which is dependent on its temperature according to Planck's law where the total radiant power, $B_\lambda(T)$, from a blackbody at an absolute temperature of T between wavelengths λ and $\lambda + d\lambda$ is:

$$B_\lambda(T)d\lambda = \frac{2hc^2}{\lambda^5}\frac{1}{e^{\frac{hc}{\lambda kT}} - 1}\,d\lambda \tag{3.11}$$

Where h is Planck's constant (h=6.626 × 10^{-34} J s), c is the speed of light in a vacuum (2.998 × 10^{8} m s^{-1}) and k is the Boltzmann constant (1.381 × 10^{-23} J K^{-1}). For example, the spectral radiance from a blackbody for three different temperatures is plotted in Figure 3-12. For increasing temperature the radiance increases. The peak of the spectrum is also seen to shift to lower wavelengths as the temperature increases, in accordance with Wiens' law.

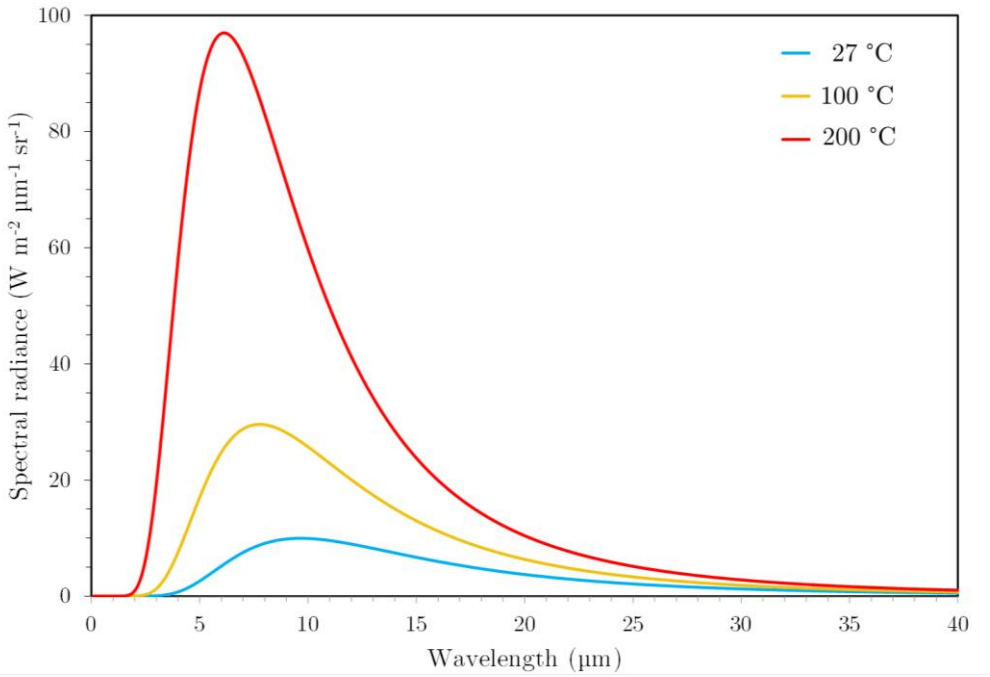

Figure 3-12: Plot showing the dependence of radiance of a black body on temperature. Data gathered from the United States Geological Survey radiance calculator[247].

However, Planck's law assumes a perfect black body, which describes an object that emits the maximum amount of thermal radiation. In reality, objects emit less than this amount, and the ratio between the actual amount of radiant heat emitted and the maximum amount, is known as *emissivity* (ε); Planck's law assumes an emissivity of 1. The actual radiance (averaged in wavelength and direction) of an object, is a factor of the emissivity of the body and its theoretical black body radiance (B_{BB}):

$$B(T) = \varepsilon\, B_{BB}(T) \tag{3.12}$$

For this reason, a uniform layer of heat resistant black paint (with a calibrated emissivity of 0.96 over the range of 40 °C to 180 °C (Figure 3-13)) was applied to the surface of each battery before testing. The calibrated emissivity was determined by comparing the temperature reading from a thermocouple on a surface ($T_{thermocouple}$) to the temperature reading from the thermal camera at the point at which the thermocouple makes contact with the surface (T_{IR})[248]. The best fit emissivity value across the aforementioned temperature range can then be

determined (Figure 3-13). However, as Hatchard *et al.*[249] demonstrated, the high emissivity black paint results in a more rapid heat loss through increased radiative heat transfer when compared to the unpainted surface (typically either stainless steel, aluminium, foil, or a plastic label), which can affect the performance and safety of lithium-ion batteries.

Experimental: For the experiments in this thesis the temperature of the battery was recorded using a thermal camera (FLIR SC5000MB, FLIR Systems France, Croissy-Beaubourg, France). The real-time thermal imaging movies and mean temperature vs. time graphs were developed using FLIR's Altair software. The noise equivalent temperature difference of the camera in the calibrated range was < 20 mK. Images were recorded at a rate of 25 Hz and the temperature measurement accuracy, as specified by the manufacturer, was $\pm$ 1 °C or $\pm$ 1 % of the temperature in °C. The thermal camera was calibrated for temperature ranges of 15 °C – 250 °C, and 250 °C – 1500 °C. The former temperature range was used for all experiments except the nail penetration tests; this change in temperature range is explicit in the relevant chapter. The emissivity value of 0.96 was applied to the thermal images in the FLIR thermal imaging software before extracting temperature information.

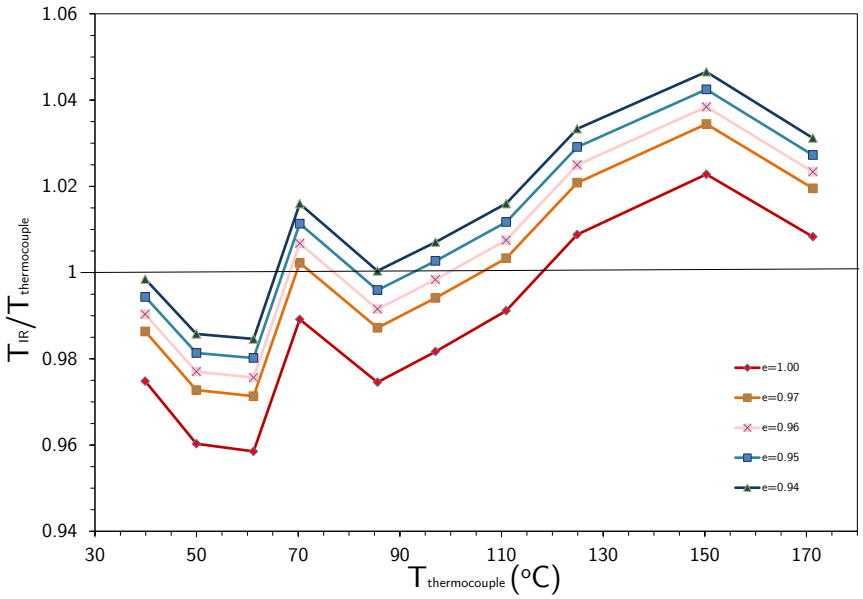

Figure 3-13: Deviation between the temperatures measured using the thermocouple and the infrared (IR) camera for different emissivity values.

The quantity of radiant power that reaches the detector plane is also dependent on the transparency of the intermediate materials to waves in the infrared spectrum. Most of the experiments described in this thesis involved imaging through a sapphire window that has a high transmittance in the infrared region. This was to ensure that the thermal camera and external equipment were safe from projectiles (sapphire, being the 3rd hardest mineral, has very high mechanical strength) while also maintaining a sealed container to prevent smoke and fumes from escaping during battery failure.

2 mm thick sapphire windows were implemented. The transmittance of this thickness of sapphire was measured using Fourier Transform Infrared Spectroscopy (FTIR) showing that the window had a transmittance of *ca.* 0.86 between 2.5 and 5 µm wavelengths in the infra-red range (Figure 3-14); the thermal camera had a wavelength detector allowing detection of infra-red wavelengths between 3 µm and 5 µm. For the infrared imaging a value of 0.86 for transmission between the sample and the thermal camera as well as an emissivity value of 0.96 were used to correct the temperature measurements from the infrared camera.

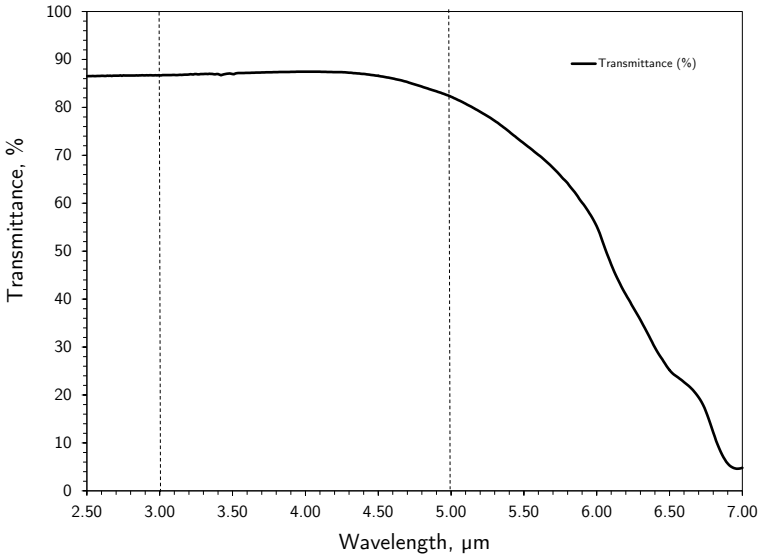

Figure 3-14: Transmittance measurement of a 2 mm thick sapphire window for wavelengths within the infrared range. The FLIR SC5000 camera is most sensitive to wavelengths between 3 and 5 µm.

3.6. Scanning Electron Microscopy

Scanning electron microscopy (SEM) is used to capture topographic images of materials with resolutions from micrometers (µm) to nanometers (nm). SEM uses an electron source and voltage to irradiate the surface of the sample material with electrons. When struck with electrons the sample emits backscattered electrons, secondary electrons, characteristic X-rays and other photons of various energies. An image is formed on the detector that can either be from backscattered electrons or secondary electrons from the sample, depending on which operational setting is used. In this thesis, the Zeiss EVO MA 10 scanning electron microscope is used, which is also equipped with an INCAx-act X-ray detector (Oxford Instruments) for energy dispersive X-ray spectroscopy (EDX). EDX involves striking the sample material with high energy electrons to emit electrons from the sample material's innermost orbitals, producing a hole. When an electron from an outer orbital falls into the inner hole a characteristic photon of energy equal to the difference in electron energies between the two states is produced. Since each element has its own characteristic emission, a spatial map of elemental composition can be

generated. Electrode and separator samples were mounted on a carbon coated SEM stub for imaging in the scanning electron microscope.

3.7. Electrical Testing

The electrical testing of lithium-ion batteries described in this thesis was performed using commercial devices. A Maccor 4300 (Maccor Inc., Tulsa, OK, USA) was used to charge and discharge batteries at rates recommended by manufactures, unless otherwise specified. A Gamry Reference 3000 potentiostat with booster (Gamry Instruments, Warminster, PA, USA) was used to apply high charge and discharge rates during synchrotron experiments.

3.8. Rig Designs for *Operando* Imaging

Most of the work described in this thesis was performed at the ESRF which has world leading photon flux at high energies that facilitates high-speed radiography and tomography of commercial lithium-ion batteries. The results discussed in the later chapters stem from two visits to the ESRF; the first visit was to beamline ID15A where a combination of thermal and electrical abuse experiments were performed while simultaneously carrying out high-speed X-ray CT. The second visit was to beamline ID19, where thermal and mechanical abuse tests were carried out; this visit did not involve X-ray CT, but solely involved high-speed radiography. The experimental setups for both visits (ID15 and D19) are described below.

3.8.1. Experiments at ESRF ID15A

A custom-built *in-situ* rig was designed for the experiments at ID15A, which provided the unique capability of real-time tomography, thermal, and electrochemical analyses during electrical and thermal abuse tests, extending dynamic failure analyses of commercial cells to include internal structural features.

The *in-situ* rig and associated equipment are shown in Figure 3-15, and the requirements for electrical and thermal abuse tests are discussed separately.

Electrical Abuse: The electrical connection between the battery and constant resistance circuit was maintained through use of an electrical slip ring (P4+ Compact Slip Ring, Moog, UK) built into the ID15A rotation stage (ABR1000, Aerotech, USA) (Figure 5-2a,b), which allowed continuous rotation while maintaining an electrical connection. Copper foil was pressed against the terminals of the battery using two copper tabs tightly wrapped with electrical tape. An electrical cable was soldered to each of the copper tabs. For the electrical cable connected to the positive terminal (top of the cell in Figure 3-15a) a relatively X-ray transparent copper mesh was used to minimise beam hardening artefacts as the cable passed in front of the field of view (leading to the electrical slip ring) during rotation.

Thermal Abuse: A safe containment system (Figure 3-15b) for thermal runaway of the selected commercial cells was designed to fit the ID15A rotation stage (ABR1000, Aerotech, USA). The containment system included a continuous inert (N_2) gas flow to flush out any evolved gases and help prevent the propagation of fire, two X-ray transparent Kapton windows in the path of the beam, an infrared transparent sapphire window for thermal imaging, and a fourth opening for inserting a heat gun (to simulate the external heating effects of battery pack failure).

The system was not completely sealed and therefore the internal environment was not entirely inert; sufficient oxygen in air was still present to allow some limited ignition of the cell contents during thermal runaway. The batteries were tightly secured between a fastening screw and the wall of the sample holder and were positioned such that the region of interest was in line with the beam. Heating was applied by a heat gun (HG 2310 LCD Electronic, Steinel, Germany) located next to the battery, which had a 9 mm reduction nozzle to focus the heat onto the battery surface, protecting neighbouring equipment and helping prevent circumferential heterogeneity in temperature. The reduction nozzle resulted in a

spot size with *ca.* 10 mm diameter on the surface of the rotating batteries. The heat gun used a Duratherm^{TM} heating element and precise control of the applied temperature was achieved by varying air flow rates and air temperature at 10 °C increments.

The heat gun was set to a temperature of 480 °C at maximum airflow and the reduction nozzle of the heat gun was carefully placed 2 cm from the cells to avoid disparities in heating between tests. The continuous rotation helped to maintain a uniform circumferential temperature distribution around the batteries. Heating continued until thermal runaway occurred. The temperature of the battery was recorded using a thermal camera (FLIR SC5000MB, FLIR Systems France, Croissy-Beaubourg, France), from the opposite side to the heat gun as shown in Figure 3-15c. To avoid radiation damage of the internal components, the thermal camera was covered in 2 mm thick lead shielding. The thermal camera was calibrated for temperature ranges of 15 – 250 °C and 250 – 1500 °C; the former temperature range was applied to ensure accurate temperature measurements over the expected temperature range[250].

A PCO Dimax (CMOS) camera was used for all synchrotron imaging experiments, and the specific imaging parameters for each experiment are provided in the associated results chapters.

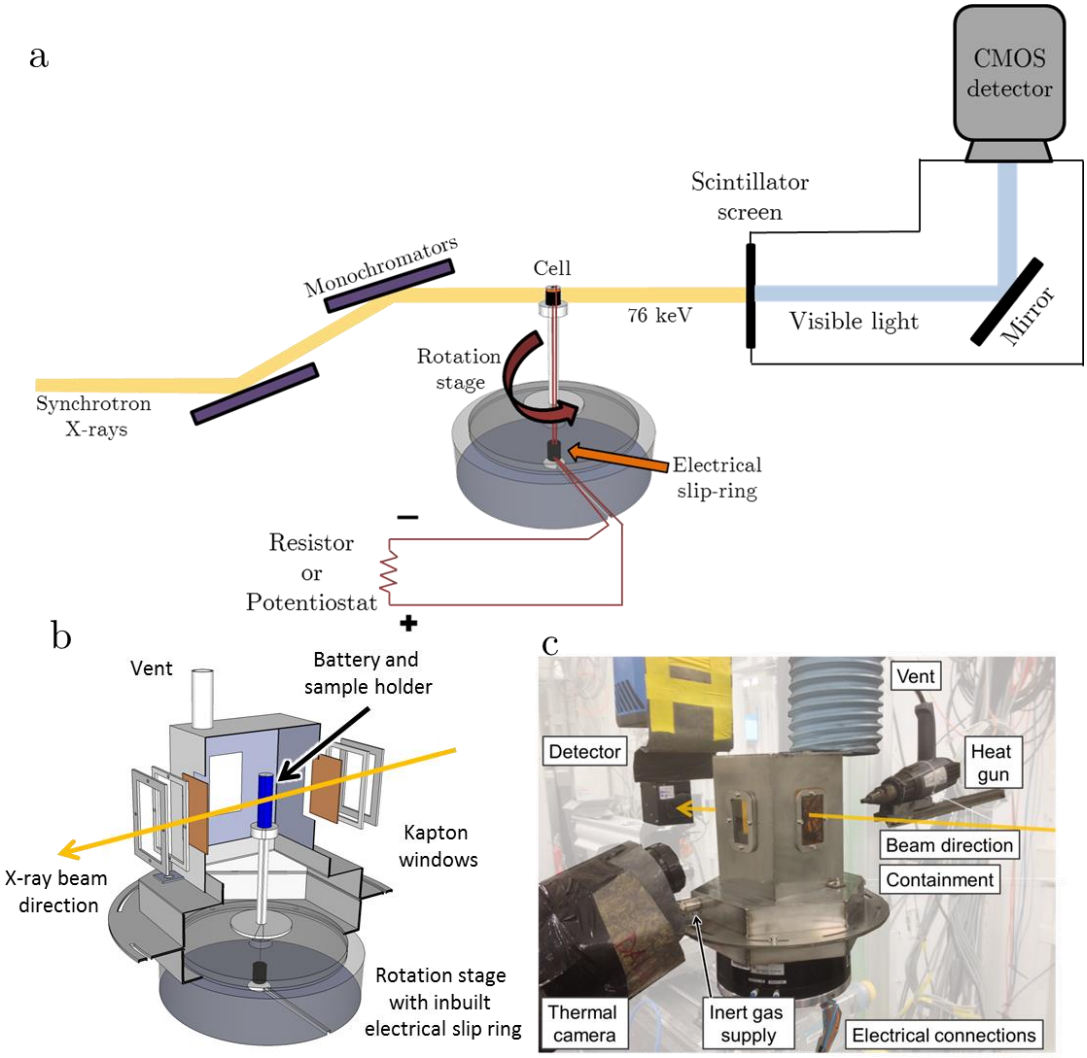

Figure 3-15: (a) Schematic of the setup in ID15A at the ESRF, showing rotation stage and in-built electrical slip ring connection. (b) Cut-away of battery containment design attached to the rotation stage for *operando* X-ray CT. (c) arrangement of apparatus for X-ray CT thermal runaway experiments, where the thermal camera is covered in lead shielding.

3.8.2. Experiments at ESRF ID19

The experiments performed at beamline ID19 involved high-speed radiography only, and not computed tomography. Therefore, rotational compatibility was not needed. A commercial battery nail penetration system (MTI Nail Penetration Tester, MSK-800-TE9002, MTI, Richmond, CA, USA) was modified to provide X-ray and infrared transparent windows for simultaneous thermal and high-speed X-

ray imaging (Figure 3-16). The front and rear doors of the nail penetration system were replaced with 2 mm thick aluminium panels that had integrated infra-red transparent sapphire, and X-ray transparent Kapton windows for simultaneous thermal imaging and radiography. The entire penetration system was mounted onto a heavy duty electronically controlled sample stage that, while under load (*ca.* 120 kg), could move in the vertical direction only. To extract the harmful gases generated during thermal runaway, the nail penetration system was connected to the beamline ventilation system via flexi-piping, and an additional wider ventilation pipe was placed over the top of the system to help exhaust escaping gases (Figure 3-16a,b).

During imaging, the lithium-ion batteries were held firmly in place by hydraulic clamps, which along with the penetration piston, was connected to a 3 bar air supply (Figure 3-16b,c). The thermal camera was mounted directly above the field of view of the beam, at a slight angle facing down at the cell being tested. Electrical connections for voltage monitoring and heating were passed through a side porthole (Figure 3-16b), and all electrical equipment (penetration system, thermal camera, heating elements and power supplies) were extended and controlled from outside the hutch in the user control room.

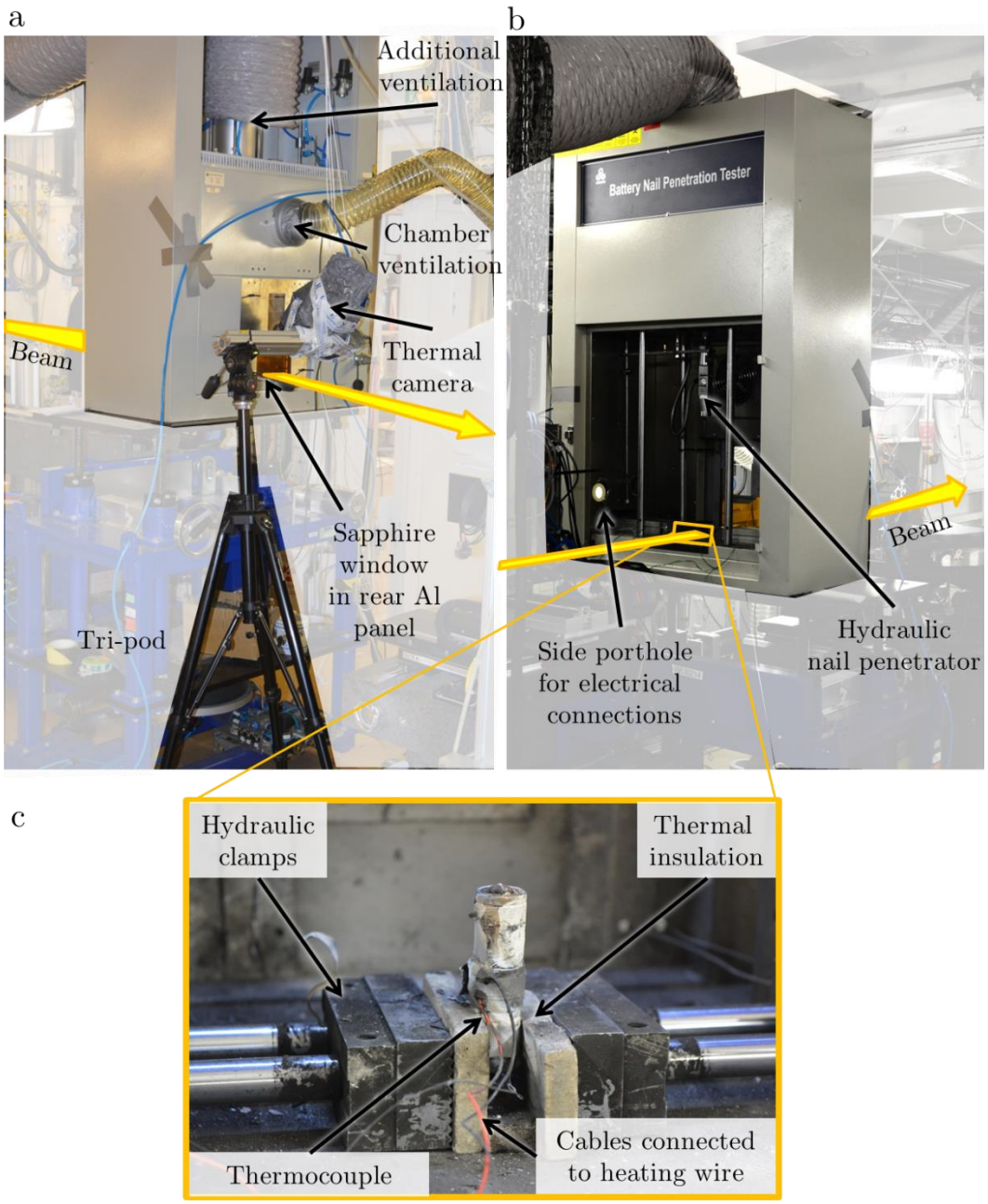

Figure 3-16: (a) Rear view of the nail penetration system showing the placement of the rear Al panel with an integrated sapphire window, the thermal camera, and ventilation pipes. (b) Front view of the nail penetration system (without the X-ray transparent Al front panel), showing the location of the battery being tested and hydraulic penetration piston. (c) Magnified view of inside of the penetration system showing a failed 18650 battery secured in place by hydraulic clamps and insulation plates.

Heating was applied to the batteries by wrapping high resistance nichrome heating wire around the base of the cells (Figure 3-17), which was connected to a power supply outside the hutch. The nichrome wire was cut to a length that provided around 22 ohms of resistance. Heating power of *ca.* 33 W was applied to the cell by passing a suitable current through the resistance coil via the power supply. K-type thermocouples were used in conjunction with the thermal camera for surface temperature measurement.

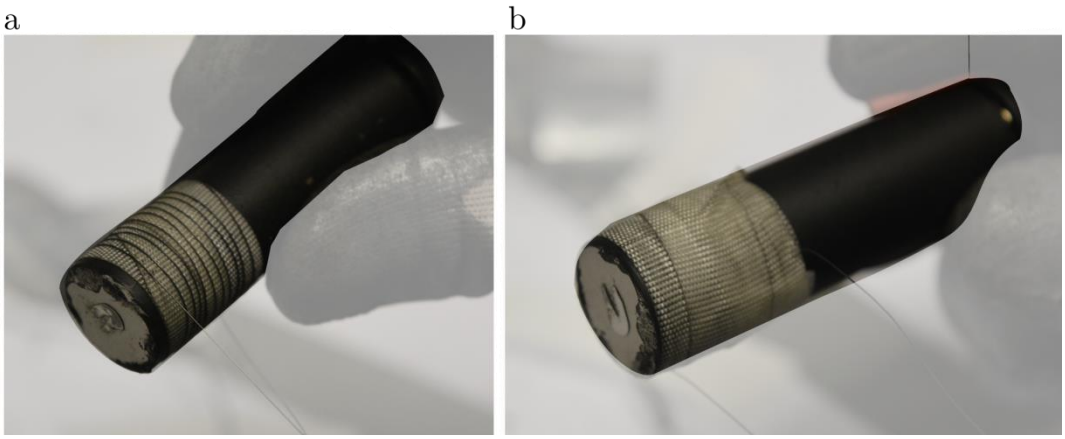

Figure 3-17: (a) Nichrome wire with a length corresponding to a resistance of *ca.* 22 Ω wrapped around the base of an 18650 cell. The wire is separated from the cell casing by a glass braid tape. (b) An additional layer of glass braid tape was wrapped around the nichrome wire to prevent the wire from connecting with itself during experiments.

The hydraulic nail penetrator shown in Figure 3-16 was used for nail penetration experiments. A custom made stainless steel nail with an integrated rapid response 0.5 mm diameter, insulated K-type thermocouple, with an operating range from -100 °C to 800 °C (Product 406-534, TC-direct, UK) (Figure 3-18a), was used to measure the temperature at the tip of the nail as it penetrates into the cells. This design was inspired by the "smart-nail" described by Hatchard *et al.* [171] but with some modifications. A 60 mm long stainless steel tube with an external diameter of 4 mm and an internal diameter of 2 mm was used. A sharp stainless steel tip (Figure 3-18b) was sharpened and shaped on a lathe. A 1 mm diameter bore was drilled to just beneath the surface of the tip; thereafter a

0.5 mm hole, which was slightly off-centred from the sharpened tip, was drilled through to the surface. The complete tip component was forced into the cylindrical tube. The 0.5 mm diameter thermocouple was coated in epoxy glue and fed through the assembly until it reached a subsurface location near the tip as shown in Figure 3-18. The subsurface placement of the thermocouple protected it from damage during insertion, and also allowed direct contact between the hot material within the cell and the thermocouple during the penetration tests. This resulted in a more rapid response and more representative temperature reading than the insulated design described by Hatchard *et al.*[171].

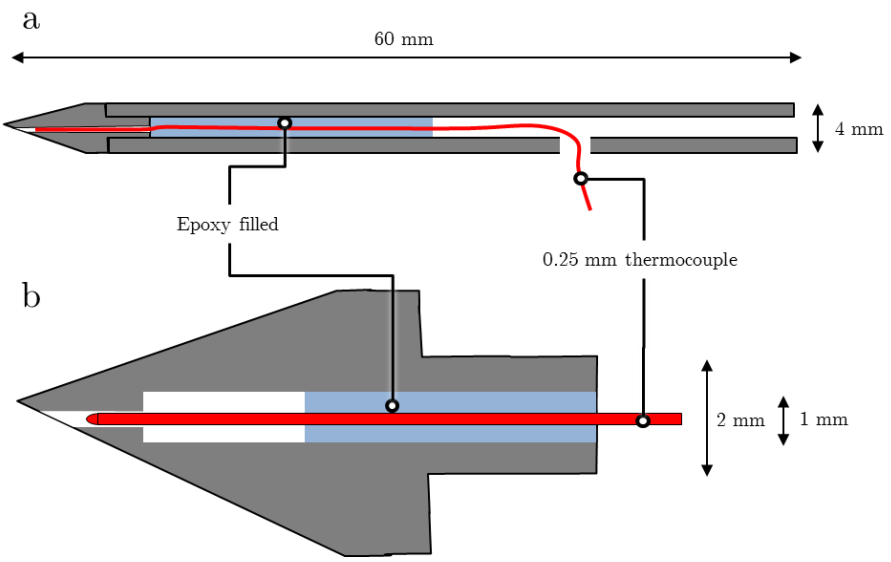

Figure 3-18: (a) Illustration showing a sectioned view of the stainless steel nail with an integrated thermocouple at its tip. The nail consisted of two components, the 'tube' and the 'tip'. (b) Magnified view of the 'tip' section showing the placement of the thermocouple just beneath the surface of the nail at a slightly off-centred position from the sharpened tip. The 'tip' section was forced into the 'tube' during assembly.

3.9. Summary

In this chapter, the basic theory behind X-ray imaging and computed tomography was explored, including absorption phase contrast imaging and advanced imaging

techniques such as Zernike phase contrast imaging. The application of X-ray imaging and the characteristics of different X-ray sources and detectors were described, and practical considerations for high-speed imaging in synchrotrons were discussed; the combination of scintillator and CMOS detectors is the preferred choice for high-speed imaging due to the commercial cameras being the most cost effective and high performance approach for achieving high frame rates where the imaging system is not flux-limited. The large working distance in synchrotrons allows novel *in-situ* rig designs to be implemented during imaging; *in-situ* rigs as well as associated thermal and electrochemical analysis equipment that were utilised at the ESRF for abuse testing of lithium-ion batteries, were described in detail and will be referred to in Chapters 5-8. Finally, image processing and image-based quantification techniques were described. The following chapter is the first of the results chapters and describes experiments carried out in a lab-based CT system, where numerous image-based quantification techniques described here were applied.

Chapter 4

Transport Properties of Polymer Separators

Sections of this work have been peer reviewed and published in Journal of Power Sources (D. P. Finegan, S. Cooper, B. Tjaden, O. O. Taiwo, J. Gelb, G. Hinds, D. J. L. Brett, P. R. Shearing, *Characterising the structural properties of polymer separators for lithium-ion batteries in 3D using phase contrast X-ray microscopy.* J. of Power Sources, 2016. 333: p.184-192, (doi:10.1016/j.jpowsour.2016.09.132).

4.1. Introduction

The separator is an integral component in lithium-ion batteries, affecting both safety and performance[66, 251, 252]. Its primary function is to electrically isolate the positive and negative electrodes, whilst ensuring facile ionic transport of Li^+ through the electrolyte; however, the design and selection of the separator can involve a trade-off between cell safety and charge/discharge rate, which may be optimised by design of the appropriate separator microstructure[253].

When considering the performance of a separator, there are three essential microstructural characteristics to take into account: porosity, tortuosity factor and pore size distribution (P_oSD). A high porosity, large mean pore size and low tortuosity contribute to a high rate capability, with low electrical impedance, commensurate with fast ion transport. However, such a structure is not effective in suppressing lithium dendrite growth between the electrodes, which can result in short circuiting. These important, and often conflicting, microstructural properties

of separator membranes contribute to the overall performance and safety of a cell, and yet they remain poorly understood.

The microstructural properties of separator membranes are conventionally quantified through experimental methods; for example, mercury intrusion porosimetry (MIP) is most frequently used to measure porosity and P_oSD[60], and is integrated into standard test methods such as ASTM D-2873. However, this technique has a number of limitations[222, 254, 255], including the 'ink-bottle' or 'bottle-neck' effect, where the intruding fluid enters a cavity at a pressure determined by the size of the cavity entrance, rather than the cavity itself. Consequently, MIP can bias the P_oSD towards smaller pore sizes, overestimating small pores and underestimating large pores. For these reasons, MIP is generally viewed as an inadequate method for accurately determining the P_oSD of complex materials[254].

The tortuosity factor of the separator is most commonly determined via electrical conductivity measurements, and alternatively described in terms of porosity through the Bruggeman relationship[60, 215, 229]; however, this has known limitations[256]. As described in Section 1.5, the two most commonly used metrics that reflect the transport resistance, and hence porosity and tortuosity factor of separator materials, are the MacMullin number[60, 77], (ratio of the specific resistivity of the electrolyte to the specific resistivity of the separator soaked in electrolyte) and the Gurley number (time required for a specific volume of air to pass through a separator under a certain pressure). Such characterisation methods have undergone little change since the advent of commercial lithium-ion batteries in the early 1990's[257], and do not adequately describe the microstructural properties of these materials. Only very recently have the transport properties of a polymer separator been characterised from a three-dimensional (3D) dataset captured using FIB-SEM tomography[258].

X-ray computed tomography (CT) is a powerful tool for characterising the microstructure of materials in 3D[174, 259] which has been successfully applied to materials within batteries[176, 177, 191, 217, 219] and other electrochemical energy devices[221, 260, 261]. Numerous studies have used X-ray CT to investigate the effect of the microstructural properties of electrode materials on the performance of

lithium-ion batteries[179, 217, 227, 262], but few studies have focused on polymer separator materials, even though they are also expected to influence performance significantly. The low X-ray attenuation coefficients of polymer separators make segmentation of tomographic images challenging, and the fine microstructural features often found in commercial separator materials compound this.

Here, the Zernike phase contrast technique (described in Section 3.1.4) is applied in nano-scale X-ray microscopy[205], to capture and characterise the local microstructural properties of polymer separators in 3D. Three commercial separator samples are analysed: Celgard 2325[263], Celgard 2500[264], and an MTI ceramic-coated membrane[265]. The porosity, tortuosity factor and P_oSD are determined locally through a combination of 3D quantification[222], stereological[224, 225], and image-based modelling[176, 191] techniques, providing spatial information on the structural properties of commonly used commercial polymer separators.

4.2. Experimental

4.2.1. Separator Materials

This study focuses on three polymer separators; Celgard 2325[263], Celgard 2500[264], and the MTI ceramic-coated membrane[265]. Celgard 2325 consists of a tri-layer of PP|PE|PP, Celgard 2500 consists of a monolayer membrane of PP, and the MTI ceramic-coated membrane consists of a PE membrane coated on both sides with aluminium oxide particles. The manufacturer's specifications (shown in Table 4-1) state that the porosity of the Celgard 2325, 2500 and the MTI membranes are 39 %, 55 %, and 37 %, respectively. This work is performed on dry separator membranes and does not account for the softening/swelling effects induced by the electrolyte.

Both Celgard separators are manufactured by dry processing, which is described in detail by Deimede and Elmasides[266]; this process involves uniaxial stretching of PP and PE lamellae, creating a highly directional 'slit-like' pore structure, which causes high anisotropy in the mechanical properties of the membranes. The MTI ceramic-coated separator is manufactured via wet processing,

which involves biaxial stretching of a polymer film, resulting in low anisotropy in the mechanical properties of the membrane[266].

The porosity of the separator is defined as the ratio of void volume to apparent geometric volume. This can be approximately determined by weighing the sample before and after solvent is allowed to absorb into the pores. For a solvent of known density, the relative volume of absorbed solvent to the geometric volume of the separator can then be calculated. MIP[60] is also used to determine porosity according to the standard test method described in ASTM D-2873. In addition, MIP is used to determine the P_oSD and mean pore size of porous samples[60]. In Table 4-1 the specifications are likely to have been determined by MIP.

Table 4-1: Manufacturer specifications of separator material properties.

Sample	Type	Thickness (µm)	Porosity (%)	Average PP Pore Diameter (µm)	Gurley number (s)
Celgard 2325	Tri-layer	25	39	0.028	620
Celgard 2500	Monolayer	25	55	0.064	200
MTI ceramic	Ceramic-coated PE monolayer	16	37	-	240

4.2.2. Phase Contrast Tomography

The separator samples were prepared by cutting triangular shaped pieces from the bulk material and imaged using a Zernike phase contrast setting in a lab-based nano-scale X-ray microscope (Zeiss Xradia 810 Ultra, Carl Zeiss Microscopy, Pleasanton, CA)[181, 205]. In this study, a 5.4 keV quasi-monochromatic beam was used and images were recorded on a 1024 × 1024 pixel CCD detector.

A total of 2001 and 1751 X-ray transmission radiographs were captured for the Celgard 2325 and Celgard 2500 samples respectively, over 180° rotation. The exposure time per radiograph for both samples was 35 s, using a detector pixel size of 63.1 nm. For the MTI ceramic-coated separator, 1601 images with a 15 s exposure time over a 180° rotation were used to reconstruct the tomograms, and a detector binning setting of 2 yielded an effective voxel size of 126.2 nm. Detector binning settings of 1 and 2 showed little difference in the effective resolution of the phase contrast images. The transmission images from both scans were reconstructed in 3D using ZEISS XMReconstructor software, which uses a filtered back-projection algorithm. Although high energy X-rays are known to damage polymer materials by inducing cross-linking of polymer chains[267, 268], any significant change in the polymer microstructure resulting from the damage during imaging could be seen via motion artefacts and poor image quality in the reconstructed tomograms. The reconstructed images showed clear edge definition, and no sign of motion artefacts, therefore any damage to the polymer material is thought to have a negligible effect on the separators microstructure.

Volume visualisation and image processing were performed using the Avizo software package (version 9, FEI, VSG). The polymer phase was segmented based on its higher greyscale value and saved as a binary TIFF file. The pore volume was separated from the solid phase using threshold segmentation. When compared to the greyscale images, the features in segmented images correlated well. Greyscale images and the segmented binary images can be compared in Figure 4-1, and further examples for comparison are provided in Section 10.1 of Appendices. The samples were oriented such that the surface of the separator was perpendicular to the *Z*-axis (through-plane direction). In the *X*, *Y* and *Z* directions, the samples were cropped to volumes consisting of 822 × 961 × 415 voxels (*ca.* 52 µm × 62 µm × 25 µm) for Celgard 2325, 672 × 654 × 409 voxels (*ca.* 42 µm × 41 µm × 26 µm) for Celgard 2500, and 379 × 465 × 138 voxels (*ca.* 48 µm × 59 µm × 17 µm) for the MTI ceramic-coated separator. 3D image reconstructions and their associated greyscale and binary slices of each sample were made, and the segmented 3D TIFF image files were then used for image-based quantification and characterisation.

4.3. Image-based Characterisation

4.3.1. Porosity

3D image reconstructions of each sample and associated greyscale and binary slices are shown in Figure 4-1.

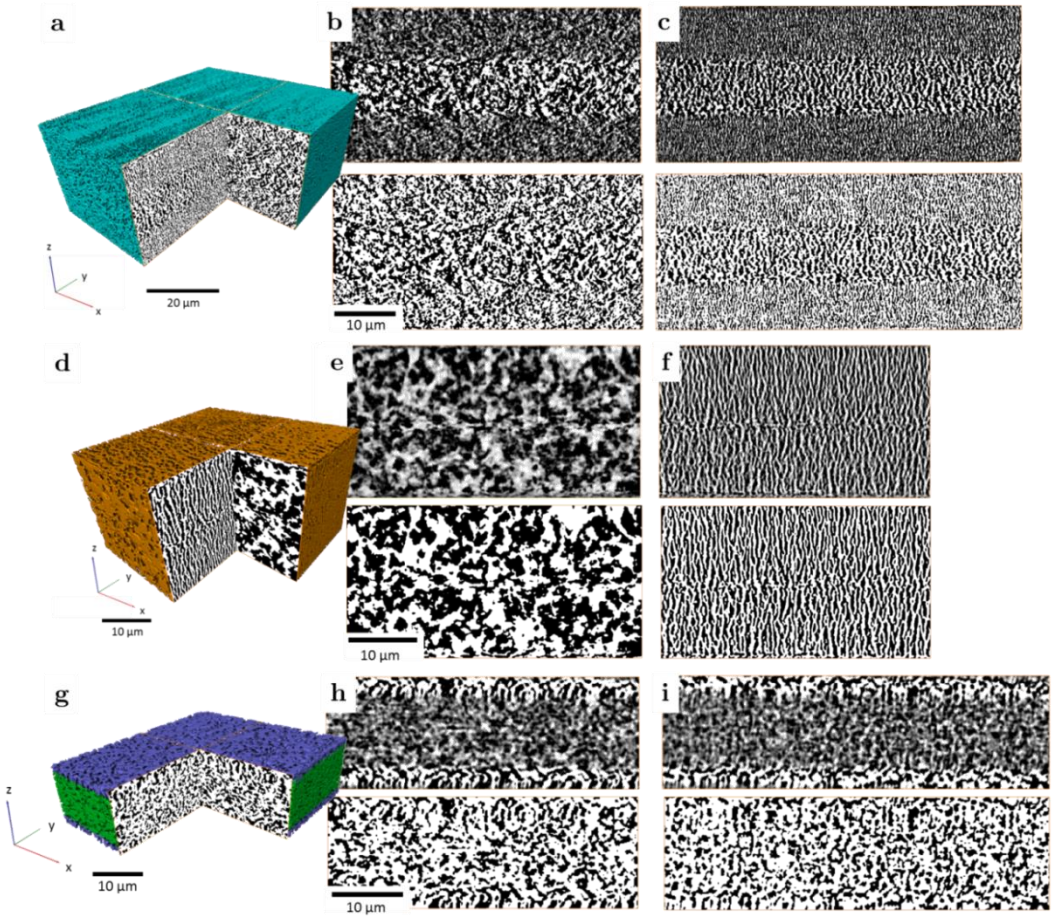

Figure 4-1: (a) Volume rendering of Celgard 2325 with binary slices in the *YZ* and *XZ* planes. (b) Greyscale (top) and binary (bottom) slices from the *XZ* plane and (c) *YZ* plane showing the tri-layer structure. (d) Celgard 2500 with binary slices in *YZ* and *XZ* planes. (e) Greyscale (top) and binary (bottom) slices from the *XZ* plane, and (f) *YZ* plane showing the monolayer structure. (g) Ceramic-coated membrane showing ceramic (blue) and PE (green) layers. (h) Greyscale (top) and binary (bottom) slices from the *XZ* plane and (i) *YZ* plane. In the binary images, white is solid and black is pore. The difference in pore structures observed in the *YZ* and *XZ* planes highlight that the pores are elongated.

The porosity of the binary images of the full volumes was 41 % for Celgard 2325, 53 % for Celgard 2500, and 38 % for the MTI ceramic-coated separator. The porosity was also calculated on a slice-by-slice basis, where each slice is a single voxel thick (63.1 nm for Celgard samples and 126.2 nm for the MTI sample), to demonstrate that the porosity in the separator samples is non-uniform and anisotropic. A representative volume analysis of the porosity of the separators (provided in Section 10.1 of Appendices) demonstrates that the samples are sufficiently large to be considered as being representative of the bulk material. Figure 4-2(a-c) shows the slice-wise plots of porosity in the X, Y and Z directions. In the Z direction, the tri-layer Celgard 2325 shows a significant difference in porosity with depth, revealing the PP layers to have a porosity of *ca.* 39 %, and the intermediate PE layer to have a porosity of *ca.* 44 %. The monolayer Celgard 2500 shows a drop in porosity of *ca.* 3 % mid-way through the separator. Upon close inspection, this region can also be seen mid-way through the sample in Figure 4-1e, and may be a consequence of applying two layers of PP during the manufacturing process, with the region surrounding the interface having an anomalous porosity. For the MTI ceramic-coated separator, a higher porosity is observed for the ceramic coating than for the PE membrane. The porosities in the X and Y directions (Figure 4-2b,c) fluctuate evenly around the mean for each sample.

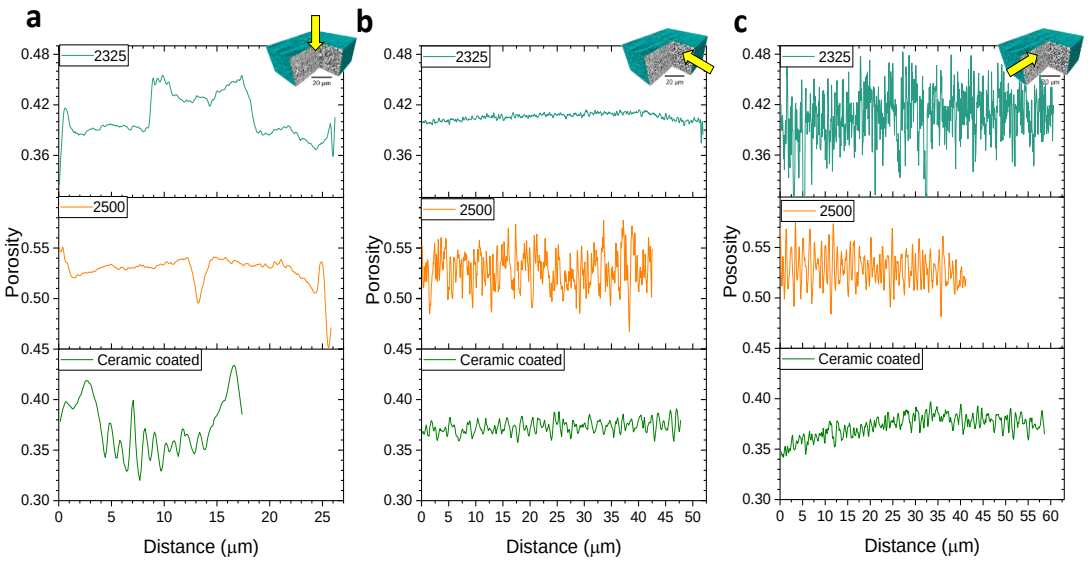

Figure 4-2: (a) Slice-wise porosity along the *Z*-axis for Celgard 2325 (top), 2500 (middle) and the MTI ceramic-coated separator (bottom). (b) Slice-wise porosity along the *X*-axis, and (c) slice-wise porosity along the *Y*-axis.

4.3.2. Pore Size Distribution

Two methods were used to determine the P_oSD: the first was a continuous P_oSD (c-P_oSD) 3D method developed by Munch and Holzer[222], and the second method is based on a stereological approach[225]; both methods are described in more detail in Section 3.4.

For each separator sample, cumulative P_oSD plots of volume fraction against pore radius, determined by the c-P_oSD method, are shown in Figure 4-3. The majority of the pore volume consists of pores of radii 70 nm - 150 nm for Celgard 2325, 200 nm - 300 nm for Celgard 2500, and 120 nm - 320 nm for the MTI ceramic-coated separator. The predominance of pores near the resolution limit for Celgard 2325 and the MTI ceramic-coated membrane suggests the quantification of P_oSD may be limited by the resolution of the scan.

Average pore sizes calculated from the P_oSD plots in Figure 4-3 are significantly larger than those specified by the manufacturer, with pore diameters that are greater by a factor of between 5 and 10 for Celgard 2325 and 2500. For Celgard 2325, the inclusion of the PE phase, which is shown to have a P_oSD consisting of much larger pores than the PP phase, would contribute to the much

larger pore size measurement observed via the c-P_oSD method. The manufacturer specifies that the average pore size of the Celgard 2325 is based on the PP phase only, which is perhaps due to limitations of the utilised P_oSD method such as the 'ink-bottle' effect. Further study on the constrictivity of pores[221] is needed to provide a quantitative explanation for the deviation between experimental measurements and image-based geometric measurements presented here.

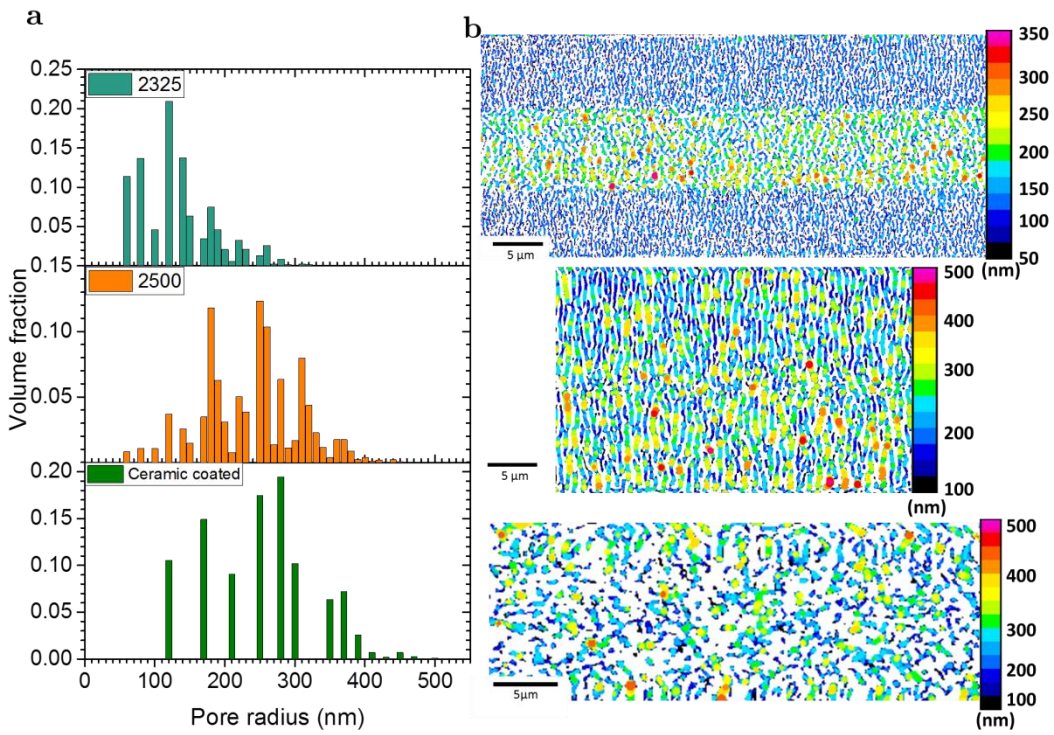

Figure 4-3: (a) P_oSD plots for Celgard 2325 (top), Celgard 2500 (middle) and the MTI ceramic-coated separator (bottom) based on the c-P_oSD method developed by Munch and Holzer[222]. (b) Corresponding 2D slices from the *YZ* plane for Celgard 2325 (top), Celgard 2500 (middle) and the MTI ceramic-coated separator (bottom), where the radius of the largest possible sphere to fit in the pore, centred on the centroid path through the network, is colour-coded. The colour-coded pore structure within the Celgard 2325 (top) tri-layer membrane (PP|PE|PP) shows that the intermediate PE layer contains the largest pores.

The X-ray microscopy imaging method in this study is limited by a pixel resolution of 63.1 nm for the Celgard samples, and 126.2 nm for the ceramic-coated

sample; any pores smaller than this would not be detected and are therefore neglected in the P_oSD calculation. Structural features such as nano-fibrils that stretch across the slit-like pore openings (these are clearly seen in Figure 4-4 and in the publication by Arora and Zhang[60]; further SEM images of the surfaces of the membranes analysed here are provided in Section 10.1 of Appendices) are also not detected, and would certainly reduce the sphere radii capable of fitting into the pore phase and hence the pore size measurement.

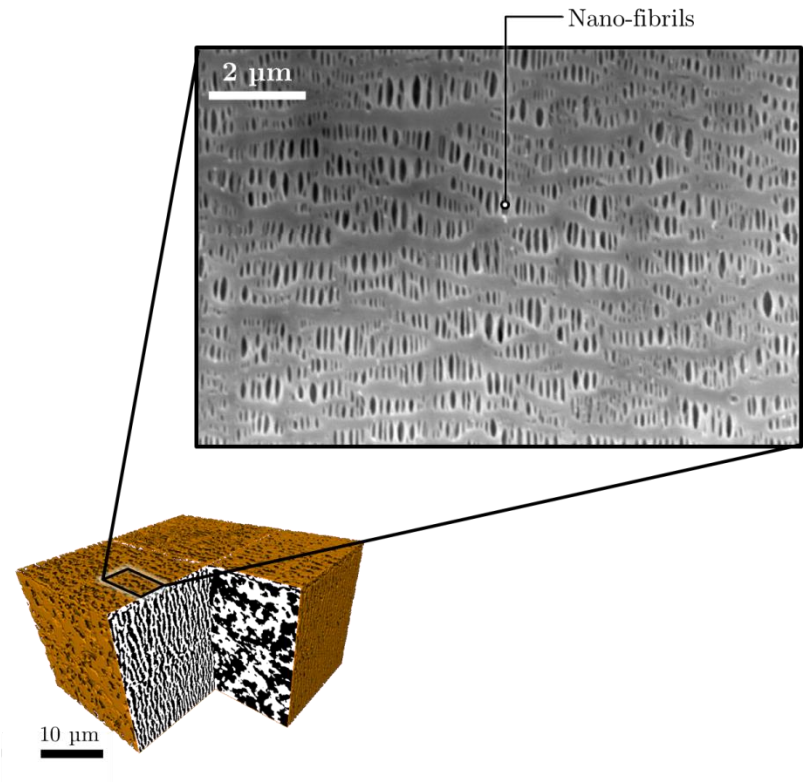

Figure 4-4: Scanning electron micrograph of the surface of the PE Celgard 2500 separator showing the presence of nano-fibrils stretching across the slit-like pores.

The stereological approach[224, 225] was used to determine the P_oSD from slice-by-slice calculations of the mean pore size in each of the axial directions, to more closely examine the anisotropic and non-uniform properties of the pore structure of the separators (Figure 4-5). In the Z (through-plane) direction, the mean pore radius increases from *ca.* 60 nm to *ca.* 90 nm between the PP and PE layers for Celgard 2325 (Figure 4-5a), which is consistent with what is observed using the c-P_oSD approach in Figure 4-3b. An increase in pore size is identified in

the Z (through-plane) direction mid-way through Celgard 2500 (Figure 4-5a). Figure 4-5a also shows that the mean pore size for the ceramic layers in the MTI ceramic-coated membrane is higher than in the central PE layer.

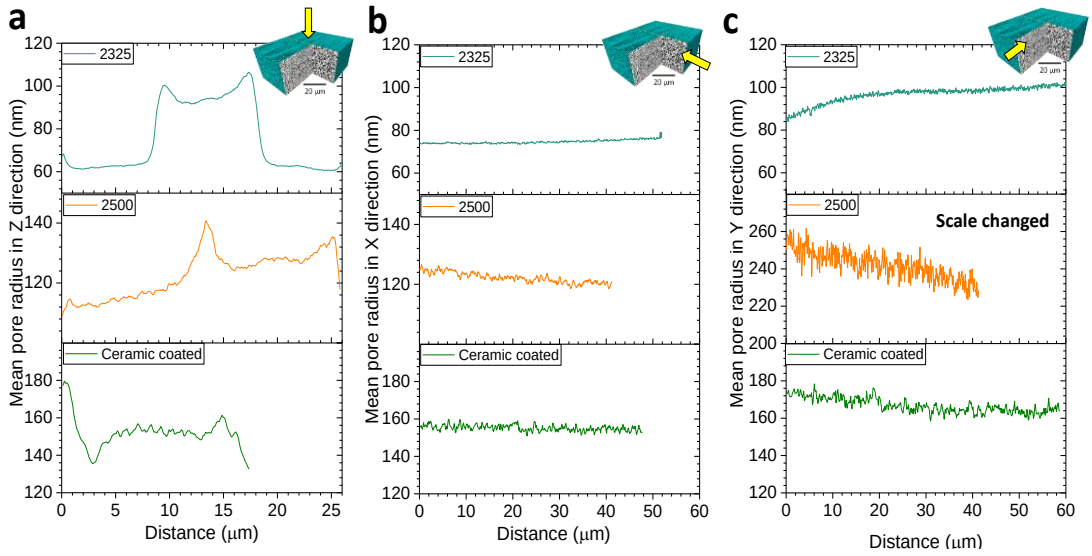

Figure 4-5: Mean pore size, calculated via a stereological approach, for individual slices in the (a) Z, (b) X, and (c) Y directions for Celgard 2325 (top), Celgard 2500 (middle) and the MTI ceramic-coated separator (bottom). Note the change in the Y-axis scale for Celgard 2500 in the Y direction.

Differences in mean pore size in the X and Y directions (Figure 4-5b,c) for each sample demonstrate the extent of elongation of the pores. The manufacturing process of both Celgard membranes involves uniaxial stretching of polymer lamellae following extrusion and annealing[266], resulting in highly-oriented, deep, slit-like pore structures. This is particularly notable for Celgard 2500, where the mean pore size in the Y direction is more than twice that in the X-direction. In contrast, the MTI ceramic-coated membrane is manufactured using a wet process; where biaxial stretching of a single extruded layer results in a relatively anisotropic mean pore diameter. In Figure 4-6, the slice-wise pore size is presented as normalised frequency plots for each of the axial directions where pores sizes are summed into 10 nm bins. The twin peaks in the Z-direction for the Celgard 2325 are caused by the region with relatively large pore size mid-way through the separator. There is a

significant difference between the calculated pore size in the X and Y direction for Celgard 2500, which shows that the pores are highly elongated; the c-P_oSD method alone does not reveal this. To aid the visualisation of the elongated slit-like pores, 3D renderings showing the pore phase as solid are presented as inset figures in Figure 4-6. In general, Celgard 2500 is shown to have significantly larger pores than Celgard 2325.

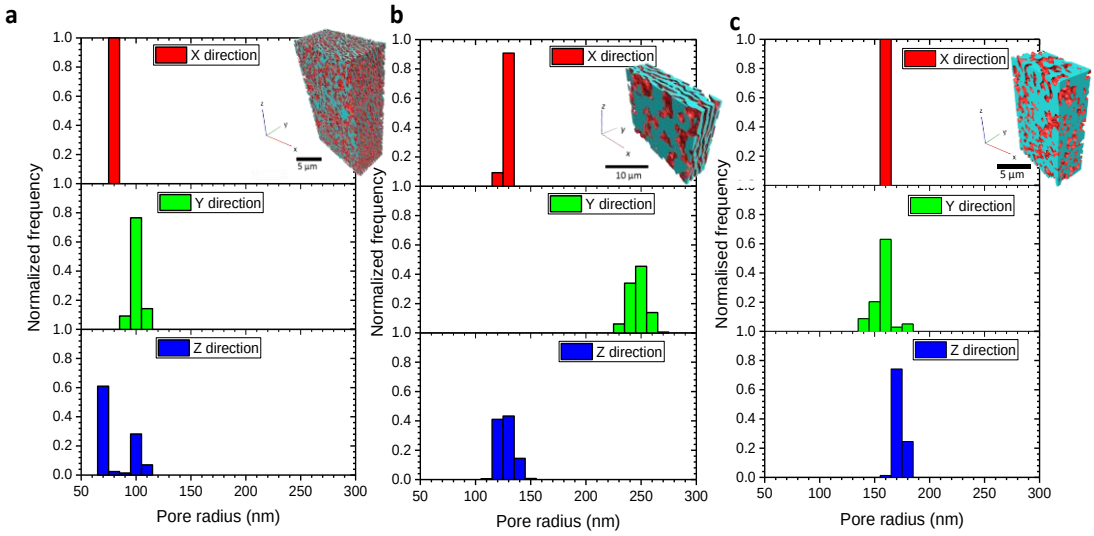

Figure 4-6: Normalised frequency plots of the mean pore size calculated by a stereological approach in the X, Y and Z directions for (a) Celgard 2325, (b) Celgard 2500, and (c) the MTI ceramic-coated membrane. Inset: Volume renderings of the three separators showing the pore phase as solid (blue). The 3D renderings highlight the differences in pore size and shape in the each of the axial directions.

4.3.3. Tortuosity Factor

Most analyses of the tortuosity factor of separator materials involve electrical conductivity measurements[228, 229, 269, 270], where the tortuosity factor (τ), is found by determining the ratio of the resistivity of the electrolyte-filled membrane, to that of the electrolyte alone:

$$\frac{\rho_s}{\rho_e} = \frac{\tau}{\varepsilon} \tag{4.1}$$

Where ρ_s is the resistivity of the membrane soaked in electrolyte, ρ_e is the resistivity of the electrolyte, and ε is the membrane porosity. This is a highly effective method for estimating the tortuosity factor of membranes, but does not provide local microstructural information, which is important for determining regions that most restrict ionic transport, particularly for multi-layer separators[271].

It is suspected that a high tortuosity factor is favourable for improving the safety of the cell by providing increased resistance to dendrite growth between electrodes, whereas a low tortuosity factor is favourable for high rate applications, where the resistance to ion transport is low. However, it should be noted that as there is still uncertainty surrounding the formation and growth of lithium dendrites[272, 273], the exact link between tortuosity factor and dendrite resistance remains unclear. To determine the tortuosity factor of the separator samples, a finite element simulation of a scalar diffusion parameter[191, 223] was used; this is described in more detail in Section 3.4.5.

A representative volume element (RVE) analysis of tortuosity factor (Figure 4-7) shows that the volume used to determine the tortuosity factor for each of the samples did not change significantly with sample size, and is therefore considered representative of the bulk material. As seen in Figure 4-7a, the MTI ceramic-coated separator has the highest tortuosity factor, followed by Celgard 2325 and Celgard 2500. However, the bulk measurements do not provide any information on the role of the individual layers in ionic transport. The tortuosity factor of Celgard 2325 was considered for four different volumes: one volume consisting of the full tri-layer sample (Figure 4-7a), and three more volumes consisting of each of the three layers (PP, PE and PP) (Figure 4-7b) separately. Similarly, the tortuosity factors of the three layers of the MTI ceramic-coated membrane (ceramic, PE and ceramic) were assessed separately (Figure 4-7c).

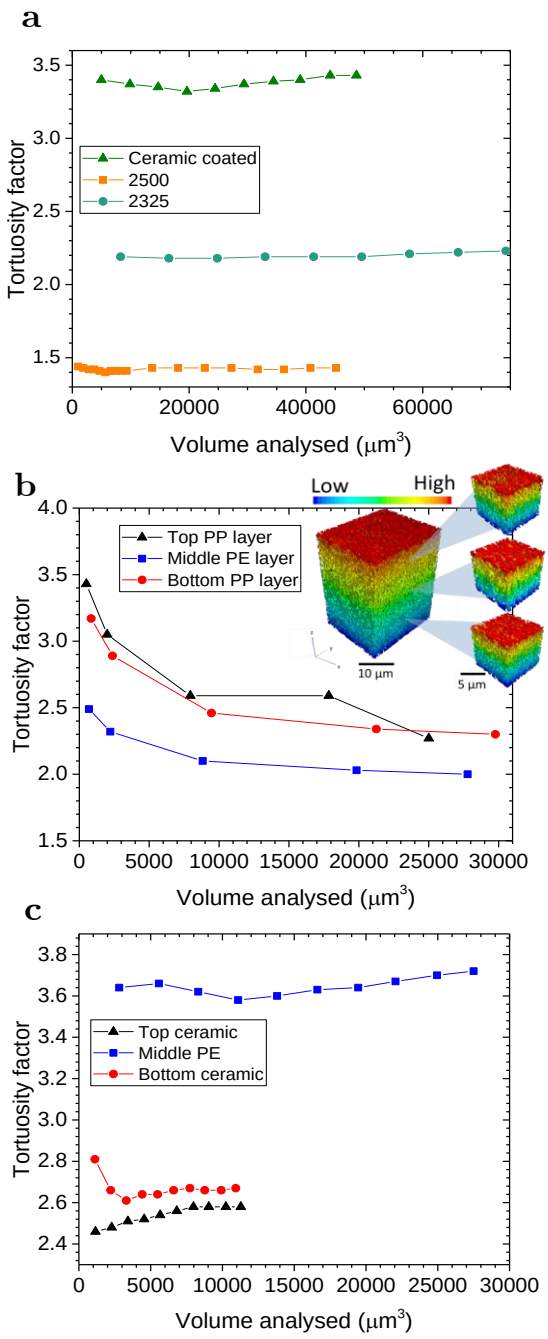

Figure 4-7: (a) RVE analysis for each of the separator samples showing that the full volumes of Celgard 2325, Celgard 2500 and the MTI ceramic-coated separator provide representative values for the tortuosity factors of the bulk materials. (b) RVE analysis of the tortuosity factor for the three individual layers (PP|PE|PP) of Celgard 2325. Inset: 3D representation of the output volumes from the scalar diffusion simulations of each of the three layers. (c) RVE analysis of the individual layers from the MTI ceramic-coated separator.

The tortuosity factor values extracted from the full volumes shown in Figure 4-7 are presented in Table 4-2. As discussed in Section 1.5 and according to equation 4.2, the membrane transport resistance is proportional to the tortuosity factor (τ), the thickness of the membrane (l), and inversely proportional to the membrane porosity (ε). The resistance factor ($\tau\ l\ /\ \varepsilon$) is therefore included in Table 4-2 to identify the contribution of the individual layers to the ionic transport resistance. Upon comparison with other studies[215, 256, 270], the tortuosity values determined here seem relatively low. However, as discussed by Holzer *et al.*[221] and Tjaden *et al.*[223], the tortuosity values are highly dependent on the measurement technique used; here, a finite difference diffusion model is used, which does not capture all factors that contribute to the resistance to ion transport, such as the dielectric constant of the electrolyte and the temperature dependence. Additionally, the tortuosity measurements are carried out on the segmented reconstruction of the polymer microstructure, which as previously mentioned, is not expected to have captured the intricate detail below the resolution of the scan.

$$R_m = \rho_e \frac{\tau l}{\varepsilon A} \tag{4.2}$$

The deviation between experimentally determined tortuosity values and those found here might also be a result of the limited resolution of the imaging technique itself. For example, as seen in Figure 4-4, the uniaxial stretching during manufacturing leaves nano-fibrils, which bridge the 'slit-like' pores shown above[60]. The presence of the nano-fibrils would certainly hinder ion transport through the membrane, which would appear as an increased tortuosity in the experimental data; however, the nano-fibrils could not be identified using the current imaging approach. Hence, although quantitative, the values provided in Table 4-2 should be considered with the caveat of the aforementioned systematic limitation of resolution.

Table 4-2: Summary of separator properties as determined via X-ray microscopy, where ε represents porosity, τ represents the tortuosity factor, l is the thickness of the membrane, and $\tau\, l/\varepsilon$ is the resistance factor.

Sample	ε	τ	l (µm)	$\frac{\tau l}{\varepsilon}$ (µm)
Celgard 2325	0.41	2.23	25	136
- *Celgard 2325 PP top*	0.39	2.27	8.3	48.5
- *Celgard 2325 PE*	0.44	2	8.3	37.9
- *Celgard 2325 PP bottom*	0.39	2.30	8.3	49.1
Celgard 2500	0.53	1.43	25	67.5
MTI ceramic-coated	0.38	3.43	16	144.3
- *Top ceramic*	0.40	2.58	2	12.9
- *Middle PE*	0.36	3.72	12	123.9
- *Bottom ceramic*	0.39	2.67	2	13.7

According to the data in Table 4-2, the PP layers in tri-layer Celgard 2325 contribute more per unit membrane thickness to the ionic transport resistance than the PE layer, which emphasises the role of the PP layers in the performance and safety of the cell. For example, an increase in the thickness of the PP layer may contribute more to help mitigate the risk of dendrite growth than an increase in the thickness of the PE layer. In an effort to minimise volume and weight, the primary function of the PE layer might only be to block the pores of the membrane upon shutdown at high temperatures, while the PP layers contribute most to preventing dendrite growth between electrodes. Table 4-2 also shows that the resistance of the monolayer Celgard 2500 to ion transport is half that of Celgard 2325. The high porosity and low tortuosity values associated with Celgard 2500 make the separator suitable for high-rate applications; whereas the tri-layer design of Celgard 2325 has a relatively high tortuosity and low porosity, which is found to

be mostly influenced by the PP layers. The high tortuosity, low porosity and small pore size may improve the safety of the membrane, but would increase its electrical resistance.

A relatively high tortuosity and high resistance to diffusive flux was determined for the MTI ceramic-coated separator. The PE layer exhibits the greatest resistance per unit thickness compared to its counterparts in the Celgard samples, which were manufactured using a dry process. The ceramic layers are shown to have little effect on the overall tortuosity of the membrane, but have been shown to improve the thermal and mechanical properties[67, 68], as well as the wettability of polymer separators[274, 275]. Hence, the combination of high tensile strength resulting from its isotropic structure, high tortuosity, and the presence of the ceramic layer[67, 68] would help mitigate the risks associated overheating, dendrite growth and electrode displacement[63, 64], making this separator favourable for safety critical applications.

4.4. Conclusions

Tortuosity factor, porosity and pore size distribution are among the most important properties to understand when discussing the performance of separator materials. Here, they have each been quantified for three commercial separator membranes via a combination of phase contrast nano-scale X-ray microscopy and image analysis on small but representative volumes. This image-based analysis overcomes some of the limitations of experimental measurement techniques, which are necessarily based on bulk measurements. For example, the possibility of determining variations in porosity and tortuosity factor between individual layers in more complex tri-layer membranes, which cannot be achieved using conventional methods, is demonstrated. This has provided new insights into the role of the individual layers within multilayer membranes in the rate capabilities and safety of commercial cells. However, this X-ray imaging approach has limitations such as spatial resolution, and the lack of understanding and quantification of relevant parameters that influence safety and performance. Nevertheless, the results in this study demonstrate that phase contrast X-ray microscopy and image-based

quantification provide an effective means of understanding the complex pore structure of separator membranes.

Furthermore, it has been shown by Peabody *et al.*[269] that when polymer separators are subject to mechanical stress, their microstructural transport properties undergo significant change, where pores close as a result of viscoelastic stress. The increase in transport resistance associated with pore closure is thought to be one of the primary causes of capacity fade and performance degradation of rechargeable cells during their lifetime. Additionally, Peabody *et al.* [269] deformed the separator materials by compression alone, which is perhaps representative of what a separator would experience in pouch cells. However, in cylindrical cells it is expected that the swelling and contraction of electrodes during operation cause unravelling of the spiral wound electrode assembly, as well as compression. Therefore, the separator would also experience shear as well as compressive strain. However, the mechanical strain experienced by separators during operation of commercial lithium-ion batteries is not well understood. Extending the phase contrast imaging technique to investigate, via *in-situ* tomography, the changes in separator pore structure when applied to shear and compressive strain would lead to a greater understanding of degradation and failure mechanisms. Capturing the deformation of the separator under actual cylindrical cell conditions is not trivial, but a progressive step towards this objective is to better understand the dynamic architecture of electrodes during operation, and their interaction with the mechanical design of commercial cells; this is the focus of the following chapter.

Chapter 5

Degradation during Operation: Tracking Displacement in 4D

Sections of this work have been peer reviewed and published in Advanced Science (D. P. Finegan, E. Tudisco, M. Scheel, J. B. Robinson, O. O. Taiwo, D. S. Eastwood, P. D. Lee, M. Di Michiel, B. Bay, S. A. Hall, G. Hinds, D. J. L. Brett, P. R. Shearing, *Quantifying Bulk Electrode Strain and Material Displacement within Lithium Batteries via High-Speed Operando Tomography and Digital Volume Correlation.* Advanced Science 3, doi:10.1002/advs.201500332 (2016)).

5.1. Introduction

As discussed in Section 1.6, lithium-ion cell assemblies can incur an chemo-mechanical force as a result of the swelling or contraction associated with the lithiation or delithiation of active materials during operation. The evolving architecture can cause significant degradation on the cell-level, causing delamination and significant strain on the separator. As Eastwood *et al.*[189] demonstrated, the lithiation induced dilation does not always occur uniformly but can occur as a function of distance from the current collector, depending on whether the cell is electrically limited or transport limited. As outlined in Section 1.6, a range of techniques have been applied to investigate the non-uniform lithiation of electrodes and the interplay between the evolving architecture and other rigid cell components, but both remain poorly understood[189].

Coupling time lapse tomography with image correlation techniques, such as 3D digital volume correlation (DVC)[233, 240] provides a powerful diagnostic tool in

materials research[39, 187-189]. In this study, the evolution of the strain in the bulk architecture of the MnO_2 electrode material in a commercial primary Li/MnO_2 lithium battery was captured during a high rate constant resistance discharge. As Li/MnO_2 cells have a high discharge rate capability (they are often used for high drain applications), the high-speed imaging capability of beamline ID15A[184, 208] at the ESRF was used.

Furthermore, two different DVC software packages (developed by Hall *et al.*[187, 188] and Bay *et al.*[233, 240]) were used to track the transient local displacements of the MnO_2 electrode in 3D as lithiation induced dilation occured. 3D displacement fields generated using continuum DVC were used to derive 3D strain profiles of the electrode material throughout operation. Additionally, the electromechanical effect of the dilating electrode on the structural integrity of the cell architecture is assessed. The extent of unravelling of the current collector is quantified using a separate DVC approach and related to the temporal continuum strain field evolution. The importance to commercial cell designs of accommodating the changes in cell architecture during operation is highlighted, and this new approach of combining high-speed tomography and DVC is demonstrated as an effective technique for identifying causes of performance loss within commercial batteries.

5.2. Experimental

5.2.1. Battery and Testing

This study focuses on a commercial, spiral wound, Duracell CR2 battery[276]. The CR2 battery was discharged at a constant resistance of 2.75 Ω between 3 V and 2 V during continuous X-ray CT imaging (Figure 5-1). During continuous X-ray CT, tomograms were captured every 40 seconds which included image acquisition time and data transfer to the ESRF central servers. No heating of the cell due to incident X-ray radiation was observed.

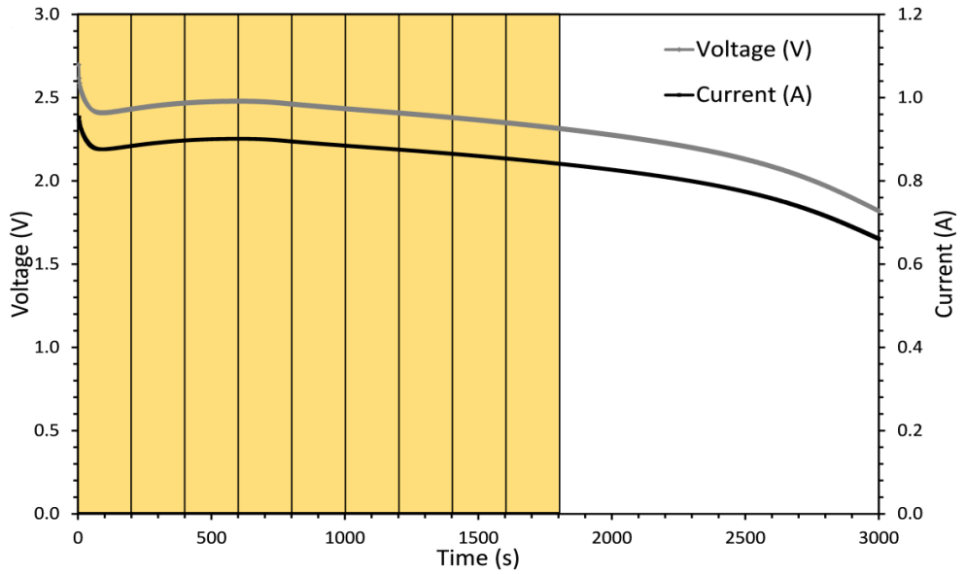

Figure 5-1: Discharge curve of the CR2 cell at constant resistance of 2.75 Ω. The yellow segments indicate the time between consecutive tomograms that were correlated using DVC.

5.2.2. Conditions for *Operando* X-ray Imaging

Experiments were performed at beamline ID15A at the ESRF. The high photon flux and brilliance of beamline ID15A generates the spatial and temporal resolution required to identify the fine granular structure of the electrode material within the short time scales over which significant material evolution occurs during battery operation. Furthermore, the DVC displacement and strain analyses subsequently performed rely on correlating consistent identifiable grain texture in consecutive images; therefore, DVC analysis requires images to be acquired at sufficiently short intervals to avoid excessive changes in the images. An electrical slip-ring allowed continuous rotation of the cell for high-speed X-ray CT while maintaining an electrical connection for simultaneous continuous discharge; the *in-situ* rig design used for this experiment is described in more detail in Section 3.8.1.

The Duracell CR2 battery was imaged in a 76 keV monochromatic X-ray beam with a field of view (FOV) of 8.6 mm × 8.7 mm and a pixel size of 10.87 µm (794 × 800 pixels), corresponding to half of the cell (see Figure 5-2a,b). The sample stage rotation axis was placed at the edge of the FOV, such that by a 360° rotation it was possible to image the entire width of the sample. Figure 5-2b shows a

reconstruction of the entire cell, and Figure 5-2c shows the volume that was captured during high-speed X-ray CT. Each tomogram was composed of 2 × 2000 half projections that were captured with angular increments of 0.09° between images. A high-speed camera, PCO Dimax (PCO AG, Germany), with an exposure time of 0.7 ms was used during imaging. Consequently, the acquisition time of each tomogram (Figure 5-2c) was 2.8 s, which was sufficiently fast to avoid image artefacts caused by sample motion during acquisition.

The reconstructed tomograms were processed using Avizo Fire 7 (FEI VSG, France) whereby the 3D images could be separated into 2D planar slices, as shown in Figure 5-2d,e. Highly attenuating materials appear white in the tomograms, while less attenuating materials are darker in appearance. Material phases of interest were isolated based on greyscale values using Avizo's segmentation editor. The casing and steel current collecting mesh displayed in Figure 5-2d,e are highly attenuating and are displayed as white, and the Li_xMnO_2, which consists of a slurry coated onto the current collecting spiral wound mesh, is displayed as light grey. Lithium metal and separator material are poorly attenuating at 76 keV and difficult to distinguish, but are situated between the spiral wound MnO_2 electrode layer. The copper mesh attached to the outside of the battery casing was cropped out of Figure 5-2d. The 3D image files were stored in 32-bit .raw file format for volume correlation. The radiographs were reconstructed into 8.7 mm high cylindrical sections (tomograms) of the cell (Figure 5-2c,d) using standard reconstruction methods[204].

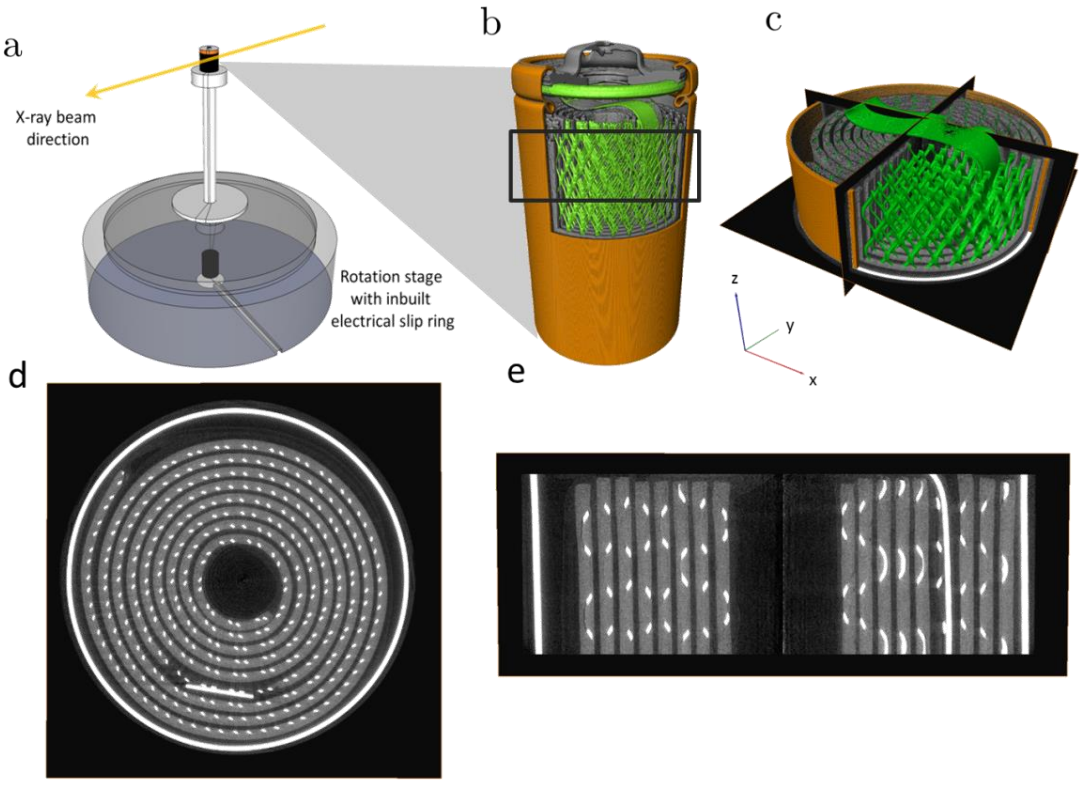

Figure 5-2: (a) Illustration showing rotation stage and in-built electrical slip ring connection. (b) Reconstruction of a full commercial CR2 battery showing the casing (orange), current collector mesh connected via a tab to the terminal (green) and MnO_2 electrode (grey). The black square represents the region that was scanned during continuous X-ray CT. (c) Reconstruction of the section captured during continuous X-ray CT with orthoslices in the *XY*, *YZ* and *XZ* planes. (d,e) Isolated *XY* and *YZ* slices showing battery casing and current collecting mesh (white) and MnO_2 electrode (grey).

5.3. Structural Evolution and Degradation

5.3.1. Material Displacement during Operation

The volume expansion observed during lithiation of Li_xMnO_2 can cause severe mechanical degradation on both the micro and macro scale[81, 277]. The exact volume expansion of the Li_xMnO_2 is difficult to determine via threshold segmentation, due to the change in attenuation of Li_xMnO_2 as it lithiates, and the

overlapping greyscale of different materials within the cell. Additionally, individual crystallites tend to break up during discharge[278] and any increased electrode material porosity would not be detected at the voxel resolution used here, which is not fine enough to identify individual Li_xMnO_2 particles. Over a single discharge at low operating voltages (2 V - 3 V) it is not expected that dissolution of Li_xMnO_2 has any significant effect on the observations in this work. Figure 5-3 shows horizontal slices taken from tomograms of a CR2 cell before and after discharge.

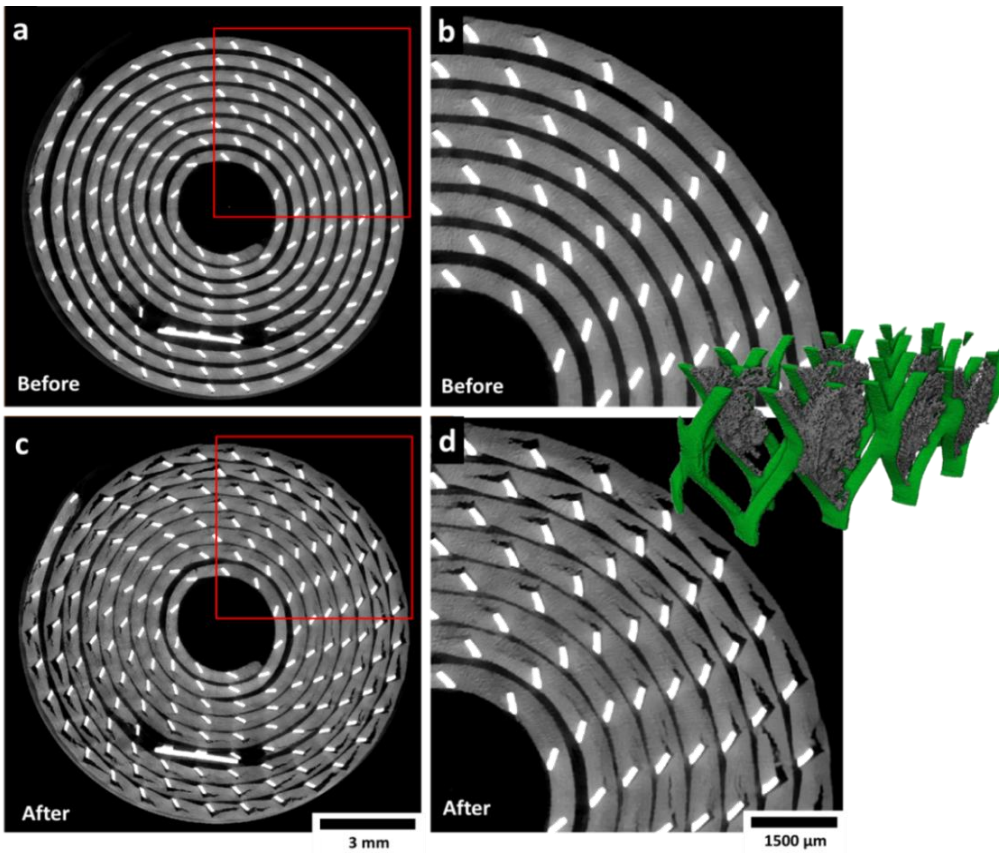

Figure 5-3: (a) Greyscale XY slice (horizontal cross section) from a tomogram captured before discharge; the red square indicates the region of interest with which the neighbouring image is associated. (b) Enlarged view of the XY slice showing pristine electrode before discharge. (c) Greyscale XY slice from a tomogram captured after discharge; the red square indicates the region of interest with which the neighbouring image is associated. (d) Enlarged view of the XY slice showing pristine electrode after discharge. Inset: Section of the current collecting mesh showing a 3D view of the crack openings.

Movies showing the intermediate stages in real-time, in both the horizontal and vertical directions, can be found online as supplementary material with reference [64], and time stamped frames taken at intermediate stages during discharge are presented in Figure 5-4. In Figure 5-3 the Li_xMnO_2 spiral wound layer (grey) expands and the thickness of the lithium region is seen to diminish during the lithiation process. Detachment of the Li_xMnO_2 from the current collecting mesh, as evidenced by the cracks emanating in the anti-clockwise direction in Figure 5-3 occured as a consequence of the spiral wound materials not being tightly wound or compressed. Additionally, as is seen in Figure 5-4, the evolving architecture of the Li_xMnO_2 electrode caused a slight degree of unravelling of the spiral wound materials, a consequence of the mechanical energy associated with the electrode-active material[79].

The internal unravelling of the electrode layers further contributed to crack propagation via the strain induced from the movement of the current collecting mesh against the active material, explaining the increased severity of cracking with distance from the centre of the cell observed in Figure 5-3 and Figure 5-4. This detachment of the Li_xMnO_2 from the current collecting mesh resulted in a significant reduction in interfacial area between the current collecting mesh and the active material. The inset in Figure 5-3 shows a 3D reconstruction of a small section of the mesh with isolated crack regions; the significant decrease in interfacial area between the electrode material and the current collecting mesh is clearly visible.

Delamination of electrode materials from the current collector is a well-known cause of increased cell impedance and capacity fade in commercial cells[277]. The interfacial area available for charge transfer is reduced leading to an increase in ohmic resistance and consequently local heating which may lead to electrolyte vaporisation. However, given that the CR2 cell is a primary cell and capacity fade with cycling is not a cause of concern, the unconstrained expansion of the Li_xMnO_2 and the formation of cracks within the Li_xMnO_2 material may also benefit the performance of the cell by exposing additional Li_xMnO_2 surface area to lithium-ion transfer, however the associated heating may still be unfavourable.

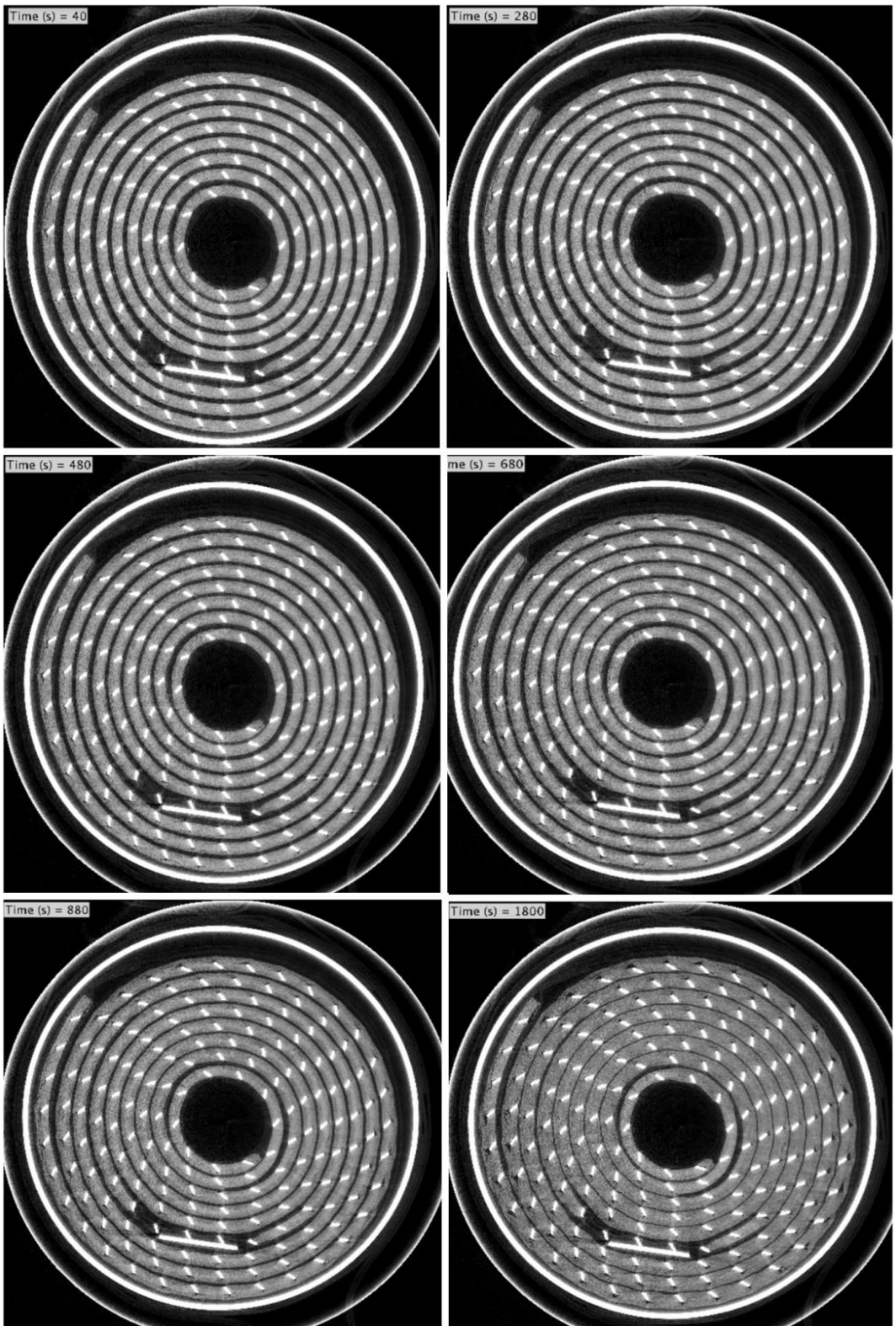

Figure 5-4: Time-stamped greyscale slices from reconstructed tomograms taken at different times during discharge.

DVC was applied to consecutive images to determine the 3D strain profiles caused by lithiation of the electrode and to explore the electrochemically-induced strain that causes unravelling of the current collecting mesh.

5.3.2. Temporal Quantification of Local Strain

5.3.2.1. Applying Digital Volume Correlation

In this study, the CR2 cell was discharged from its fully charged state (3 V) to below 2 V, as shown in Figure 5-1. The MnO_2 is reduced from tetravalent to trivalent state to form Li_xMnO_2 (where $0 \leq x \leq 1$) as the Li^+ ion inserts into the MnO_2 lattice[278, 279]. 3D displacement measurements of textured materials can be performed by comparing X-ray CT images via DVC[188, 233, 240, 280].

Following the continuum DVC approach described in Section 3.4.6, the evolution of the Li_xMnO_2 electrode architecture was quantified in 3D by correlating successive tomograms. Tomograms were captured every 40 seconds during discharge, and increments between sequential tomograms which showed significant material displacement were chosen for correlation. The discharge profile of the CR2 battery in Figure 5-1 shows image increments of 5 between the reference and deformed images for DVC, which corresponds to a difference of 200 seconds during discharge. Note that the images were cropped to 1487 × 1387 × 501 voxel volumes to remove artefacts at the edges of the FOV and to isolate the regions of interest. Also, the size of the search windows for DVC varied between each increment and, due to its high impact on computation time, was optimised before the entire volumes were loaded. For each volume correlation the correlation coefficient of the Li_xMnO_2 material was > 0.97 (see Figure 10-17 to Figure 10-21 in Section 10.2 of Appendices); whereas poor correlation was observed for all other materials. Poorly correlating (< 0.97) materials were filtered out.

Continuum displacement DVC between consecutive tomograms was applied to plot the evolution of 3D displacement and strain profiles. Consistent grain detail is required between consecutive images to measure continuum displacement with a high correlation coefficient. An example of the fine detail present in the

tomography images is shown in Figure 5-5 where the texture is provided by the electrode microstructure (particle size distribution of Li_xMnO_2, binder and conductive material, and electrolyte-filled pore phase). The correlation window was set as a cube of 15 voxels which, with a voxel resolution of 10.87 µm, tracks grain detail up to 163 μm^3. The distance between nodes was set as 5 voxels or 54.35 µm.

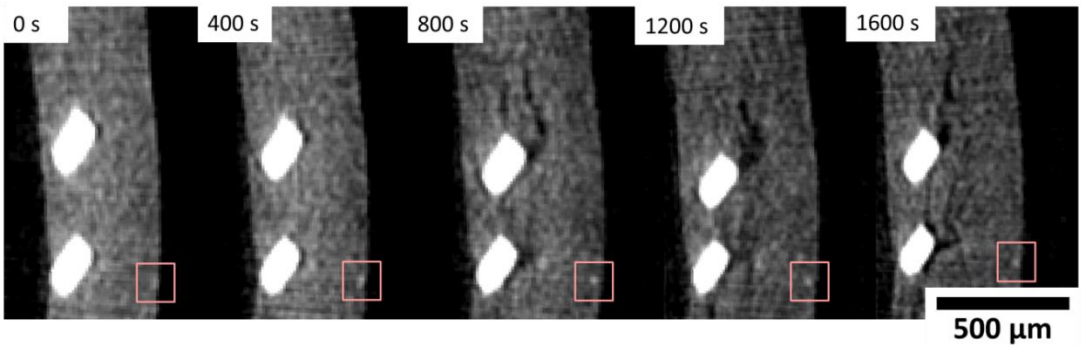

Figure 5-5: Magnified sections of an XY slice from consecutive tomography images. The red squares indicate the size of the correlation windows (but in 3D cubes) for feature tracking and contain a consistent grain feature (white spot), typical of one that would be tracked for displacement measurements during DVC.

5.3.2.2. Electrode Displacement and 3D Strain

During lithiation, it is expected that the induced volume expansion of Li_xMnO_2 will be observed as bulk deformation of the active electrode layer on the sub-millimeter scale via interaction and displacement of the Li_xMnO_2 active crystallites, binder and the conductive carbon substrate. The continuum DVC provided averaged displacement profiles between 3D images that were 200 s apart during discharge, utilising every fifth consecutive tomogram to allow enough displacement for tracking. Displacements were plotted in 3D and the associated strain maps were generated by differentiating the vector displacements with respect to the X, Y and Z directions, as described in Section 3.4.6. Figure 5-6 shows a 3D reconstruction of a colour map of volumetric strain of the Li_xMnO_2 electrode measured between 200 s and 400 s into discharge. Correlation windows (individual voxels in Figure 5-6 which showed a poor correlation ($\leq$0.97) were filtered out of the displacement

profiles by replacing the voxels with not-a-number (NaN) value, creating a sparse matrix.

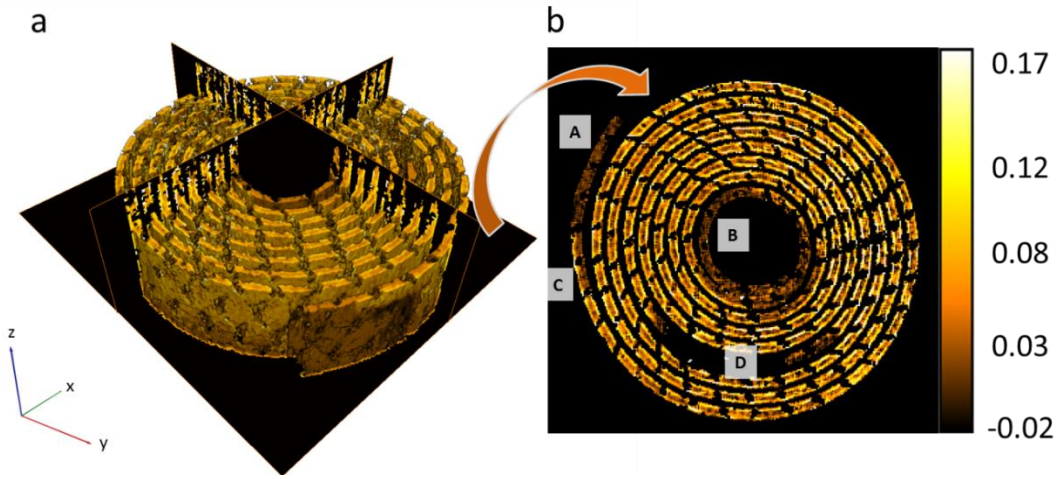

Figure 5-6: (a) 3D reconstruction of volumetric strain extracted from DVC of images 200 s and 400 s into discharge, including ortho-slices in the *XY*, *YZ* and *XZ* planes. (b) Extracted *XY* slice showing volumetric strain profile. Labels A and B identify inactive regions at the inner and outer ends of the Li_xMnO_2 layer, label C highlights a region in which lithiation occurs from one side only and label D shows a dark region from which the current collecting tab was filtered.

Clear strain features are observed which correspond to the local extent of dilation induced by lithiation over the correlated time period; for example, the ends of the spiral wound Li_xMnO_2 electrode labelled as regions A and B in Figure 5-6a,b exhibit no activity. Upon deconstruction of the cell it was found that the intermediate lithium metal foil stops before reaching the end of the Li_xMnO_2 layer which would explain the inactive regions (areas of low strain in Figure 5-6b labelled A and B) at the inner and outer ends of the Li_xMnO_2 layer. At region C in Figure 5-6b, lithiation is seen to occur on one side of the Li_xMnO_2 layer only. The one-sided activity around this region indicates that the lithium metal foil extends further on the outside of the electrode layer than on the inside. The area surrounding region D in Figure 5-6b is where the current collecting tab, shown in Figure 5-2c and Figure 5-2d, travels down through the cell. The current collecting mesh and tab were filtered out of this image and are tracked separately; hence there is a large black region where the current collecting tab would otherwise be.

Figure 5-7 shows the evolution of volumetric strain of the XY slice shown in Figure 5-6b (this can also be seen online as a movie in supplementary material with reference [64], where each frame displays the strain of consecutive correlated volumes 200 s apart during discharge).

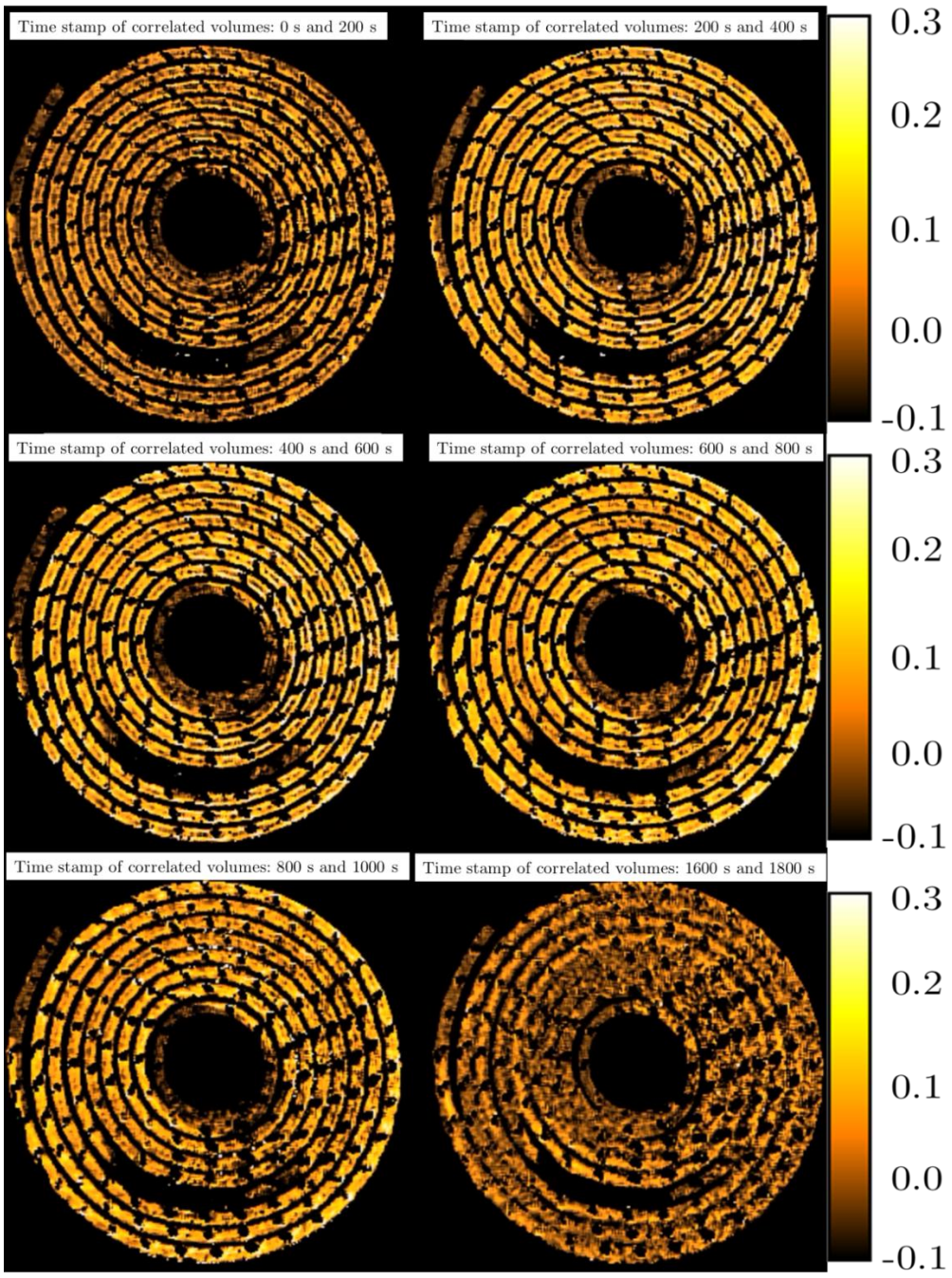

Figure 5-7: Time-stamped slices from 3D strain maps generated from digital volume correlation of consecutive images.

Figure 5-8a shows selected XY slices from the volumetric strain profiles at initial, mid, and end stages of discharge, and Figure 5-8b shows a plot of the time dependent strain profiles across several of the electrode layers from beginning to end of the discharge, averaged across a 5 voxel wide line (blue lines in Figure 5-8a). The low correlation voxels that were previously given NaN values were reassigned a value of zero when plotting the graphs in Figure 5-8b. Initially a region of high strain is observed around the surface and subsurface of the active Li_xMnO_2 layer, indicating a mass transport limited electrode and consequently, a concentration gradient of lithium across the active layer. The non-uniform dilation caused by the lithium concentration gradient across the thick electrode challenges the mechanical integrity and can result in crack evolution and particle isolation. During the early stages of discharge, very little strain is observed around the inner regions of the Li_xMnO_2 layers.

As lithiation progresses deeper into the active material, the dilation front progresses towards the centre of the electrode layer, and hence the strain in this region begins to increase, which is already evident between 400 s and 600 s in Figure 5-8b. As time progresses, the concentration inside the layers becomes larger, but the overall strain and strain gradient reduces, as the rate of lithiation induced expansion and displacement of the Li_xMnO_2 decreases. This results in non-uniform insertion stresses on the microscale[98]. However, due to the flexibility of the electrode material on the sub-millimeter scale, where the displacement of microparticles can change the porosity of the bulk material[39], the strain observed on the bulk material is not expected to be representative of the local strain on the active Li_xMnO_2 crystallites[98].

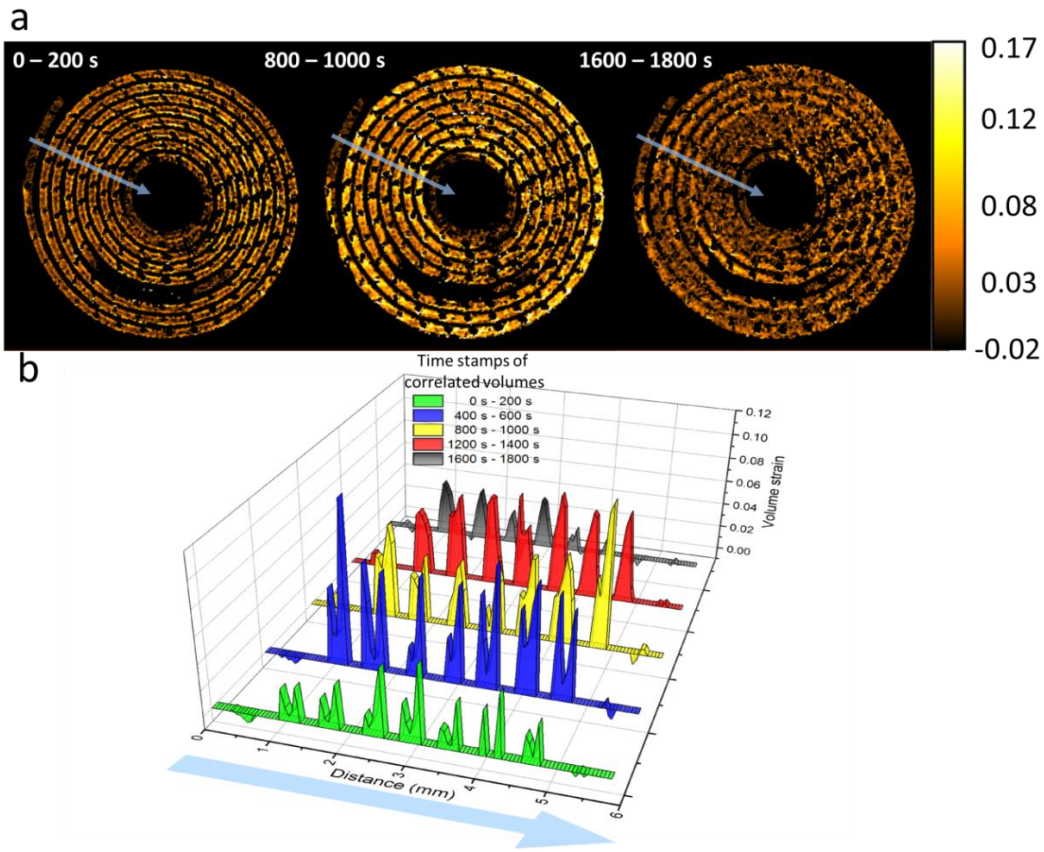

Figure 5-8: (a) *XY* slices from the 3D volume strain images corresponding to DVC of the tomographs taken at the labelled times; consecutive correlated volumes 200 s apart during discharge. The average strain is measured across the 5 voxel wide blue lines from the outside to the inside of the electrode layer. (b) Time series plot showing strain values that are averaged across 5 voxel wide lengths, shown as blue lines in the *XY* slices from the 3D strain profiles. Distance is plotted from outside to inside of the battery spiral.

A significant difference in strain is evident between both sides of each electrode layer, as identified in the twin peaks at these locations in Figure 5-8. During operation lithium metal is consumed from both sides of the electrode and lithium ions diffuse into both sides of the Li_xMnO_2, however the strain observed on the inner side of the electrode layer (right of the twin peaks in Figure 5-8b) is generally higher than that on the outer side (left of the twin peaks in Figure 5-8). This is most likely an attribute of the positioning of the current collecting mesh in the electrode material[281]. As seen in Figure 5-3 and more closely in Figure 5-5, the

current collecting mesh is positioned close to the inner edge of the Li_xMnO_2 layer, an artefact of the manufacturing process in which the mesh is placed on a surface and coated with active material. This results in the effective electrode thickness (and therefore resistance) being different on each side of the current collecting mesh[282]. The effective electrode thickness is greater when the tortuous path of the lithium ions through the porous electrode material is considered, as discussed in Section 1.5. The differing effective electrode thicknesses arising from the placement of the current collector prevent optimised utilisation of electrode material. A large gradient in lithium concentration can cause a drop in the electrode potential and can result in underutilised electrode material by the time the cell reaches the cut-off voltage[281, 283], resulting in reduced cell capacity. Hence, thick electrodes can result in a significant potential drop between the surface of the electrode layer and the current collector during operation, which highlights the importance of optimising electrode thickness for particular operating conditions.

In battery modelling the current density is given by the reaction current density at the surface of the electrode particles, which is determined by the surface lithium diffusion flux. The surface area of the outer side of the electrode layer is greater than the surface area of the inner side of the electrode due to its larger radius of curvature. If the current density is assumed to be uniform on both sides of the current collecting mesh, then with the increased surface area on the outer side of the Li_xMnO_2 material it is expected that the local current density and hence activity would be lower, which is consistent with a lower strain on the outside of the Li_xMnO_2 layers in Figure 5-8b.

On the outer end of the Li_xMnO_2 layer the one sided activity in Figure 5-9 indicates that the lithium foil ends at different points between the outside and inside of the Li_xMnO_2. At this location, lithium diffuses into the Li_xMnO_2 in one direction only, radially inward. The progression of lithiation can be seen from the strain front travelling through the electrode material during operation, as shown in Figure 5-9a. Figure 5-9b shows a plot of the strain across a labelled region of interest calculated from consecutive correlated volumes during discharge. Between 0 s and 600 s during discharge the strain profile shows an increasing strain around the sub-surface region of the electrode as lithium inserts into the Li_xMnO_2 from the

outer surface. As the lithiation progresses, the strain front travels deeper into the active material. The observed strain decreases near the end of discharge as the Li_xMnO_2 becomes increasingly concentrated with lithium and the rate of lithiation (and particle dilation) slows down. The travelling strain front[283] is indicative of the progressing lithium concentration distribution within the electrode during discharge, which emphasizes the potential for DVC as a model validation technique for evolving lithium concentration in active materials during operation.

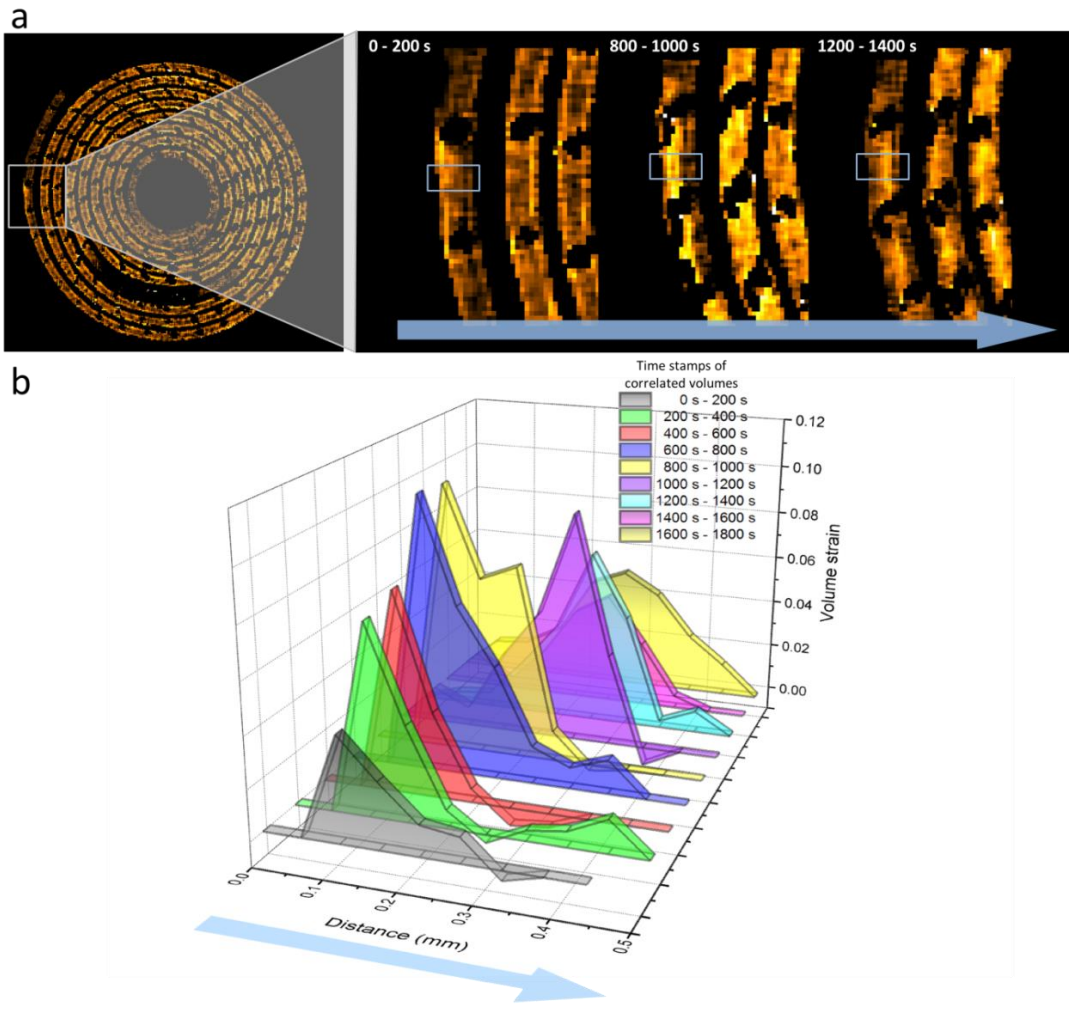

Figure 5-9: (a) Enlarged views of a region of interest where lithiation occurs on one side only (outside to inside). The progression of lithium into the Li_xMnO_2 is observed by the strain front propagating through the material during discharge as seen in the regions highlighted by the grey box. (b) Averaged strain in the vertical direction of the boxed region of interest showing the evolution of strain across the Li_xMnO_2 layer during one-sided lithiation.

5.3.3. Influence of Mechanical Design on Battery Degradation

The measurements above have demonstrated that the evolving Li_xMnO_2 architecture displaces the rigid current collecting mesh which detaches from the electrode material. This leads to increased contact resistance between the electrode and current collector which can significantly affect the performance of the cell[99] and cause capacity loss due to electrical isolation[284]. At the bottom of Figure 5-4, the Li_xMnO_2 electrode is seen to expand against the shell of the casing on one side only; consequently, the spiral wound layers shift towards the vacant side of the cell. As a separate measurement, the DVC methodology was used to determine the deformation of the collector mesh during battery discharge. The current collector is a metallic mesh of diamond pattern, embedded within the electrode material, and spirally wound within the battery case. The mesh contains distinct nodes where individual wires meet (Figure 5-10a), creating unique features that can be tracked as deformation occurs.

The shift of the current collecting mesh was quantified by using a point tracking method developed by Bay *et al.*[233, 240] where sub-volumes containing consistent textures are tracked between subsequent images through correlation methods. Sub-volumes of the current collecting mesh of 40 × 40 × 80 voxels in size (Figure 5-10a) were extracted from 176 manually selected points on three layers along the current collecting mesh (Figure 5-10b,c). These sub-volumes were tracked between images associated with the charged and discharged state of the battery. The displacement of the current collecting mesh resulting from the electrode expansion is quantified and the displacement vector plots are shown in Figure 5-10d and Figure 5-10e. Most of the displacement occurs in the XY plane, whereas very little displacement is observed in the vertical Z direction. Figure 5-10e shows the point displacements in the XY plane where displacements up to 0.8 mm are observed. As seen in the late stages of Figure 5-4, the spiral wound layers are only in contact with one side of the casing; as the electrode expands during lithiation the contents of the cell are pushed in the opposite direction, as shown in Figure 5-10e. The breakage of the Li_xMnO_2 electrode material resulting from displacement

of the current collector can cause electrically isolated electrode sections as a result of loss of direct electrical contact with the current collector[95]. Sufficient compression is necessary to hold the electrode together and help mitigate loss of contact with the current collector. However, as observed in this cell, the electrode layers are mostly unconfined allowing the active material to freely expand and unravel, which is detrimental to the structural integrity of the active layers.

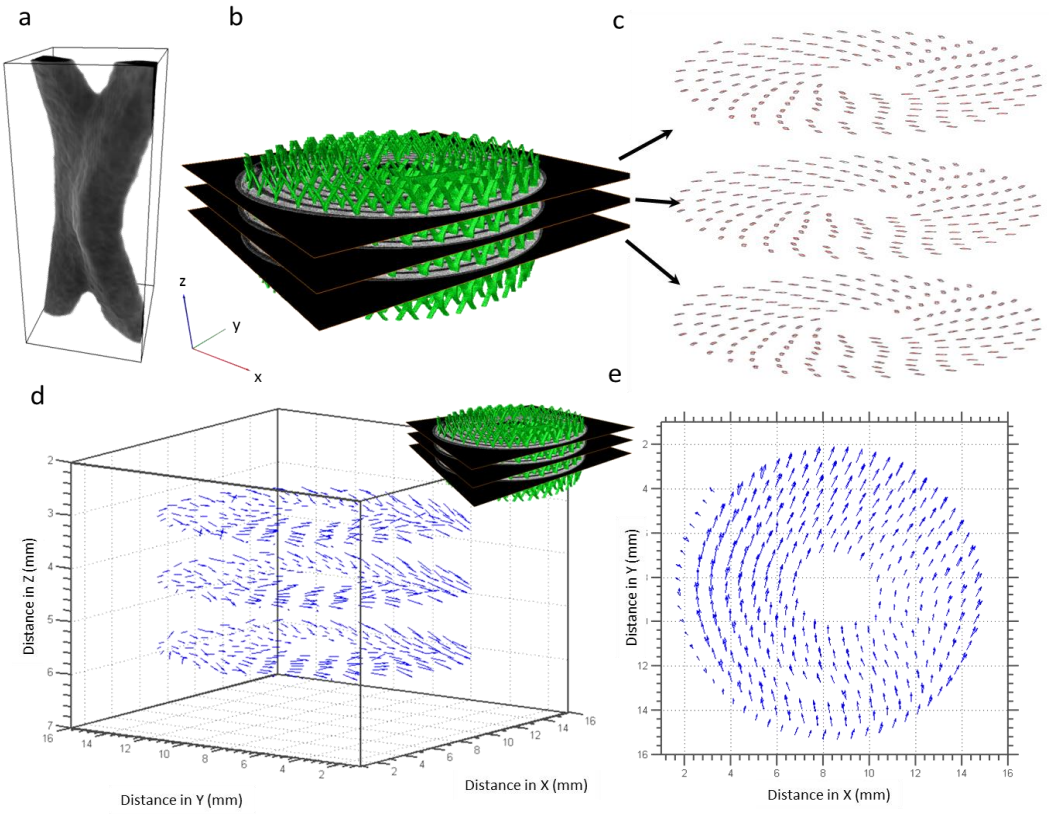

Figure 5-10: (a) A typical collector grid junction point and the rectangular sub-volume used for DVC. The sub-volume is 40 × 40 × 80 voxels in size. (b) 3D reconstruction of the current collecting mesh with XY slices for point tracking. (c) Binarised current collector points selected for point tracking in three XY slices along the Z direction. (d) Vector plot showing the magnitude and direction of translation of the current collector points in 3D. Most displacement occurs in the XY plane. (e) Top-down view of the vector plots in the XY planes showing displacement of the rigid current collector points in the X and Y directions.

5.4. Conclusions

DVC software has been applied to high-speed *operando* X-ray CT of commercial primary lithium batteries during discharge. By quantifying the movement of discrete sections of the electrode material between sequential images during discharge, a spatial and temporal map of material activity and strain profiles was generated. The progression of the lithiation front has been tracked by measuring the local displacement of electrode material during dilation, which has provided valuable insights into the transient structural mechanics that take place within commercial cells during operation. For example, relatively inactive regions were identified and large concentration gradients within the electrode layers could be deduced from the evolving strain patterns, giving the capability to pinpoint inefficiencies and identify means through which the performance of the cell could be improved and optimised.

Although this cell is a primary cell, this novel diagnostic approach has provided a means of identifying numerous sources of performance loss, which may also be applied to rechargeable cells. The placement of the current collecting mesh to one side of a thick electrode during manufacturing has resulted in a significant variation in dilation between sides of the electrode layer causing an uneven distribution of activity and strain. The cell was identified as being limited by Li^+ transport since throughout the discharge the material dilation progressed from the surface of the electrode towards the current collector. There is significant scope for further studies to assess the interaction of different mechanical features, such as the design and placement of current collectors, with evolving active materials and to determine the likelihood of the cell to incur capacity loss via breakage and isolation of electrode material. This technique could also provide empirical evidence which could indicate whether optimum electrode thickness is achieved for particular operating conditions and to assess the tension and compression effects associated with thick spiral wound electrodes. Additionally, electrode material properties are highly dependent on composition; the strain profile of the bulk material is expected to be entirely different to the strain profile associated with solid state diffusion due

to the propensity of the material properties (porosity and tortuosity) to change during mechanical deformation.

This novel diagnostic approach also provides valuable information for cell-level multi-physics modelling of operating lithium batteries by providing real-time, structural and strain information in 3D. As demonstrated here, the interaction between evolving materials and their environment is imperative to accurately predict the performance of a particular cell design during operation, as crack formation and delamination can have a significant impact on the rate of aging and degradation of cells. The extent of expansion, cracking and delamination observed during discharge of the cell affects the local ionic diffusivity and electrical conductivity of the material.

To date, very few experimental studies have quantitatively captured the temporal local activity of electrode material within lithium batteries; in this work the combination of the high-resolution, high-speed imaging capabilities of synchrotrons and image correlation has been demonstrated as a powerful tool for linking local strain, material displacement and degradation to the performance of the cell. This approach could also be extended to capture even more rapid degradation mechanisms, such as those that occur leading up to and during thermal runaway. In a similar way, the elucidation of the degrading active materials and their interaction with commercial mechanical designs would help guide the optimisation and design of commercial cells. High-speed tomography and radiography of lithium-ion cells is the focus of the following chapters.

Chapter 6

Thermal Abuse: Degradation during Thermal Runaway

Sections of this work have been peer reviewed and published in Nature Communications (D. P. Finegan, M. Scheel, J. B. Robinson, B. Tjaden, M. Di Michiel, G. Hinds, D. J. L. Brett, P. R. Shearing, *In-operando high-speed tomography of lithium-ion batteries during thermal runaway.* Nat Communications 6, doi:10.1038/ncomms7924 (2015)).

6.1. Introduction

Although there have been studies on compositional and structural evolution of electrode materials at elevated temperatures[100, 285], there is limited understanding of the change in the internal architecture of commercial cells leading up to and during thermal runaway and failure. For example, gas evolution during thermal runaway is known to distort the structure of prismatic cells, causing delamination of electrode and current collecting layers[139]. Internal short circuits may develop as a result of the displacement or distortion of the battery structure, particularly in pouch cells where gas evolution induced distortions are unconstrained. Improved understanding of the internal structural dynamics during failure and thermal runaway of commercial cells should help cell developers to design effectively against the initiation and propagation of failure.

In this Chapter, two commercial 18650 cells were subject to extreme thermal abuse, similar to the conditions presented in UL testing standards, as described in Section 2.6.1. High-speed synchrotron radiation X-ray CT is combined with

thermal imaging to achieve insight into the structural and thermal dynamics associated with thermal runaway and failure of commercial 18650 lithium-ion batteries. High-speed tomography at 1.25 Hz and 2.5 Hz is performed during thermal runaway in the ID15A beamline at the ESRF, which is renowned for its high frequency imaging capability[208]. Through 3D reconstructions and 2D radiographs captured at a rate of up to 1250 frames per second (fps), the progression of rapid internal structural deformation leading up to and during thermal runaway is tracked. This approach allowed observation of the effects of gas pocket formation, venting and elevated temperature on the architecture of internal spiral-wound layers of commercial lithium-ion batteries and to evaluate the influence of engineering design on battery safety and performance.

6.2. Experimental

6.2.1. Setup and Thermal Abuse

As described in Section 3.8.1, an *in-situ* containment rig was designed to allow simultaneous high-speed X-ray CT and thermal imaging, during extreme thermal abuse tests of commercial 18650 cells. A uniform layer of heat resistant black paint (with a calibrated emissivity[248] of 0.96 over the range of 40 °C to 180 °C) was applied to each battery before testing. Two commercial LG 18650 NMC batteries (2.6 Ah and 2.2 Ah)[286, 287] in fully charged states were subjected to elevated temperatures ($>$ 250 °C) by the application of a heat gun, which was activated when the batteries began to rotate. For simplicity, the 2.6 Ah and 2.2 Ah cells will henceforth be referred to as *Cell 1* and *Cell 2*, respectively. Cell 1 contains an internal cylindrical mandrel with inherent safety advantages[288-290], and Cell 2 does not. The continuous rotation of the cells during high-speed CT meant that a uniform circumferential temperature profile was generated around the cell. The cells were continuously heated until thermal runaway occurred.

6.2.2. Conditions for X-ray Imaging and CT

The imaging experiments were carried out using a 76 keV monochromatic beam at the ESRF[208], with a field of view of 10.5 mm × 7.6 mm. The exposure time was set to 0.35 ms and the high-speed camera used for the imaging was a PCO Dimax (PCO AG, Germany) which achieved 1250 fps. A region of interest of 960 × 700 pixels (horizontal × vertical) was used. The tomograms were captured at a rate of 1.25 Hz (Cell 1) and 2.5 Hz (Cell 2), which comprised 1000 and 500 projections respectively. The tomograms with the lower number of projections were captured at a higher rate but significantly sacrificed image quality. Higher image quality and lower frequency are preferred where little movement within the batteries is expected. Tomograms composed of 500 projections with a resolution of 10.87 µm were captured every 0.4 s over a 360 ° rotation at 150 rpm. Tomograms composed of 1000 projections with a resolution of 10.87 µm were captured every 0.8 s over a 360° rotation at 75 rpm. To achieve the required tomogram frequencies the images were stored on the PCO Dimax camera which, with 36 GB of on-board memory for fast intermediate storage, could store 17 s of recordings under these conditions. A post-event triggering capability was implemented whereby the detector recorded continuously until triggered at which point it would store the previous 17 s of high speed tomograms. The post-event triggering for recording the images was activated *ca.* 2 s after the catastrophic outcome of thermal runaway (explosion or violent venting). This resulted in *ca.* 15 s of high frequency tomograms being captured before the event and *ca.* 2 s of tomograms being captured after the event. During high-speed tomography the sample was continuously rotated through 360 °.

The 2.5 Hz and 1.25 Hz tomogram projections were taken over a 360 ° rotation of the cell at angular increments of 0.72 ° and 0.36 ° respectively. The monochromatic beam had a field of view of 10.5 mm × 7.6 mm, which captured half of the cell in the radiographs. The transmission images were reconstructed in 3D using standard filtered back projection[204] and saved as 32 bit float files. The reconstructed tomograms consist of greyscale image stacks in which the most highly X-ray attenuating materials are displayed as white and the least attenuating as black; steel and copper are highly attenuating materials and are displayed as

white in the tomography and radiography images (Figure 6-1). The nickel manganese cobalt oxide (NMC) electrode material is displayed as bright grey. Aluminium, graphite and the separator materials exhibit low attenuation of the X-ray beam and are difficult to distinguish; however, their position can be derived relative to the copper and NMC phase.

The reconstructed tomograms were processed using Avizo Fire 7 (FEI VSG, France), where the 3D images were displayed as stacks of 2D image slices (Figure 6-1). An edge preserving non-local means filter[210] was applied to the images to remove noise while preserving fine features and edge definition. Material phases were defined by greyscale value using Avizo's segmentation editor and selectively displayed (Figure 6-1).

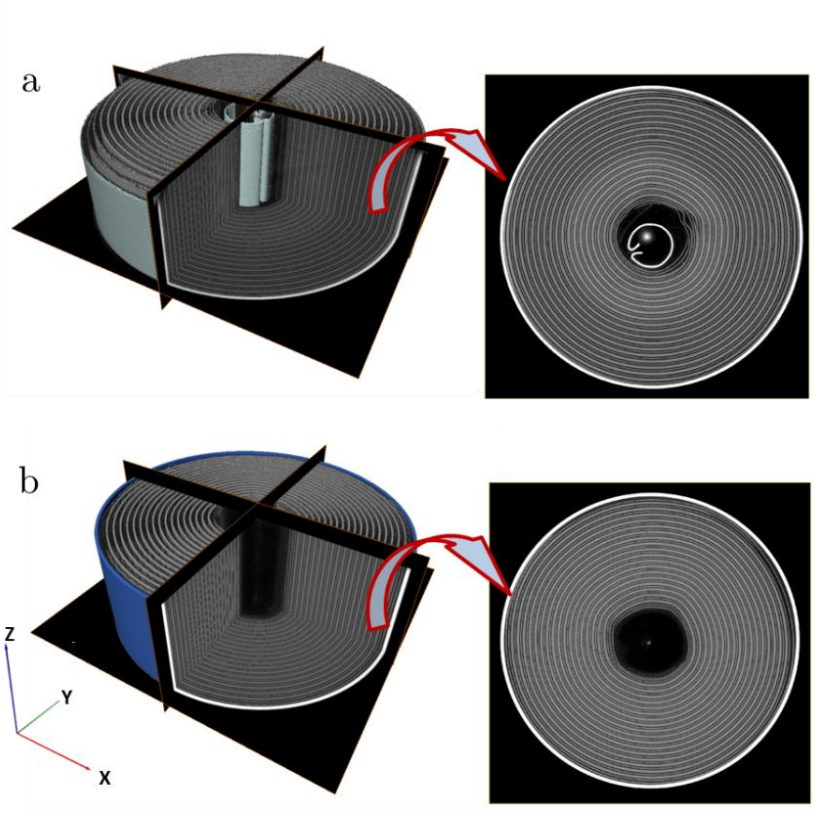

Figure 6-1: (a) 3D reconstructions with orthoslices in the XY, YZ and XZ planes of the 2.6 Ah battery (Cell 1) with isolated XY slice; (b) 3D reconstructions with orthoslices in the XY, YZ and XZ planes of the 2.2 Ah battery (Cell 2) with isolated XY slice.

The radiograph images were produced using MATLAB R2013a. Flat field correction was applied to the raw radiographs to remove artefacts and the greyscale image contrast was enhanced using MATLAB's 'adapthisteq' function for improved feature recognition. Images were converted to 16-bit unsigned integers before compiling into .avi movies.

6.3. Thermal and Structural Dynamics

6.3.1. Thermal Behaviour of Cells

The batteries were continuously rotated during the fast tomography experiments, which resulted in a circumferentially uniform heat distribution around the cylindrical shell. A vertical temperature gradient was observed due to alignment of the heat gun with the lower part of the cell. The evolution of the mean temperature of surface regions at three different heights was recorded with the thermal camera and is shown for each cell in Figure 6-2. Real-time thermal imaging movies of the cells during testing are available online as supplementary material with reference [63].

The surface temperature of both cells rose rapidly for the first 10 s of the test and then continued to increase at a quasi-steady rate. Thermal runaway of Cell 1 occurred after 168 s (Figure 6-2a) when its shell temperature reached *ca.* 230 °C; thereafter the temperature of the battery exceeded the temperature range of the thermal camera (up to 260 °C). During thermal runaway, the shell and cap of Cell 1 remained intact, allowing the exothermic reactions to run to completion, and the rapid pressure rise inside the shell caused the molten contents to eject through the vent in the form of a jet of fluid. In the seconds leading up to thermal runaway a jet of hot gas, consisting of gaseous products from breakdown reactions, was observed emanating from the vent of Cell 1 (this can be observed from the thermal imaging movies accompanying reference [63]). This was followed by liquid, believed to consist of molten separator material, bubbling on the cap of the battery.

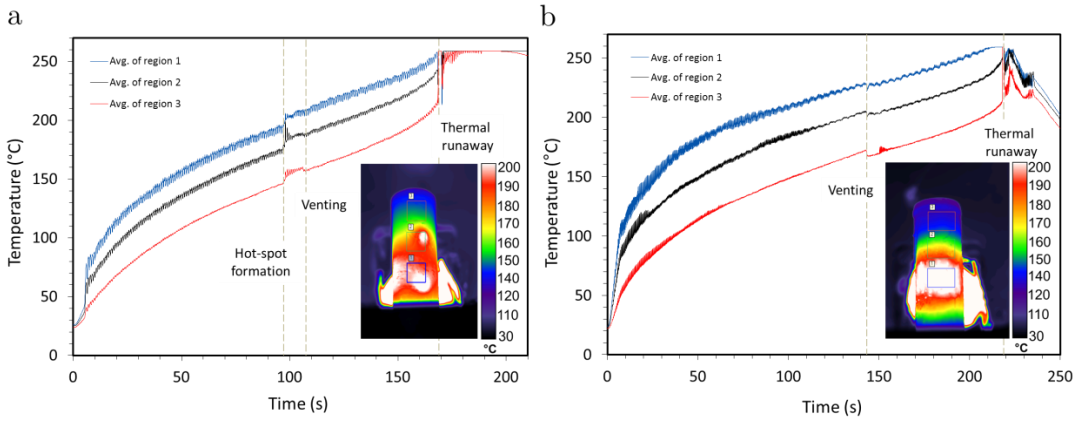

Figure 6-2: (a) Mean surface temperature profiles of the three regions (shown in the thermal image) on Cell 1 during the thermal abuse test showing thermal runaway after 168 s. The hotspots shown in the thermal image occurred on the surface of the shell after 97 s. As judged from the thermal image, the spot size of the heat gun on the surface of the cells was *ca.* 10 mm in diameter. (b) Mean surface temperature profiles of the three regions on Cell 2 during the thermal abuse test showing thermal runaway after 217 s. The inset thermal image was extracted after 80 s of heating.

Thermal runaway of Cell 2 occurred after 217 s (Figure 6-2). Venting of both cells (Cell 1 and Cell 2) is evident in the thermographs as a slight cooling due to the Joule-Thompson effect[115], as observed after 105 s in Figure 6-2a and 145 s in Figure 6-2b. Venting at an earlier stage might expose the internal decomposition reactions to oxygen and moisture in the air, accelerating the occurrence of thermal runaway. The rapid pressure rise inside Cell 2 during thermal runaway caused the entire cap of the cell to detach and the mostly unreacted cell contents to eject from the casing before the exothermic reactions could run to completion. Consequently, the internal temperature of Cell 2 is not expected to have reached that of Cell 1, which largely remained intact during failure.

The thermal image in Figure 6-2a shows the formation of two hotspots on the surface of the Cell 1 casing, evidenced by the sudden rise in temperature after 97 s. These hotspots are believed to originate from internal short circuits. The sudden appearance and transient nature of the hotspots suggest a mechanism involving a rapid but short-lived release of energy (Joule heating or exothermic reaction) which

would be consistent with a severe short circuit, i.e. one which results in a rapid local temperature rise with the greatest risk of initiating thermal runaway. Such short circuits are usually associated with the contact between highly conducting layers such as that between the two current collector foils or between the aluminium current collector and the graphite electrode, which could occur as a result of dendrite growth, impurities/shrapnel in the cell or internal structural collapse.

At temperatures above 130 °C the most likely internal short circuit is expected to occur between the positive and negative electrode as the separator layer begins to melt and lose its mechanical integrity. However, short circuits involving the positive electrode (NMC) and any other components are limited by the relatively poor conductivity of the positive electrode material and are not expected to exhibit local, rapid and short-lived temperature rises[153, 154]. The rapid temperature rise observed over such a short time span is indicative of a short circuit between two highly conducting layers allowing high current flow; either between the aluminium current collector and copper current collector (Al-Cu) or between the aluminium current collector and the negative electrode (Al-negative electrode) [148, 149]. Given the characteristics of the hotspots and their proximity in time to venting, it is inferred that they were either caused by gas-induced structural collapse inside the cell or by the aluminium current collector coming into contact with the negative shell casing, as a result of the separator material melting or contracting at elevated temperatures. Internal short circuiting is a major safety concern and cannot be prevented by mechanical or electrical safety devices[151]. This highlights the potential of thermal imaging both as a diagnostic tool which could enhance thermal analyses during abuse testing, identifying short circuiting resistances via dynamic thermal events, and as an effective method for thermal model validation[147].

6.3.2. High Frequency Tomography

Tomograms were captured at a rate of 1.25 Hz and 2.5 Hz for Cell 1 and Cell 2 respectively, allowing visual monitoring of the internal structural degradation in the seconds leading up to thermal runaway. The lower frequency tomograms were reconstructed using a larger number of images taken at smaller angular increments which gave significantly improved 3D images (see Section 6.2.2 for more details). Higher frequency with reduced image quality was used where a large degree of movement was anticipated within the cell.

At the core of Cell 1, there is a cylindrical mandrel which aids in cell winding and provides mechanical support during manufacturing (Figure 6-1). Structural deformation around the inner layers of Cell 1 was observed leading up to thermal runaway (Figure 6-3). The tightly wound electrode, current collector and separator layers remained mostly intact during thermal abuse; however, a small degree of delamination occurred around the inner region of the cell where the spiral-wound layers are least compressed. The separation of layers stemmed from the region between the positive and negative electrodes, i.e. the separator/electrolyte region. The positive and negative electrodes in Figure 6-3 are believed to have diverged due to melting of the separator layer and local gas generation from reactions such as SEI breakdown and electrolyte degradation. The extent of separation of the positive and negative electrode can be gauged from the side views in Figure 6-3b and Figure 6-3d, which show that the delamination continues vertically through the cell.

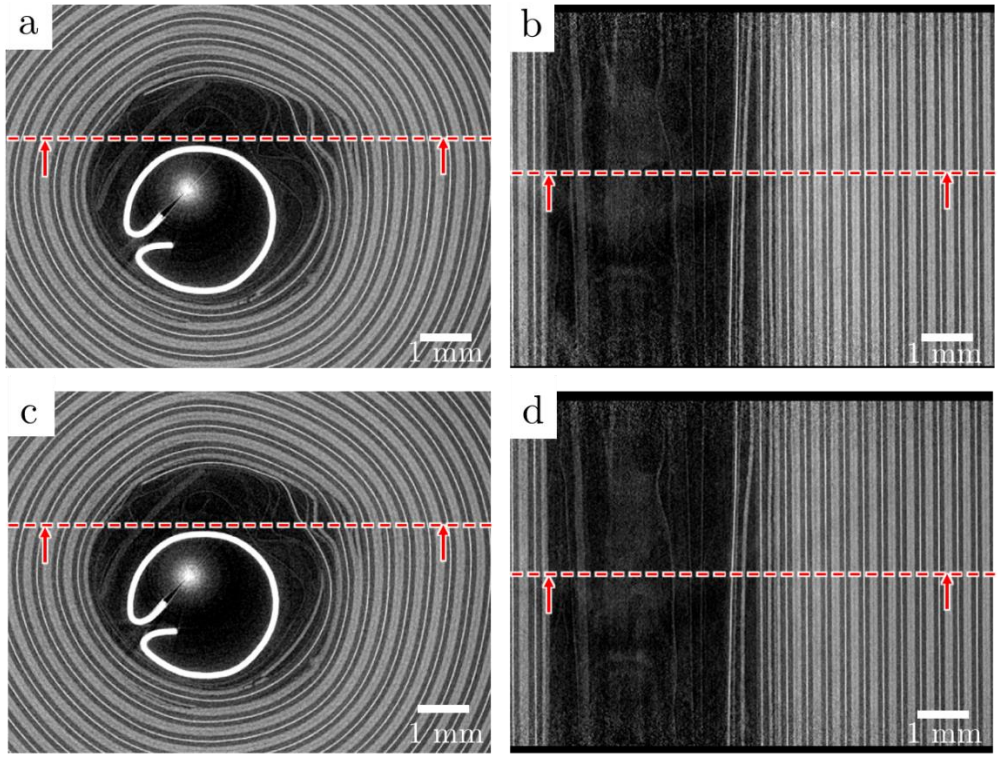

Figure 6-3: Enlarged greyscale slices from 3D reconstructions during *operando* high frequency tomography of Cell 1 showing (a) XY plane 15 s before thermal runaway, (b) the YZ plane 15 s before thermal runaway, (c) the XY plane 1 s before thermal runaway and (d) the YZ plane 1 s before thermal runaway. The dotted red lines indicate the through-plane slice with which the neighbouring image is associated.

The effect of the central mandrel is evident from the comparison of cell architecture after venting. Cell 1 has a tightly packed core with a steel cylindrical mandrel which helps prevent against internal collapse (Figure 6-1). No severe collapse was observed in Cell 1 as demonstrated in Figure 6-4a. In contrast, no cylindrical mandrel is present in Cell 2, which showed a severe distortion of its architecture after venting (Figure 6-4b). Prior to venting, thermally and electrochemically driven degradation reactions resulted in the formation of gas pockets between the electrode layers. It is believed that during pressure relief the gas pockets were rapidly channelled towards the vent via the path of least resistance, causing a sudden collapse in the structure of the spiral-wound layers. This collapse induced structural deformation including sharp bends in the layered materials, heightening the risk of severe internal short circuits and consequent

thermal runaway, a risk which could have been reduced by incorporating a central mandrel in Cell 2.

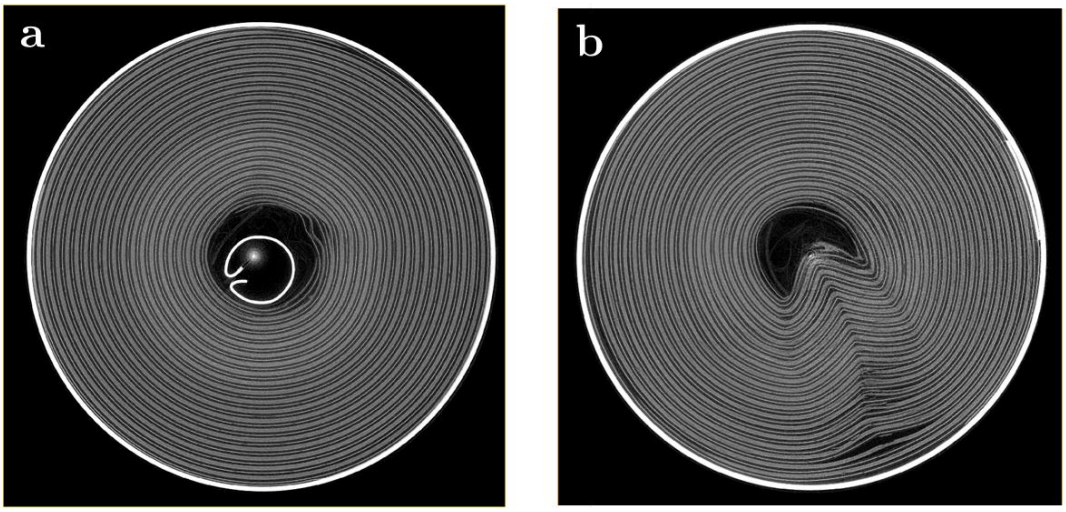

Figure 6-4: Images in the XY plane comparing the spiral layered structure of (a) Cell 1 with and (b) Cell 2 without, an internal mandrel. Cell 2, without the internal mandrel, showed a severe structural collapse after venting.

Little change in the internal architecture of Cell 1 was observed in the 15 s leading up to thermal runaway, with neither the NMC nor the graphite electrode showing any obvious signs of microstructural degradation. Both the NMC and graphite electrodes are expected to exothermically break down within a narrow temperature range (200 °C – 250 °C) causing the cell contents to rapidly degrade[108].

In the 15 s leading up to thermal runaway, expansion of the collapsed region of Cell 2 and increasing divergence of the electrode layers was observed (Figure 6-5). The progression of delamination and divergence originated from the interface between the positive and negative electrode, i.e. the separator region in which gas generation from SEI and solvent decomposition is most prominent during thermal abuse[115]. Prior to thermal runaway, when the shell temperature was *ca.* 200 °C, broadening of the collapsed region was observed as gaseous products continued to flow towards the vent (Figure 6-5a and Figure 6-5c).

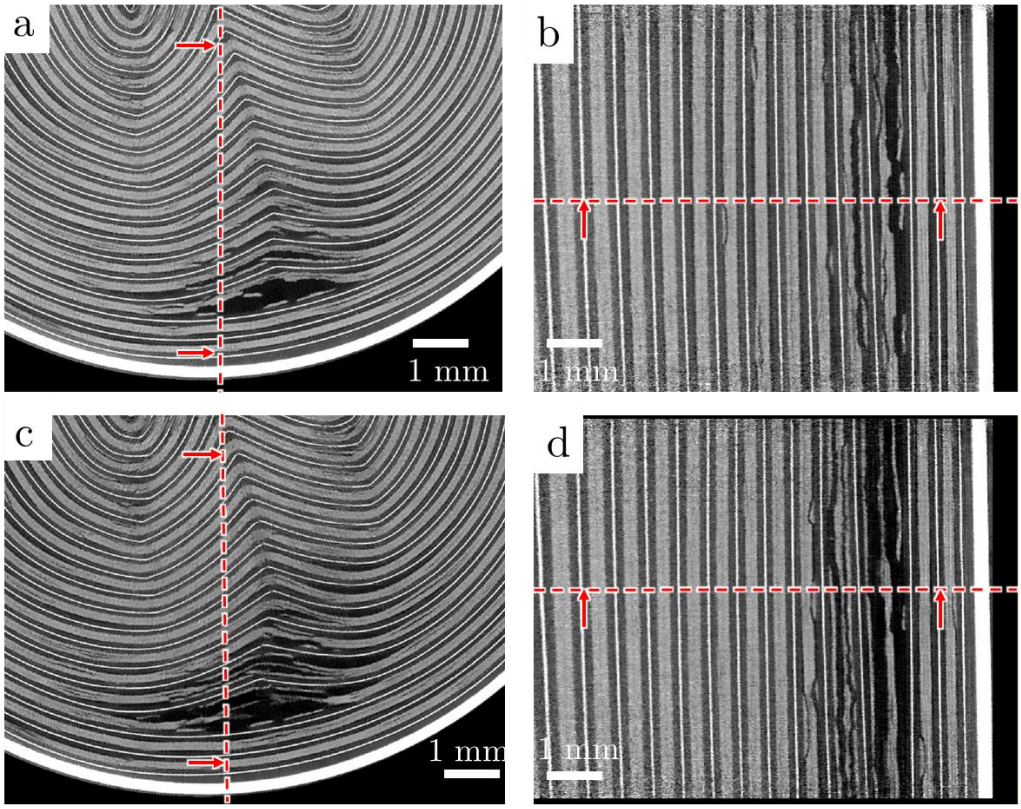

Figure 6-5: Enlarged greyscale slices from 3D reconstructions during *operando* high frequency tomography of Cell 2 showing (a) slice from the *XY* plane 15 s before thermal runaway, (b) the *YZ* plane 15 s before thermal runaway, (c) the *XY* plane 1 s before thermal runaway and (d) the *YZ* plane 1 s before thermal runaway. The dotted red lines indicate the through-plane slice to which the neighbouring image is associated.

After venting the cell became open to the atmosphere and the growing collapsed region allowed penetration of the atmosphere deep into the cell, although only after initial venting when the flow rate had reduced sufficiently to allow diffusion back into the cell. For safety reasons a nitrogen atmosphere was used in this work but in real world situations this could accelerate the decomposition of the electrode materials and thermal runaway through the provision of oxygen. High frequency tomography at 2.5 Hz could not capture the initiation and propagation of thermal runaway as the substantial movement inside the cell during the catastrophic failure prevented reconstruction in 3D. However, the sequence of

events during the initiation and propagation of thermal runaway was captured in the individual radiographs taken at 1250 fps.

6.3.3. High-speed Radiography

By using high-speed radiography, events that were too rapid to be captured by high-speed tomography could be observed, thereby providing insight into the mechanism behind initiation and propagation of thermal runaway. The radiographs show a 2D integrated representation of the whole cell rather than individual focal plane slices like those selected from the tomograms. Time-stamped radiographs taken at 1250 fps and showing half the cell during thermal runaway were compiled into movies and are presented as supplementary material online with reference [63]. Still radiographs captured at various points during thermal runaway for Cell 1 and Cell 2 are presented in Figure 6-6 and Figure 6-7 respectively.

The initiation of thermal runaway in Cell 1 occurred above the field of view in Figure 6-6. As the NMC electrode exothermically decomposed, the combination of local gas generation and increasing temperature resulted in a rapid pressure rise within the cell. The consequent pressure difference between the region undergoing thermal runaway and the atmosphere appears to have fractured the electrode materials and directed the fragments towards the vent of the battery. Initially, the exothermic decomposition reactions proceeded between the copper current collecting foil, which for as long as its mechanical integrity was maintained, channelled the electrode material fragments towards the top of the cell. The breakdown and ejection of electrode material spread radially outwards, providing evidence that the propagation of thermal runaway in Cell 1 occurred from the inner to the outer layers, despite the heat being applied to the external surface. This may be due to the thermally insulating effect of the outer layers when exothermic reactions and internal short circuiting occur, so that the temperature of the inner layers is first to significantly exceed the temperature of the shell.

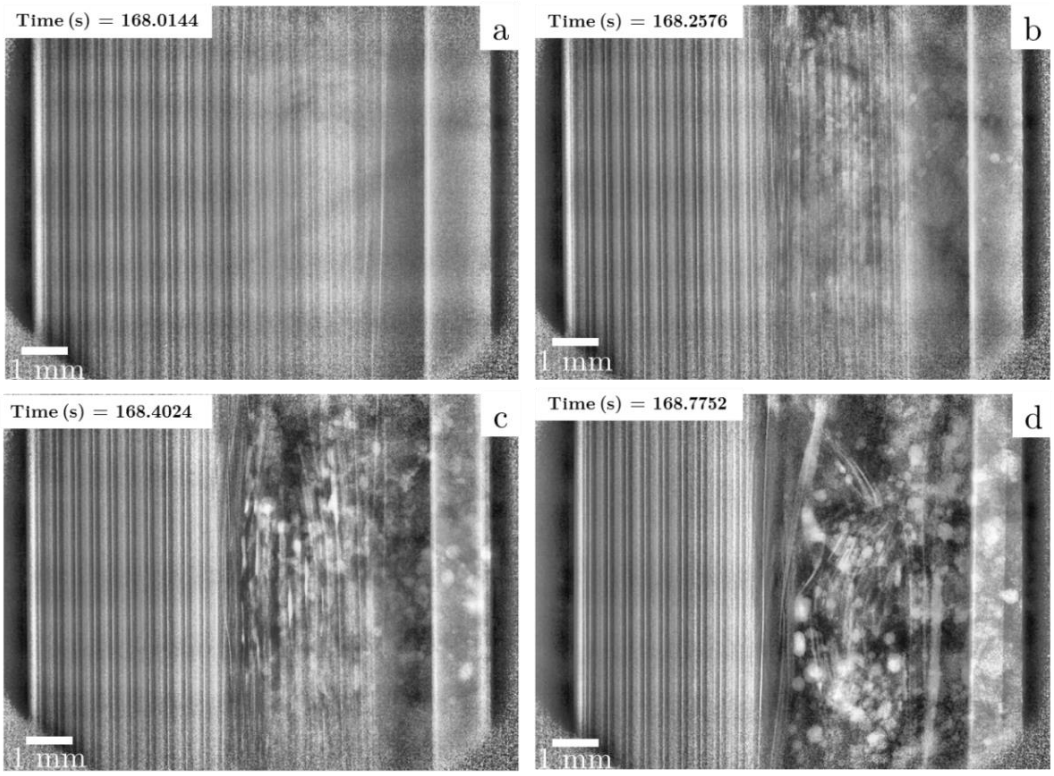

Figure 6-6: Radiographs showing the propagation of thermal runaway in Cell 1. (a) Radiograph of the *YZ* plane before thermal runaway; (b, c and d) sequential images showing the propagation of thermal runaway through the cell. The thermal runaway initiates at the inner layers where the maximum temperature is apparent and spreads radially outwards. The formation of copper globules can be observed as highly attenuating white blots in images b, c and d. Heating is applied from the right of the images but continuous rotation at 180 ° every 0.4 s maintains an even circumferential temperature distribution.

Locally, the heating rate exceeds the heat dissipation rate. The resulting increase in temperature can be deduced from the observation of the copper current collecting material melting and collecting into globules (highly attenuating white spots in Figure 6-6) around the region of apparent electrode breakdown. This suggests the presence of a very large temperature gradient between the inside and the outside of the cell, since the inner region has reached the melting point of copper (1085 °C) while the outer electrode layers remain intact. NMC and lithiated graphite are known to decompose at 300 °C[108, 115], implying a transient

temperature difference of over 700 °C within the cell during the propagation of thermal runaway. Following loss of mechanical integrity of the spiral layers, large portions of the spiral-wound materials were ejected together. Heat transfer from the exothermic reactions to the neighbouring layers was therefore interrupted as large sections of reacting material were ejected. The ejection of material to the atmosphere effectively dissipated the heat and mitigated the propagation of thermal runaway, although the effect on any surrounding cells would be exacerbated by the presence of air.

In contrast to Cell 1, thermal runaway was not observed to propagate throughout Cell 2 shortly after the onset of significant motion and degradation within the cell. The bulk of the intact contents were ejected soon after signs of material degradation and thermal runaway initiation had been observed. The layered structure of Cell 2 remained intact up until 217.60 s (Figure 6-7a), when the electrode layer indicated in Figure 6-7b began to break down, followed by a sudden shift of bulk material towards the vent of the cell between 217.66 s and 217.70 s. Less than one tenth of a second later, the cell cap detached, the internal contents of the cell were ejected (Figure 6-7c) and the propagation of thermal runaway was halted. The upward shift of intact material may have prevented the release of pressure during thermal runaway by blocking the vent. An uncontrolled failure occurred due to the hindered pressure relief and a rapid pressure rise inside the cell. The propagation of thermal runaway within the cell was hampered by the rapid dissipation of heat and the ejection of reacting contents to the atmosphere.

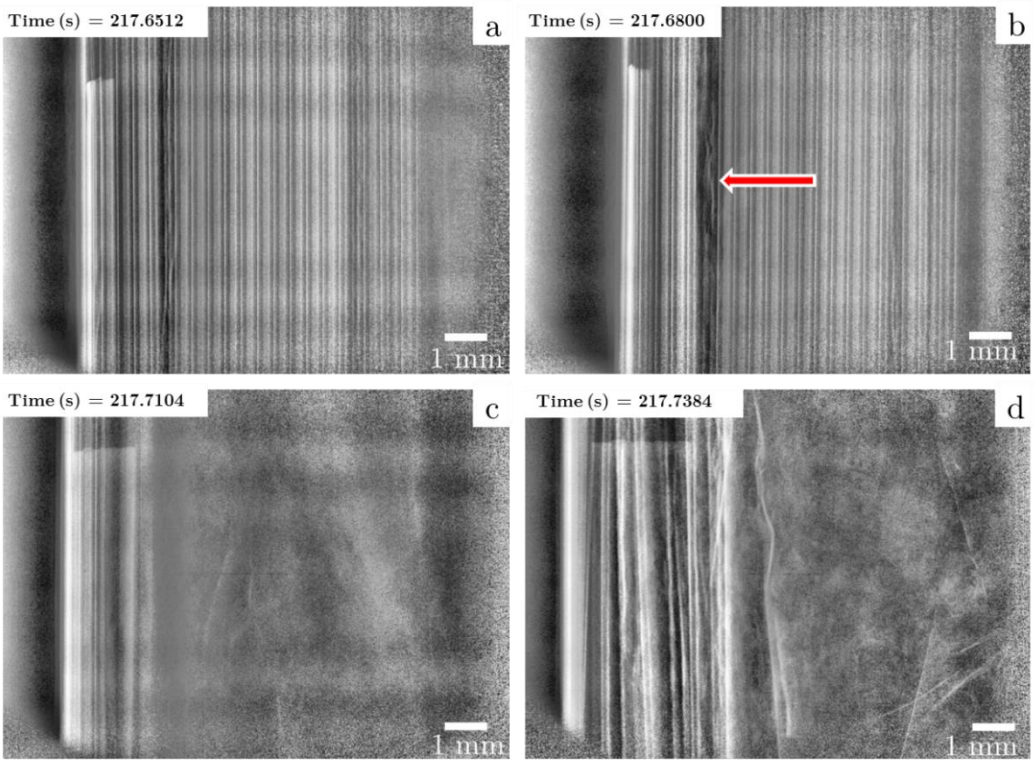

Figure 6-7: Radiographs showing the propagation of thermal runaway in Cell 2. (a) Radiograph of the *YZ* plane before thermal runaway, (b) radiograph during thermal runaway where the red arrow indicates the region in which structural breakdown is first observed, (c) radiograph during ejection of contents and (d) radiograph immediately after ejection of contents. The time-stamped radiographs show that the entire process of initiation and ejection lasted less than 0.1 s. Heating is applied from the right of the images but continuous rotation at 180 ° every 0.2 s maintains an even circumferential temperature distribution.

6.3.4. *Post-mortem* Investigations

Post-mortem tomography scans were taken to assess the internal structure following thermal runaway in both cells. The *post-mortem* 3D reconstructions of Cell 1 shown in Figure 6-8 reveal a complete destruction of the original spiral-wound architecture. The copper phase is easily distinguished from the rest of the material in the reconstructed images due to its high attenuation and has been isolated from the rest of the contents in Figure 6-8b. The presence of the large

copper globules indicates that temperatures within the cell reached in excess of 1085 °C (the melting point of copper).

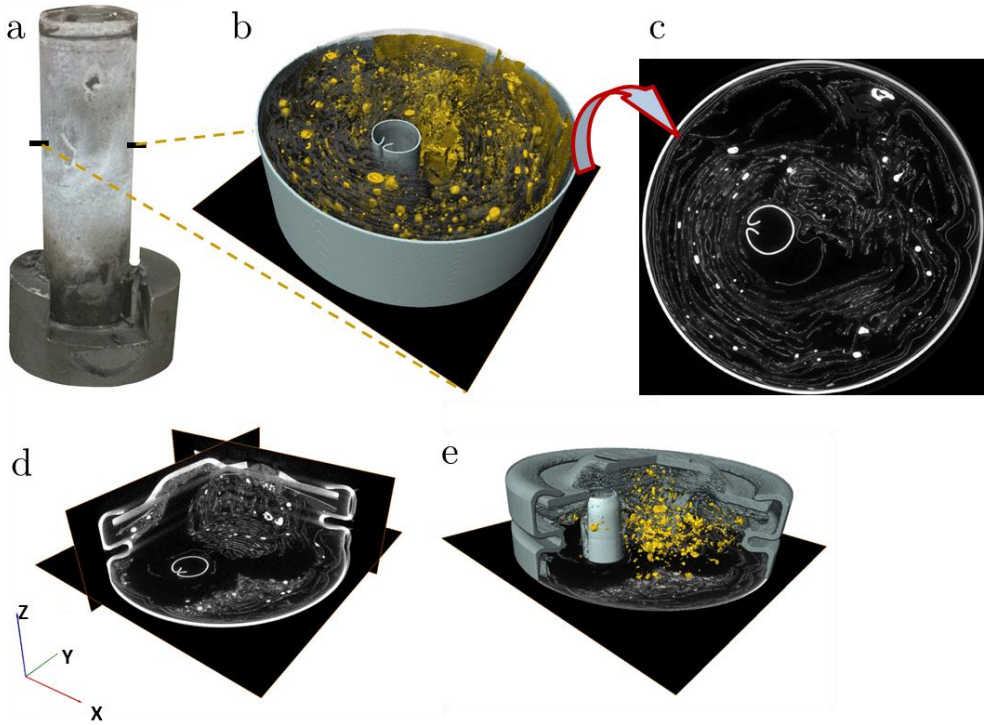

Figure 6-8: (a) External view of Cell 1 after thermal runaway where the black marks indicate the points at which the bottom slice of the corresponding tomogram begins; (b) 3D reconstruction showing isolated copper phase (yellow), other broken down material (semi-transparent dark grey), battery casing (teal) and central cylindrical mandrel (teal); (c) greyscale slice from the XY plane; (d) tomogram of the battery vent region showing greyscale slices from the XY, YZ and XZ planes; (e) 3D reconstruction of the cap region showing the placement of the central mandrel near the vent.

Some intact remains of the copper current collecting foil can be observed around the outer walls of the battery. The high concentration of large copper globules around the inner regions of the 3D reconstructions, compared to the presence of intact current collector remains around the outside, indicates an uneven temperature distribution within the cell during thermal runaway. The propagation of thermal runaway from the centre of the battery to the outer edges is consistent

with the presence of a significant temperature gradient between the inner and outer layers. A large mass of fragmented material is seen to have gathered near the vent of Cell 1 and the central mandrel has aligned with one of the vent holes (Figure 6-8e), which supports the hypothesis that the position of the mandrel hindered venting and ejection of material during thermal runaway.

In contrast to Cell 1, the copper current collecting foil in Cell 2 mostly remained in its original laminar form (Figure 6-9). The ejection of the cell contents mitigated the propagation of thermal runaway and consequently, the melting point of copper was not reached in the majority of the cell. As shown in Figure 6-9b, small copper globules formed around the inner regions of the cell which indicates that local temperatures reached above 1085 °C but the propagation of exothermic reactions and heat transfer to the rest of the cell was interrupted by the sudden ejection of the cell contents. The radiographs of Cell 2 in Figure 6-7 showed that the internal layered materials had not decomposed up until the point of rupture, suggesting that uncontrolled failure (detachment of the battery cap) is linked to the distance between the point of failure initiation and the vent. For example, initiation of thermal runaway near the bottom of the cell would result in the unreacted material above that point being forced towards the vent, hence increasing the likelihood of the vent region becoming clogged and the cap detaching from the cell. The possibility of the vent region clogging was previously highlighted in a study by Golubkov *et al.*[115] where two venting events occurred during thermal abuse tests of 18650 NMC cells; one was due to the normal operation of the bursting plate and the second was attributed to relief after clogging of the vent. The 3D reconstruction in Figure 6-9b and the slice in Figure 6-9c show that the majority of the material remains are copper. In contrast to Cell 1, most of the softer electrode and separator materials, i.e. the active materials which allow the propagation of thermal runaway, were ejected from the cell during the rupture. The *post-mortem* tomography in combination with the radiography results demonstrate that the bursting-cap failure mechanism may be advantageous in mitigating reaction propagation and heat generation inside such cells during thermal runaway.

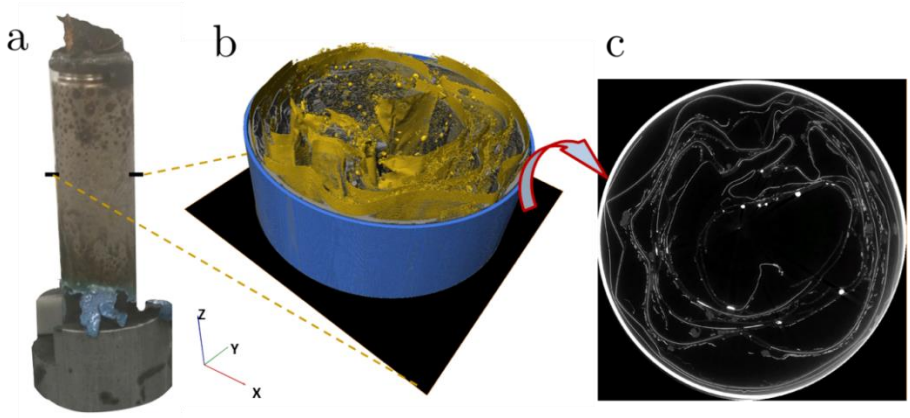

Figure 6-9: (a) External view of Cell 2 after thermal runaway showing the burst cap and protruding internal contents. The black marks indicate the points at which the bottom slice of the corresponding tomogram begins; (b) 3D reconstruction showing isolated copper phase (yellow), other broken down material (semi-transparent dark grey) and battery casing (blue) where the copper phase is mostly still intact; (c) greyscale slice from the XY plane.

6.4. Conclusions

Operando high-speed tomography and radiography of lithium-ion batteries during thermal runaway has proven to be an effective diagnostic tool for visualising rapid failure mechanisms. The elucidation of internal structural features and dynamics has highlighted the effect of battery design on the safety and behaviour of cells during failure. This can only be achieved using non-invasive high frequency imaging techniques. The evolution of gas pockets between the electrode layers was observed in the tomograms when the shell temperature exceeded 100 °C, resulting in electrode layer delamination. The formation of gas pockets reduces the electronically and ionically conducting interfacial area between the electrode layers and sustained gas generation leads to venting of the cell, a sudden release of pressure which can lead to collapse of the internal structure of the cell, depending on its design.

The magnitude of structural collapse observed in this study compromises the safety of the cell. A severe internal collapse increases the risk of internal short circuits, exposes decomposing material to oxygen and moisture in the air, and

consequently increases the risk of and accelerates thermal runaway at lower external temperatures. This risk may be avoided by including a tightly packed core or an internal structural support in the battery design[288-290].

Additionally, the location of thermal runaway initiation may have an effect on the failure mechanism of the battery; initiation of thermal runaway near the bottom of the cell may result in a mass ejection of intact contents above the point of failure, whereas initiation near the top of the cell would allow the propagation of thermal runaway to travel vertically down into the cell over time while contents are continuously ejected. The propulsion of the cell contents towards the vent may also render the function of the vent redundant if clogged, a phenomenon that is investigated further in Chapter 8.

The failure mechanism of the battery can have a significant influence on the final temperature of the cell, and on the rate and quantity of heat generated during failure. As Kim *et al.*[105] highlighted, thermal runaway of a battery pack is likely to be induced by thermal runaway of a single failing cell, emphasising the need to limit the heat transfer to adjacent cells. This can be achieved by installing heat barriers or intumescent layers between cells. As demonstrated in this study, mitigating heat generation and limiting the maximum temperature reached during thermal runaway by ejecting the degrading material could also contribute to safer modular designs.

High-speed radiography of Cell 1 provided striking images of the propagation of thermal runaway and the presence of an inhomogeneous temperature distribution within the cell, with the outer regions remaining intact while the inner regions lost their structural integrity as temperatures exceeded 1085 °C. The relatively slow venting of Cell 1 helped contain the process of thermal runaway and allowed the decomposition reactions to run to completion, generating large amounts of heat, which emphasises the importance of effective thermal management systems[291]. The early ejection of battery contents in the case of Cell 2 holds the advantage of preventing further heat generation and temperature increase thus protecting neighbouring cells and the rest of the pack from the risk of thermal runaway. However, this should be balanced against the risk of heat

generation on the external surface of neighbouring cells arising from oxidation of the ejected cell contents in air.

In summary, *operando* high-speed synchrotron radiation X-ray tomography and radiography, in combination with thermal imaging, have provided great insight into the structural and thermal dynamics leading up to and during thermal runaway and failure of lithium-ion batteries during external thermal abuse. These discoveries enhance our understanding of the most dangerous failure mechanism of such devices and highlight the impact of engineering design on the performance and safety of 18650 cells. The containment design and arrangement of apparatus, including the electrical slip-ring described in this work, also facilitates X-ray imaging and thermal analysis of lithium-ion batteries during electrical abuse, which is the focus of the following chapter (Chapter 7). However, the PTC in the commercial 18650 cells studied here prevents the high charge/discharge rates and extreme states of overcharge and undercharge required for catastrophic failure. In the following chapter, a pouch cell with no PTC is investigated using the same *in-situ* rig design.

Chapter 7

Electrical Abuse: A Multi-scale Analysis

Sections of this work have been peer reviewed and published in the journal of Physical Chemistry Chemical Physics (D. P. Finegan, M. Scheel, J. B. Robinson, B. Tjaden, M. Di Michiel, G. Hinds, D. J. L. Brett, P. R. Shearing, *Investigating lithium-ion battery materials during overcharge-induced thermal runaway: an* operando *and multi-scale X-ray CT study*, Physical Chemistry Chemical Physics, doi: 10.1039/c6cp04251a (2016)).

7.1. Introduction

Overcharge of lithium-ion batteries poses a significant safety risk and is one of the primary causes of thermal runaway. Consequently, overcharge tests have been integrated into safety test standards for lithium-ion batteries, as discussed in Section 2.6.2. The magnitude of the energy released during failure increases with increasing state-of-charge (SOC), and as the chemical energy stored in the electrode materials is released, thermal runaway resulting from overcharge is particularly catastrophic[292]. It is well known that the microstructure of electrode materials plays an important role in determining the performance of cells[73, 227], but the role of particle morphology in the safety of cells is not yet well understood.

Here, high-speed *operando* synchrotron X-ray CT is combined with thermal and electrochemical measurements to link, and assess, the observed morphological, thermal and electrical response of a commercial $LiCoO_2$ battery during overcharge-induced failure. A multi-scale comparative analysis of the cell in its fresh and failed

state is also performed to elucidate failure mechanisms across multiple length scales, from individual electrode particles to the full cell architecture. Image-based quantification is used to determine the change in electrode particle morphology via a particle size distribution analysis, and the effects of particle morphology on the failure mechanism of lithium-ion batteries are discussed.

7.2. Experimental

7.2.1. Setup and Electrical Abuse Testing

The *in-situ* containment system described in Section 3.8.1 was used in this study, which allowed simultaneous high-speed X-ray CT, electrical testing, and thermal imaging. The overcharge abuse test was performed on a Turnigy nanotech 160 mAh lithium-ion pouch cell (dimensions 39 mm × 12 × 8 mm) which consists of a $LiCoO_2$ positive electrode, polymer separator and graphite negative electrode. The Turnigy cell is designed to cater for high charge (10 C) and discharge (30 C) rates (where a C-rate is the rate at which a battery is discharged relative to its maximum capacity). In this study the battery was overcharged from 100 % SOC (4.2 V) at a constant current of 3 A (18.75 C) until failure, which is well outside the safe operating limits recommended by manufacturers, but similar to the extreme UL testing standards outlined in Section 2.6.2.

The surface temperature of the battery was recorded using a thermal camera (FLIR SC5000MB, FLIR Systems, France) as shown in Figure 7-1a. The thermal camera was set to the calibrated range of 15 °C to 200 °C during these experiments. A uniform layer of high emissivity black paint (with a calibrated emissivity of 0.96 over the range 40 °C to 180 °C) was applied to the surface of the cell. A real-time thermal imaging video can be found online as supplementary material to reference[293].

The cell voltage plot during overcharge is shown alongside the surface temperature profile in Figure 7-1b; the temperature presented in the plot was taken as an average over an area *ca.* 9 mm^2 on the surface of the cell (shown in Figure 7-1a).

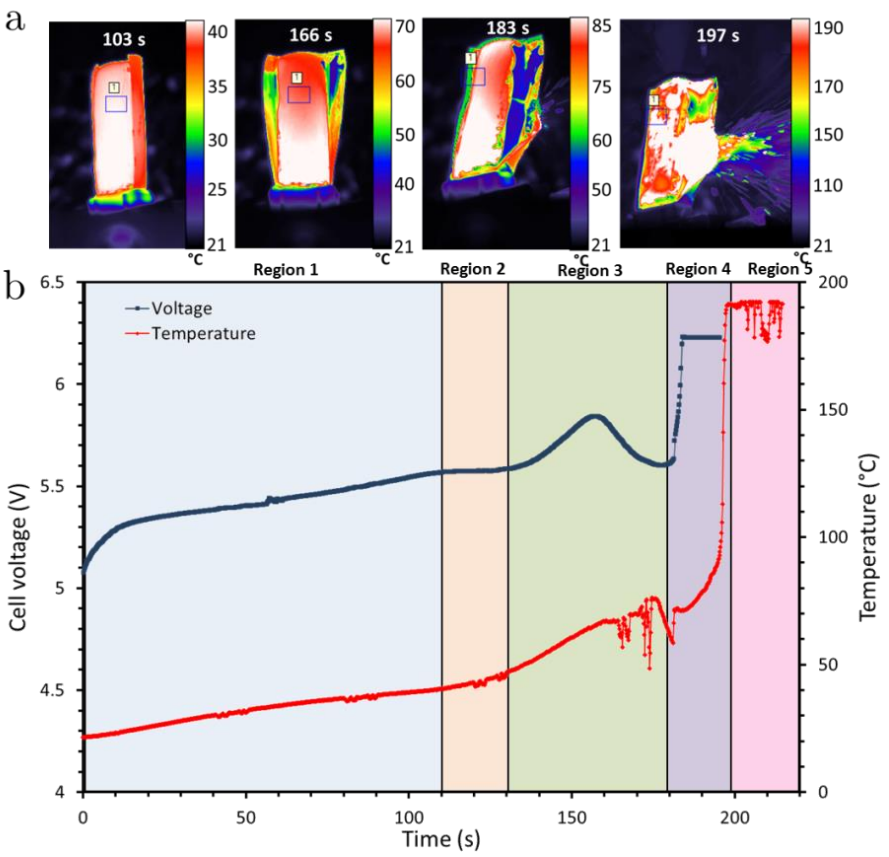

Figure 7-1: (a) Sequence of time-stamped thermal images showing the increasing surface temperature of the $LiCoO_2$ pouch cell leading up to thermal runaway. The average temperature within the labelled square is plotted. (b) Plot of the cell voltage and surface temperature, leading up to and during thermal runaway. The battery was charged at a constant current of 3 A (18.75 C), from 100% SOC (4.2 V) until failure.

7.2.2. *Operando* Synchrotron CT

Fast tomographic imaging was performed at beamline ID15A at the ESRF[184, 208]. The Turnigy cell was imaged using a 76 keV monochromatic synchrotron X-ray beam. The X-ray absorption signal was converted into a visible light signal by a LuAG:Ce scintillator screen and then collected by a 1× macro objective. The field of view (FOV) was 10.5 mm × 7.6 mm, which consisted of 960 × 700 pixels (horizontal × vertical) and gave a pixel resolution of 10.9 µm. The sample rotation

axis was at the edge of the FOV, such that through a 360 ° rotation it was possible to double the size of the 3D image in the horizontal direction[294]. The resulting 3D reconstruction was then 1785 × 1785 × 700 pixels (19.2 mm × 19.2 mm × 7.6 mm). Similar to before, each tomogram consisted of 2 × 2000 half projections using an exposure time of 0.7 ms. The acquisition time for each tomogram was 2.8 s and one tomogram was captured every 40 s.

7.2.3. Lab-based X-ray Imaging

Using material extracted from the same Turnigy cell imaged in the synchrotron, tomographic reconstructions of varying sample size and resolution were produced using lab-based X-ray CT systems (Zeiss Xradia Versa 520 and Zeiss Xradia Ultra 810, Carl Zeiss XRM, Pleasanton, CA, USA). The specific imaging properties for each scan are provided in Section 10.3 in the Appendices. Materials were imaged with a pixel resolution of 63.1 nm (Zeiss Xradia Ultra 810), 0.36 µm (Zeiss Xradia Versa 520) and 7.92 µm (Zeiss Xradia Versa 520). The CT system used for the remaining scans (Zeiss Xradia Versa 520), and the specific imaging parameters are also provided in Section 10.3 of the Appendices. The transmission images from all scans were reconstructed using a commercial software package (Zeiss XMReconstructor), which uses an algorithm based on standard filtered back-projection.

7.2.4. Data Processing

The reconstructed tomograms were processed using Avizo Fire 9 software (FEI VSG, France). An edge preserving non-local means filter[210] was applied to the images to reduce noise while maintaining phase boundaries for segmentation. Phases were separated based on greyscale values. Measurements of sample porosity and particle size distribution were performed using Avizo Fire 9's label analysis tool. The temperature data and thermal imaging videos were extracted using FLIR's Altair software.

7.3. Multi-scale Analyses of Failure

7.3.1. Voltage, Temperature and *Operando* CT

During overcharge of lithium-ion batteries, a sequence of events related to the evolution of voltage, temperature and chemistry of the cell occurs leading up to thermal runaway and failure. In Figure 7-1b, distinctive features can be identified in the temperature and voltage curves. For the initial 110 s (Region 1), the external temperature of the cell increases from 20 °C to *ca.* 40 °C. This initial heating is expected to derive primarily from irreversible heat generation mechanisms, such as Ohmic losses, which are most prevalent at high C rates[295]. A plateau in cell voltage is observed after 110 s (Region 2 in Figure 7-1b), followed by a significant increase in the rate of temperature rise after 120 s. The simultaneous voltage plateau and temperature rise indicates the initiation and progression of the decomposition / formation of the solid electrolyte interphase (SEI)[108, 296]. At high temperatures (> 80 °C), the SEI becomes unstable and self-discharge initiates. Lee *et al.*[297] suggested that the lithium becomes more active within the carbon structure at temperatures above 80 °C due to a large reduction in charge transfer resistance. The combination of the accelerated loss of lithium and the instability of the SEI layer results in an increasing rate of the exothermic SEI decomposition / formation reactions and consumption of lithium.

After *ca.* 80 s, corresponding to an external temperature of 40 °C, the pouch of the cell has begun to swell (Figure 7-2) as gas is generated from reduction of the electrolyte and decomposition of the SEI[115, 117, 298]. After 120 s, severe delamination is observed around the separator regions in the outer layers. Within Region 3 in Figure 7-1b, a distinctive peak in cell voltage occurs over the space of *ca.* 40 s, consistent with the behaviour observed by Belov and Yang[299]. The pouch structure is seen to diverge from its original packaged structure, which corresponds with this voltage peak, as observed in Figure 7-1b. It is expected that the rise in voltage is caused by the resistance increase associated with the gas pockets forming between the active layers, and the subsequent fall in voltage by the decrease in resistance when the pouch bursts and the gases are channelled

away. The tightly wound active layers channel gases out into the exterior pouch when the pouch begins to lose its original package structure and starts to swell.

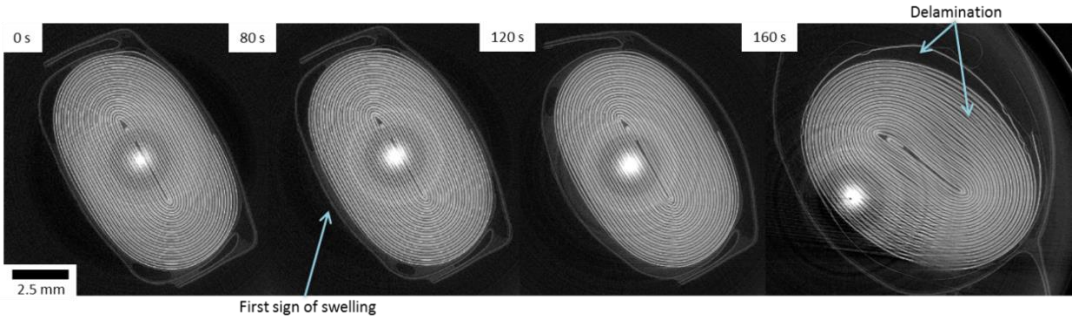

Figure 7-2: Time-stamped horizontal slices taken from sequential tomograms during electrical overcharge of the $LiCoO_2$ cell. Pouch swell begins after 80 s (blue arrow), and the electrode layers begin to deform and delaminate after 160 s. The $LiCoO_2$ electrode also delaminates from the Al current collector after 160 s (blue arrow pointing to inner region)

Finally, within Region 4 in Figure 7-1b, the cell voltage rises sharply to the maximum voltage of the potentiostat, the most likely cause of which is the shutdown of the separator and damage to the internal circuit caused by the rupture of the cell at that time. The tomogram taken at 160 s in Figure 7-2 shows delamination of the $LiCoO_2$ layers from the aluminium current collector in various places, which may be evidence of the electrolyte vaporising or initial stages of decomposition of the $LiCoO_2$ resulting in gas pockets forming between the aluminium current collector and the $LiCoO_2$ layer. This may also be due to the current collector being oxidised by the electrolyte, or the products of electrolyte decomposition[299, 300].

The thermal decomposition of $Li_{0.5}CoO_2$ can occur at temperatures above 200 °C[123] and the reaction between $Li_{0.5}CoO_2$ and solvent (ethylene carbonate), to produce CO_2 and H_2O, can occur at temperatures as low as 130 °C[114, 123], according to equation 7.1.

$$Li_{0.5}CoO_2 + 0.1C_3H_4O_3 \rightarrow 0.5LiCoO_2 + 0.5CoO + 0.3CO_2 + 0.2H_2O \qquad (7.1)$$

Although the surface temperature of the cell appears to be too low for the decomposition of the $LiCoO_2$ to occur, as Lin *et al.* suggested[301], the positive electrode side with the aluminium current collector is most susceptible to high temperatures during overcharge abuse. It is also recognised that the temperature measured at the surface of the pouch cell is not representative of the temperature of the internal active materials, due to the thermal insulating effect of the gas between the active materials and the surface of the pouch.

Fluctuations in the surface temperature of the cell occur after around 160 s as the cell ruptures, at which point the unstable electrodes are exposed to air and the process of thermal runaway is accelerated. The reaction between the $LiCoO_2$ and electrolyte, along with the decomposition of the SEI layer provide heat for the occurrence of thermal runaway which soon ensues, following which the surface temperature of the cell exceeds the limit of the thermal camera's calibrated range (Region 5 in Figure 7-1b).

7.3.2. *Post-mortem* CT and Battery Architecture

For comparison, the full cell was imaged in its fresh state (Figure 7-3a) and also *post-mortem* (Figure 7-3b), with a pixel size of 7.92 µm. The structure of the complete cell before and after thermal runaway is compared and the extent of structural damage and material degradation investigated. The aluminium (Al) phase was segmented (blue phase in Figure 7-3b), and is shown to have agglomerated at the top and bottom of the wound electrode layers. The rapid gas generation from the decompositon of the $LiCoO_2$ and electrolyte is likely to have carried the molten Al to the ends of the roll as the gas was channeled from the inner layers to the outer pouch. The porous structure of the Al globules at either end of the cell supports the hypothesis that gas played a part in carrying the molten metal. The uneven gas generation may also have had a peristaltic effect between the tightly wound layers, forcing the molten Al to either end.

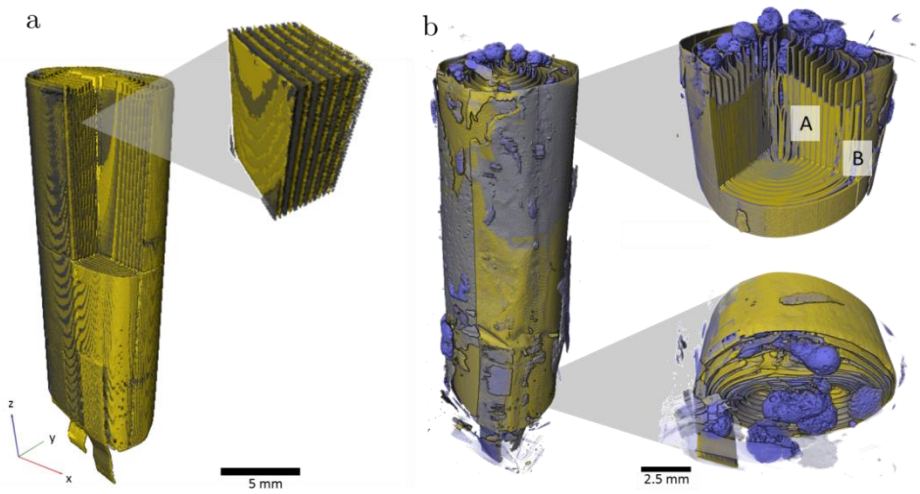

Figure 7-3: (a) 3D reconstruction of the pouch cell in its fresh state. The $LiCoO_2$ electrode is displayed as grey, and the copper current collector and tabs are shown in yellow. (b) 3D reconstruction showing the pouch cell after overcharge-induced thermal runaway. Copper and $LiCoO_2$ phases are labelled as yellow and aluminium is shown in blue. Samples were taken from regions A and B for further analysis using micro-X-ray CT.

Figure 7-4a-d compares the structure of the $LiCoO_2$ electrode before and after thermal runaway. The pixel sizes for the fresh and *post-mortem* tomograms in Figure 7-4 were 0.424 µm and 0.36 µm respectively. In its fresh state the $LiCoO_2$ is coated uniformly onto the Al current collector (Figure 7-4a-b) which is *ca.* 13 µm thick. As seen in Figure 7-4c-d, the Al layer between the remains of the $LiCoO_2$ is highly porous following thermal runaway and cooling. The $LiCoO_2$ layers are much further apart, now *ca.* 40 – 50 µm, which would have aided the escape of gases generated during the thermal runaway process. The high specific heat and thermal conductivity of Al would also have enhanced the heat dissipation of local exothermic reactions leading up to and during thermal runaway. The melting point of Al is 660 °C and hence the distribution of molten aluminium remnants in Figure 7-3 and Figure 7-4 demonstrates that the interior of the cell reached in excess of 660 °C. As seen at the bottom of the cell in Figure 7-3b, only a small portion of the cell in the region of the current collecting tab appears to have reached the melting point of copper (1085 °C). The temperature range between 660 °C and 1085 °C presents the possibility of further decomposition reactions occuring, evidence of

which is found upon further investigation of the individual $LiCoO_2$ particles *post-mortem*.

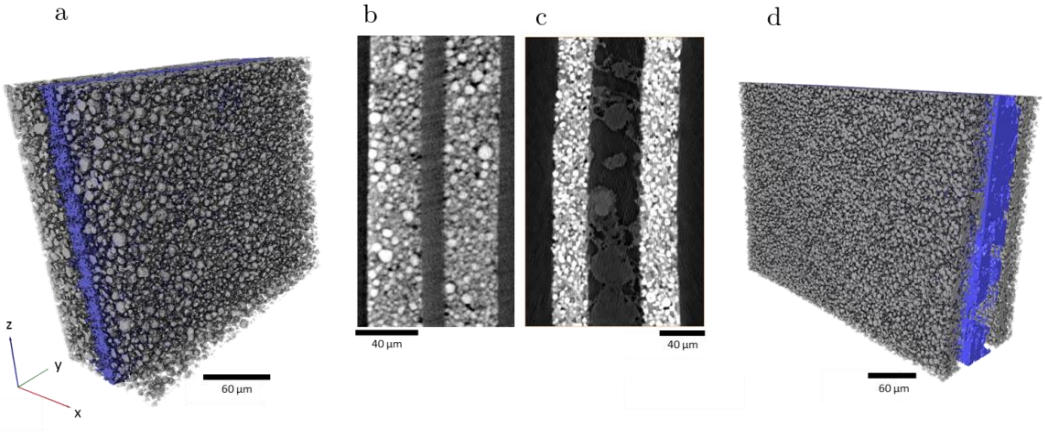

Figure 7-4: (a) 3D reconstruction of aluminium current collector (blue) coated with $LiCoO_2$ (grey) in its fresh state alongside an *XZ* orthoslice (b). (c) and (d) show an *XZ* orthoslice and 3D reconstruction of the current collector and the remains of $LiCoO_2$ after thermal runaway.

7.3.3. Particle Structure Degradation

The size and shape of particles have been shown to play a significant role in the thermal stability of electrode materials and influence the magnitude of catastrophic failure upon thermal runaway[125, 126]. Most decomposition reactions occur at the interface between the transition metal oxide and electrolyte. Larger particle surface area increases the probability of surface degradation reactions; hence, with reduced particle size the specific surface area exposed to the electrolyte increases and the rate at which exothermic degradation reactions occur would be greater. *Post-mortem* micro-CT of the $LiCoO_2$ particles shows severe microstructural degradation (Figure 7-5). Evidence of a surface layer of Co metal on the electrode particles is seen in Figure 7-5a. Figure 7-5b shows a greyscale 2D slice with the highly attenuating Co layer (white) at the surface of the particle. A semi-transparent 3D rendering of the particle (Figure 7-5c) shows the presence of Co (teal) on the surface and Co channels within the particle. As a result of changes in density of materials during decomposition, a reduction in particle volume and delamination of phases is expected to occur. The density of Co metal is almost twice that of

$LiCoO_2$ and accordingly there is evidence of delamination of the Co layer from the bulk of the particle, shown in Figure 7-5(d-e). During thermal runaway, this delamination would have exposed further surface material to exothermic reduction.

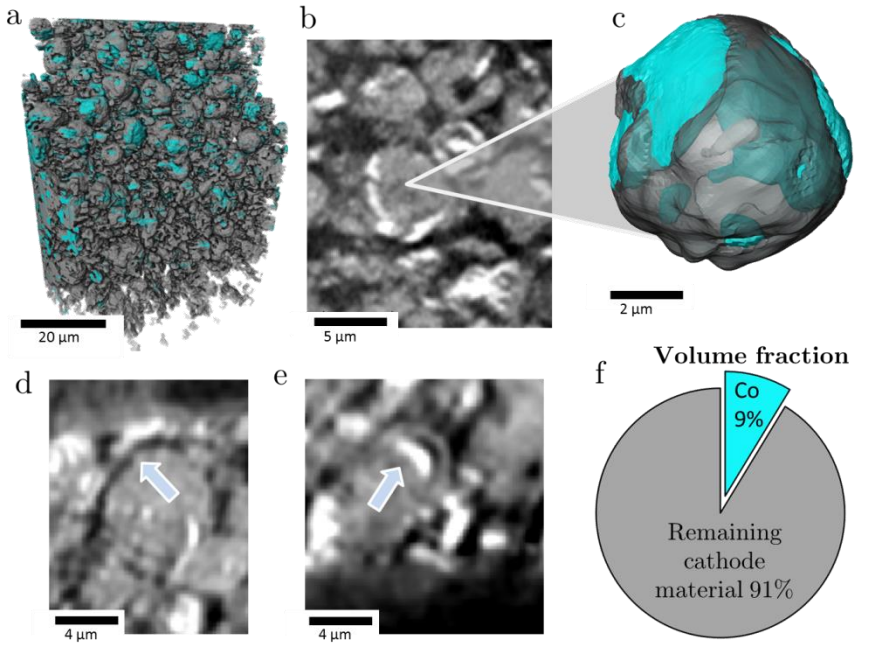

Figure 7-5: (a) 3D rendering of a portion of $LiCoO_2$ electrode showing isolated Co phase (teal); (b) greyscale slice view of $LiCoO_2$ particle showing evidence of phase separation based on attenuation and (c) semi-transparent 3D visualisation of $LiCoO_2$ particle (grey) showing surface and sub-surface presence of Co (teal); (d, e) greyscale slice views showing delamination of Co metal surface layer; (f) 2D representation of the volume fraction of Co within the remaining $LiCoO_2$ electrode material. This sample was extracted from an inner region labelled as A in Figure 7-3.

The decomposition reactions of $LiCoO_2$ to Co_3O_4, CoO and further to Co metal occur at elevated temperatures and in the presence of organic electrolyte at the surface of the particles. For example, at $>$ 150 °C, the following reduction reactions can occur where *solv.* indicates the reaction step occurs in the presence of electrolyte solvent[114]:

$$Li_{0.5}CoO_2 \xrightarrow{>150\,^{\circ}C} 0.5LiCoO_2 + \frac{1}{6}Co_3O_4 + \frac{1}{6}O_2 \tag{7.2}$$

$$Co_3O_4 \xrightarrow{>150\,^{\circ}C,solv.} 3CoO + \frac{1}{2}O_2 \tag{7.3}$$

$$CoO \xrightarrow{>150\,^{\circ}C,solv.} Co + \frac{1}{2}O_2 \tag{7.4}$$

Additionally, CO_2 evolved from degradation reactions (7.1) and combustion reactions of the solvent and separator, could react with any remaining $LiCoO_2$ particles according to (7.5), resulting in additional formation of Co metal. However, with the rapid dissipation of gases, it is likely that the reaction outlined in equation 7.5 contributes less to the formation of Co than the reaction described by equation 7.4.

$$2LiCoO_2 + CO_2 \xrightarrow{>150\,^{\circ}C,solv.} Li_2CO_3 + 2Co + \frac{3}{2}O_2 \tag{7.5}$$

From attenuation coefficients of expected decomposition products (see Section 10.3.2 in Appendices) the composition of the particle surface layer and interior can be inferred; the difference in greyscale between the Co surface layer and the particle interior suggests that most of the particle consists of CoO, which is consistent with previous XRD experiments[114]. The volume fraction of Co metal in the remaining positive electrode material is calculated to be 9 % (Figure 7-5f). SEM images and EDS (Figure 7-6a,b) show that the surface of the particle consists of Co globules rather than the smooth surface presented in Figure 7-5 this is due to the limited resolution of the X-ray CT technique to resolve fine surface features[176]. The surface of the $LiCoO_2$ particles after thermal runaway appears relatively rough when compared to the fresh sample presented in Figure 7-6c, which is ascribed to shrinkage of the Co-oxide as it is reduced, and delamination and agglomeration of Co metal. Additionally, subsurface Co metal seams are present in the tomograms which could also be explained by the infiltration of

electrolyte through micro-cracks and fractures, which could not be resolved in the CT images.

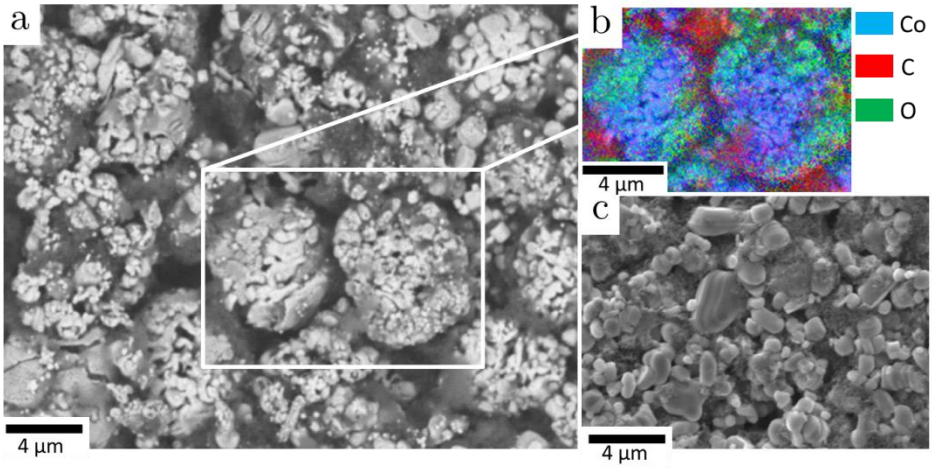

Figure 7-6: (a) Scanning electron micrograph of the $LiCoO_2$ material after overcharge and thermal runaway, (b) EDS of the highlighted region showing that the surface layer consists of Co metal, and (c) SEM microgram of the fresh $LiCoO_2$ particles.

Without excess electrolyte and high temperature ($>$ 350 °C) it is expected that the air-stable Co_3O_4 and CoO would not be reduced to Co[302]. Three samples were taken from subsurface layers (Region A in Figure 7-3b), each of which showed the presence of Co on the surface when analysed under CT; however, a sample taken from the surface of the cell (region B in Figure 7-3b) did not show any presence of Co on the surface of the particles (Figure 7-7). This may have been due to the outer regions having a lower local temperature (due to enhanced heat rejection) and insufficient quantities of electrolyte for the final reduction step to occur.

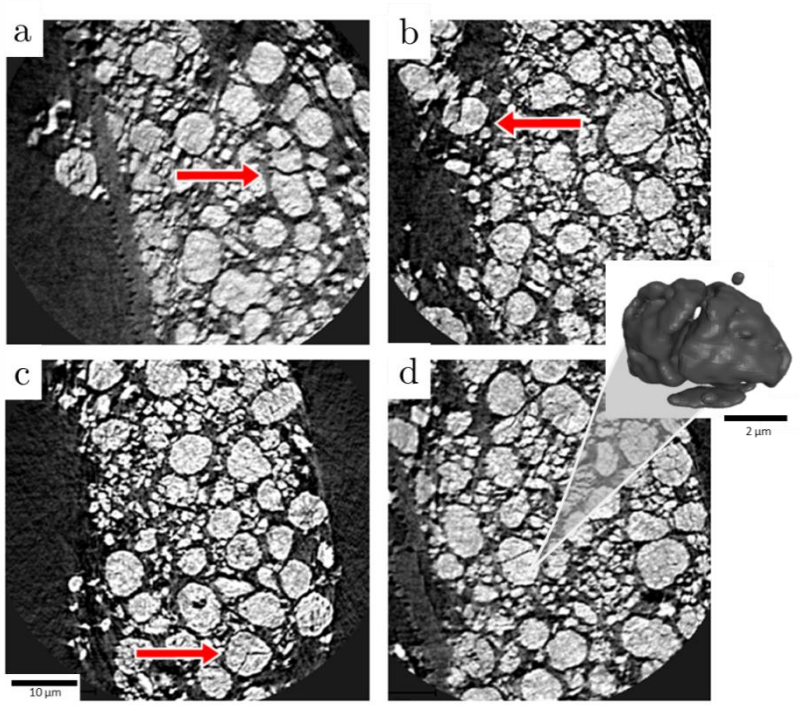

Figure 7-7: (a-d) Orthoslices highlighting cracked $LiCoO_2$ particles. Sample was extracted from the outer region labelled as B in Figure 7-3. Inset: an isolated 3D volume of the cracked particle in (d).

As shown in a previous study[63], temperature gradients of $>$ 700 °C can occur over as little as 7 mm during thermal runaway, where the outer regions of the cell remain relatively cool and the inner regions can reach $>$ 1000 °C. Hence, at the outer regions the conditions (temperature and retention of electrolyte) are less favourable to sustaining the propagation of thermal runaway, making the extent of exothermic degradation location dependent. In contrast to the subsurface samples, the surface sample presented in Figure 7-7 contains numerous fractured particles. As Geder *et al.*[126] demonstrated, a reduced particle size (and increased specific surface area) results in unfavourable consequences, such as a higher rate of heat generation and lower onset temperatures for thermal runaway.

7.3.4. Particle Size Distribution

Mass loss occurs at each reduction step according to equations (7.2) to (7.4), and the electrode particles are expected to reduce in mass and volume, and increase in

density. The particle size distribution (PSD) of a fresh sample is compared with that of both *post-mortem* samples; the inner sample (showing presence of a Co surface layer) and the outer sample (showing significant cracking and the absence of Co). The particle volumes used for the PSD of the three samples were *ca.* 25,000 μm^3 (fresh), 35,000 μm^3 (inner), and 34,000 μm^3 (outer). The PSD for each sample is presented in Figure 7-8. In its fresh state the PSD centres around a mean diameter 3.87 µm with a relatively low standard deviation. There is a significant decrease in the mean diameter of the remaining particles for both *post-mortem* samples to approximately half their original size (to 1.99 µm and 1.97 µm for the inner and outer samples respectively), but the spread of data in the PSD greatly differs (Figure 7-8). The PSD for the inner sample shows a single peak which has shifted below 2 µm, which is due to a combination of particle shrinkage during phase transitions and the presence of significant debris consisting of fractured particles and delaminated Co. In contrast, a bimodal PSD is observed for the outer sample (cracked particles). When compared to the PSD of the fresh sample, the twin peaks correspond to the occurrence of particle cracking, where the majority of the distribution is shifted to a smaller equivalent particle diameter. However, a second peak which consists of particles < 1 µm in diameter contains the highest frequency of particles. This second peak may reflect smaller particle fragments from the fractured larger particles. Due to the limited resolution of the X-ray CT technique, the specific surface area of the particles could not be accurately determined; however, the dramatic reduction in particle size observed between the fresh and outer samples is expected to significantly affect the rate of decompositon of the electrode at elevated temperatures. Additional surface area would be exposed to reaction with the electrolyte and the smaller fragmented particles would exhibit a lower onset temperature[125, 126]. For example, as demonstrated by Jiang and Dahn[125], a reduction in particle size of $LiCoO_2$ from 5 µm to 0.8 µm results in decreased thermal stability, with lower onset temperatures.

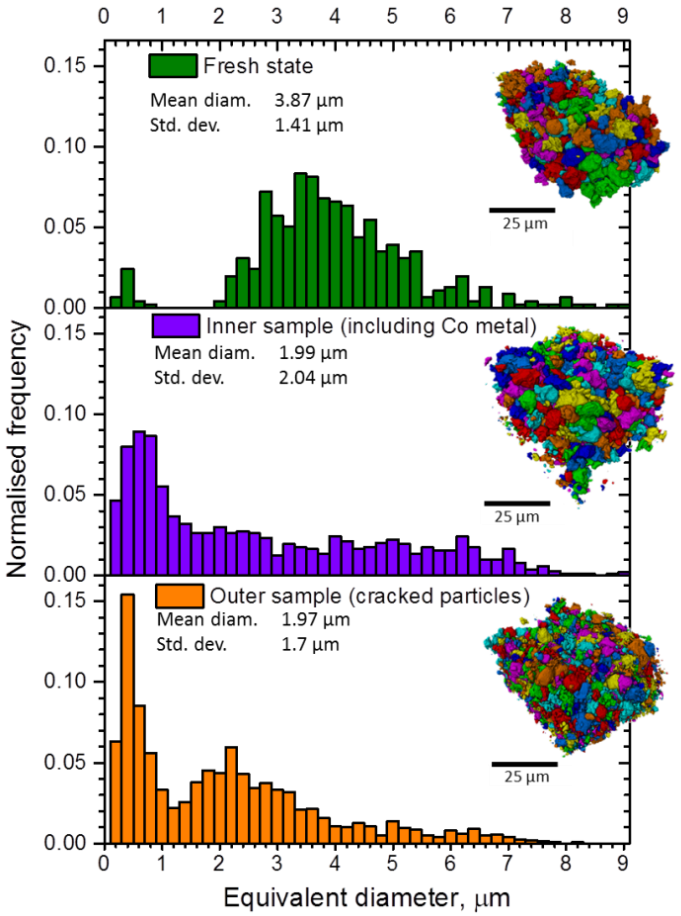

Figure 7-8: Particle size distributions for $LiCoO_2$ particles from a fresh sample (top), a sample taken from the inner regions of the failed overcharged cell showing evidence of complete reduction to Co metal (middle), and a sample taken from the outer region of the failed overcharged cell showing evidence of particle cracking with no formation of Co (bottom).

Although it is well known that the particle shape and size significantly affect the onset temperature and rate of heat generation during thermal runaway, it is not well understood how the evolving microstructure and likelihood of particle fracture influence these properties leading up to and during the runaway process. Further work is required to quantify the change in particle structure based on the conditions to which the particles are subjected, and the effect of initial particle morphology on the rate and quantity of heat generation during thermal runaway are required. As X-ray CT techniques continue to achieve higher spatial and

temporal resolution, the dependence of morphological evolution on particle size, and its consequent effect on the magnitude of failure, could also be explored via *operando* micro-CT. A large particle size with low surface area may provide a more thermally stable electrode, but can also result in a reduction of the cell's power density; hence a balance between battery performance and safety may exist. Understanding the mechanisms through which particle architecture and properties change during thermal runaway is also essential to progress towards an optimised particle size distribution for both performance and safety.

7.4. Conclusions

This comprehensive approach of combined high-speed *operando* X-ray CT and thermal imaging, followed by *post-mortem* multi-scale X-ray CT and SEM analyses, has provided new insights into the failure mechanisms of lithium-ion batteries. The effects of heating and gas generation on the architecture of the cell have been explored during failure via high-speed *operando* tomography, showing electrode layer delamination, gas pocket formation and consequent swelling of the pouch. Multi-scale comparative analyses of the complete cell, as well as separate components of the cell, before and after thermal runaway, have elucidated key phenomena that contribute to the propagation and severity of thermal runaway; the presence of agglomerated aluminium at both ends of the cell demonstrates the effective heat transfer throughout the cell via molten Al during failure.

X-ray CT of the electrode particle microstructures in samples taken from different locations within the cell, presents valuable information on the local kinetics and progress of exothermic reduction reactions at the positive $LiCoO_2$ electrode. The volume fraction of Co, and its presence on the surface of the electrode particles, indicates that the rate of exothermic reduction steps, and therefore heat generation, is dependent on the surface area and PSD of the positive electrode. The extreme thermal and electrical conditions during overcharge-induced thermal runaway cause the particle morphology, and hence the PSD and specific surface area, to change. The results of this work also show that X-ray CT could be

used to elucidate the relationship between electrode microstructure and overall safety of commercial cells.

Over the past two chapters battery failure has been induced by exposing the commercial cells to extreme conditions, thermal and electrical abuse. In real-world applications, these conditions would occur as a result of faulty safety devices and malfunctioning battery management systems. However, there remains the risk of internal short circuiting without any external influence, which is unavoidable and presents one of the greatest concerns to battery manufacturers. This is discussed in more detail in the following chapter.

Chapter 8

Internal Short Circuiting and Venting

8.1. Introduction

The reliability and safety of lithium-ion batteries is of utmost importance for mission critical applications such as in emergency, military and aerospace systems[303, 304]. An understanding of the thermal and structural dynamics associated with internal short circuits would help manufactures develop safer battery designs and modules to avoid and mitigate catastrophic failures. However, the thermal behaviour associated with internal short circuits is not well understood. Currently, the standard test method that is most representative of an internal short circuit is the forced internal short circuit (FISC), which is outlined in the 2015 IEC testing standard[162]. This test involves inserting a Ni particle into the internal electrode windings and forcing a short circuit through crushing; this test and its drawbacks are described in detail in Section 2.6.2. Alternatively, nail penetration tests are also widely used by manufacturers in an attempt to replicate the occurrence of an internal short circuit. However, as discussed in Section 2.6.3, the nail penetration test is not considered to be representative of an internal short circuit, and consequently it is not a requirement in today's safety testing standards. The nail penetration test is recommended by the FreedomCAR and SAND99 testing manuals (discussed in Section 2.6.3), but only to determine how a cell behaves when punctured by an external object. In this work, to examine the various failure mechanisms associated with nail penetrations, tests are carried out at different locations along commercial 18650 cells using a custom designed nail with an integrated thermocouple at its tip. Internal temperatures are linked with

the degradation occurring inside the cell, as observed through high-speed radiography at 2000 fps.

There is need for a reliable test method that replicates the behaviour of an unmodified commercial cell design undergoing an internal short circuit to better understand thermal runaway propagation and evaluate the efficacy of safety devices[305]. Here, an internal short circuiting (ISC) device developed by Keyser *et al.*[157] is implanted inside an 18650 test-cell during its assembly process. Use of the ISC device can achieve an on-demand failure that is representative of a field-failure culminating from a latent defect, allowing insight into cell design vulnerabilities under worst-case scenarios and furthermore, the ability to verify hazard mitigation features for battery modules, containments and suppression systems. Additionally, the provision of internal short circuits 'on-demand' and at a known location allows greater accessibility for analysis of the failure initiation and propagation through the use of X-ray imaging. Until now, capturing the rapid events surrounding initiation and propagation of thermal runaway was left to chance, due to the small field of view associated with high-speed imaging (with sufficiently high resolution). Through the use of the ISC device, the initiation and propagation of thermal runaway resulting from an internal short circuit is captured using high-speed (2000 fps) X-ray imaging at ID19 at the ESRF[184, 208], providing unprecedented insights into the failure mechanisms and the influence of cell design[63] on the safety and efficacy of 18650 cells. The failure mechanism initiated from the ISC device is compared to that resulting from nail penetrations at different locations within the cells.

Furthermore, the venting mechanisms of commercial cell designs are explored using ultra-high-speed radiography imaging (up to 20,272 fps) to capture the most rapid failure events. As discussed in Section 2.6, cell rupture and projectiles present a great risk during battery failure and as revealed in Chapter 6, commercial cell designs can undergo thermal runaway in two ways; either containing the active materials as the reactions run to completion within the cell, or ejecting the electrode assembly and integrated safety devices via cell bursting. Here, the cause of cell bursting and the influence of cylindrical mandrels and their designs on failure mechanisms and associated risks are assessed.

8.2. Experimental

8.2.1. Internal Short circuiting Device

The ISC device was designed to short the negative electrode active material to the positive electrode current collector, bypassing the less conductive positive electrode active material (see Figure 8-1a). This has been suggested by Santhanagopalan *et al.*[154] to be the type of short most likely to result in thermal runaway. To further increase the likelihood of a thermal runaway response, the batch of cells were made with a single layer polypropylene (no shutdown feature) separator.

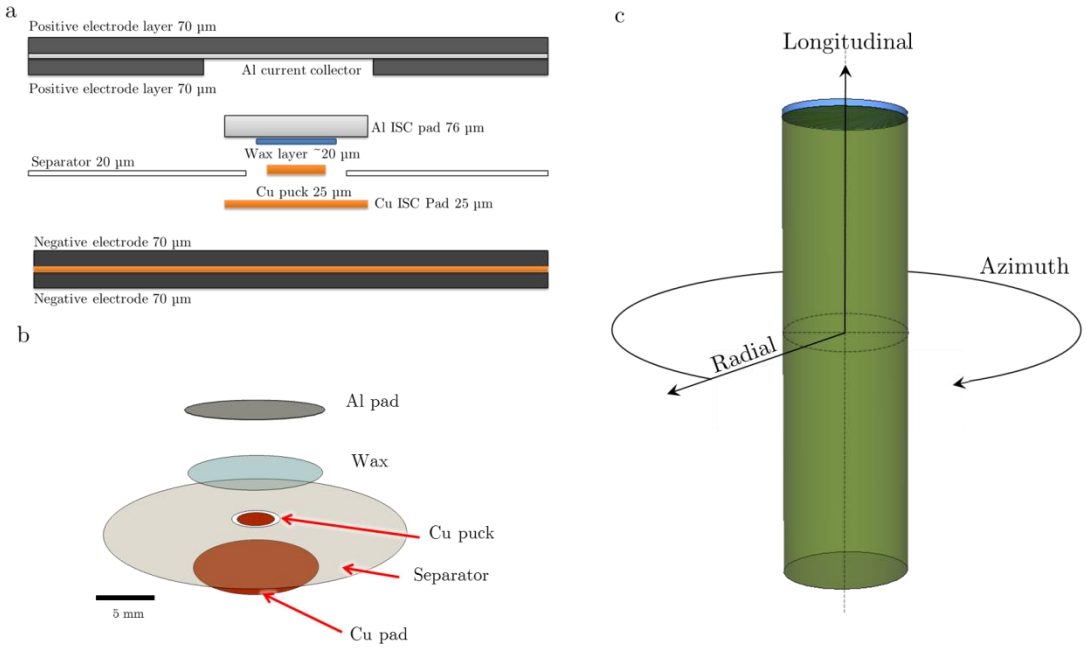

Figure 8-1: (a) Illustration showing the placement of the ISC components between the positive and negative electrodes. (b) 3D representation of the individual components. (c) Coordinate system used for describing placement within cylindrical 18650 cells.

The key component of the device is a thin (10-20 µm) coating of wax that melts at 57 °C and produces a short circuit between aluminium and copper foils (Figure 8-1). A batch of 2.4 Ah 18650 cells (Figure 8-2) was manufactured to maximize the likelihood of on-demand thermal runaway response. The device was

implanted in the dry electrode assemblies at mid longitudinal height (see coordinate system in Figure 8-1c) and 6 winds in from the external surface of the electrode assembly (Figure 8-2). The wax-coated aluminium pad was oriented towards the centre of the electrode assembly. At the designated location for the ISC device, the active positive electrode coating was removed to expose the current collector and to enable proper seating of the device against the current collector. The electrode coating was removed by unravelling the electrode, placing a nylon template with a 9/16" hole on the surface of the electrode layer, and using an acetone-soaked cloth to remove the electrode and expose the Al. To date, this batch of over 50 cells is yielding $>$ 90 % chance of a thermal runaway response. The cell was in its fully charged state at 4.2 V for testing.

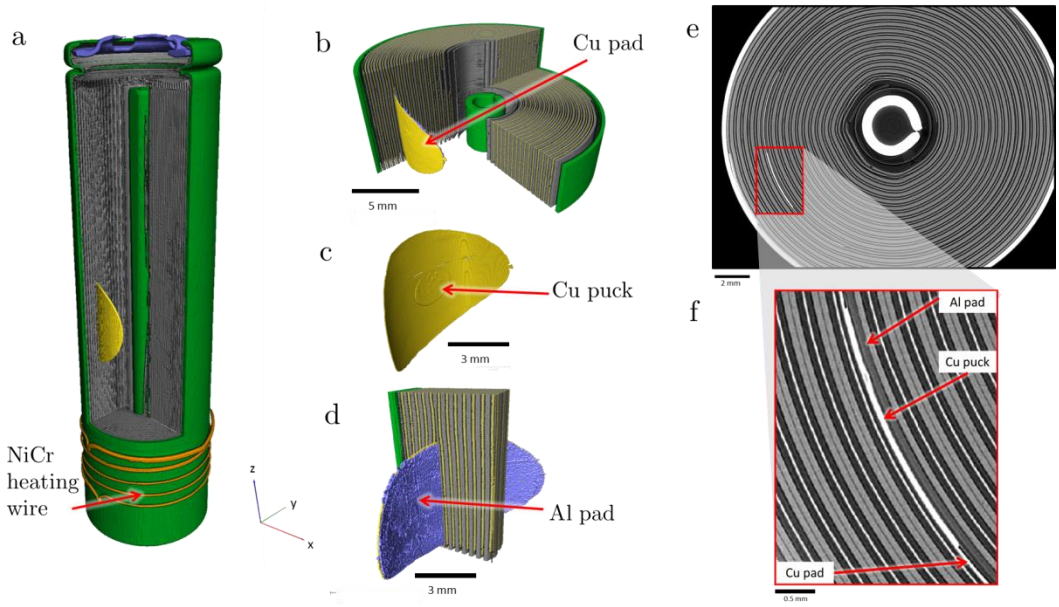

Figure 8-2: (a) Sectioned view from a 3D reconstruction from an X-ray tomogram showing the location of the ISC device within an 18650 battery. The high resistance nichrome (NiCr) heating wire (orange) is also shown. (b) Sectioned view showing the placement of the ISC device between the spiral wound electrodes. (c) Isolated Cu pad and inner puck. (d) A view from the inside of the battery showing the Al pad. (e) Horizontal (XY) slice and (f) magnified section showing the Cu puck separated from the Al pad by a thin layer of wax.

8.2.2. Setup and Heating

As described in Section 3.8.2, a modified nail penetration tester with infra-red and X-ray transparent windows were used as a containment system for this experiment. The batteries were held firmly in place by hydraulic clamps to keep the region of interest in the field of view for the duration of the battery failure. Three different tests were carried out: nail penetration tests, ISC tests, and vent tests. The nail penetration test is first described as precedent for the need of an ISC device to achieve a representative battery failure. The setup and types of cells used for each individual test are described below.

Nail penetration tests: A 4 mm diameter stainless steel nail with an integrated fast response thermocouple at its tip (see Section 3.8.2. for a more detailed description) was used to penetrate fully charged (4.2 V) 2.2 Ah LG 18650 cells (LG ICR18650S3). The 18650 cells were secured by hydraulic clamps at a pressure of 3 bar (as described in Section 3.8.2). The nail penetration test was set to occur at a velocity of 20 mm s^{-1}, however due to the force exerted by the tightly packed 18650 cell's, the velocity of the penetration varied as the nail passed through layers of different mechanical resistance. After penetration the nail was left in the cell for 5 mins before being withdrawn.

Cells with ISC device: A single batch of 2.2 Ah test cells containing an ISC device were manufactured. The test cells were heated using a custom, 12 mm tall, circumferential NiCr wire heater with 5 Ω resistance located at the bottom side wall of the cell (Figure 8-2a). The high resistance coil was connected to a DC power supply that was operated at 10 V and 1.83 A, providing heating power of *ca.* 18.3 W to the cells. After prolonged heating at a power of 16.7 W, the cells in which the ISC device had not activated were exposed to gradually increasing power until activation occurred.

Cells for venting study: The venting mechanisms of five different commercial cell designs were examined via high-speed radiography during thermal runaway. The specifications of the tested cells are presented in Table 8-1. As described in Section 3.8.2, around 33 W of heating power was applied through the use of a 22 Ω resistance coil wrapped around the base of each cell.

Table 8-1: Specifications of lithium-ion batteries used for the nail penetration and vent tests. The voltage at which the cells were tested is also provided.

Type	Positive electrode	Capacity (Ah)	Voltage (V)
LG ICR18650S3	NMC	2.2	4.2
LG ICR18650B4	NMC	2.6	4.2
Panasonic NCR18650B	NCA	3.4	4.2
Samsung INR18650-25R	NCA	2.5	4.2
Sanyo UR18650ZY	LMO and LCO	2.6	4.2

Temperature measurement: The temperature of the surface of the batteries was measured using a thermal camera (FLIR SC5000MB, FLIR Systems France, Croissy-Beaubourg, France), that was separated from the battery failure by a 2 mm thick infrared transparent sapphire window (setup shown in Section 3.8.2). The batteries were painted with a uniform layer of heat resistant black paint with a calibrated emissivity[248] of 0.96 over the range of 40 °C to 180 °C. Thermal images were recorded at a rate of 25 Hz. The thermal camera was calibrated for temperature ranges of 15 °C to 250 °C, and 250 °C to 1500 °C. The former temperature range was used for the ISC and vent tests, whereas the latter (high temperature) range was used for the nail penetration tests.

8.2.3. X-ray CT and Radiography

8.2.3.1. X-ray CT

A full-body tomography of the ISC cell was captured using a lab-based X-ray CT system (Zeiss Xradia Versa 520). A binning setting of 2 was used with 0.4× optical magnification, and the sample to source, and source to detector, distances were 32.2 mm and 79.4 mm respectively, giving a pixel size of 19.82 µm. With an exposure time of 2 s and a source voltage of 160 kV, 2001 images of 1024 × 1024 pixels were used to reconstruct the individual tomograms. Five tomograms along the length of the 18650 battery were reconstructed using Zeiss XMReconstructor software, and stitched together using the Zeiss automatic stitching option.

A higher resolution tomogram of the section of the cell with the integrated ISC device was achieved at ID19 at the ESRF. The cell was imaged using a monochromatic 71 keV beam with a field of view (FOV) of 9.65 mm × 15.20 mm (horizontal × vertical) which consisted of 1302 × 2048 pixels with a pixel resolution of 7.42 µm. This FOV corresponded to half the cell in the horizontal direction. The rotation axis of the sample was located at the edge of the FOV such that by rotating the sample 360 ° it was possible to image and reconstruct the entire sample[294]. 3600 images with an exposure time of 0.2 s, and taken at angular increments of 0.1 °, were used for the reconstruction. A high-speed PCO Dimax (PCO AG, Germany) and a LuAG:Ce scintillator were used for all imaging experiments described here, unless otherwise stated.

8.2.3.2. High-speed Radiography

A polychromatic 'white' beam was used for high-speed radiography in the ID19 beamline of the ESRF[184]. Similar to Chapter 6, a post-event triggering of high-speed recordings was implemented whereby the camera would record continuously until triggered, at which point it would save the 36 GB of prior data recordings.

Imaging conditions for ISC and nail penetration tests: The FOV was 22.89 mm × 14.67 mm (2016 × 1292 pixels) with a pixel size of 11.35 µm.

Radiography of the nail penetration tests was carried out at rate of 2000 frames per second (fps) (with an exposure time of 0.461 ms). For the ISC tests, six samples in total were imaged; samples 1 to 5 were imaged at a rate of 2000 frames per second (fps) (with an exposure time of 0.461 ms), and sample 6 was imaged at 1000 fps (with an exposure time of 0.957 ms). The best radiography view to observe the initiation and propagation of failure from the ISC device was from the side where the Cu puck was placed such that it was parallel with the beam. This orientation gave a clear view of how the failure propagated in the radial and vertical directions.

Imaging conditions for the venting study: Two high-speed imaging modes were used to capture the most rapid failure mechanisms: Mode 1 consisted of imaging at 2000 fps with a field of view of 22.89 mm × 14.67 mm (2016 × 1292 pixels), an exposure time of 460 µs on a GGG scintillator, and a pixel size of 11.35 µm. Mode 2 consisted of imaging at 20,272 fps with a field of view of 18.52 mm × 5.35 mm (816 × 236 pixels), an exposure time of 40 µs on a LuAG:Ce scintillator, and a pixel resolution of 22.7 µm.

8.3. Internal Short Circuit and Propagation

8.3.1. Nail Penetration Tests

To examine the response of cells when thermal runaway is initiated at different locations, nail penetration tests were carried out on 18650 cells placed in three different positions: horizontally being punctured in the middle of the cell, vertically being punctured at a slightly offset position from the centre of the cell, and horizontally being punctured near the crimp and vent components of the cell (Figure 8-3), henceforth to be referred to as ‘Cell 1’, ‘Cell 2, and ‘Cell 3’ respectively. The force required to puncture the three cells was 666 N, 784 N, and 647 N for cells 1, 2 and 3 respectively.

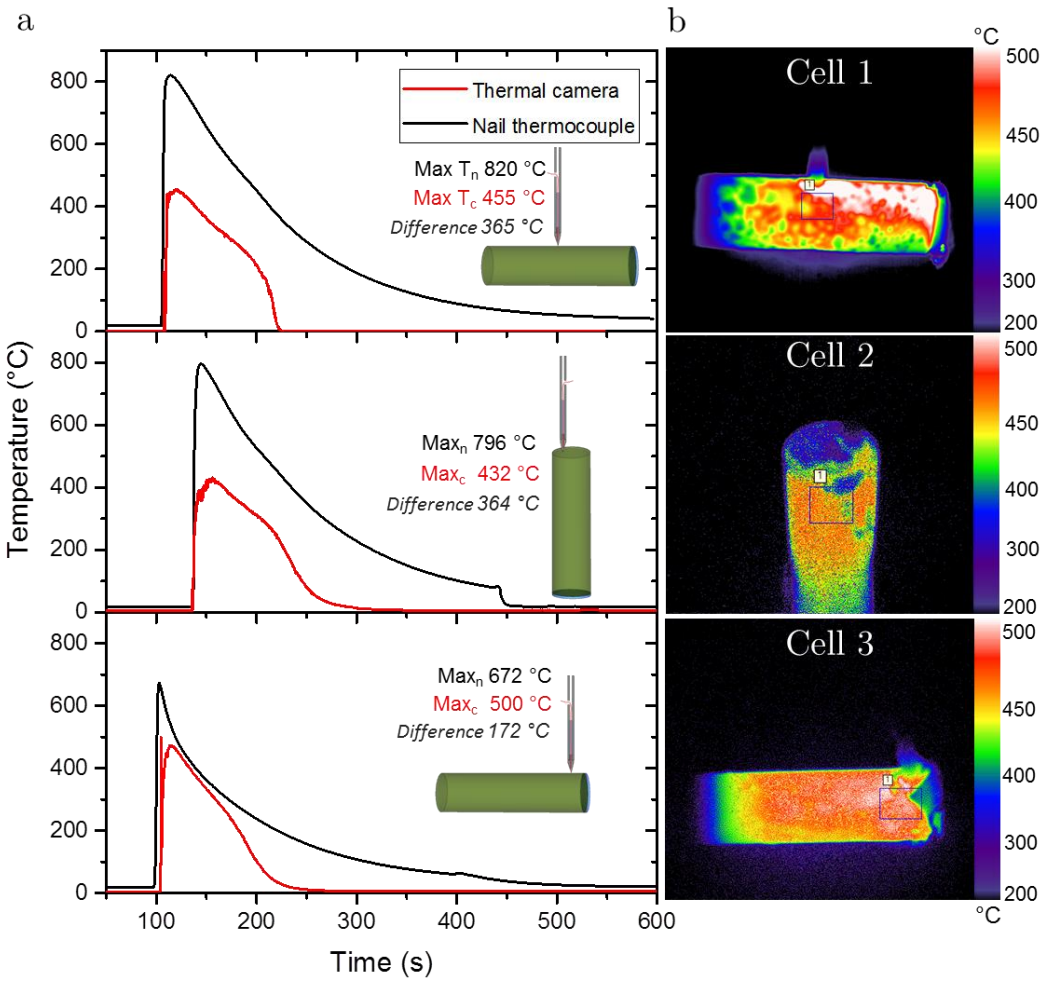

Figure 8-3: (a) Temperature plots showing the difference between measured temperatures inside the cell and on the surface of the cell after being penetrated by a nail at the three locations shown in the inset illustrations. The internal temperatures were measured using a fast response thermocouple integrated into the tip of the penetrating nail. (b) Thermal images taken at the times when the maximum external temperatures were reached. The surface temperature measurement was an average of the areas within the labelled boxes.

A custom-made nail design with an integrated fast response thermocouple at its tip (see section 3.8.2) was used to measure the temperature at the point of initiation within the cells; Figure 8-3a shows the difference between the temperatures measured by the thermocouple inside the cells (black) and the temperature measured on the surface of the cells using the thermal camera (red), where the associated thermal images from the time where the maximum surface

temperature was measured are shown in Figure 8-3b. In Chapter 6, a temperature difference of over 700 °C was observed between the inner and outer windings of the spiral wound electrode assembly; here a temperature difference of up to 365 °C between the tip of the nail inside the cell and the hottest section of the surface of the cell (Cell 1 in Figure 8-3b) is observed.

Contrary to the observation of internal temperatures exceeding the melting point of copper (1085 °C) in Chapter 6, the internal temperature measurements in Figure 8-3 appear to stay below 900 °C. Images from high-speed radiography during the nail penetration tests (Figure 8-4) verify that the copper current collector did not melt, since there is no evidence of the highly attenuating globules that were observed before. As seen in Figure 8-4, in each instance the penetrating nail causes short circuits across multiple layers in the electrode assembly, resulting in the short circuit occurring over a large volume with reduced localisation of heat generation as the cell discharges, which is referred to as a 'soft' short. Furthermore, the conducting steel of the nail is a medium through which short circuiting can occur, and also acts as a large heat sink. Heat from the short circuit is dissipated into the steel and conducted out through the stem of the nail, reducing the local temperatures reached. In each test, the maximum temperature is reached within 5 s after heating begins.

From each of the three tests shown in Figure 8-4, the entire electrode assembly in view is seen to break down, where initiation and propagation occurs from the most outer layer first; thermal runaway propagates in the longitudinal direction from the surface of the nail and initiates along each layer of the electrode assembly as the nail penetrates through, which is most clearly seen as the broadening 'V-shaped' reaction zone between 1.9520 s and 2.1860 s in Figure 8-4a. The temperature profile for Cell 1 (Figure 8-3b) shows that a high-temperature zone spans from the point of penetration to the vent. The cause of this anisotropic high-temperature zone from the point of initiation is revealed in the radiographs, where the nail is shown to block the flow of the broken down electrode material towards the vent, whereas the material on the vent-side is ejected more freely. Therefore, the high-temperature zone is caused by the increased fluidization of the reacting

materials and hence more rapid heat generation and dissipation on the vent-side of the nail.

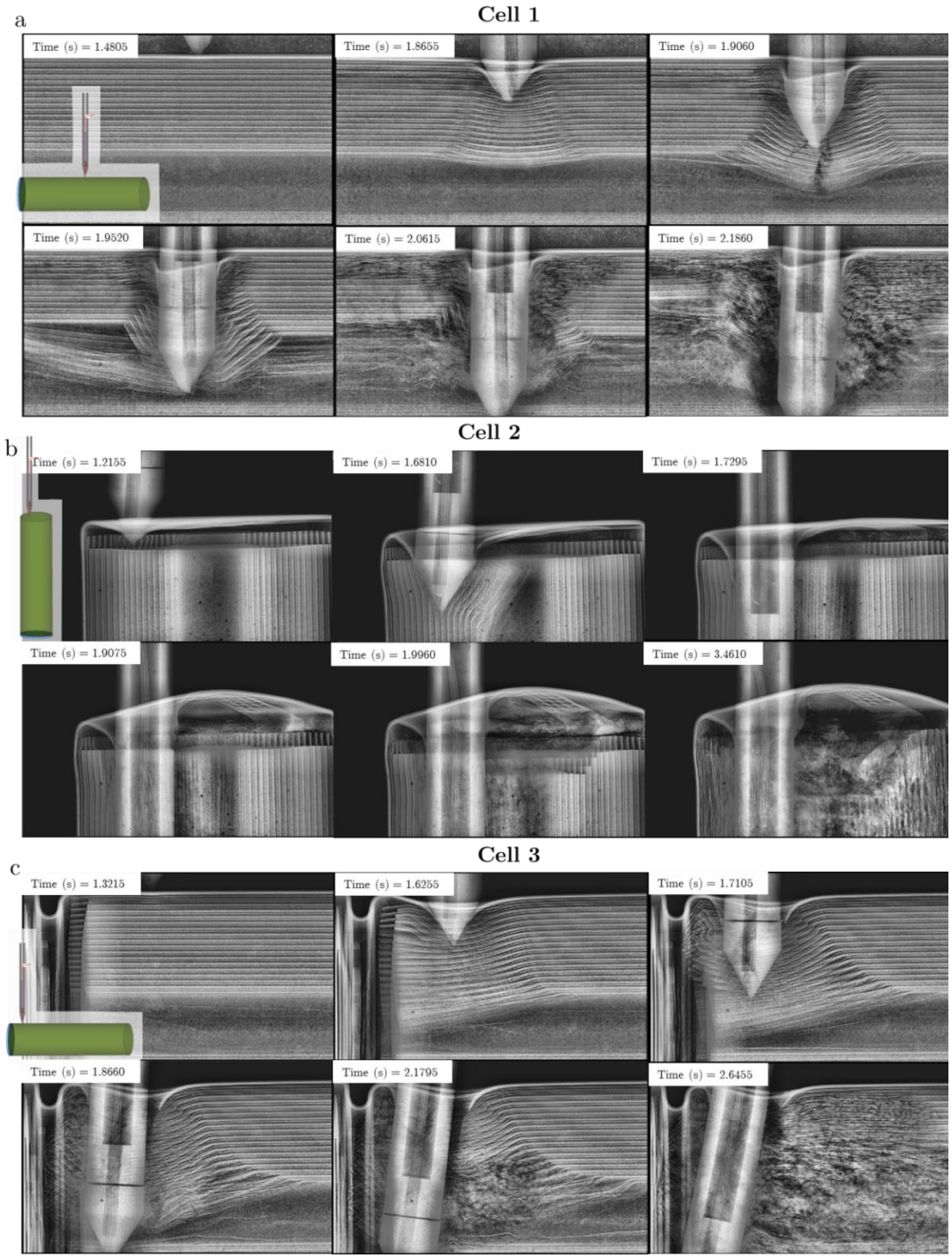

Figure 8-4: Time-stamped radiographs taken during nail penetration tests where the 18650 cells were (a) in a horizontal position being penetrated in the middle, (b) in a vertical position being penetrated at a slightly off-set location from the centre, and (c) in a horizontal position being penetrated near the vent of the cell.

In Figure 8-4b, the nail penetrates Cell 2 in the longitudinal direction, causing short circuiting across few electrode layers but spanning across a wide area. The electrode assembly is pushed into the hollow core and the gases resulting from the initiation and propagation of thermal runaway at the base of the cell cause the cell casing to expand into a convex shape allowing an increased volume of gas to gather there. As discussed in Chapter 6, the initiation of thermal runaway at the base of the cell is expected to cause a rapid local pressure rise, pushing the intact electrode assembly towards the vent and increasing the risk of vent clogging; the radiographs in Figure 8-4b demonstrate that gas builds up at the base of the cell, and as seen between 1.9075 s and 1.9960 s the intact core of the electrode assembly shifts towards the vent of the cell. Between individual radiographs there also appears to be a clear flow of broken down material through the vacant core of the electrode assembly.

The large difference in maximum temperature reached between Cell 3 and Cells 1 and 2, is thought to be primarily due to two factors; increased heat dissipation at the vent, and unidirectional (longitudinal) propagation of thermal runaway. In Cell 3, propagation occurs in one longitudinal direction only (towards the base of the cell) which is expected to result in around half the rate of heat generation that would occur if propagation occurred in both directions, as is the case for Cell 1. Furthermore, in Cell 3 the broken-down and reacting materials have immediate access to the vent and can be ejected soon after detaching from the electrode assembly, dissipating the heat more effectively.

As discussed previously, nail penetration tests are not representative of how a cell behaves when undergoing an internal short circuit. Although the nail penetration test can achieve longitudinal control of where thermal runaway initiates, there is no control in the radial direction. Furthermore, the nail spreads the short circuit across multiple layers and acts as a heat sink at the point of initiation. Internal short circuits occur between two distinct layers where the risk of thermal runaway is dependent on the electrical and thermal conductive properties of the materials involved. Therefore, a more controlled method is required for examining the behaviour of cells during an internal short circuit under highly controlled conditions. Ideally, a testing method that would allow control of the two

materials between which short circuiting occurs, as well as control of the longitudinal, azimuthal, and radial location of initiation, would be employed. The internal short circuiting device, described in Section 8.2.1 can achieve such conditions.

8.3.2. Activation of the ISC Device

When activated, the wax layer separating the positive Al current collector and the negative carbon electrode melts and is wicked by the separator, causing a short circuit between the Al and the carbon electrode. This contact of the active negative electrode material and the positive Al current collector is considered to cause the most detrimental short circuit[153, 154].

As outlined in Section 2.4, short circuits can occur when either the positive electrode, or the positive current collector, make contact with either the negative electrode, or negative current collector. The resulting rate of heat generation is determined by the electrical and thermal conductivities of the materials involved; for example, a short between the positive Al current collector and the negative Cu current collector would provide the most rapid heat generation, but both materials also have high heat conduction properties allowing the heat to be carried away quickly. Whereas a short between the Al current collector and the porous carbon negative electrode (which has high electrical conductivity but poor thermal conductivity due to its porous structure) would incur rapid heat generation but relatively poor dissipation resulting in high a temperature being reached locally, creating the most likely conditions for thermal runaway to occur. The cell being tested was at 100 % SOC.

The Al is isolated from the Cu pad by the separator, except for in the vicinity of the Cu puck (Figure 8-1). A possible pinch point on the separator is observed around the circumference of the Al and Cu pads due to slight misalignment of the pads; this is seen as a slight overlap of the Al and Cu in Figure 8-5.

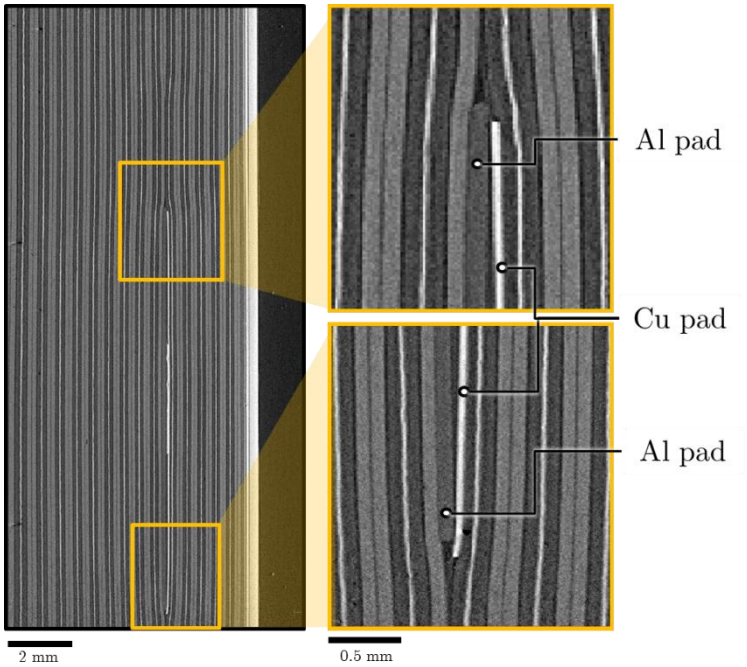

Figure 8-5: *XZ* orthoslice showing a side view of the ISC device, with magnified views of both ends. A slight overlap and possible pinch point is seen at the ends.

The wax layer is expected to melt and the short circuit to occur when the battery reaches 57 °C. Four out of six samples exhibited the expected behaviour (Samples 2 to 5 in Figure 8-6a,b), whereas two samples showed a delayed response and required further heating to *ca.* 100 °C (Sample 1 and Sample 6); it is assumed that for these samples the separator did not wick away the wax from Cu puck. When thermal runaway occurred, the surface of the battery exceeded the maximum calibrated temperature of the thermal camera, which is seen as a plateau in temperature at just below 250 °C in Figure 8-6b,c. The surface of each of the cells exceeded 250 °C in less than 2 seconds when thermal runaway occurred, similar to the results from the model of the short circuit between Al current collector and graphite electrode, developed by Santhanagopalan *et al.*[154].

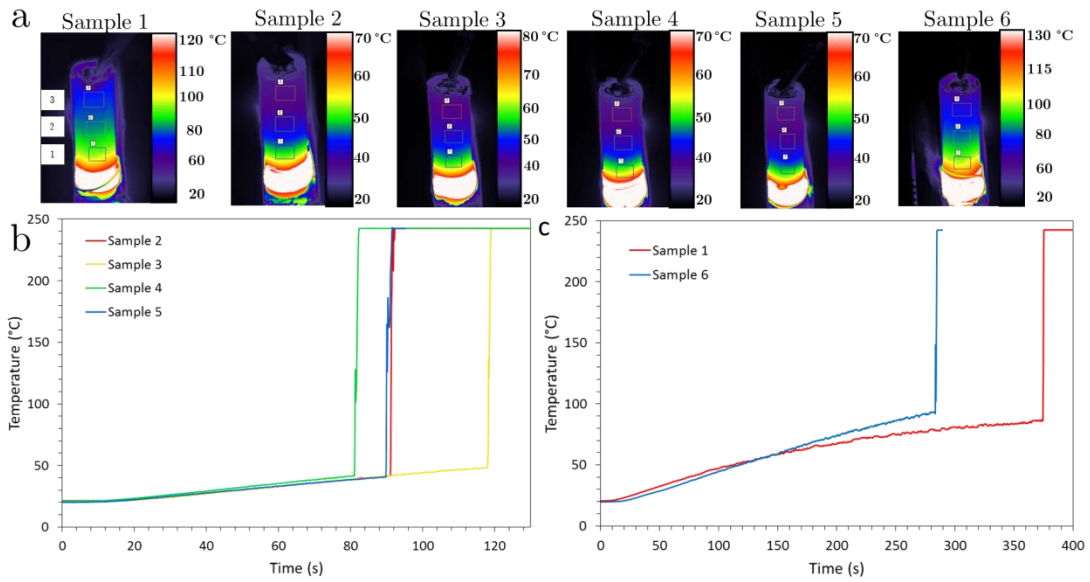

Figure 8-6: (a) Thermal images taken 1 second before the ISC device activates and triggers thermal runaway. A delayed activation occurred for sample 1 and 6. (b) Temperature plots for the cells activated at 50 °C, showing the mean temperature from the surface area of the cell within region 2 (middle square) in the thermal images. (c) Temperature plots for the cells that underwent delayed activation.

8.3.3. Short Circuit and Thermal Runaway

Until now, capturing the initiation and subsequent propagation of thermal runaway proved challenging[63], requiring high-speed and high resolution radiography at the exact longitudinal location to get a clear, side-on view of the occurrence. Consistent failure mechanisms are identified during each of the thermal runaway processes described in this section; different samples are referred to for particular failure mechanisms as radiographs from some samples exhibit consistent phenomena better than others.

Thermal runaway propagates from the outer circumference of the Cu and Al pads (Figure 8-7) rather than the inner Cu puck for each of the samples. However, in samples 1 and 5, there appears to be slight movement around the puck region approximately 0.005 s before propagation of thermal runaway begins at the outer circumference of the pad. This indicates that thermal runaway activates at the puck where local gas generation causes movement of the layers. Shorting then

occurs at the perimeter of the pad, from where the degradation of the active materials is seen to occur most rapidly. It is suspected that due to the separator being pinched between the Al and Cu around the perimeter of the pads (Figure 8-5), the local temperature rise resulting from the short circuit (initiating at the puck) causes shrinkage and strain on the separator. The separator consists of a polypropylene (PP) monolayer that was manufactured by dry processing[266], which involves uniaxial stretching of polymer lamellae resulting in the formation of 'slit-like' pores (described in more detail in Chapter 4); this causes inherent differences in the tensile strength in the machine direction (MD) and transverse direction (TD). When placed in an 18650 cell, the transverse and machine directions of the separator corresponds to the longitudinal and azimuthal directions of the cylinder, respectively. Having the lowest tensile strength in the longitudinal direction, the top or bottom of the pinched separator circumference are the most likely locations for tearing of the separator, and therefore shorting, to occur (Figure 8-7); 5 out of the 6 samples clearly show propagation of thermal-runaway from the top or bottom of the pads. In this case, propagation stems from a short between the Al and Cu current collectors, resulting in rapid discharge of the cell and high rate of Ohmic heat generation locally. The Cu and Al current collectors are seen to melt within 0.003 s after the short initiates (Figure 8-7c) indicating that local temperatures reach in excess of the melting point of Cu ($>$ 1,085 °C).

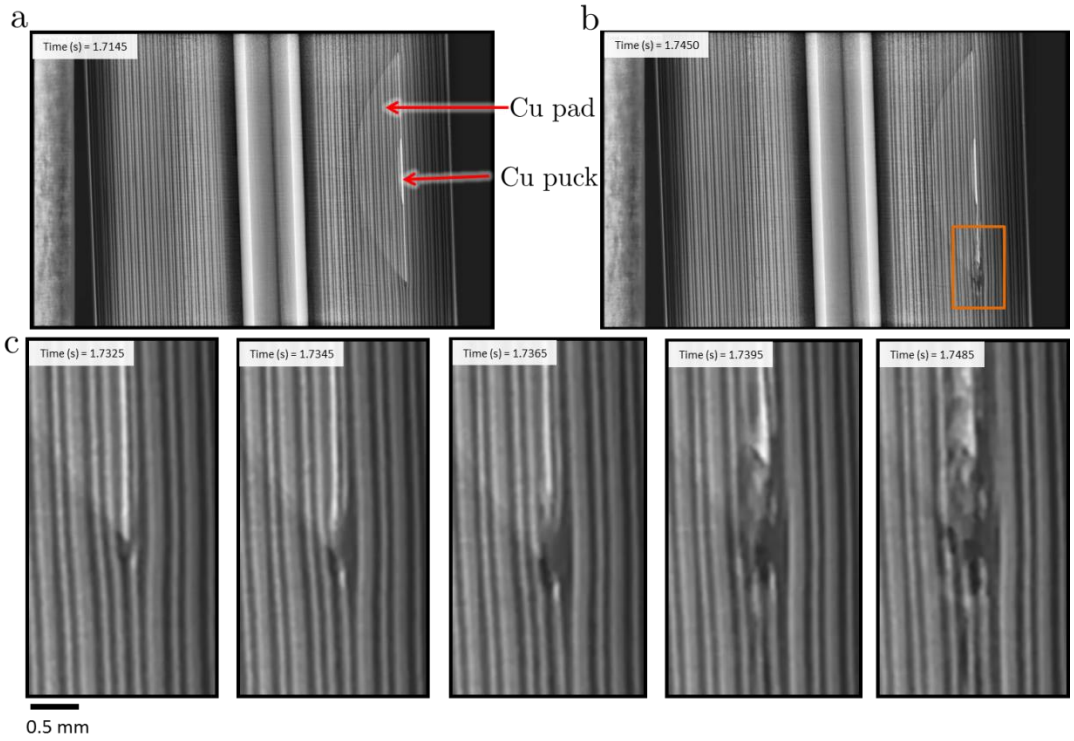

Figure 8-7: (a) Radiograph showing the location of the ISC device within Sample 6. (b) Radiograph highlighting the location from where propagation of thermal runaway occurs (orange square). (c) Time-stamped magnified section of radiographs showing the early stages of thermal runaway propagation.

8.3.4. Propagation of Thermal Runaway

Gas pockets form at either side of the ISC device within 0.05 s following initiation, causing delamination in the longitudinal and azimuthal directions. It is likely that the heat produced from the short circuit caused the electrolyte to vaporise and react with the electrodes. At elevated temperatures the metal oxide (NMC) electrode is reduced by the electrolyte producing further gaseous reaction products[100, 115, 123, 129]. The reaction between the positive electrode material and the electrolyte involves the electrode surface undergoing a series of reduction steps and ultimately ending with the formation of pure transition metals if sufficient electrolyte is present and sufficiently high temperatures are reached[100, 125, 126]. The highly exothermic reaction between the positive electrode material and the electrolyte contributes to the rapid propagation in the azimuthal and longitudinal directions through particle-to-particle propagation. This surface

reaction process would generate gaseous products between the electrode particles, increasing the porosity of the electrode, causing the electrode to delaminate from the current collector, and ultimately helping to fluidize the microstructure as gaseous products are displaced due to local pressure differentials.

The greyscale (and therefore X-ray attenuation) of the positive electrode material in the radiographs reduces rapidly in the longitudinal direction in steps along the radial axis; this is clearly seen in Figure 8-8. The reduced greyscale is most likely caused by an increase in the electrode porosity, and this is soon followed by fluidization and ejection of the electrode material. Delamination of the positive electrode from the Al current collector prior to ejection also occurs in each of the six samples. The propagation of thermal runaway occurs significantly faster in the longitudinal and azimuthal directions (estimated from Samples 1 and 4 to be between 200 – 400 mm/s) than the radial direction (estimated from all samples to be *ca.* 6 - 8 mm/s).

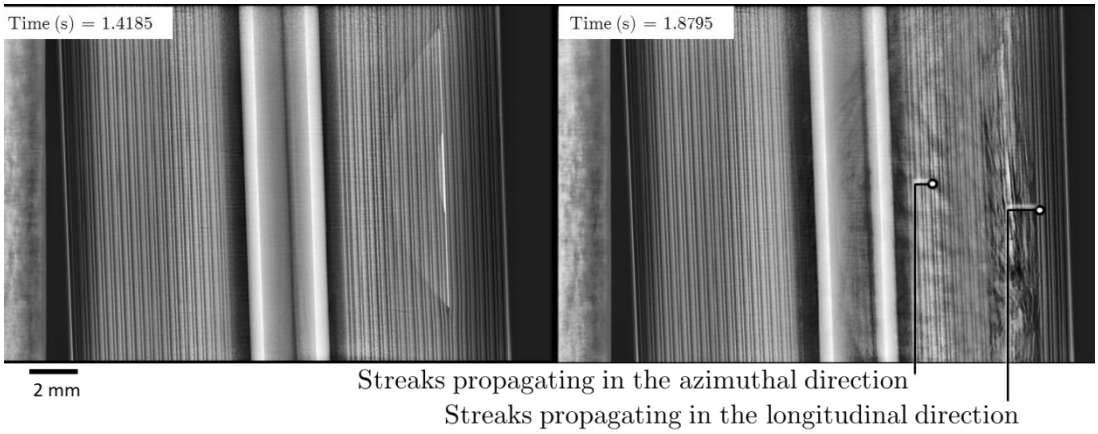

Figure 8-8: The propagation of thermal runaway is observed by the decrease in greyscale (dark streaks) that is observed to propagate more rapidly in the longitudinal and azimuthal directions.

Within the first 0.2 s after initiation, the separator next to the ISC device is observed to snap, causing a jolt in the spiral wound architecture and accelerating the propagation of thermal runaway (Figure 8-9). The pores of the PP separator start to close and the membrane starts to shrink at temperatures below 90 °C, causing strain particularly in the longitudinal direction[306]. Subsequently, the

separator starts to melt at 165 °C. Here, the fracture of the separator is likely to have been caused by a combination of temperature induced strain, and softening at elevated temperatures.

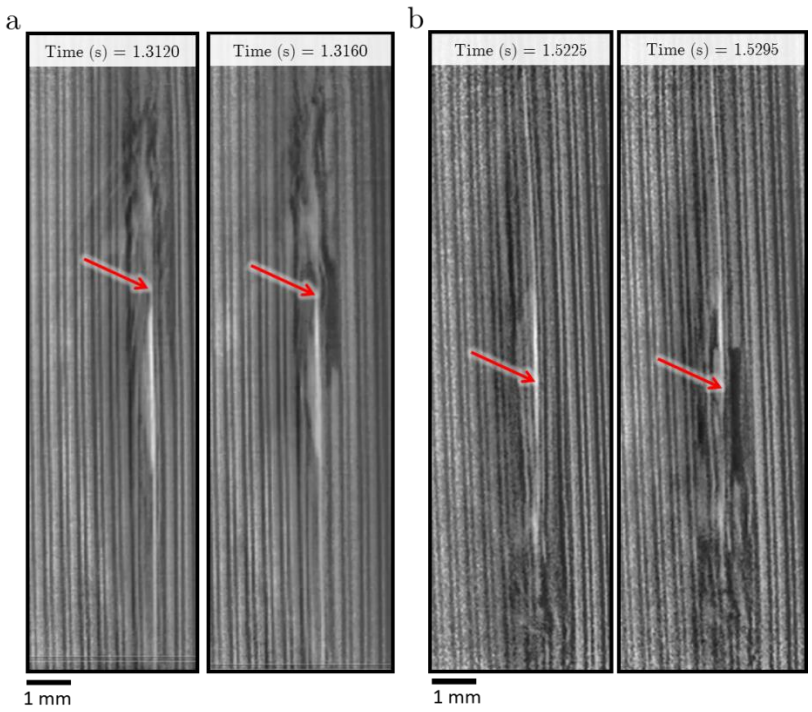

Figure 8-9: Radiographs showing before and after separator fracture for (a) Sample 3 and (b) Sample 5.

Following the initial separator fracture, several additional jolts occur at different locations, but are less severe. In a step-wise manner, thermal runaway propagates radially at approximately equal velocities in both directions, until the active material undergoes significant displacement, at which point the propagation of thermal runaway is interrupted (Figure 8-10). From the ISC device, the propagation spreads across 4 layers in each direction, as shown in Figure 8-10b. The interruption of thermal runaway usually occurs due to large sections of the electrode ejecting or undergoing significant displacement; for example, Figure 8-10b-c show the state of the electrode layer before and after ejection. The rate of propagation significantly decreases when large sections of the heat source (degrading active material) are ejected or displaced.

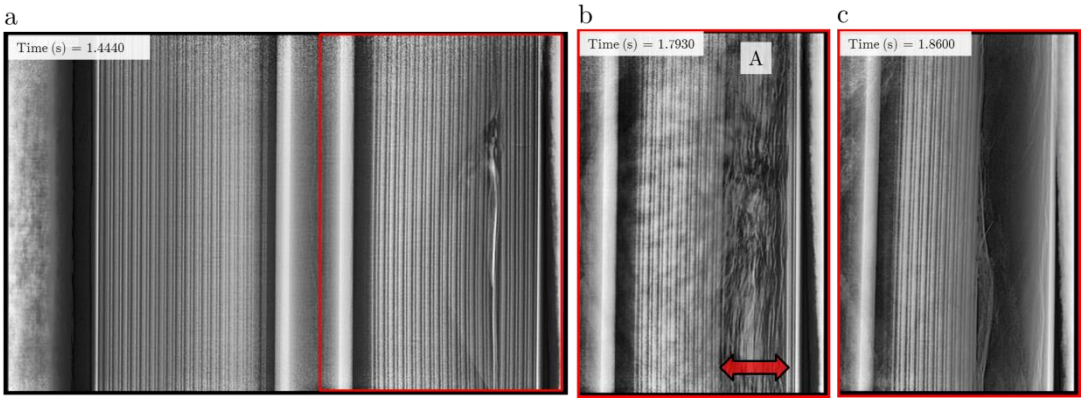

Figure 8-10: Radiographs from Sample 1 demonstrating that from the time of initiation (a), heat transfer and thermal runaway continue radially inwards and outwards (b), until interrupted by detachment or ejection of the active materials (c).

The consistent sequence of events that occur during the propagation of thermal runaway are presented in Figure 8-11a-c. Thermal runaway propagates in all directions from the ISC device, but significantly faster in the azimuthal and longitudinal directions from the point of initiation (Figure 8-11a). Within 0.5 s, the reaction zone (shown as red in Figure 8-11) resembles a hollow cylindrical shape where the reaction zone itself becomes noticeably more fluid-like as gases are generated and the degrading materials begin to lose their mechanical integrity (Figure 8-11b). Within this cylindrically shaped reaction zone, the electrode material remains intact and the central mandrel in place (shown as semi-transparent blue cylinder in Figure 8-11b-d). Kim *et al.*[105] modelled local heat release to resemble a cylindrical cell undergoing an internal short circuit, showing a similar cylindrical reaction zone resulting from fastest propagation in azimuthal and longitudinal directions. Kim *et al.* also predicted that thermal runaway would propagate faster radially inwards than outwards; however, it is not clear in this study whether there is a significant difference between the rates of propagation inwards and outwards.

Prior to ejection, the broken down active materials surrounding the ISC device shift downwards, towards the base of the cell for each sample (Figure 8-11c). The electrode material begins to eject towards the vent of the cell within *ca.* 0.04 s after

the material initially shifts towards the base. It is suspected that ignition of the electrolyte and gaseous products from decomposition reactions[307] (EC/DMC, ethane, hydrogen, methane and oxygen) occurs at the vent of the cell causing a short-lived backflow due to the pressure at the vent building up faster than the gases can escape.

The shift towards the base of the cell is followed by either partial or complete ejection of the cell contents (Figure 8-11d). Before the reaction zone reaches the inner layers of the spiral wound cell, the reacting material begins to eject and disrupt the propagation of thermal runaway. As the reaction zone becomes more fluid-like, the intact core (blue region in Figure 8-11) detaches and moves independently. In both cells that ejected their contents (Sample 2 and Sample 5) the intact core shifts upwards towards the vent and pauses just before the entire spiral wound assembly ejects, similar to what was seen in Chapter 6. This suggests that, as a consequence of the reaction zone weakening the spiral wound architecture, the inner intact core is no longer anchored to the base of the cell, and shifts up towards the vent causing it to block. The pressure within the cell then exceeds the burst pressure of the crimp causing the sudden ejection.

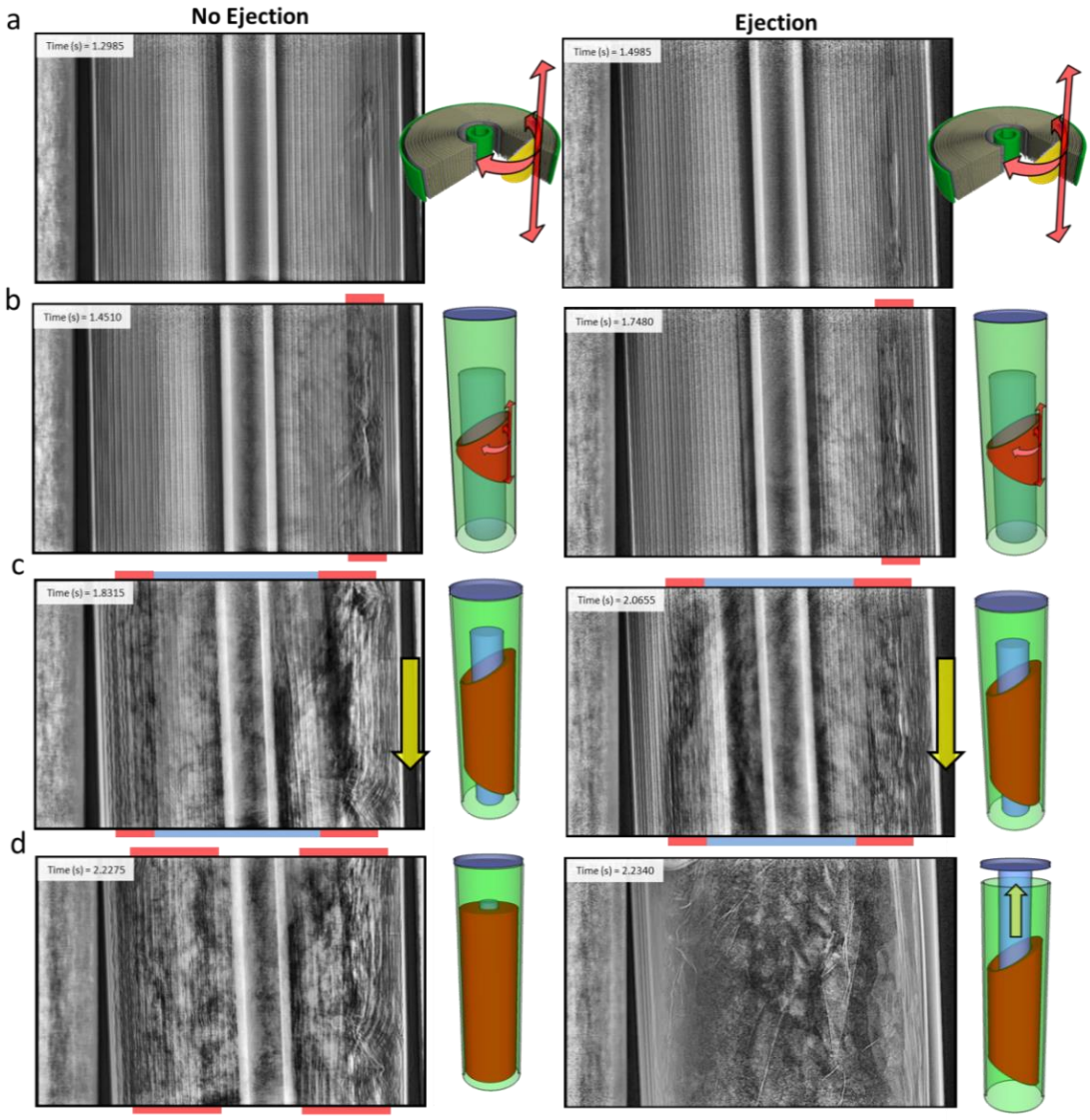

Figure 8-11: Radiographs and 3D illustrations showing the propagation of thermal runaway within the cell resulting in either complete breakdown of active materials within the cell (Sample 3 – left column) or ejection of contents (Sample 5 – right column). Radiographs and 3D illustrations showing that (a) propagation occurs fastest in the longitudinal and azimuthal directions, (b) the azimuthal propagation results in a ring-shaped reaction zone (red) around an intact core (semi-transparent blue), (c) as propagation continues in all directions, the intact core (blue) begins to move independently, and (d) the reaction either runs to completion within the cell, or the intact core shifts up towards the vent which is followed by ejection of the electrode assembly.

8.3.5. Role of the Central Mandrel

The cylindrical mandrel at the centre of the spiral wound electrode assembly plays an important role in the failure mechanism of commercial cells[63]. Numerous mandrel designs have been developed for a multitude and combination of purposes, such as reinforcing cells against crushing and external forces[308], exerting pressure on the electrode assembly[289, 309], preventing collapse, and maintaining an open channel for gases to reach the vent during failure[310]. The mandrel used in the test cell for this study has a hollow core and an opening on one side in the longitudinal direction (Figure 8-12a).

During thermal runaway, the mandrel maintains an open channel from the base to the vent through the centre of the cell (Figure 8-12b,c) creating a low resistance path for gases to flow. Even though there is no indication of degradation reactions occurring around the inner windings, during the propagation of thermal runaway the intact inner layers of the electrode assembly peel away from the bulk electrode assembly and flow towards the vent (yellow arrows in Figure 8-12b). At the same time the mandrel wobbles and shifts position. This indicates that the flow rate of gases through and around the mandrel is enough to shear the electrode layers from the bulk assembly.

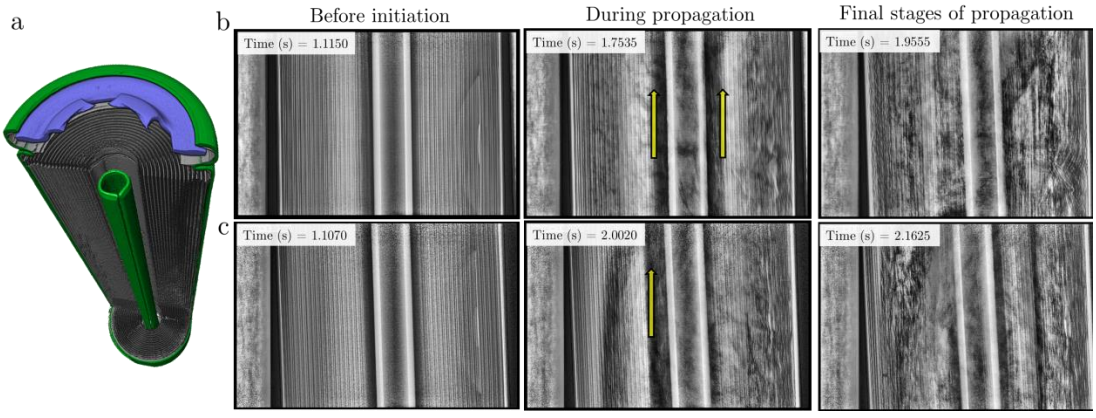

Figure 8-12: Radiographs of (a) Sample 3 and (b) Sample 5, showing an opening forming around the mandrel due to inner spiral wound layers peeling away and ejecting.

As seen in Chapter 6, without an internal mandrel the electrode assembly can collapse, increasing the risk of short circuiting, blocking the flow of gas and increasing the risk of the cell reaching its burst pressure. By preventing internal collapse of the electrode assembly and providing a clear path through which gases can flow during thermal runaway, it is expected that the central mandrel helps reduce the risk of the cell reaching its bursting pressure and hence mitigate unfavourable occurrences such as side wall rupture, and ejection of the electrode assembly. The bursting pressure was reached and the contents ejected in two of the six samples tested here. In both cases, the mandrel shifted up towards the vent immediately before ejection; the mandrel can then lodge into the vent holes as shown in Section 6.3.4. Although the mandrel may lodge into the vent holes, it may still provide a clear path for gases to flow from the base of the cell to the vent (through the centre of the mandrel), it may partially block the vent to degraded electrode material. Being the only component within the cell that maintains its rigidity during thermal runaway, the mandrel may also damage the safety devices and components at the crimp of the cell when forced upwards; this is investigated further in the following section.

Ejection of the electrode assembly prevents the thermal runaway reactions from reaching completion, hence the rate and quantity of heat generation are inextricably linked to the cell venting mechanism and its propensity to rupture or eject its contents. Failure mechanisms such as ejection of contents, side-wall rupture, or full containment during thermal runaway, each pose different risks; the mechanical design of a cell and its propensity to undergo such failures should be considered when assessing their suitability for powering systems. For example, a cell with a high probability of rupturing or bursting, is less favourable in systems where hot ejecta and projectiles may contact otherwise isolated flammable material. On the contrary, it may happen that if thermal runaway runs to completion within an 18650 shell, the local heat generation and risk of cell-to-cell propagation would be greater. Hence, more in-depth studies of the behaviour of specific cell designs under ‘worst-case’ failure scenarios need to be performed to achieve a greater understanding of the cell-specific risk.

8.4. Venting and Vent Clogging

8.4.1. Cell Designs

The failure and venting mechanisms of five different cells from four of the largest 18650 lithium-ion cell manufactures were examined (LG ICR18650B3, LG ICR18650B4, Panasonic NCR18650B, Samsung INR18650-25R, and Sanyo UR18650ZY). The properties of the cells are provided in Section 8.2.2; the five cells represent a broad range of chemistries, capacities and mechanical designs. Figure 8-13 shows the safety features and designs of the LG, Panasonic, Samsung and Sanyo cells. The LG cell (Figure 8-13a and c) has the broadest CID vent disk whereas the Sanyo cell (Figure 8-13e and g) appears to have the smallest vent and the smallest area through which escaping gas can pass. The CID vent disk in the Samsung cell (Figure 8-13f and h) contains two weakened notches that are most clearly seen in Figure 8-13f, which are thought to facilitate two stages of venting. The first CID notch breaks and allows the slow release of gas, and the second notch breaks when more vigorous gas generation occurs and increased fluid escape is needed. Unlike the LG, Panasonic and Sanyo cells, the Samsung cell does not appear to contain a PTC device which is most likely to facilitate its high rate capability (20 A continuous discharge and 4 A continuous charge, according to manufacturer's specifications).

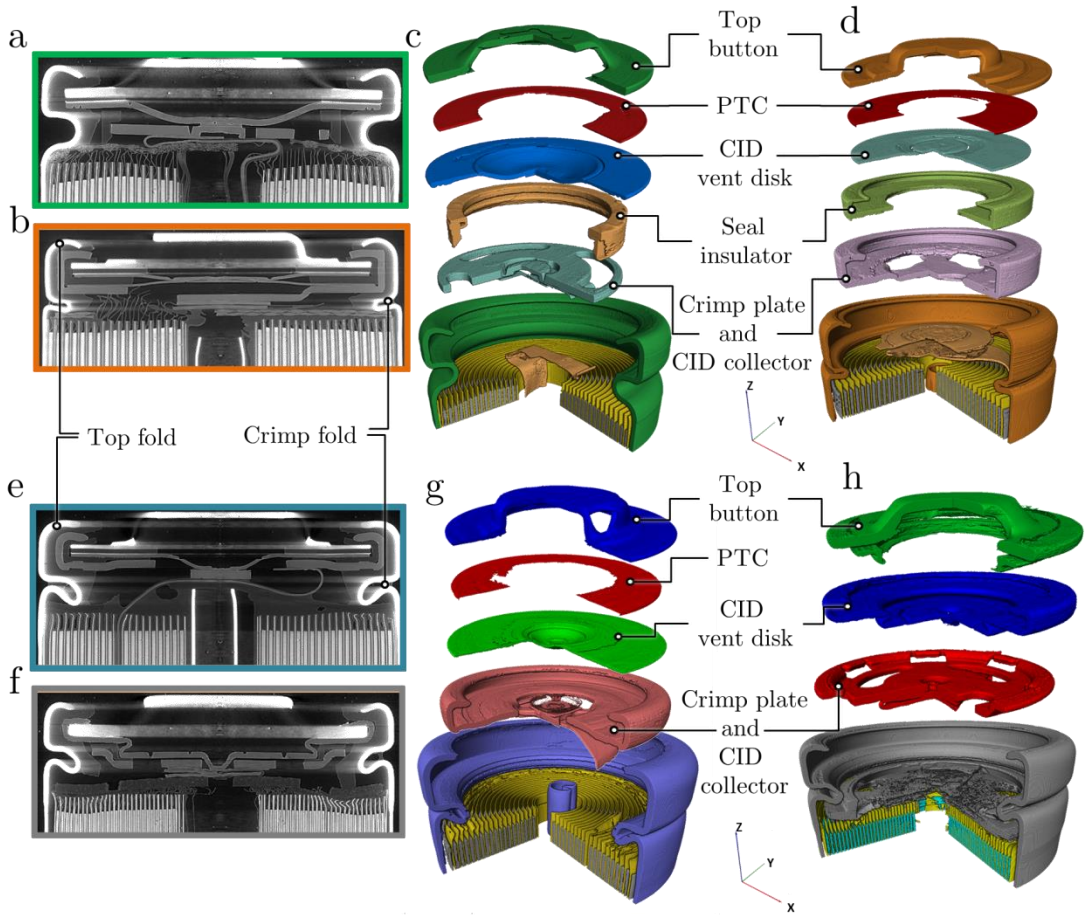

Figure 8-13: Greyscale *XZ* orthoslices from (a) LG ICR18650S3 and (b) Panasonic NCR18650B. Exploded 3D reconstructions of (c) LG ICR18650S3 and (d) Panasonic NCR18650B, showing the placement of the integrated safety devices. Greyscale *XZ* orthoslices from (e) Sanyo UR18650 ZY and (f) Samsung INR18650-25R. Exploded 3D reconstructions of (g) Sanyo UR18650ZY and (h) Samsung INR18650-25R, showing the placement of the integrated safety devices.

As seen in the orthoslices in Figure 8-13, the Panasonic cell contains the shortest length within its crimp fold (the fold of the cylindrical casing around the integrated safety devices). Since the crimp fold tends to stretch as a result of rapid pressure rise during thermal runaway, its architecture is what determines the volume of gas that can accumulate within the cell before it bursts, as well as the bursting pressure itself. The Sanyo and Samsung cells appear to have similar crimp styles with a deep fold into the cylindrical core of the cell, and the LG cells have the thickest wall with a shallow fold.

In Section 8.3.3, the characteristic event that preceded the cell bursting was an intact section of the electrode assembly detaching from the bulk and shifting towards the vent, which was thought to thereafter cause vent clogging. Through numerous repeat tests, characteristic failure mechanisms that determine the outcome and risk of lithium-ion battery failure are identified in the following section.

8.4.2. High-speed Radiography

Panasonic cells: Ten Panasonic cells in total were tested; two cells maintained their crimp structure but the central mandrel punctured through and escaped the cell (Figure 8-14a), whereas eight cells burst and ejected their electrode assemblies (Figure 8-14b). Most cell failures occur over a time span where radiography at 2000 fps is sufficient to capture the dynamic events, but the process of cell rupture occurs over around 0.01 s which is beyond the capability of 2000 fps to capture certain short-lived events. To capture the stages of cell rupture and vent clogging, the cell was imaged at 20,272 fps with a smaller field of view.

At the initial stages of thermal runaway (within 0.1 s from initiation), the cylindrical mandrel within the Panasonic cells shifts upwards and presses against the CID current collector (Figure 8-14a at 1.97 s). The CID current collector stretches and breaks, allowing the mandrel to pass through and press against the underside of the top button (Figure 8-14a at 2.066 s). The intact inner layers of the electrode assembly also shift upwards against the crimp components when the mandrel punctures through the CID vent and CID current collector. The gases within the cell then have a direct path through the mandrel from the base of the cell to the vent. It is expected that the crimp and top button of the cell reach temperatures $>$ 700 °C, reducing the tensile strength of the steel top button. The cylindrical mandrel then punctures the top button and ejects from the cell as a high-velocity hazardous projectile, leaving a large hole in the vent for rapid gas release thereafter (Figure 8-15a).

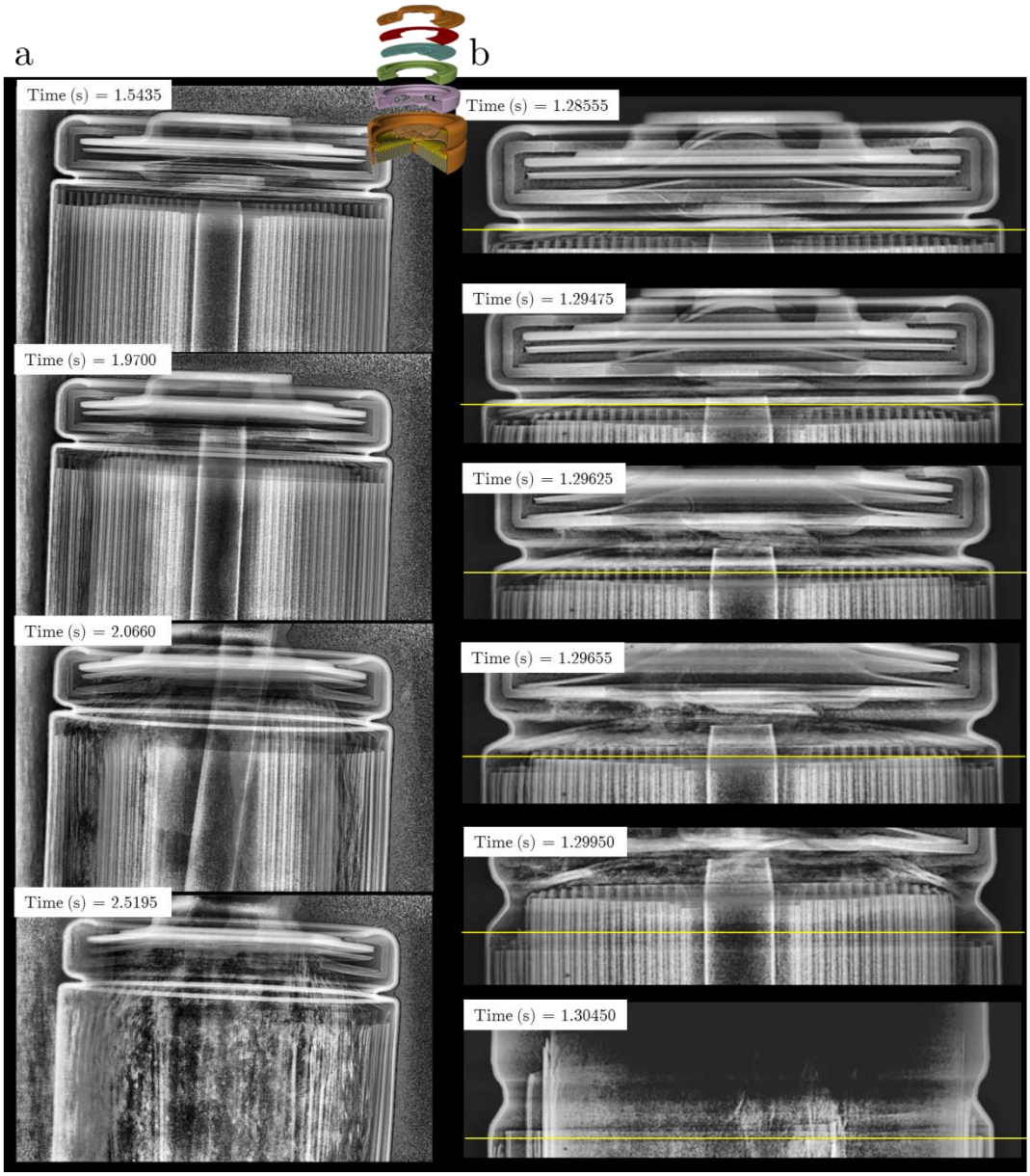

Figure 8-14: Radiographs of the Panasonic NCR18650B cell taken at (a) 2000 fps, and (b) 20,272 fps. The radiographs capture two different failure mechanisms, where (a) the central mandrel breaks through the top button, independently ejecting, and the remaining active materials degrade within the casing and (b) the cell bursts due to the central mandrel and electrode assembly clogging the vent, and the contents eject. A yellow reference line is placed on each image to highlight the displacement of the crimp and crimp components away from the base of the cell.

When compared to the scenario where the cell bursts, the two main differences in the lead-up to the mandrel ejection (without bursting) are that the crimp fold does not straighten/extend, and the mandrel moves independently from the electrode assembly. In Figure 8-14b, the crimp fold of the Panasonic cell is seen to straighten without any influence of the electrode assembly. The cylindrical mandrel vigorously wobbles between individual radiographs, indicating a high flow rate of gas through the centre of the electrode assembly. A gas pocket accumulates directly beneath the CID vent which bends the top button and CID vent plate. However, the top fold (refer to Figure 8-13) continues to hold the crimp plate until the mandrel and electrode assembly both shift up into the crimp region, blocking the gas flow and clogging the vent. The top fold then releases the crimp plate and the cell bursts. The *post-mortem* photograph in Figure 8-15b shows that the top fold was completely straight after rupture, indicating that it was the crimp and top fold that determined the bursting pressure of the cell. During the shift of the electrode assembly, it shears against itself directly beneath the internal crimp fold. There appears to be a 'no-slip' zone directly against the wall of the 18650 casing.

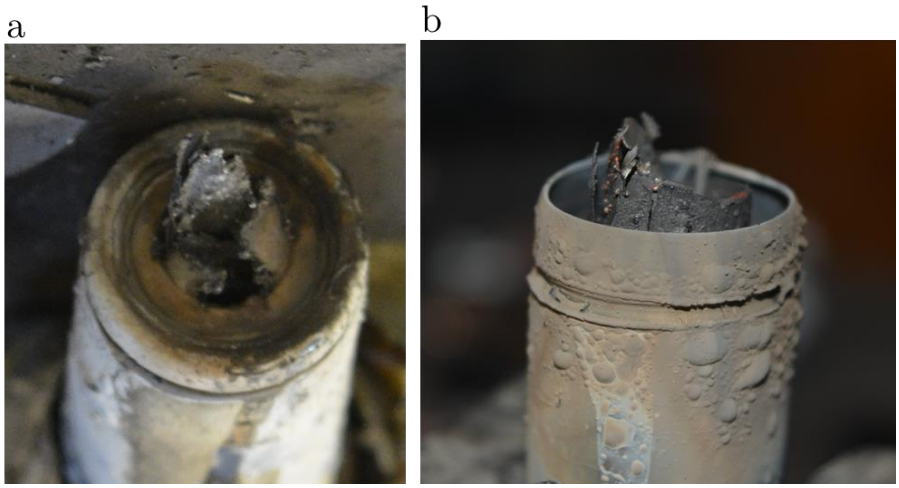

Figure 8-15: *Post-mortem* photographs of the Panasonic NCR18650 cells after undergoing thermal runaway where (a) the cylindrical mandrel punctured the top button and (b) the cell burst.

Samsung cells: Eight Samsung cells (Figure 8-1h) were also examined, four of which exhibited slow propagation of thermal runaway and four that burst. The Samsung cells do not contain an internal cylindrical mandrel, and consequently one of the first signs of the influence of gas generation between the spiral wound layers leading up to thermal runaway is the shift and the swell of the electrode assembly into the hollow core (Figure 8-16a). For the cell failure presented in Figure 8-16, thermal runaway appears to initiate 7 winds in from the casing wall, which is observed from the split in the longitudinal direction of the electrode assembly at 1.7950 s in Figure 8-16a; this split would also travels along the azimuth of the electrode assembly. However, as also observed in Chapter 6, thereafter the propagation mostly occurs from the inner winds of the electrode assembly (at 1.9105 s in Figure 8-16a). This is thought to occur due to the high flow rate of gas passing through the centre of the cell towards the vent, distorting and peeling the inner layers causing soft short circuits and a temperature rise at the core (also seen in Section 8.3.3).

The top button of the Samsung cell consistently melted at early stages of thermal runaway, which indicates that Samsung use a relatively low melting point alloy for the top button that provides additional clearance for escaping material (Figure 8-17a). In the instance where the cell did not burst, thermal runaway ran to completion within the cell and evidence of molten copper is seen throughout the cell at 2.5235 s in Figure 8-16a.

Figure 8-16: Radiographs of the Samsung INR18650-25R cell taken at (a) 2000 fps, and (b) 20,272 fps. The radiographs capture two different failure mechanisms, where (a) the active material mostly reacts within the casing and (b) the cell bursts due to the electrode assembly clogging the vent, and the contents eject. A yellow reference line is placed on each image to highlight the displacement of the crimp and crimp components away from the base of the cell.

Figure 8-16b shows the critical moments leading up to the bursting of a Samsung cell. In contrast to the Panasonic cell, the electrode assembly of the Samsung cell is seen to block the flow of gases through the vent. The unsupported

spiral wound structure shifts up towards the vent and the assembly converges into the vacant core as it pushes past the crimp fold, blocking the path of outflowing gases. The rigid crimp fold of the Samsung cells provides much greater resistance to straightening, and does not provide as clear a path for the electrode assembly to pass upon ejection. It is seen in Figure 8-17b that the top fold of the Samsung cell is not completely straight but still curled into the cell; this indicates that the bursting pressure of the cell was determined by the flexural strength of the crimp components rather than the strength of the crimp and top fold. The vent disk and the crimp plate of the Panasonic cell provided greater flexural strength than the Samsung components, the top button of which was shown to melt at early stages of thermal runaway.

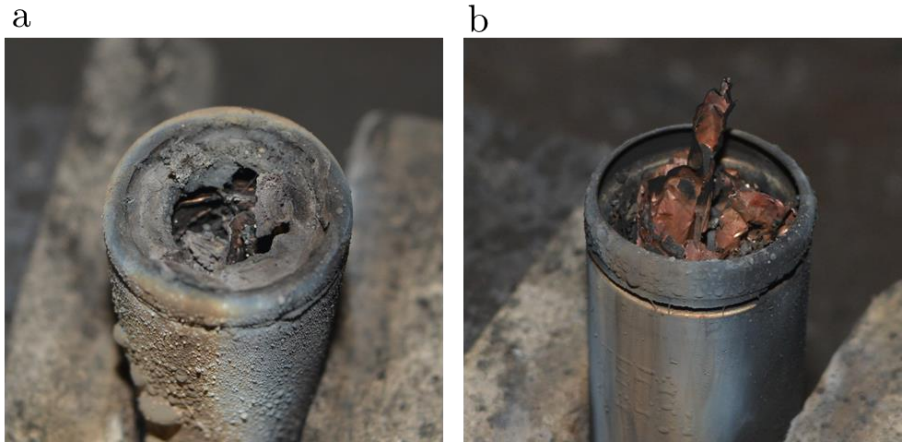

Figure 8-17: *Post-mortem* photographs of the Samsung INR18650-25R cells after undergoing thermal runaway where (a) the top button melted and (b) the cell burst.

LG and Sanyo cells: Five of each of the LG 18650B3, LG 18650B4, and Sanyo UR18650Z cells were also tested. Thermal runaway ran to completion without bursting in all cells except one LG 18650B4. Figure 8-18 presents a side by side comparison of the venting mechanisms of the cells during thermal runaway. In each of the tests the 2.2 Ah LG 18650B3 displayed a controlled release of broken-down material. In each instance, the unsupported electrode assembly started to peel from the inner layers out, creating a 'V' shaped structure as seen in Figure 8-18. The broken down material accumulated beneath the top button but did not appear to

hinder the release of generated gases. The LG 18650B3 is a 2.2 Ah cell, which is expected to generate the least amount of gas of all tested cells, according to the recent report from Sandia National Labs that estimates 1.8 L of gas is generated per Ah of an NMC cell[128].

The LG 18650B4 contains the same NMC chemistry but has a 2.6 Ah capacity and cylindrical mandrel to support the core of the spiral wound electrode assembly. The efficacy of the cylindrical mandrel in improving the safety of the cells can be assessed by making a direct comparison between the failure mechanisms of the LG cells with and without its presence. For example, the primary role of central mandrels is to prevent the collapse of the electrode assembly upon venting and to aid the flow of generated gases towards the vent. The LG mandrel design contains a slit along its entire length with an indent at its top and bottom. The slit along the length of the mandrel allows gas to enter the mandrel at any depth within the cell, from the bottom to the top. The indent at the top of the mandrel allows gas to escape the mandrel channel and leave via the holes in the top button, which appears to be particularly beneficial when the mandrel pierces through the crimp plate and CID, and presses against the underside of the top button, as shown after 1.615 s in Figure 8-18. When compared to the 2.2 Ah LG cell, the mandrel is clearly beneficial in preventing the build-up of debris underneath the top button, providing a clear path for the gas to escape from deep within the cell.

The Sanyo cell contains a similar mandrel design and behaves in a similar way to the LG cell during thermal runaway; the mandrel shifts towards the vent, breaks through the crimp plate and CID, and presses against the underside of the top button. However, the propagation of thermal runaway is significantly slower than all other cells; this is most likely an attribute of the Sanyo cell containing the more thermally stable LMO electrode composition.

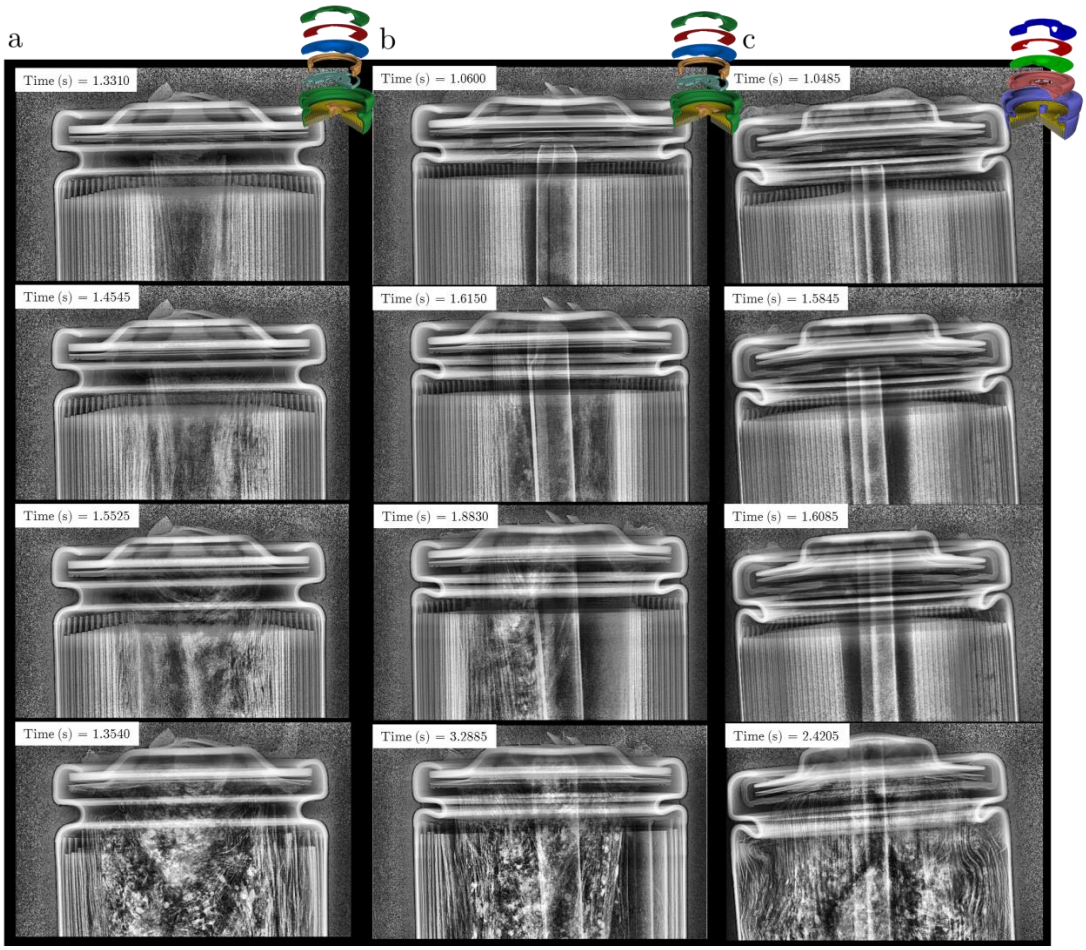

Figure 8-18: Radiographs taken at 2000 fps showing the venting process of (a) LG 18650B3, (b) LG 18650B4, and (c) Sanyo UR18650ZY cells during thermal runaway. The LG 18650B3 and LG 18650B4 have the same vent design, but LG 18650B4 contains an internal cylindrical mandrel that is seen to break through the CID vent during thermal runaway.

As seen in Figure 8-19, the top button of each of the LG cells as well as the Sanyo cell remains intact after thermal runaway. In addition, there was no indication that the cells were approaching their bursting pressure during the thermal runaway process; the crimp folds did not straighten/extend, nor did the crimp components appear to bend. The wide vent disks appeared to provide sufficient flow of reacting components and gases, while high flexural strength of the crimp and the crimp components helped maintain the mechanical integrity of the casing and contain the reaction process.

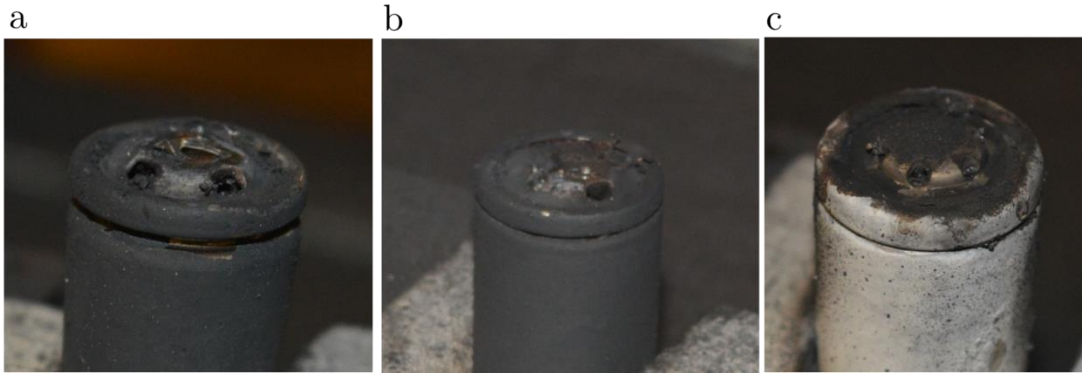

Figure 8-19: *Post-mortem* photographs of (a) LG 18650B3, (b) LG 18650B4, and (c) Sanyo UR18650ZY cells after undergoing thermal runaway. The top button and crimp of each cell remained intact.

8.4.3. *Post-mortem* CT and Mandrel Escape

Typically, the failure of 18650 cells is characterised depending on whether the cell bursts or not. However, it has been demonstrated here that an additional failure mechanism can occur where the internal cylindrical mandrel can pierce the crimp components and escape the cell as a single, high velocity, rigid projectile. This type of failure presents significant risks and would cause the cell to fail some international testing standards such as the UL thermal abuse test described in Section 2.6.1, where the cell fails to pass the test if a projectile punctures an external mesh. Consequently, the process of mandrel piercing needs to be better understood.

Two instances of where the cylindrical mandrel pierced and wedged into the top button were captured using X-ray CT and are presented in Figure 8-20a and Figure 8-20b. In both instances the surrounding area of the top button where the mandrel pierced shows globular features indicative of the steel being previously in a molten state. Additionally, the ends of the mandrels appear to be distorted, most likely from the force that they applied to the underside of the top button. In the previous section, the mandrel is seen to puncture through the crimp plate and vent indicating that at that point in time they were both still intact to present a resistance to movement. However, as seen in the corresponding greyscale slices in

Figure 8-20a and Figure 8-20b, the remnants of the crimp plate and the vent disks appear to have previously been in a molten state.

The only two remaining rigid components within the cell are the top button and the mandrel. Of the two mandrel designs, the solid cylinder in the Panasonic cell (Figure 8-20a), and split cylinder in the Sanyo cell (Figure 8-20b), the mandrel with the split is shown to contain debris and molten copper inside its stem (see orthoslices in Figure 8-20b) whereas the solid mandrel in the Panasonic cell does not. It's clear from the presence of debris and remains of molten metals that the fluid transport through the split mandrel is enhanced and would help mitigate peeling of the inner layers by reducing the shear from the gas flow through provision of entry to a clear flow path at all depths through the electrode assembly. The presence of molten copper in the Sanyo mandrel indicates that the temperature of the fluid flowing through the mandrel channel was $>$ 1085 °C, which when directed at the underside of the top button would weaken the metal facilitating the mandrel puncturing through.

For all cells that did not burst, the top button of the Samsung cells melted. Further indication of the manufacturer using a low melting point alloy is that there is little presence of molten copper within the cell indicating that most of the internal volume of the cell did not exceed 1085 °C. The melting top button, vent disk and crimp plate, opened a clear path for gases and reacting contents to escape. This would help prevent clogging and reduce the risk of the cell bursting.

However, the combination of a low melting point alloy for a top button and an internal mandrel could increase the risk of rigid projectiles escaping the cell. Therefore, to avoid dangerous projectiles, rigid mandrels should only be used in cells where the crimp structure and top button are expected to maintain their mechanical integrity. From the results presented here, the mandrel is shown to provide improved gas and fluid flow to the vent within the cells as well as reducing the risk of clogging and cell bursting; however, the trade-off is that the mandrel can become an external projectile, either through piercing the top button or by the cell bursting. A more stable and stationary mandrel design is favourable to avoid the drawbacks of its incorporation, in particular for high capacity cells such as the

Panasonic NCR cells where up to 30 % more gas is expected to be generated within the same time period than the lower capacity LG and Sanyo cells.

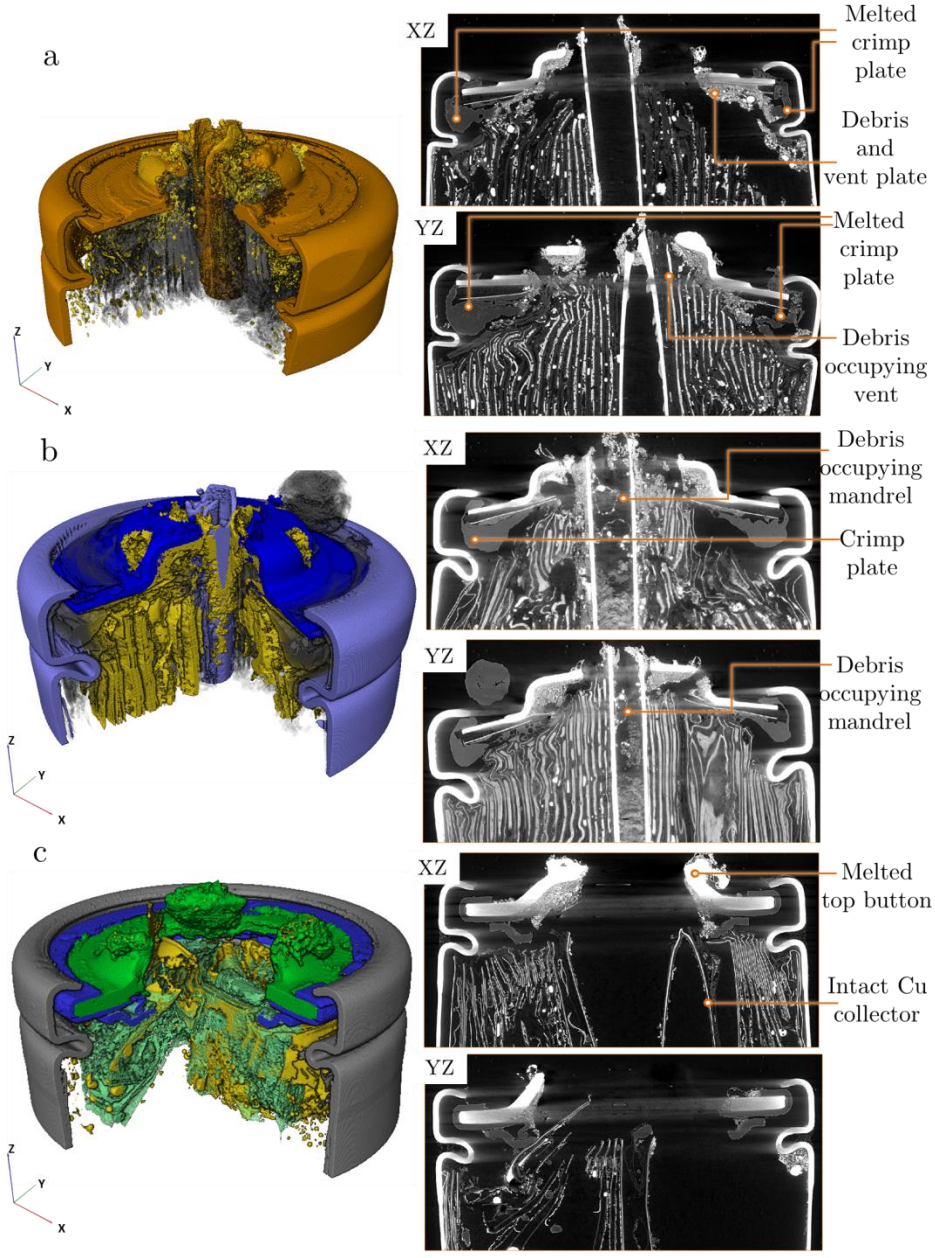

Figure 8-20: *Post-mortem* 3D reconstructions and corresponding *XZ* and *YZ* orthoslices of (a) Panasonic NCR18650B, (b) Sanyo UR18650ZY, and (c) Samsung INR18650-25R cells showing the damage to the top button after thermal runaway. The cylindrical mandrel in (a) and (b) is seen to protrude after puncturing the top button.

8.5. Conclusions

Up until now, inducing short circuits similar to those that can occur unpredictably in field scenarios remained a challenge. The nail penetration test is sometimes carried out to assess how a cell would behave when undergoing an internal short; however, as shown in this chapter the nail penetration method has several drawbacks; most notably that it acts as a heat sink at the point of initiation, it spreads the short circuit across multiple layers and a large area, and blocks the propulsion of broken down materials towards the vent. In addition, the nail penetration method does not provide any control of the location of thermal runaway initiation in the radial direction.

The ISC device described here, with a low melting point wax interface between electrodes, provided a means for activating an internal short circuit on-demand and at a known location within the cell. As the location of short circuiting is now controlled, the initiation and propagation of thermal runaway could be captured using high-speed radiography. Consistent failure mechanisms such as fastest propagation in the longitudinal and azimuthal directions causing cylindrically shaped fluidized reaction zones, were explored through several repeat tests. The geometric evolution of the reaction zone leads to an intact core being encompassed by a fluidized region, reducing the shear force required for propulsion of the intact core towards the vent, which causes clogging (one of the primary causes of the cell bursting and ejecting its contents).

To identify the root cause of cell bursting and to test the efficacy of safety devices and vent designs, five popular commercial cells were examined using high speed radiography during thermal runaway. The cell with the highest capacity (Panasonic NCR18650B) almost always burst and ejected its contents. A two-step process towards bursting was observed, where the crimp fold first extended as a result of gas build-up beneath the vent disk. Thereafter, the intact electrode assembly and central mandrel shifted up against the crimp disk, blocking the vent and forcing the top fold to bend and release the integrated safety components. Similarly, the lead up to the Samsung cell venting involves the electrode assembly shifting up and converging in on the vent, blocking the escape of gases and causing

the cell to burst. The burst pressure of the Panasonic cell was determined by the flexural strength of the crimp, whereas the bursting pressure of the Samsung cells was determined by the flexural strength of the crimp disk where the crimp disk bent under pressure and was pushed past the top fold.

The presence and design of cylindrical mandrels within 18650 cells was also shown to play a significant role in the failure mechanism of cells, and the associated risks of failure. Inserting a mandrel involves a trade-off between improved gas flow and reduced risk of clogging, and increased risk of it becoming a dangerous projectile upon escaping the cell, either through ejection of contents or piercing through the crimp components. Stronger crimp disks and top buttons are therefore recommended to avoid bending and puncture, where the crimp and top folds determine the bursting pressure. Mandrels mitigate clogging and improve gas escape through the vent, while designs with a vertical slit allow generated gases greater access to a clear flow path from all depths within the cell. However, the converging or pointed ends of the mandrels appear to only increase the risk of the mandrel puncturing the top button.

In summary, the mechanism in which thermal runaway initiates and propagates, as well as the cause and effect of vent clogging, has been elucidated. This insight could lead to new cell designs to provide alternate means of pressure release, such as secondary bursting disks which would relieve pressure build-up before the cell ruptures, avoiding the risk of projectiles. The venting process is also influenced by the presence and design of the cylindrical mandrel in the core of the electrode assembly, which maintains an opening for gaseous flow but may also damage the vent and safety devices at the cap of the cell when propelled in that direction. A possible way to avoid this drawback would be to spot-weld the mandrel to the base of the cell, anchoring it during thermal runaway, or to broaden the top end of the mandrel to increase the resistance that it experiences before escape.

Chapter 9

Conclusions and Future Work

This thesis describes the use of X-ray imaging, across multiple time and length scales, to explore the micro- and macroscopic properties of lithium-ion batteries and battery materials during operation and failure. The thesis starts with an analysis of the transport properties of polymer separators and their relation to the safety and performance of cells. The polymer separators are analysed in their unstrained state, whereas during operation it is expected that separators are subject to stress as a result of the evolving architectures of active materials.

The extent of architectural evolution within a commercial cell is then analysed and quantified in 3D using an approach that combines high-speed X-ray CT and digital volume correlation, generating a temporal 3D strain map of the MnO_2 electrode. Thereafter, complementing previous investigations of the rate and quantity of heat and gas production during thermal runaway, this thesis explores the dynamic architectural phenomena that occur, across multiple length scales, leading up to and during failure through the use of high-speed synchrotron X-ray tomography and ultra-high-speed radiography.

The key outcomes and insights arising from this work are outlined in the following section, and their application to improving the safety and performance of cells is explained. This work has also demonstrated the application of advanced X-ray CT and radiography techniques as powerful diagnostic tools; the scope to extend these techniques to examine dynamic degradation mechanisms of electrochemical energy devices is also discussed.

9.1. Insights and Improving Battery Safety

9.1.1. Considerations for Microstructural Design

In Chapter 4, the individual layers of multilayer separator membranes were digitally separated and their relative impact on the overall transport resistance of the membrane was revealed. Some polymer layers were shown to be more tortuous than others, in particular for the popular Celgard 2325 tri-layer membrane, the outer PP layers presented significantly more transport resistance per unit length than the PE layer showing scope for optimisation of individual layer thickness to minimise overall membrane volume while maintaining high safety and performance.

In Chapter 7, the connection between electrode microstructure (particle size and geometry) and the thermal stability of the electrode is examined. This study shows that the electrode particles undergo a significant change in geometry and size during failure, which is location dependent due to the heterogeneities in temperature and the presence of electrolyte throughout the cell. This raises the question of how microstructure influences the safety of cells, and whether there is an optimum structure for high performance and safety, which can counteract each other due to their inherent link to specific surface area. This is discussed further in future work.

9.1.2. Considerations for Cell Design

By capturing sequential 3D images using high-speed synchrotron X-ray CT, the evolution of electrode architectures within commercial cells during operation and failure was shown to be largely influenced by the rigid mechanical designs of the cell. The challenge of designing the rigid components to minimise degradation and improve safety then arises. For example, in Chapter 4 chemo-mechanical force from the expansion of the MnO_2 electrode during operation caused the electrode assembly to unravel; the use of an unconstrained current collecting mesh in this instance did not prove to be a favourable design due to the early development of cracks and delamination. To avoid such early degradation, it may be beneficial for the manufacturers to use a foil current collector, constrain the mesh current

collector to prevent movement, or apply compressive force to the layers via packing the hollow core of the spiral wound electrode assembly. Each of these suggestions is expected to improve the contact between the electrode and current collector.

In the commercial rechargeable 18650 cells, the results in Chapter 6 and Chapter 8 demonstrated that the design and presence of the cylindrical mandrel greatly affects the behaviour of a cell leading up to and during failure via thermal runaway. The mandrel occupying the core of the electrode assembly prevented its structural collapse upon initial venting, avoiding the risk of separator tearing and the early occurrence of internal short circuiting and thermal runaway. Thereafter, when thermal runaway ensues, the mandrel improves gaseous transport to the vent, but presents the additional risk of puncturing the top button and vent disk. If the mandrel could be fastened or its geometry changed to reduce the risk of puncture, then the benefits of improved support and gas transport could be maintained with less risk of damaging components and forming projectiles.

The propagation of thermal runaway within a cell was characterised in Chapter 6 and Chapter 8. Stemming from a point of initiation, the exothermic decomposition reactions propagate faster in the azimuthal (in plane) direction by a factor of > 25 than the radial (through plane) direction within 18650 cells, where temperatures have been shown to reach > 1085 °C. This anisotropic rate of propagation leads to cylindrical reactions zones that loosen intact sections of the electrode assembly for propulsion towards the vent, causing clogging. As commercial cells continue to increase in capacity, new designs are needed to accommodate the increased quantity and rate of gas generation during thermal runaway and to counteract the increased risk of vent clogging and cell rupture. Solutions to this may involve secondary vents on 18650 cells, or larger vents with greater flexural strength than those studied in this thesis.

In collaboration with NREL and NASA, the efficacy of an ISC device was explored and was shown to reliably and effectively generate internal short circuits within commercial cell designs. There is scope for integrating this ISC device into new commercial cell designs and comparing the effectiveness of the next generation of safety devices, as well as determining the worst case scenarios of specific cell designs.

As well as providing opportunity for improved cell designs, the insights described in thesis may also provide valuable information for multi-physics modelling of lithium-ion battery failure and degradation since structural distortion, breakdown and material ejection are not considered in current modelling strategies but are critical for accurate prediction of performance degradation, as well as heat generation and dissipation. Dynamic visualisation of structural degradation during operation, and in the moments leading up to and during thermal runaway, would support the development of multi-physics models of the effects of various operating and abuse conditions on degradation and the onset of thermal runaway.

9.2. X-ray Imaging as a Diagnostic Tool for Lithium-ion Batteries

The work presented in this thesis provides further testimony that X-ray microscopy is a powerful diagnostic tool for analysing material properties and capturing dynamic events within lithium-ion batteries in 3D. Polymer separators found in lithium-ion batteries are challenging to image using conventional X-ray absorption contrast CT due to their low attenuation. The application of Zernike phase contrast X-ray nano-CT for capturing the microstructure of polymer separators was the first of its kind and is precedent for future studies of low attenuation materials, such as polymer separators and graphite electrodes.

The complementary capabilities of lab-based systems and synchrotron facilities have also been demonstrated here. The high photon flux achievable at synchrotron sources was used for *operando* studies where significant changes in material architectures occur over short periods of time, requiring fast tomography capabilities. The dynamic structural evolution that plays a central role in degradation and failure of lithium-ion batteries was captured across multiple time scales, from 3D images captured every few minutes, to 2D radiographs capturing events at $>$ 20,000 fps. Lab-based CT systems were used for 3D analyses across multiple length scales before and after the dynamic events and may also be used to effectively analyse cell degradation occurring over extended calendar and cycle life.

X-ray tomography and radiography, in combination with thermal imaging; has provided great insight into the structural and thermal dynamics leading up to and during failure of lithium-ion batteries. There remains great potential for combining other diagnostic techniques such as calorimetry, mass spectroscopy, and electrochemical impedance spectroscopy to connect thermal, reaction, and electrochemical information with structural evolutions, which could present the most comprehensive degradation and failure analyses to date.

Finally, the combination of X-ray CT techniques with available image-based quantification tools such as the open-source software packages for determining particle size distributions, tortuosity factors, and tracking the displacement of features in 3D (DVC), provides an effective means of understanding the complex microstructures of materials within electrochemical energy devices, and presents the possibility of comparing results between publications.

9.3. Ongoing and Future Work

9.3.1. Assessment of Risks Associated with Failure

Sprays and hot projectiles from lithium-ion battery ruptures are among the primary risks associated with battery failure, along with toxic/flammable gases from reactions, high temperatures, and high quantities and rates of heat generation. By combining high-speed radiography with *in-situ* calorimetry and mass spectroscopy, a comprehensive description of the risks associated with different types of battery failure (heat output, maximum temperatures, the occurrence of projectiles, gas compositions and quantities) could be generated. The three techniques in concert could be used to explore the causation and magnitude of each risk by capturing structural, thermal and compositional information during highly controlled lithium-ion battery failures. The location of failure initiation within the cell would be controlled by placing the ISC device in different regions within the cell. How the location of failure initiation impacts the failure mechanism of the cell (i.e. venting, side-wall rupture, ejection) could then be assessed, as well

as how current safety devices such as bursting disks mitigate the consequences of failure.

A custom single-cell calorimeter with X-ray transparent Al walls is being designed by collaborators at the NASA Johnson Space Centre to record the rate and quantity of heat generated during failure. A 3D drawing of the current calorimeter design is shown in Figure 9-1, and includes a chamber to hold the test cell, a chamber to catch the debris from exploding cells, and a gas tube to extract most of the residual heat in the gases and to catch any particulate before the gas enters the mass spectrometer. This calorimeter design would allow separate measurement of the heat output from the 18650 cell casing, the ejected solids, and the released gases. The localities of failure along with their interaction with safety devices would be compared with respect to overall risk; concluding with how certain design features influence the risks associated with failing cells. This experiment would ideally be carried out at the ESRF beamline ID19, which has a large field of view and high energy flux.

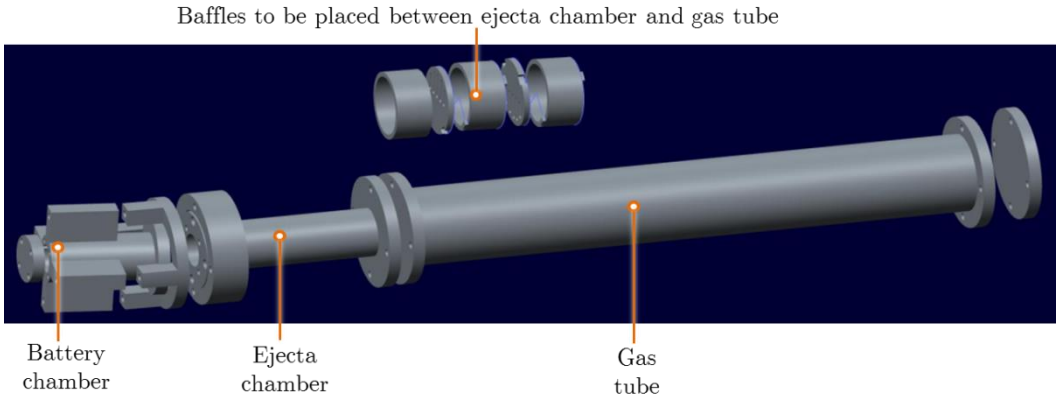

Figure 9-1: *In-situ* X-ray transparent aluminium calorimeter design, with a test battery chamber, ejecta chamber to measure the heat within the ejecta, and a gas tube to extract any residual heat and prevent hot debris from entering the mass spectrometer.

9.3.2. Module Testing

The behaviour of individual cells is expected to change when they become part of a module or system. The heat dissipation properties will change with the presence of other batteries acting as additional heat sinks, and the cells may also be contained within a closed environment with higher or lower thermal conductivity. It is expected that the likelihood of side-wall rupture would increase if cells are in contact with each other within a module, due to the high conductivity of the cell walls and the consequent rapid heat transfer. The tensile strength of the casings significantly decreases at high temperature, eventually reaching a critical point where the pressure required to burst through the casing becomes less than the bursting pressure of the crimp and vent components. Side-wall rupture significantly increases the risk of cell-to-cell propagation as hot material is ejected in the direction of neighbouring cells.

As well as being used to examine the internal failure mechanisms, cells with implanted ISC devices could also be placed in large modules to assess the risk of side-wall rupture and cell-to-cell propagation in the event of a defective cell short circuiting. The first step would be to demonstrate the application of ISC cells in simple modules where cells are in direct contact and open to standard temperature and pressure. After identifying the worst case failure mechanism (future work outlined in the previous section), the efficacy of more advanced heat dissipation strategies to mitigate the risk of cell-to-cell propagation would be examined. The combined understanding of individual cell failure as well as the consequences in modular systems would provide valuable insight for the design of safer cells and modules.

The initial study of cell-to-cell propagation with simple 18650 modules with an implanted ISC cell has already been performed at the I12 beamline at Diamond Light Source, which is capable of performing continuous high-speed X-ray imaging ($>$ 500 fps) with a large field of view (*ca.* 50 mm $\times$ 30 mm). As shown in Figure 9-2, the 2 $\times$ 2 18650 configuration has resulted in every cell undergoing side-wall rupture. Processing and disseminating the results from this experiment, as well

building on the this study through the use of more advanced module designs is part of the future work plan.

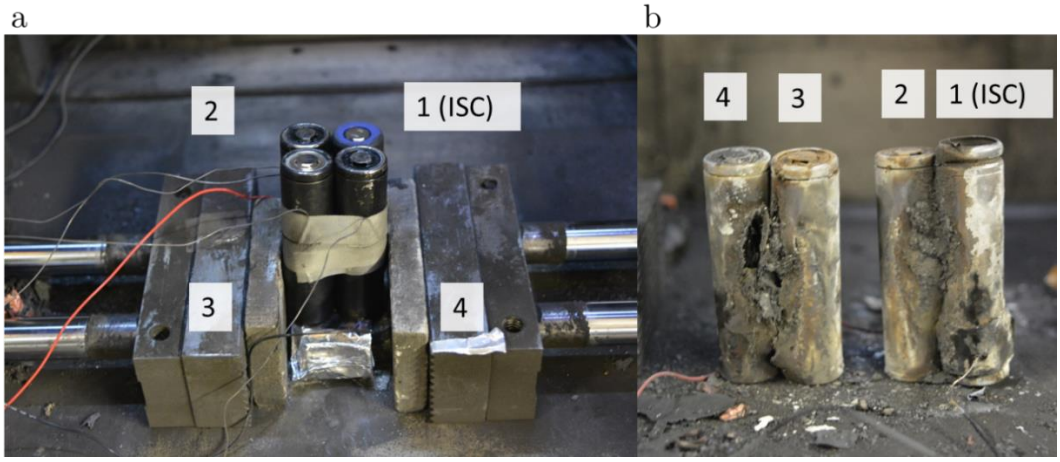

Figure 9-2: (a) Arrangement of 18650 cells before the ISC cell was triggered during high-speed X-ray imaging. (b) *Post-mortem* photograph showing evidence of side-wall ruptures.

9.3.3. Evolution of Particle Morphology

The intensity of the thermal runaway reactions is inherently connected to the particle microstructure, however this relationship is not well understood and there is little published information on the topic. As demonstrated in Chapter 7, the initial particle microstructure is not the only factor that determines the rate of reaction during thermal runaway; the phase transitions that occur during the exothermic reduction steps of the metal-oxide electrodes involve significant changes in material densities, causing delamination and cracking, and exposing additional surface area to reactions with the electrolyte. Therefore, the rate of heat generation during thermal runaway is also dependent on the propensity of particle structures to decompose and expose additional surface area at elevated temperatures.

A high-speed, *operando* X-ray CT and XRD study of the evolution of positive electrode particles could provide a spatial and temporal understanding of the dynamic particle microstructure and phase transitions that occur at elevated temperatures and during thermal runaway. Different electrode compositions with varying particle sizes, and varying concentrations of electrolytes, would be tested to

examine the influence of particle morphology, specific surface area, and the presence of excess electrolyte on the reaction processes. This experiment will be carried out at the ID15A beamline at the ESRF in February 2017, which has the high energy flux necessary for high speed X-ray CT, and a Dectris Pilatus 3X CdTe detector for high speed XRD.

Publications and Conferences

Primary Publications

1. Finegan, D. P.; Scheel, M.; Robinson, J. B.; Tjaden, B.; Hunt, I.; Mason, T. J.; Millichamp, J.; Di Michiel, M.; Offer, G. J.; Hinds, G.; Brett, D. J. L.; Shearing, P. R., *In-operando* high-speed tomography of lithium-ion batteries during thermal runaway. *Nature Communications* 2015, 6.
2. Finegan, D. P.; Tudisco, E.; Scheel, M.; Robinson, J. B.; Taiwo, O. O.; Eastwood, D. S.; Lee, P. D.; Di Michiel, M.; Bay, B.; Hall, S. A.; Hinds, G.; Brett, D. J. L.; Shearing, P. R., Quantifying Bulk Electrode Strain and Material Displacement within Lithium Batteries via High-Speed *Operando* Tomography and Digital Volume Correlation. *Advanced Science* 2016, 3.
3. Finegan, D. P.; Scheel, M.; Robinson, J. B.; Tjaden, B.; Hunt, I.; Mason, T. J.; Millichamp, J.; Di Michiel, M.; Offer, G. J.; Hinds, G.; Brett, D. J. L.; Shearing, P. R., Morphological transformations of lithium-ion battery materials undergoing overcharge induced thermal runaway: An *operando* and multi-scale CT study, *Chem. Phys. Phys. Chem.*, 2016.
4. Finegan, D. P.; Tjaden, B.; Taiwo, O. O.; Eastwood, D. S.; M.; Gelb, J.; Hall, S. A.; Hinds, G.; Brett, D. J. L.; Shearing, P. R., Characterising the structural properties of battery polymer separators in 3D using Zernike phase contrast X-ray microscopy, *Journal of Power Sources 2016, 333, 184-192.*

Secondary Publications

1. Meyer, Q.; Ashton, S.; Jervis, R.; Finegan, D. P.; Boillat, P.; Cochet, M.; Curnick, O.; Reisch, T.; Adcock, P.; Shearing, P. R.; Brett, D. J. L., The Hydro-electro-thermal Performance of Air-cooled, Open-cathode Polymer Electrolyte Fuel Cells: Combined Localised Current Density, Temperature and Water Mapping. *Electrochimica Acta* 2015, 180, 307-315.
2. Robinson, J. B.; Engebretsen, E.; Finegan, D. P.; Darr, J.; Hinds, G.; Shearing, P. R.; Brett, D. J. L., Detection of Internal Defects in Lithium-Ion

Batteries Using Lock-in Thermography. *ECS Electrochemistry Letters* 2015, 4, A106-A109.

3. Obeisun, O. A.; Meyer, Q.; Engebretsen, E.; Finegan, D. P.; Robinson, J. B.; Hinds, G.; Shearing, P. R.; Brett, D. J. L., Study of water accumulation dynamics in the channels of an open-cathode fuel cell through electro-thermal characterisation and droplet visualisation. *International Journal of Hydrogen Energy 2015*, 40, 56, 16786-16796.
4. Meyer, Q.; Ashton, S.; Torija, S.; Gurney, C.; Boillat, P.; Cochet, M.; Engebretsen, E.; Finegan, D. P.; Adcock, P.; Shearing, P. R.; Brett, D. J. L., Nitrogen Blanketing and Hydrogen Starvation in Dead-Ended-Anode Polymer Electrolyte Fuel Cells Revealed by Hydro-Electro-Thermal Analysis. *Electrochimica Acta*, 2016, 203, 198-205.
5. Engebretsen, E.; Robinson, J. B.; Obeisun, O.; Mason, T.; Finegan, D.P.; Hinds, G.; Shearing, P. R.; Brett, D. J. L., Electro-thermal impedance spectroscopy applied to an open-cathode polymer electrolyte fuel cell. *Journal of Power Sources* 2016, 302, 210-214.
6. Paz-Garcia, J.M.; Tudisco, E.; Taiwo, O.O.; Finegan, D.P.; Brett, D.J.L.; Shearing, P.R.; Hall, S. A., 4D Analysis of the Microstructural Evolution of Si-based Electrodes during Lithiation: Time-lapse X-ray Imaging and Digital Volume Correlation, *Journal of Power Sources* 2016, 320, 196-203.
7. Taiwo, O. O.; Finegan, D. P.; Fife, J.L.; Eastwood, D.S.; Lee, P.L.; Brett, D.J.L.; Shearing, P.R., Comparison of Three Dimensional Analysis and Stereological Techniques for Quantifying Lithium Ion Battery Electrode Microstructures, *Journal of Microscopy*, 2016.
8. Meyer, Q.; Ashton, S.; Boillat, P.; Cochet, M; Engebretsen, E.; Finegan, D.P.; Lu, X.; Bailey, J.; Mansor, N.; Abdulaziz, R.; Taiwo, O.O.; Jervis, R.; Torija, S.; Benson, P.; Foster, S.; Adcock, P.; Shearing, P.R.; Brett, D.J.; Effect of gas diffusion layer properties on water distribution across air-cooled, open-cathode polymer electrolyte fuel cells: A combined ex-situ X-ray tomography and in-operando neutron imaging study, *Electrochimica Acta* 2016, 211, 478-487.

9. Taiwo, O. O.; Finegan, D. P.; Paz-Garcia, J.M.; Eastwood, D.S.; Bodey, A.; Rau, C.; Hall, S.A.; Brett, D.J.L.; Lee, P.L.; Shearing, P.R., Three-dimensional visualization of the evolution of lithium metal electrodes during battery operation using X-ray Tomography, *Scientific Reports*, in press.
10. Jervis, R.; Brown, L.; Neville, T.; Millichamp, J.; Finegan, D.P.; Heenan, T.; Brett, D.; Shearing, P., Design of a miniature flow cell for *in situ* X-ray imaging of redox flow batteries, *Journal of Physics D*, 2016, 49, 434002.
11. Taiwo, O.O.; Finegan, D.P.; Gelb, J.; Holzner, C.; Brett, D.J.L.; Shearing, P.R., The use of contrast enhancement techniques in multi-scale X-ray imaging of lithium ion battery electrodes, *Chemical Engineering Science*, in press.
12. Heenan, T.M.M.; Bailey, J.J.; Lu, X.; Robinson, J.B.; Iacoviello, F.; Finegan, D.P.; Brett, D.J.; Shearing, P. R.; Three-Phase Segmentation of Solid Oxide Fuel Cell Anode Materials Using Lab Based X-ray Nano-Computed Tomography, *Journal of Power Sources*, submitted.
13. Tjaden, B.; Finegan, D.P.; Lane, J.; Brett, D.J.L.; Shearing, P.R., A correlative study of mass transport resistance in porous oxygen transport membrane supports, *Chem. Eng. Sci.*, submitted.
14. Obeisun, M.; Finegan, D.P.; Robinson, J.; Engebretsen, E.; Taiwo, O.O.; Hinds, G.; Shearing, P.R.; Brett, D.J.; Ex-situ characterisation of water droplet dynamics on the surface of a fuel cell gas diffusion layer through wettability analysis and thermal characterisation, *International Journal of Hydrogen Energy*, under review.

Conferences Attended

Talks

- *2014 UK Energy Storage (UKES) Conference, Warwick University, UK, Nov 2014.*

  Title: *Operando* tomography of lithium-ion batteries during operation and failure.

- *2015 STFC Early Career Researchers Conference (ECRC), Abingdon, UK.*

  Title: Application of digital volume correlation to *operando* tomography of Lithium-ion batteries.

- *2015 International Conference on Tomography of Materials and Structures (ICTMS), Quebec, Canada, May 2015.*

  Title: Understanding battery failure: An X-ray CT approach.

- *Invited speaker to ElectroChem Conference 2015, Durham University, UK, Sept 2015.*

  Keynote talk for The Sheelagh Campbell Memorial Award by the Royal Society of Chemistry.

  Title: Fast tomography of lithium-ion batteries during operation and failure.

- *2016 STFC Early Career Researchers Conference (ECRC), Abingdon, UK, Apr 2016.*

  Title: Understanding battery failure: A multi-scale and *operando* X-ray CT approach.

- *2016 Advanced Battery Power Conference, Münster, Germany, Apr 2016.*

  Title: Understanding battery failure via advanced X-ray CT.

- *2016 X-ray Microscopy (XRM) Conference, Oxford University, UK, Aug 2016*

  Title: Understanding battery degradation and failure: A high-speed imaging approach.

Poster presentations

- *2013 Grove Fuel Cell Conference, Amsterdam, Netherlands, Sept 2013.*

  Title: Studies of thermal anisotropy in operating PEMFC.

- *2014 Diamond User Meeting, Diamond Light Source, UK, Sept 2014.*

  Title: *Operando* tomography of lithium-ion batteries.

- *2016 18th International Meeting on Lithium Batteries: IMLB, Chicago, USA, Jun 2016.*

  Title: Understanding battery failure: A multi-scale and high-speed *operando* approach.

References

1. Owen, N.A., O.R. Inderwildi, and D.A. King, *The status of conventional world oil reserves—Hype or cause for concern?* Energy Policy, 2010. 38(8): p. 4743-4749.
2. *Countries - U.S. Energy Information Administration (EIA).* 2012 [cited 2012 3/11/12]; Available from: http://www.eia.gov/countries/index.cfm?view=consumption.
3. Agency, I.E., *World Energy Outlook 2012.* 2012, International Energy Agency: Paris.
4. Armand, M. and J.M. Tarascon, *Building better batteries.* Nature, 2008. 451: p. 652-657.
5. Scrosati, B., J. Hassoun, and Y.-K. Sun, *Lithium-ion batteries. A look into the future.* Energy & Environmental Science, 2011. 4(9): p. 3287-3295.
6. Nykvist, B. and M. Nilsson, *Rapidly falling costs of battery packs for electric vehicles.* Nature Clim. Change, 2015. 5(4): p. 329-332.
7. AAIB, *Report on the serious incident to Boeing B787-8, ET-AOP London Heathrow Airport on 12 July 2013*, in *Aircraft Accident Report 2/2015.* 2015.
8. Yayathi, S., et al., *Energy distributions exhibited during thermal runaway of commercial lithium ion batteries used for human spaceflight applications.* Journal of Power Sources, 2016. 329: p. 197-206.
9. Doughty, D. and P. Roth, *A General Discussion of Li Ion Battery Safety.* The Electrochemical Society Interface, 2012. 21(2).
10. Jeong, G., et al., *Prospective materials and applications for Li secondary batteries.* Energy & Environmental Science, 2011. 4(6): p. 1986-2002.
11. Jacoby, M. *Assessing the Safety OF Lithium-Ion Batteries.* 2013. 91, 33-37.
12. JTSB, *Aircraft Serious Incident Investigation Report, All Nippon Airways Co., LTD JA804A.* 2014, Japan Transport Safety Board.
13. NTSB, *Aircraft Incident Report, Auxiliary Power Unit Battery Fire, Japan Airlines Boeing 787-8, JA829J.* 2014, National Transport Safety Board.
14. Bruce, P.G., et al., *Li-O2 and Li-S batteries with high energy storage.* Nat Mater, 2012. 11(1): p. 19-29.
15. Bruce, P.G., B. Scrosati, and J.-M. Tarascon, *Nanomaterials for Rechargeable Lithium Batteries.* Angewandte Chemie International Edition, 2008. 47(16): p. 2930-2946.
16. WHITTINGHAM, M.S., *Electrical Energy Storage and Intercalation Chemistry.* Science, 1976. 192(4244): p. 1126-1127.
17. Jasinski, R., *High-energy Batteries.* 1967, Plenum Press: New York.

18. Mizushima, K., et al., *LixCoO2 (0<x<-1): A new cathode material for batteries of high energy density.* Materials Research Bulletin, 1980. 15(6): p. 783-789.
19. Thackeray, M.M., W.I.F. David, and J.B. Goodenough, *Structural characterization of the lithiated iron oxides LixFe3O4 and LixFe2O3 (0<x<2).* Materials Research Bulletin, 1982. 17(6): p. 785-793.
20. David, W.I.F., et al., *Structure refinement of the spinel-related phases Li2Mn2O4 and Li0.2Mn2O4.* Journal of Solid State Chemistry, 1987. 67(2): p. 316-323.
21. Thackeray, M.M., et al., *Lithium insertion into manganese spinels.* Materials Research Bulletin, 1983. 18(4): p. 461-472.
22. Endo, M., et al., *Recent development of carbon materials for Li ion batteries.* Carbon, 2000. 38(2): p. 183-197.
23. Mohri, M., et al., *Rechargeable lithium battery based on pyrolytic carbon as a negative electrode.* Journal of Power Sources, 1989. 26(3–4): p. 545-551.
24. Padhi, A.K., K.S. Nanjundaswamy, and J.B. Goodenough, *Phospho-olivines as Positive-Electrode Materials for Rechargeable Lithium Batteries.* Journal of The Electrochemical Society, 1997. 144(4): p. 1188-1194.
25. Chikkannanavar, S.B., D.M. Bernardi, and L. Liu, *A review of blended cathode materials for use in Li-ion batteries.* Journal of Power Sources, 2014. 248: p. 91-100.
26. Chung, S.-Y., J.T. Bloking, and Y.-M. Chiang, *Electronically conductive phospho-olivines as lithium storage electrodes.* Nat Mater, 2002. 1(2): p. 123-128.
27. Ritchie, A. and W. Howard, *Recent developments and likely advances in lithium-ion batteries.* Journal of Power Sources, 2006. 162(2): p. 809-812.
28. Winter, M. and R.J. Brodd, *What Are Batteries, Fuel Cells, and Supercapacitors?* Chemical Reviews, 2004. 104(10): p. 4245-4270.
29. Salomon, M., *Linden's Handbook of Batteries*, in *Linden's Handbook of Batteries*, T. Reddy and D. Linden, Editors. 2011, McGraw-Hill Companies Inc.: USA.
30. Ehrlich, G., *Chapter 35: Lithium ion batteries*, in *Handbook of Batteries*, D. Linden and T. Reddy, Editors. 2002.
31. Zheng, T., J.N. Reimers, and J.R. Dahn, *Effect of turbostratic disorder in graphitic carbon hosts on the intercalation of lithium.* Physical Review B, 1995. 51(2): p. 734-741.
32. Dahn, J. and G. Ehrlich, *Linden's Handbook of Batteries*, T. reddy, Editor. 2011, McGrawHill: USA.
33. Dahn, J.R., et al., *Mechanisms for Lithium Insertion in Carbonaceous Materials.* Science, 1995. 270(5236): p. 590-593.
34. Raccichini, R., et al., *The role of graphene for electrochemical energy storage.* Nat Mater, 2015. 14(3): p. 271-279.

35. Chattopadhyay, S., et al., *In Situ X-ray Study of the Solid Electrolyte Interphase (SEI) Formation on Graphene as a Model Li-ion Battery Anode.* Chemistry of Materials, 2012. 24(15): p. 3038-3043.
36. Harris, S.J. and P. Lu, *Effects of Inhomogeneities—Nanoscale to Mesoscale—on the Durability of Li-Ion Batteries.* The Journal of Physical Chemistry C, 2013. 117(13): p. 6481-6492.
37. Fong, R., U. von Sacken, and J.R. Dahn, *Studies of Lithium Intercalation into Carbons Using Nonaqueous Electrochemical Cells.* Journal of The Electrochemical Society, 1990. 137(7): p. 2009-2013.
38. Park, Y.-S., et al., *Effect of carbon coating on thermal stability of natural graphite spheres used as anode materials in lithium-ion batteries.* Journal of Power Sources, 2009. 190(2): p. 553-557.
39. Qi, Y. and S.J. Harris, *In Situ Observation of Strains during Lithiation of a Graphite Electrode.* Journal of The Electrochemical Society, 2010. 157(6): p. A741-A747.
40. Park, Y.-S. and S.-M. Lee, *Effects of particle size on the thermal stability of lithiated graphite anode.* Electrochimica Acta, 2009. 54(12): p. 3339-3343.
41. Ji, L., et al., *Recent developments in nanostructured anode materials for rechargeable lithium-ion batteries.* Energy & Environmental Science, 2011. 4(8): p. 2682-2699.
42. Hwang, J. and H. Jang, *Evolution of Solid Electrolyte Interphase during Cycling and Its Effect on Electrochemical Properties of LiMn2O4.* Journal of The Electrochemical Society, 2015. 162(1): p. A103-A107.
43. Julien, C., et al., *Comparative Issues of Cathode Materials for Li-Ion Batteries.* Inorganics, 2014. 2(1): p. 132.
44. Lin, F., et al., *Surface reconstruction and chemical evolution of stoichiometric layered cathode materials for lithium-ion batteries.* Nat Commun, 2014. 5.
45. Yoshio, M., et al., *Preparation and properties of LiCoyMnxNi1−x−yO2 as a cathode for lithium ion batteries.* Journal of Power Sources, 2000. 90(2): p. 176-181.
46. Tran, N., et al., *Layered Li1 + x (Ni0.425Mn0.425Co0.15) 1 − x O2 Positive Electrode Materials for Lithium-Ion Batteries.* Journal of The Electrochemical Society, 2006. 153(2): p. A261-A269.
47. Lu, J., et al., *Effectively suppressing dissolution of manganese from spinel lithium manganate via a nanoscale surface-doping approach.* Nat Commun, 2014. 5.
48. Zhan, C., et al., *Mn(II) deposition on anodes and its effects on capacity fade in spinel lithium manganate–carbon systems.* Nat Commun, 2013. 4.
49. Xia, Y., Y. Zhou, and M. Yoshio, *Capacity Fading on Cycling of 4 V Li / LiMn2 O 4 Cells.* Journal of The Electrochemical Society, 1997. 144(8): p. 2593-2600.

50. Lim, J., et al., *Origin and hysteresis of lithium compositional spatiodynamics within battery primary particles.* Science, 2016. 353(6299): p. 566-571.
51. Besenhard, J.O. and G. Eichinger, *High energy density lithium cells: Part I. Electrolytes and anodes.* Journal of Electroanalytical Chemistry and Interfacial Electrochemistry, 1976. 68(1): p. 1-18.
52. Suo, L., et al., *"Water-in-salt" electrolyte enables high-voltage aqueous lithium-ion chemistries.* Science, 2015. 350(6263): p. 938-943.
53. Goodenough, J.B. and P. Singh, *Review—Solid Electrolytes in Rechargeable Electrochemical Cells.* Journal of The Electrochemical Society, 2015. 162(14): p. A2387-A2392.
54. Tan, G., et al., *Solid-State Li-Ion Batteries Using Fast, Stable, Glassy Nanocomposite Electrolytes for Good Safety and Long Cycle-Life.* Nano Letters, 2016. 16(3): p. 1960-1968.
55. Meyer, W.H., *Polymer Electrolytes for Lithium-Ion Batteries.* Advanced Materials, 1998. 10(6): p. 439-448.
56. Roth, P. and C. Orendorff, *How Electrolytes Influence Battery Safety.* The Electrochemical Society Interface, 2012(Summer).
57. Aurbach, D., et al., *Design of electrolyte solutions for Li and Li-ion batteries: a review.* Electrochimica Acta, 2004. 50(2–3): p. 247-254.
58. Jiang, J., et al., *Thermal Stability of 18650 Size Li-Ion Cells Containing LiBOB Electrolyte Salt.* Journal of The Electrochemical Society, 2004. 151(4): p. A609-A613.
59. Zhang, S.S., *A review on electrolyte additives for lithium-ion batteries.* Journal of Power Sources, 2006. 162(2): p. 1379-1394.
60. Arora, P. and Z. Zhang, *Battery separators.* Chemical Reviews, 2004. 104(10): p. 4419-4462.
61. Zhang, S.S., *A review on the separators of liquid electrolyte Li-ion batteries.* Journal of Power Sources, 2007. 164(1): p. 351-364.
62. Chen, X., et al., *Effects of cell positive cans and separators on the performance of high-voltage Li-ion batteries.* Journal of Power Sources, 2012. 213: p. 160-168.
63. Finegan, D.P., et al., *In-operando high-speed tomography of lithium-ion batteries during thermal runaway.* Nat Communications, 2015. 6.
64. Finegan, D.P., et al., *Quantifying Bulk Electrode Strain and Material Displacement within Lithium Batteries via High-Speed Operando Tomography and Digital Volume Correlation.* Advanced Science, 2016. 3(3).
65. Celgard. *Celgard High Performance Battery Separators.* 2014 26/10/14]; Available from: http://www.celgard.com/pdf/library/celgard_product_comparison_10002.pdf.

66. Roth, E.P., D.H. Doughty, and D.L. Pile, *Effects of separator breakdown on abuse response of 18650 Li-ion cells.* Journal of Power Sources, 2007. 174(2): p. 579-583.
67. Zhu, X., et al., *A Highly Thermostable Ceramic-Grafted Microporous Polyethylene Separator for Safer Lithium-Ion Batteries.* ACS Applied Materials & Interfaces, 2015. 7(43): p. 24119-24126.
68. Jeon, H., et al., *A water-based Al2O3 ceramic coating for polyethylene-based microporous separators for lithium-ion batteries.* Journal of Power Sources, 2016. 315: p. 161-168.
69. Newman, J., *Optimization of Porosity and Thickness of a Battery Electrode by Means of a Reaction-Zone Model.* Journal of The Electrochemical Society, 1995. 142(1): p. 97-101.
70. Doyle, M. and J. Newman, *The use of mathematical modeling in the design of lithium/polymer battery systems.* Electrochimica Acta, 1995. 40(13–14): p. 2191-2196.
71. Pals, C.R. and J. Newman, *Thermal Modeling of the Lithium/Polymer Battery: II . Temperature Profiles in a Cell Stack.* Journal of The Electrochemical Society, 1995. 142(10): p. 3282-3288.
72. Newman, J. and W. Tiedemann, *Porous-electrode theory with battery applications.* AIChE Journal, 1975. 21(1): p. 25-41.
73. Jo, M., et al., *Effect of LiCoO2 Cathode Nanoparticle Size on High Rate Performance for Li-Ion Batteries.* Journal of The Electrochemical Society, 2009. 156(6): p. A430-A434.
74. Kehrwald, D., et al., *Local Tortuosity Inhomogeneities in a Lithium Battery Composite Electrode.* Journal of The Electrochemical Society, 2011. 158(12): p. A1393-A1399.
75. Epstein, N., *On tortuosity and the tortuosity factor in flow and diffusion through porous media.* Chemical Engineering Science, 1989. 44(3): p. 777-779.
76. Billaud, J., et al., *Magnetically aligned graphite electrodes for high-rate performance Li-ion batteries.* Nature Energy, 2016. 1: p. 16097.
77. MacMullin, R.B. and G.A. Muccini, *Characteristics of porous beds and structures.* AIChE Journal, 1956. 2(3): p. 393-403.
78. Wang, X., et al., *Understanding Volume Change in Lithium-Ion Cells during Charging and Discharging Using In Situ Measurements.* Journal of The Electrochemical Society, 2007. 154(1): p. A14-A21.
79. Chin, T.E., et al., *Lithium Rechargeable Batteries as Electromechanical Actuators.* Electrochemical and Solid-State Letters, 2006. 9(3): p. A134-A138.
80. Kostecki, R. and F. McLarnon, *Microprobe study of the effect of Li intercalation on the structure of graphite.* Journal of Power Sources, 2003. 119–121(0): p. 550-554.

81. Ebner, M., et al., *Visualization and Quantification of Electrochemical and Mechanical Degradation in Li Ion Batteries.* Science, 2013. 342(6159): p. 716-720.
82. Eastwood, D.S., et al., *Lithiation-Induced Dilation Mapping in a Lithium-Ion Battery Electrode by 3D X-Ray Microscopy and Digital Volume Correlation.* Advanced Energy Materials, 2013.
83. Nelson Weker, J. and M.F. Toney, *Emerging In Situ and Operando Nanoscale X-Ray Imaging Techniques for Energy Storage Materials.* Advanced Functional Materials, 2015. 25(11): p. 1622-1637.
84. Liu, X., et al., *Distinct charge dynamics in battery electrodes revealed by in situ and operando soft X-ray spectroscopy.* Nat Commun, 2013. 4.
85. Siegel, J.B., et al., *Neutron Imaging of Lithium Concentration in LFP Pouch Cell Battery.* Journal of The Electrochemical Society, 2011. 158(5): p. A523-A529.
86. Nelson, J., et al., *In Operando X-ray Diffraction and Transmission X-ray Microscopy of Lithium Sulfur Batteries.* Journal of the American Chemical Society, 2012. 134(14): p. 6337-6343.
87. Murayama, H., et al., *Spectroscopic X-ray Diffraction for Microfocus Inspection of Li-Ion Batteries.* The Journal of Physical Chemistry C, 2014. 118(36): p. 20750-20755.
88. Ulvestad, A., et al., *Single Particle Nanomechanics in Operando Batteries via Lensless Strain Mapping.* Nano Letters, 2014. 14(9): p. 5123-5127.
89. Ulvestad, A., et al., *In situ strain evolution during a disconnection event in a battery nanoparticle.* Physical Chemistry Chemical Physics, 2015. 17(16): p. 10551-10555.
90. Lee, K.T. and J. Cho, *Roles of nanosize in lithium reactive nanomaterials for lithium ion batteries.* Nano Today, 2011. 6(1): p. 28-41.
91. Etacheri, V., et al., *Challenges in the development of advanced Li-ion batteries: a review.* Energy & Environmental Science, 2011. 4(9): p. 3243-3262.
92. Favors, Z., et al., *Stable Cycling of SiO2 Nanotubes as High-Performance Anodes for Lithium-Ion Batteries.* Sci. Rep., 2014. 4.
93. Beaulieu, L.Y., et al., *Colossal Reversible Volume Changes in Lithium Alloys.* Electrochemical and Solid-State Letters, 2001. 4(9): p. A137-A140.
94. Liu, X.H., et al., *Size-Dependent Fracture of Silicon Nanoparticles During Lithiation.* ACS Nano, 2012. 6(2): p. 1522-1531.
95. Kostecki, R. and F. McLarnon, *Local-Probe Studies of Degradation of Composite LiNi0.8Co0.15Al0.05 O 2 Cathodes in High-Power Lithium-Ion Cells.* Electrochemical and Solid-State Letters, 2004. 7(10): p. A380-A383.
96. Vetter, J., et al., *Ageing mechanisms in lithium-ion batteries.* Journal of Power Sources, 2005. 147(1–2): p. 269-281.

97. Woodford, W.H., Y.-M. Chiang, and W.C. Carter, *"Electrochemical Shock" of Intercalation Electrodes: A Fracture Mechanics Analysis.* Journal of The Electrochemical Society, 2010. 157(10): p. A1052-A1059.
98. Park, J., W. Lu, and A.M. Sastry, *Numerical Simulation of Stress Evolution in Lithium Manganese Dioxide Particles due to Coupled Phase Transition and Intercalation.* Journal of The Electrochemical Society, 2011. 158(2): p. A201-A206.
99. Gaberscek, M., et al., *The Importance of Interphase Contacts in Li Ion Electrodes: The Meaning of the High-Frequency Impedance Arc.* Electrochemical and Solid-State Letters, 2008. 11(10): p. A170-A174.
100. Lin, C.-k., et al., *Probing Thermally Induced Decomposition of Delithiated Li1.2–xNi0.15Mn0.55Co0.1O2 by in Situ High-Energy X-ray Diffraction.* ACS Applied Materials & Interfaces, 2014. 6(15): p. 12692-12697.
101. Röder, P., N. Baba, and H.D. Wiemhöfer, *A detailed thermal study of a Li[Ni0.33Co0.33Mn0.33]O2/LiMn2O4-based lithium ion cell by accelerating rate and differential scanning calorimetry.* Journal of Power Sources, 2014. 248: p. 978-987.
102. Spotnitz, R. and J. Franklin, *Abuse behavior of high-power, lithium-ion cells.* Journal of Power Sources, 2003. 113(1): p. 81-100.
103. Choi, N.-S., et al., *Challenges Facing Lithium Batteries and Electrical Double-Layer Capacitors.* Angewandte Chemie International Edition, 2012. 51(40): p. 9994-10024.
104. Goodenough, J.B. and Y. Kim, *Challenges for Rechargeable Li Batteries†.* Chemistry of Materials, 2009. 22(3): p. 587-603.
105. Kim, G.-H., A. Pesaran, and R. Spotnitz, *A three-dimensional thermal abuse model for lithium-ion cells.* Journal of Power Sources, 2007. 170(2): p. 476-489.
106. Hatchard, T.D., et al., *Thermal Model of Cylindrical and Prismatic Lithium-Ion Cells.* Journal of The Electrochemical Society, 2001. 148(7): p. A755-A761.
107. Roth, E.P. and D.H. Doughty, *Thermal abuse performance of high-power 18650 Li-ion cells.* Journal of Power Sources, 2004. 128(2): p. 308-318.
108. Chen, Z., et al., *Multi-scale study of thermal stability of lithiated graphite.* Energy & Environmental Science, 2011. 4(10): p. 4023-4030.
109. Abraham, D.P., et al., *Diagnostic examination of thermally abused high-power lithium-ion cells.* Journal of Power Sources, 2006. 161(1): p. 648-657.
110. Haik, O., et al., *On the Thermal Behavior of Lithium Intercalated Graphites.* Journal of The Electrochemical Society, 2011. 158(8): p. A913-A923.
111. Wang, Q., et al., *Thermal Behavior of Lithiated Graphite with Electrolyte in Lithium-Ion Batteries.* Journal of The Electrochemical Society, 2006. 153(2): p. A329-A333.

112. Gachot, G., et al., *Thermal behaviour of the lithiated-graphite/electrolyte interface through GC/MS analysis.* Electrochimica Acta, 2012. 83(0): p. 402-409.
113. Doh, C.-H., et al., *Thermal and electrochemical behaviour of C/LixCoO2 cell during safety test.* Journal of Power Sources, 2008. 175(2): p. 881-885.
114. MacNeil, D.D. and J.R. Dahn, *The Reactions of Li0.5CoO2 with Nonaqueous Solvents at Elevated Temperatures.* Journal of The Electrochemical Society, 2002. 149(7): p. A912-A919.
115. Golubkov, A.W., et al., *Thermal-runaway experiments on consumer Li-ion batteries with metal-oxide and olivin-type cathodes.* RSC Advances, 2014. 4(7): p. 3633-3642.
116. Jhu, C.-Y., et al., *Thermal explosion hazards on 18650 lithium ion batteries with a VSP2 adiabatic calorimeter.* Journal of Hazardous Materials, 2011. 192(1): p. 99-107.
117. Ohsaki, T., et al., *Overcharge reaction of lithium-ion batteries.* Journal of Power Sources, 2005. 146(1–2): p. 97-100.
118. Golubkov, A.W., et al., *Thermal runaway of commercial 18650 Li-ion batteries with LFP and NCA cathodes - impact of state of charge and overcharge.* RSC Advances, 2015. 5(70): p. 57171-57186.
119. Richard, M.N. and J.R. Dahn, *Accelerating Rate Calorimetry Study on the Thermal Stability of Lithium Intercalated Graphite in Electrolyte. I. Experimental.* Journal of The Electrochemical Society, 1999. 146(6): p. 2068-2077.
120. Wang, Q., et al., *Thermal stability of LiPF6/EC + DEC electrolyte with charged electrodes for lithium ion batteries.* Thermochimica Acta, 2005. 437(1–2): p. 12-16.
121. Leising, R.A., et al., *A study of the overcharge reaction of lithium-ion batteries.* Journal of Power Sources, 2001. 97–98(0): p. 681-683.
122. Leising, R.A., et al., *Abuse Testing of Lithium-Ion Batteries: Characterization of the Overcharge Reaction of LiCoO2/Graphite Cells.* Journal of The Electrochemical Society, 2001. 148(8): p. A838-A844.
123. MacNeil, D.D. and J.R. Dahn, *The Reaction of Charged Cathodes with Nonaqueous Solvents and Electrolytes: I. Li0.5CoO2.* Journal of The Electrochemical Society, 2001. 148(11): p. A1205-A1210.
124. MacNeil, D.D., D. Larcher, and J.R. Dahn, *Comparison of the Reactivity of Various Carbon Electrode Materials with Electrolyte at Elevated Temperature.* Journal of The Electrochemical Society, 1999. 146(10): p. 3596-3602.
125. Jiang, J. and J.R. Dahn, *Effects of particle size and electrolyte salt on the thermal stability of Li0.5CoO2.* Electrochimica Acta, 2004. 49(16): p. 2661-2666.
126. Geder, J., et al., *Impact of active material surface area on thermal stability of LiCoO2 cathode.* Journal of Power Sources, 2014. 257: p. 286-292.

127. Dahn, J.R., et al., *Thermal stability of LixCoO2, LixNiO2 and λ-MnO2 and consequences for the safety of Li-ion cells.* Solid State Ionics, 1994. 69(3–4): p. 265-270.
128. Orendorff, C., et al., *Quantification of lithium-ion cell thermal runaway energetics*, in *Sandia Report*. 2016, Sandia National Labs: Sandia National Labs.
129. Ribiere, P., et al., *Investigation on the fire-induced hazards of Li-ion battery cells by fire calorimetry.* Energy & Environmental Science, 2012. 5(1): p. 5271-5280.
130. Kong, W., et al., *Gas evolution behaviors for several cathode materials in lithium-ion batteries.* Journal of Power Sources, 2005. 142(1–2): p. 285-291.
131. Holzapfel, M., et al., *Oxygen, hydrogen, ethylene and CO2 development in lithium-ion batteries.* Journal of Power Sources, 2007. 174(2): p. 1156-1160.
132. Lee, J.-H., et al., *Effect of Carboxymethyl Cellulose on Aqueous Processing of Natural Graphite Negative Electrodes and their Electrochemical Performance for Lithium Batteries.* Journal of The Electrochemical Society, 2005. 152(9): p. A1763-A1769.
133. Yang, C.R., Y.Y. Wang, and C.C. Wan, *Composition analysis of the passive film on the carbon electrode of a lithium-ion battery with an EC-based electrolyte.* Journal of Power Sources, 1998. 72(1): p. 66-70.
134. Aurbach, D., et al., *The behaviour of lithium electrodes in propylene and ethylene carbonate: Te major factors that influence Li cycling efficiency.* Journal of Electroanalytical Chemistry, 1992. 339(1–2): p. 451-471.
135. Onuki, M., et al., *Identification of the Source of Evolved Gas in Li-Ion Batteries Using #2#1 -labeled Solvents.* Journal of The Electrochemical Society, 2008. 155(11): p. A794-A797.
136. Botte, G.G. and T.J. Bauer, *MRSST a new method to evaluate thermal stability of electrolytes for lithium ion batteries.* Journal of Power Sources, 2003. 119–121(0): p. 815-820.
137. Belharouak, I., et al., *Safety characteristics of Li(Ni0.8Co0.15Al0.05)O2 and Li(Ni1/3Co1/3Mn1/3)O2.* Electrochemistry Communications, 2006. 8(2): p. 329-335.
138. Sloop, S.E., J.B. Kerr, and K. Kinoshita, *The role of Li-ion battery electrolyte reactivity in performance decline and self-discharge.* Journal of Power Sources, 2003. 119–121(0): p. 330-337.
139. Yufit, V., et al., *Investigation of lithium-ion polymer battery cell failure using X-ray computed tomography.* Electrochemistry Communications, 2011. 13(6): p. 608-610.
140. Lee, K.H., et al., *Mechanism of gas build-up in a Li-ion cell at elevated temperature.* Journal of Power Sources, 2004. 132(1–2): p. 201-205.
141. Gaines, L. and R. Cuenca *Costs of Lithium-Ion Batteries for Vehicels.* 2000.

142. Ozawa, K., *Lithium-ion rechargeable batteries with LiCoO2 and carbon electrodes: the LiCoO2/C system.* Solid State Ionics, 1994. 69(3–4): p. 212-221.
143. Wang, Q., et al., *Thermal runaway caused fire and explosion of lithium ion battery.* Journal of Power Sources, 2012. 208(0): p. 210-224.
144. Aiken, C.P., et al., *An Apparatus for the Study of In Situ Gas Evolution in Li-Ion Pouch Cells.* Journal of The Electrochemical Society, 2014. 161(10): p. A1548-A1554.
145. Balakrishnan, P.G., R. Ramesh, and T. Prem Kumar, *Safety mechanisms in lithium-ion batteries.* Journal of Power Sources, 2006. 155(2): p. 401-414.
146. Coman, P.T., S. Rayman, and R.E. White, *A lumped model of venting during thermal runaway in a cylindrical Lithium Cobalt Oxide lithium-ion cell.* Journal of Power Sources, 2016. 307: p. 56-62.
147. Robinson, J.B., et al., *Non-uniform temperature distribution in Li-ion batteries during discharge – A combined thermal imaging, X-ray micro-tomography and electrochemical impedance approach.* Journal of Power Sources, 2014. 252(0): p. 51-57.
148. Feng, X.M., X.P. Ai, and H.X. Yang, *A positive-temperature-coefficient electrode with thermal cut-off mechanism for use in rechargeable lithium batteries.* Electrochemistry Communications, 2004. 6(10): p. 1021-1024.
149. Baginska, M., et al., *Autonomic Shutdown of Lithium-Ion Batteries Using Thermoresponsive Microspheres.* Advanced Energy Materials, 2012. 2(5): p. 583-590.
150. Lu, L., et al., *A review on the key issues for lithium-ion battery management in electric vehicles.* Journal of Power Sources, 2013. 226(0): p. 272-288.
151. Darcy, E., *Screening Li-ion batteries for internal shorts.* Journal of Power Sources, 2007. 174(2): p. 575-578.
152. Tobishima, S.-i. and J.-i. Yamaki, *A consideration of lithium cell safety.* Journal of Power Sources, 1999. 81–82: p. 882-886.
153. Spotnitz, R. and R. Mullar, *Simulation of Abuse Behaviour of Lithium-Ion Batteries.* The Electrochemical Society Interface, 2012. 21(2).
154. Santhanagopalan, S., P. Ramadass, and J. Zhang, *Analysis of internal short circuit in a lithium ion cell.* Journal of Power Sources, 2009. 194(1): p. 550-557.
155. Maleki, H. and J.N. Howard, *Internal short circuit in Li-ion cells.* Journal of Power Sources, 2009. 191(2): p. 568-574.
156. Orendorff, C.J., E.P. Roth, and G. Nagasubramanian, *Experimental triggers for internal short circuits in lithium-ion cells.* Journal of Power Sources, 2011. 196(15): p. 6554-6558.
157. Keyser, M., et al., *Passive safety device and internal short tested method for energy storage cells and systems*, U.S. Patent, Editor. 2015, Alliance for Sustainable Energy, LLC: United States. p. US 9142829B2.

158. NTSB, *Interim Factual Report, DCA13IA037*, M. Boston, Editor. 2013, Office of Aviation Safety.
159. Lisbona, D. and T. Snee, *A review of hazards associated with primary lithium and lithium-ion batteries.* Process Safety and Environmental Protection, 2011. 89(6): p. 434-442.
160. IATA. *Lithium Batteries as Cargo in 2016 update III.* 2016; Available from: http://www.iata.org/whatwedo/cargo/dgr/Documents/lithium-battery-update.pdf.
161. *UN Manual of Tests and Criteria*, in *Section 38.3, Lithium metal and lithium ion batteries.* 2009, United Nations: New York.
162. IEC, *Battery Safety Test Standard IEC 62133*, in *Section 8.3.9 Forced short circuit test.* 2015.
163. Underwriters-Laboratories, *UL 1642 - Standard for Lithium Batteries.* 2012.
164. Underwriters-Laboratories, *UL 2054 - Standard for Household and Commercial Batteries.* 2004.
165. Doughty, D.H. and C. Crafts, *FreedomCAR Electrical Energy Storage System Abuse Test Manual for Electric and Hybrid Electric Vehicle Applications* in *Sandia Report*, S.N. Laboratories, Editor. 2006, Sandia National Laboratories: Sandia National Laboratories.
166. Unkelhaeuser, T. and D. Smallwood, *SAND99-0497 Sandia National Laboratories Electrochemical Storage System Abuse Test Procedure Manual.* 1999, Sandia National Labs.
167. Xia, Y., et al., *Damage of cells and battery packs due to ground impact.* Journal of Power Sources, 2014. 267: p. 78-97.
168. Huang, P., et al., *Experimental and modeling analysis of thermal runaway propagation over the large format energy storage battery module with Li4Ti5O12 anode.* Applied Energy, 2016. 183: p. 659-673.
169. Sahraei, E., J. Campbell, and T. Wierzbicki, *Modeling and short circuit detection of 18650 Li-ion cells under mechanical abuse conditions.* Journal of Power Sources, 2012. 220(0): p. 360-372.
170. Lamb, J. and C.J. Orendorff, *Evaluation of mechanical abuse techniques in lithium ion batteries.* Journal of Power Sources, 2014. 247(0): p. 189-196.
171. Hatchard, T.D., S. Trussler, and J.R. Dahn, *Building a "smart nail" for penetration tests on Li-ion cells.* Journal of Power Sources, 2014. 247(0): p. 821-823.
172. Chen, Z., Y. Qin, and K. Amine, *Redox shuttles for safer lithium-ion batteries.* Electrochimica Acta, 2009. 54(24): p. 5605-5613.
173. Lopez, C.F., J.A. Jeevarajan, and P.P. Mukherjee, *Experimental Analysis of Thermal Runaway and Propagation in Lithium-Ion Battery Modules.* Journal of The Electrochemical Society, 2015. 162(9): p. A1905-A1915.
174. Maire, E. and P. Withers, *Full Critical Review - Quantitative X-ray Tomography.* International Materials Reviews, 2014. 59(1): p. 1-43.

175. Eastwood, D.S., et al., *Three-dimensional characterization of electrodeposited lithium microstructures using synchrotron X-ray phase contrast imaging.* Chemical Communications, 2015. 51(2): p. 266-268.
176. Shearing, P.R., et al., *Multi Length Scale Microstructural Investigations of a Commercially Available Li-Ion Battery Electrode.* Journal of The Electrochemical Society, 2012. 159(7): p. A1023-A1027.
177. Shearing, P.R., et al., *Characterization of the 3-dimensional microstructure of a graphite negative electrode from a Li-ion battery.* Electrochemistry Communications, 2010. 12(3): p. 374-377.
178. Tariq, F., et al., *Three-dimensional high resolution X-ray imaging and quantification of lithium ion battery mesocarbon microbead anodes.* Journal of Power Sources, 2014. 248(0): p. 1014-1020.
179. Ebner, M., et al., *X-Ray Tomography of Porous, Transition Metal Oxide Based Lithium Ion Battery Electrodes.* Advanced Energy Materials, 2013. 3(7): p. 845-850.
180. Chen-Wiegart, Y.-c.K., et al., *3D morphological evolution of Li-ion battery negative electrode LiVO2 during oxidation using X-ray nano-tomography.* Electrochemistry Communications, 2012. 21(0): p. 58-61.
181. Eastwood, D.S., et al., *The application of phase contrast X-ray techniques for imaging Li-ion battery electrodes.* Nuclear Instruments and Methods in Physics Research Section B: Beam Interactions with Materials and Atoms, 2014. 324(0): p. 118-123.
182. Taiwo, O.O., et al., *The use of contrast enhancement techniques in X-ray imaging of lithium–ion battery electrodes.* Chemical Engineering Science, 2016. 154: p. 27-33.
183. Paz-Garcia, J.M., et al., *4D analysis of the microstructural evolution of Si-based electrodes during lithiation: Time-lapse X-ray imaging and digital volume correlation.* Journal of Power Sources, 2016. 320: p. 196-203.
184. Rack, A., et al., *Exploiting coherence for real-time studies by single-bunch imaging.* Journal of Synchrotron Radiation, 2014. 21(4): p. 815-818.
185. Dobson, K.J., et al., *4-D imaging of sub-second dynamics in pore-scale processes using real-time synchrotron X-ray tomography.* Solid Earth, 2016. 7(4): p. 1059-1073.
186. Cnudde, V. and M.N. Boone, *High-resolution X-ray computed tomography in geosciences: A review of the current technology and applications.* Earth-Science Reviews, 2013. 123: p. 1-17.
187. Hall, S., et al., *Localised deformation patterning in 2D granular materials revealed by digital image correlation.* Granular Matter, 2010. 12(1): p. 1-14.
188. Hall, S.A., et al., *Discrete and continuum analysis of localised deformation in sand using X-ray μCT and volumetric digital image correlation.* Géotechnique, 2010. 60: p. 315-322.

189. Eastwood, D.S., et al., *Lithiation-Induced Dilation Mapping in a Lithium-Ion Battery Electrode by 3D X-Ray Microscopy and Digital Volume Correlation.* Advanced Energy Materials, 2014. 4(4).
190. Röntgen, W.C., *Ueber eine neue Art von Strahlen.* Annalen der Physik, 1898. 300(1): p. 12-17.
191. Cooper, S.J., et al., *Image based modelling of microstructural heterogeneity in LiFePO4 electrodes for Li-ion batteries.* Journal of Power Sources, (0).
192. Thiedmann, R., et al., *Stochastic simulation model for the 3D morphology of composite materials in Li–ion batteries.* Computational Materials Science, 2011. 50(12): p. 3365-3376.
193. Salvo, L., et al., *X-ray micro-tomography an attractive characterisation technique in materials science.* Nuclear Instruments and Methods in Physics Research Section B: Beam Interactions with Materials and Atoms, 2003. 200(0): p. 273-286.
194. Banhart, J., *Advanced Tomographic Methods in Materials Research and Engineering*, ed. O.U. Press. 2008, Oxford: Oxford University Press.
195. Willmott, P., *Synchrotron Physics*, in *An Introduction to Synchrotron Radiation*. 2011, Wiley.
196. Willmott, P., *An Introduction to Synchrotron Radiation: Techniques and Applications*. 2011: Wiley.
197. Poludniowski, G., et al., *SpekCalc : a program to calculate photon spectra from tungsten anode x-ray tubes.* Physics in Medicine and Biology, 2009. 54(19): p. N433.
198. Buzug, T., *Computed tomography: From statistics to modern cone-beam CT*. 2008: Springer.
199. Buzug, T., *Fundamentals of X-ray Physics*, in *Computed tomography: From statistics to modern cone-beam CT*. 2008, Springer. p. 16-22.
200. Chantler, C., et al. *X-ray Form Factor, Attenuation and Scattering Tables.* Detailed Tabulation of Atomic Form Factors, Photoelectric Absorption and Scattering Cross Section, and Mass Attenuation Coefficients for Z = 1-92 from E = 1-10 eV to E = 0.4-1.0 MeV, 2005.
201. Hubbell, J.H. and S.M. Seltzer, *Tables of X-Ray Mass Attenuation Coefficients and Mass Energy-Absorption Coefficients from 1 keV to 20 MeV for Elements Z = 1 to 92 and 48 Additional Substances of Dosimetric Interest*, in *NIST Physical Reference Data, NIST Standard Reference Database 126*, NIST, Editor. 2004: http://www.nist.gov/pml/data/xraycoef/.
202. Banhart, J., *Radiation Sources and Interaction of the Radiation with Matter*, in *Advanced Tomographic Methods in Materials Research and Engineering*. 2008, Oxford University Press. p. 107-138.
203. Salvo, L., et al., *3D imaging in material science: Application of X-ray tomography.* Comptes Rendus Physique, 2010. 11(9–10): p. 641-649.
204. Slaney, M. and A.C. Kak, *Principles of Computerized Tomographic Imaging*, ed. I. Press. 1988: IEEE Press.

205. Holzner, C., et al., *Zernike phase contrast in scanning microscopy with X-rays.* Nat Phys, 2010. 6(11): p. 883-887.
206. Tkachuk, A., et al., *X-ray computed tomography in Zernike phase contrast mode at 8 keV with 50-nm resolution using Cu rotating anode X-ray source*, in *Zeitschrift für Kristallographie - Crystalline Materials*. 2007. p. 650.
207. Neuhäusler, U., et al., *X-ray microscopy in Zernike phase contrast mode at 4 keV photon energy with 60 nm resolution.* Journal of Physics D: Applied Physics, 2003. 36(10A): p. A79.
208. Di Michiel, M., et al., *Fast microtomography using high energy synchrotron radiation.* Review of Scientific Instruments, 2005. 76(4): p. -.
209. Boas, F.E. and D. Fleischmann, *CT artifacts: causes and reduction techniques.* Imaging in Medicine, 2012. 4(2): p. 229-240.
210. Buades, A., B. Coll, and J. Morel, *A Review of Image Denoising Algorithms, with a New One.* Multiscale Modeling & Simulation, 2005. 4(2): p. 490-530.
211. Newman, J.S. and C.W. Tobias, *Theoretical Analysis of Current Distribution in Porous Electrodes.* Journal of The Electrochemical Society, 1962. 109(12): p. 1183-1191.
212. Doyle, M. and J. Newman, *Modeling the performance of rechargeable lithium-based cells: design correlations for limiting cases.* Journal of Power Sources, 1995. 54(1): p. 46-51.
213. Doyle, M., et al., *Comparison of Modeling Predictions with Experimental Data from Plastic Lithium Ion Cells.* Journal of The Electrochemical Society, 1996. 143(6): p. 1890-1903.
214. Fuller, T.F., M. Doyle, and J. Newman, *Simulation and Optimization of the Dual Lithium Ion Insertion Cell.* Journal of The Electrochemical Society, 1994. 141(1): p. 1-10.
215. Thorat, I.V., et al., *Quantifying tortuosity in porous Li-ion battery materials.* Journal of Power Sources, 2009. 188(2): p. 592-600.
216. Paul Shearing, Y.W., Stephen Harris, Nigel Brandon, *In Situ X-Ray Spectroscopy and Imaging of Battery Materials.* The Electrochemical Society Interface, 2011. Fall 2011.
217. Ebner, M., et al., *Tortuosity Anisotropy in Lithium-Ion Battery Electrodes.* Advanced Energy Materials, 2014. 4(5): p. n/a-n/a.
218. Ebner, M., et al., *Electrode Materials: X-Ray Tomography of Porous, Transition Metal Oxide Based Lithium Ion Battery Electrodes (Adv. Energy Mater. 7/2013).* Advanced Energy Materials, 2013. 3(7): p. 825-825.
219. Ebner, M. and V. Wood, *Tool for Tortuosity Estimation in Lithium Ion Battery Porous Electrodes.* Journal of The Electrochemical Society, 2015. 162(2): p. A3064-A3070.

220. Taiwo, O.O., et al., *Comparison of three-dimensional analysis and stereological techniques for quantifying lithium-ion battery electrode microstructures.* Journal of Microscopy, 2016: p. n/a-n/a.
221. Holzer, L., et al., *The influence of constrictivity on the effective transport properties of porous layers in electrolysis and fuel cells.* Journal of Materials Science, 2012. 48(7): p. 2934-2952.
222. Münch, B. and L. Holzer, *Contradicting Geometrical Concepts in Pore Size Analysis Attained with Electron Microscopy and Mercury Intrusion.* Journal of the American Ceramic Society, 2008. 91(12): p. 4059-4067.
223. Tjaden, B., et al., *The application of 3D imaging techniques, simulation and diffusion experiments to explore transport properties in porous oxygen transport membrane support materials.* Solid State Ionics.
224. Exner, H.E., *STEREOLOGY AND 3D MICROSCOPY: USEFUL ALTERNATIVES OR COMPETITORS IN THE QUANTITATIVE ANALYSIS OF MICROSTRUCTURES?* 2011, 2011. 23(2): p. 10.
225. Russ, J.C., *Manual Methods*, in *Practical Stereology*. 1986, Plenum Press: New York. p. 42,43.
226. Yamamoto, O., et al., *Proceedings of the Eighth International Meeting on Lithium BatteriesInfluence of the LiCoO2 particle size on the performance of lithium-ion batteries.* Journal of Power Sources, 1997. 68(2): p. 533-535.
227. Chung, D.-W., et al., *Particle Size Polydispersity in Li-Ion Batteries.* Journal of The Electrochemical Society, 2014. 161(3): p. A422-A430.
228. Landesfeind, J., et al., *Tortuosity Determination of Battery Electrodes and Separators by Impedance Spectroscopy.* Journal of The Electrochemical Society, 2016. 163(7): p. A1373-A1387.
229. Cannarella, J. and C.B. Arnold, *Ion transport restriction in mechanically strained separator membranes.* Journal of Power Sources, 2013. 226: p. 149-155.
230. Kishimoto, M., et al., *Quantitative evaluation of solid oxide fuel cell porous anode microstructure based on focused ion beam and scanning electron microscope technique and prediction of anode overpotentials.* Journal of Power Sources, 2011. 196(10): p. 4555-4563.
231. JØRgensen, P.S., et al., *Geometrical characterization of interconnected phase networks in three dimensions.* Journal of Microscopy, 2011. 244(1): p. 45-58.
232. Cooper, S. *TauFactor*. 2016 [cited 2016 03/May/2016]; Available from: www.sourceforge.net/projects/taufactor/.
233. Bay, B.K., et al., *Digital volume correlation: Three-dimensional strain mapping using X-ray tomography.* Experimental Mechanics, 1999. 39(3): p. 217-226.
234. Liu, L. and E.F. Morgan, *Accuracy and precision of digital volume correlation in quantifying displacements and strains in trabecular bone.* Journal of Biomechanics, 2007. 40(15): p. 3516-3520.

235. Quinta Da Fonseca, J., P.M. Mummery, and P.J. Withers, *Full-field strain mapping by optical correlation of micrographs acquired during deformation.* Journal of Microscopy, 2005. 218(1): p. 9-21.
236. Gillard, F., et al., *The application of digital volume correlation (DVC) to study the microstructural behaviour of trabecular bone during compression.* Journal of the Mechanical Behavior of Biomedical Materials, 2014. 29: p. 480-499.
237. Hall, S.A., *A methodology for 7D warping and deformation monitoring using time-lapse seismic data.* GEOPHYSICS, 2006. 71(4): p. O21-O31.
238. Marrow, T.J., et al., *High-resolution, in-situ, tomographic observations of stress corrosion cracking*, in *Environment-Induced Cracking of Materials*, S.A. Shipilov, et al., Editors. 2008, Elsevier: Amsterdam. p. 439-447.
239. Buffière, J.Y., et al., *Characterization of internal damage in a MMCp using X-ray synchrotron phase contrast microtomography.* Acta Materialia, 1999. 47(5): p. 1613-1625.
240. Bay, B.K., *Methods and applications of digital volume correlation.* The Journal of Strain Analysis for Engineering Design, 2008. 43(8): p. 745-760.
241. Bing, P., et al., *Two-dimensional digital image correlation for in-plane displacement and strain measurement: a review.* Measurement Science and Technology, 2009. 20(6): p. 062001.
242. Wu, B., et al., *Coupled thermal–electrochemical modelling of uneven heat generation in lithium-ion battery packs.* Journal of Power Sources, 2013. 243(0): p. 544-554.
243. Troxler, Y., et al., *The effect of thermal gradients on the performance of lithium-ion batteries.* Journal of Power Sources, 2014. 247: p. 1018-1025.
244. Doughty, D. and A. Pesaran, *Vehicle Battery Safety Roadmap Guidance*, NREL, Editor. 2012, National Renewable Energy Laboratory: NREL.
245. Shi, C., et al., *Effect of a thin ceramic-coating layer on thermal and electrochemical properties of polyethylene separator for lithium-ion batteries.* Journal of Power Sources, 2014. 270: p. 547-553.
246. Chen, Z., et al., *Fast and reversible thermoresponsive polymer switching materials for safer batteries.* Nature Energy, 2016. 1: p. 15009.
247. Vaughan, G. *USGS Radiance Calculator*. 2016 13/08/16]; Available from: http://astrogeology.usgs.gov/tools/thermal-radiance-calculator/.
248. Vollmer, M. and K.-P. Mollmann, *Infrared Thermal Imaging: Fundamentals Research and Applications*, ed. W.-. VCH. 2010: Wiley - VCH. 612.
249. Hatchard, T.D., et al., *Importance of Heat Transfer by Radiation in Li - Ion Batteries during Thermal Abuse.* Electrochemical and Solid-State Letters, 2000. 3(7): p. 305-308.
250. Robinson, J.B., et al., *A novel high-temperature furnace for combined in situ synchrotron X-ray diffraction and infrared thermal imaging to investigate the effects of thermal gradients upon the structure of ceramic materials.* Journal of Synchrotron Radiation, 2014. 21(5): p. 1134-1139.

251. Orendorff, C.J., *The Role of Separators in Lithium-Ion Cell Safety.* The Electrochemical Society Interface, 2012. 21(2): p. 61-65.
252. Lee, Y., et al., *In-depth correlation of separator pore structure and electrochemical performance in lithium-ion batteries.* Journal of Power Sources, 2016. 325: p. 732-738.
253. Huang, X., *A facile approach to make high performance nano-fiber reinforced composite separator for lithium ion batteries.* Journal of Power Sources, 2016. 323: p. 17-22.
254. Diamond, S., *Mercury porosimetry: An inappropriate method for the measurement of pore size distributions in cement-based materials.* Cement and Concrete Research, 2000. 30(10): p. 1517-1525.
255. Giesche, H., *Mercury Porosimetry: A General (Practical) Overview.* Particle & Particle Systems Characterization, 2006. 23(1): p. 9-19.
256. Tjaden, B., et al., *On the origin and application of the Bruggeman correlation for analysing transport phenomena in electrochemical systems.* Current Opinion in Chemical Engineering, 2016. 12: p. 44-51.
257. Venugopal, G., et al., *Characterization of microporous separators for lithium-ion batteries.* Journal of Power Sources, 1999. 77(1): p. 34-41.
258. Lagadec, M.F., et al., *Communication—Technique for Visualization and Quantification of Lithium-Ion Battery Separator Microstructure.* Journal of The Electrochemical Society, 2016. 163(6): p. A992-A994.
259. Stock, S.R., *Recent advances in X-ray microtomography applied to materials.* International Materials Reviews, 2008. 53(3): p. 129-181.
260. Chen-Wiegart, Y.-c.K., et al., *Tortuosity characterization of 3D microstructure at nano-scale for energy storage and conversion materials.* Journal of Power Sources, 2014. 249(0): p. 349-356.
261. Tötzke, C., et al., *Three-dimensional study of compressed gas diffusion layers using synchrotron X-ray imaging.* Journal of Power Sources, 2014. 253(0): p. 123-131.
262. Vijayaraghavan, B., et al., *An Analytical Method to Determine Tortuosity in Rechargeable Battery Electrodes.* Journal of The Electrochemical Society, 2012. 159(5): p. A548-A552.
263. *Celgard 2325.* 2016 04/May/16]; Available from: http://www.ldcgm.com/Celgard/CELGARD-2400.pdf.
264. *Celgard 2500.* 04/May/16]; Available from: http://www.ldcgm.com/Celgard/CELGARD-4550.pdf.
265. *MTI ceramic coated membrane.* 04/May/16]; Available from: http://www.mtixtl.com/CeramicCoatedMembraneforLi-ionBatteryRandD-EQ-bsf-0016-500A.aspx.
266. Deimede, V. and C. Elmasides, *Separators for Lithium-Ion Batteries: A Review on the Production Processes and Recent Developments.* Energy Technology, 2015. 3(5): p. 453-468.

267. Kim, K.J., et al., *Effect of gamma ray irradiation on thermal and electrochemical properties of polyethylene separator for Li ion batteries.* Journal of Power Sources, 2010. 195(18): p. 6075-6080.
268. Coffey, T., S.G. Urquhart, and H. Ade, *Characterization of the effects of soft X-ray irradiation on polymers.* Journal of Electron Spectroscopy and Related Phenomena, 2002. 122(1): p. 65-78.
269. Peabody, C. and C.B. Arnold, *The role of mechanically induced separator creep in lithium-ion battery capacity fade.* Journal of Power Sources, 2011. 196(19): p. 8147-8153.
270. Miranda, D., et al., *Modeling separator membranes physical characteristics for optimized lithium ion battery performance.* Solid State Ionics, 2015. 278: p. 78-84.
271. Lee, H., et al., *A review of recent developments in membrane separators for rechargeable lithium-ion batteries.* Energy & Environmental Science, 2014. 7(12): p. 3857-3886.
272. Love, C.T., O.A. Baturina, and K.E. Swider-Lyons, *Observation of Lithium Dendrites at Ambient Temperature and Below.* ECS Electrochemistry Letters, 2015. 4(2): p. A24-A27.
273. Harry, K.J., et al., *Detection of subsurface structures underneath dendrites formed on cycled lithium metal electrodes.* Nat Mater, 2014. 13(1): p. 69-73.
274. Fu, D., et al., *Nano SiO2 particle formation and deposition on polypropylene separators for lithium-ion batteries.* Journal of Power Sources, 2012. 206: p. 325-333.
275. Prasanna, K., C.-S. Kim, and C.W. Lee, *Effect of SiO2 coating on polyethylene separator with different stretching ratios for application in lithium ion batteries.* Materials Chemistry and Physics, 2014. 146(3): p. 545-550.
276. Duracell *Ultra CR2 Lithium/Manganese dioxide datasheet.*
277. Cannarella, J. and C.B. Arnold, *Stress evolution and capacity fade in constrained lithium-ion pouch cells.* Journal of Power Sources, 2014. 245(0): p. 745-751.
278. Thackeray, M.M., *Manganese oxides for lithium batteries.* Progress in Solid State Chemistry, 1997. 25(1–2): p. 1-71.
279. Shao-Horn, Y., et al., *Structural Characterization of Layered LiMnO2 Electrodes by Electron Diffraction and Lattice Imaging.* Journal of The Electrochemical Society, 1999. 146(7): p. 2404-2412.
280. Lenoir, N., et al., *Volumetric Digital Image Correlation Applied to X-ray Microtomography Images from Triaxial Compression Tests on Argillaceous Rock.* Strain, 2007. 43(3): p. 193-205.
281. Zhang, G., et al., *In-Situ Measurement of Current Distribution in a Li-Ion Cell.* Journal of The Electrochemical Society, 2013. 160(4): p. A610-A615.

282. Zheng, H., et al., *A comprehensive understanding of electrode thickness effects on the electrochemical performances of Li-ion battery cathodes.* Electrochimica Acta, 2012. 71(0): p. 258-265.
283. Wang, M., et al., *The effect of local current density on electrode design for lithium-ion batteries.* Journal of Power Sources, 2012. 207(0): p. 127-133.
284. Feng, L., et al., *MnO(2) prepared by hydrothermal method and electrochemical performance as anode for lithium-ion battery.* Nanoscale Research Letters, 2014. 9(1): p. 290-290.
285. Yoon, W.-S., et al., *In situ soft XAS study on nickel-based layered cathode material at elevated temperatures: A novel approach to study thermal stability.* Sci. Rep., 2014. 4.
286. LGChem *Model ICR18650S3 Lithium-Ion Battery MSDS*. 2010.
287. LGChem *Model ICR18650B4 Lithium-Ion Battery MSDS*. 2010.
288. Kim, J., et al., *Secondary Battery*, L. Samsung Sdi Co., Editor. 2011, United States Patent Office: USA. p. US7955730 B2.
289. Kim, J.K. and S.K. Woo, *Cylindrical lithium secondary battery*, U.S. Patent, Editor. 2010, Google Patents: USA. p. US 7691530B2.
290. Woo, S.K., Y.T. Kim, and K.S. Chun, *Lithium battery with short circuit preventing core member*, L. Samsung Sdi Co., Editor. 2011, United States Patent Office: USA. p. US7939196 B2.
291. Kizilel, R., et al., *An alternative cooling system to enhance the safety of Li-ion battery packs.* Journal of Power Sources, 2009. 194(2): p. 1105-1112.
292. Larsson, F. and B.-E. Mellander, *Abuse by External Heating, Overcharge and Short Circuiting of Commercial Lithium-Ion Battery Cells.* Journal of The Electrochemical Society, 2014. 161(10): p. A1611-A1617.
293. Finegan, D.P., et al., *Investigating lithium-ion battery materials during overcharge-induced thermal runaway: an operando and multi-scale X-ray CT study.* Physical Chemistry Chemical Physics, 2016.
294. Kyrieleis, A., et al., *Image stitching strategies for tomographic imaging of large objects at high resolution at synchrotron sources.* Nuclear Instruments and Methods in Physics Research Section A: Accelerators, Spectrometers, Detectors and Associated Equipment, 2009. 607(3): p. 677-684.
295. Heubner, C., M. Schneider, and A. Michaelis, *Detailed study of heat generation in porous LiCoO2 electrodes.* Journal of Power Sources, 2016. 307: p. 199-207.
296. Yang, H., et al., *Investigations of the Exothermic Reactions of Natural Graphite Anode for Li-Ion Batteries during Thermal Runaway.* Journal of The Electrochemical Society, 2005. 152(1): p. A73-A79.
297. Lee, H.H., C.C. Wan, and Y.Y. Wang *Thermal Stability of the Solid Electrolyte Interface on Carbon Electrodes of Lithium Batteries.* Journal of The Electrochemical Society, 2004. 151(4): p. A542-A547.

298. Kim, J.-H., N.P.W. Pieczonka, and L. Yang, *Challenges and Approaches for High-Voltage Spinel Lithium-Ion Batteries.* ChemPhysChem, 2014. 15(10): p. 1940-1954.
299. Belov, D. and M.-H. Yang, *Failure mechanism of Li-ion battery at overcharge conditions.* Journal of Solid State Electrochemistry, 2008. 12(7-8): p. 885-894.
300. Krämer, E., S. Passerini, and M. Winter, *Dependency of Aluminum Collector Corrosion in Lithium Ion Batteries on the Electrolyte Solvent.* ECS Electrochemistry Letters, 2012. 1(5): p. C9-C11.
301. Lin, C.-K., et al., *In situ high-energy X-ray diffraction to study overcharge abuse of 18650-size lithium-ion battery.* Journal of Power Sources, 2013. 230(0): p. 32-37.
302. Lendzion-Bieluń, Z., R. Jędrzejewski, and W. Arabczyk, *The effect of aluminium oxide on the reduction of cobalt oxide and thermostabillity of cobalt and cobalt oxide.* Central European Journal of Chemistry, 2011. 9(5): p. 834-839.
303. NASA, *Technical Report: NASA Aerospace Flight Battery Program.* 2008, NASA Engineering and Safety Centre.
304. Tsujikawa, T., et al., *Safety of large-capacity lithium-ion battery and evaluation of battery system for telecommunications.* Journal of Power Sources, 2013. 244: p. 11-16.
305. Cabrera-Castillo, E., F. Niedermeier, and A. Jossen, *Calculation of the state of safety (SOS) for lithium ion batteries.* Journal of Power Sources, 2016. 324: p. 509-520.
306. Chen, J., et al., *Probing the Roles of Polymeric Separators in Lithium-Ion Battery Capacity Fade at Elevated Temperatures.* Journal of The Electrochemical Society, 2014. 161(9): p. A1241-A1246.
307. Harris, S.J., A. Timmons, and W.J. Pitz, *A combustion chemistry analysis of carbonate solvents used in Li-ion batteries.* Journal of Power Sources, 2009. 193(2): p. 855-858.
308. Kim, J., et al., *Deformable core for a cylindrical lithium secondary battery.* 2012, United States Patent. p. US 7955730B2.
309. Kim, D.K., *Rechargeable battery*, U.S. Patent, Editor. 2014. p. US 2014/0045052A1.
310. Murashige, S. and A. Naoto, *Cylindrical lithium ion secondary battery and fabrication method thereof*, U.S. patent, Editor. 2004. p. US 6811920B2.

Appendices

10.1. Chapter 4 Appendix

10.1.1. Comparison of Greyscale and Segmented Images

The reconstructed greyscale images were segmented using Avizo Fire 9's threshold segmentation editor. Figure 10-1 to Figure 10-10 show the original greyscale images alongside the segmented images for comparison; Figure 10-1 to Figure 10-4 show Celgard 2325, Figure 10-5 to Figure 10-7 show Celgard 2500, and Figure 10-8 to Figure 10-10 show the MTI ceramic coated separator.

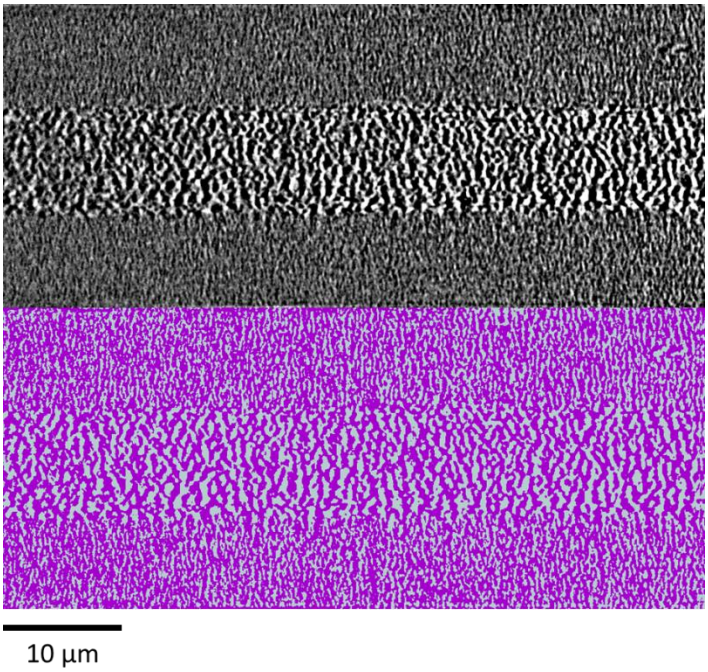

Figure 10-1: Greyscale (top) and corresponding binary slice (bottom) from the *YZ* plane of Celgard 2325.

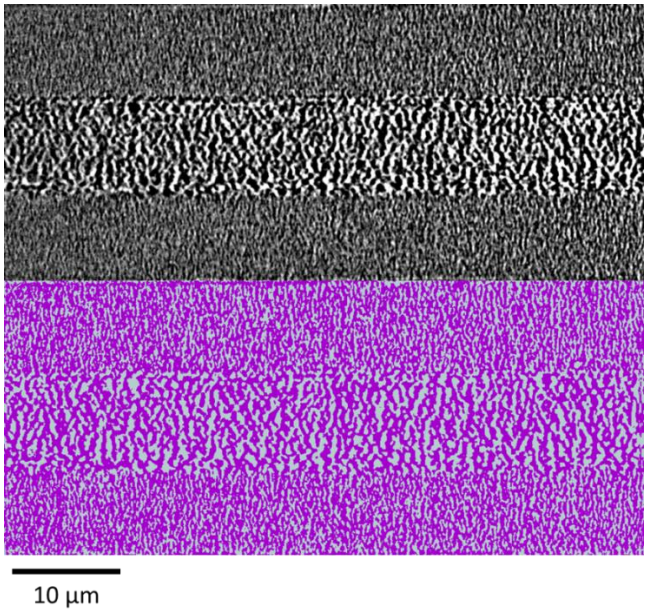

Figure 10-2: Greyscale (top) and corresponding binary slice (bottom) from the *YZ* plane of Celgard 2325.

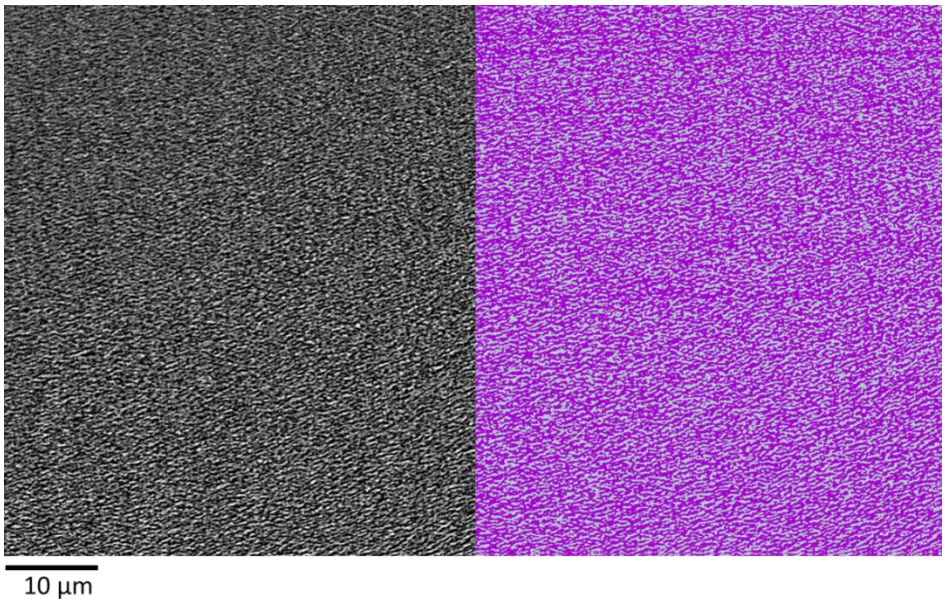

Figure 10-3: Greyscale (left) and corresponding binary slice (right) from the *XY* plane of PP layer of Celgard 2325.

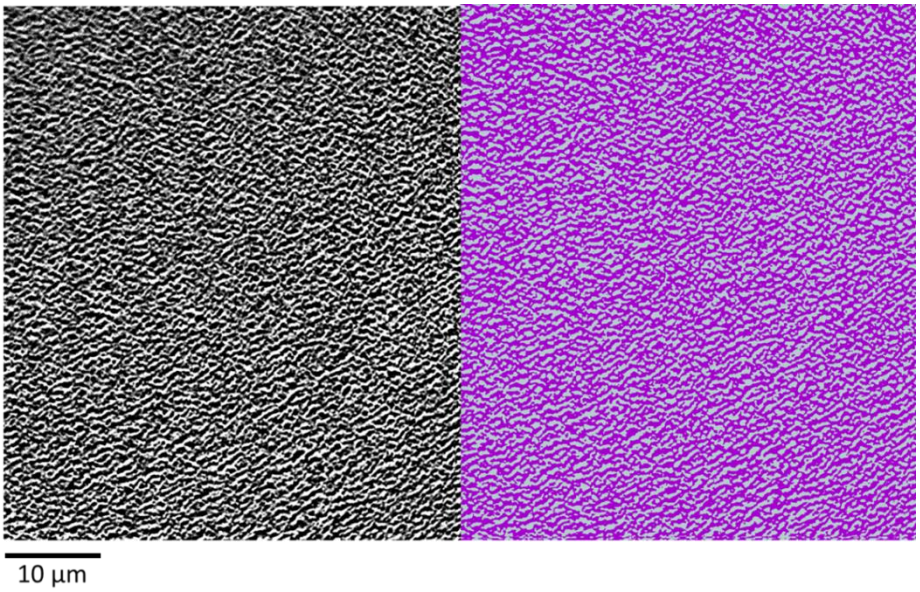

Figure 10-4: Greyscale (left) and corresponding binary slice (right) from the XY plane of central PE layer of Celgard 2325.

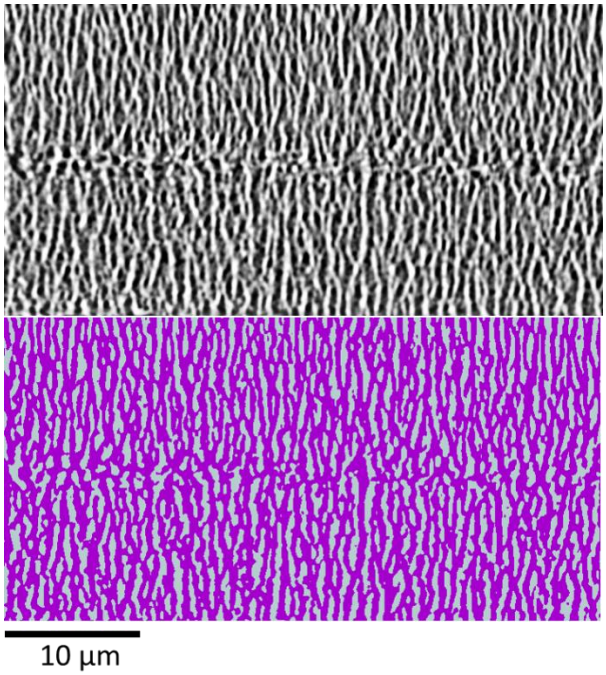

Figure 10-5: Greyscale (top) and corresponding binary slice (bottom) from the YZ plane of Celgard 2500.

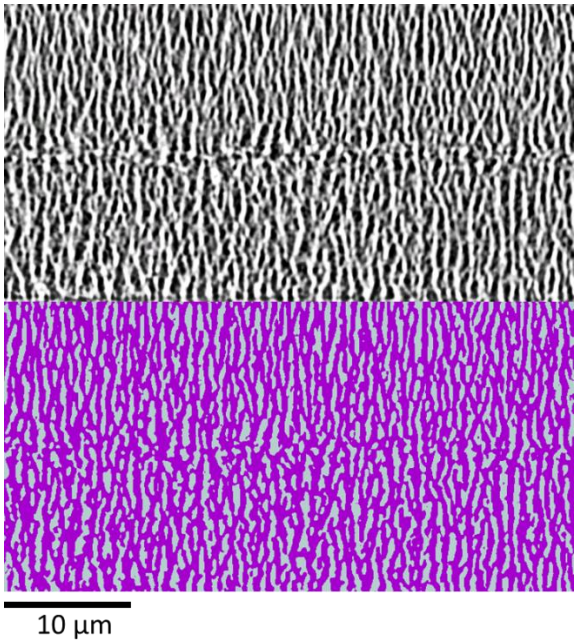

Figure 10-6: Greyscale (top) and corresponding binary slice (bottom) from the *YZ* plane of Celgard 2500.

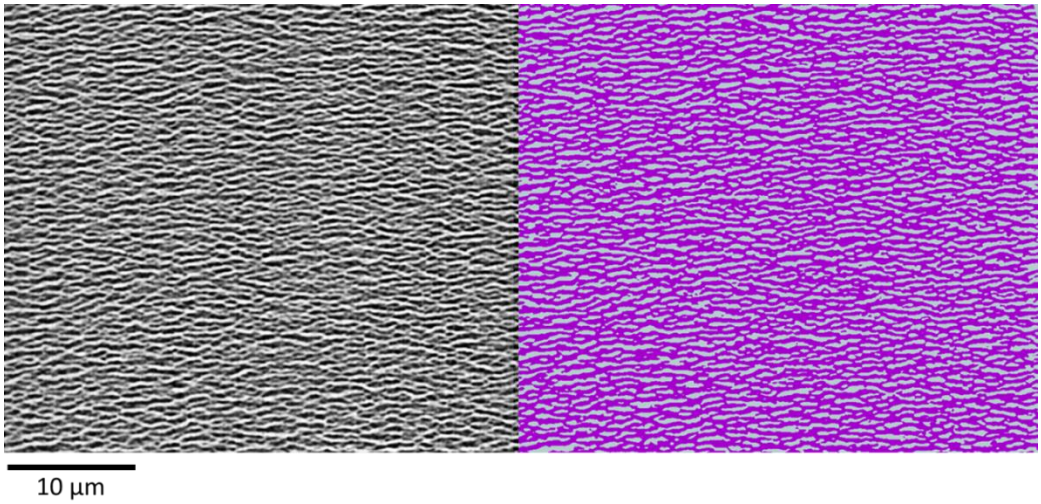

Figure 10-7: Greyscale (left) and corresponding binary slice (right) from the *XY* plane of Celgard 2500.

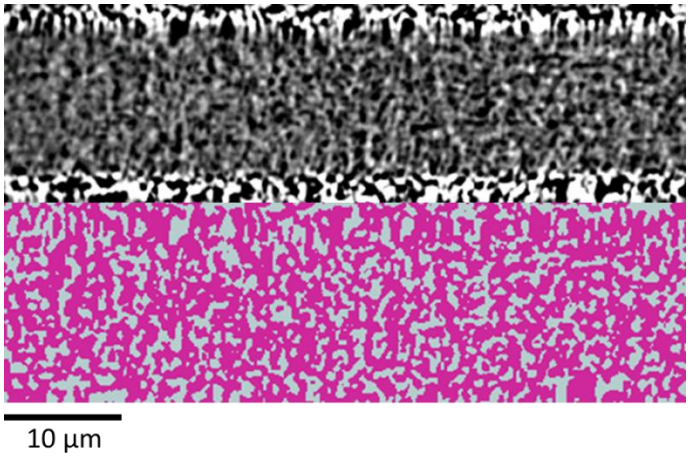

Figure 10-8: Greyscale (top) and corresponding binary slice (bottom) from the *YZ* plane of the MTI ceramic coated separator.

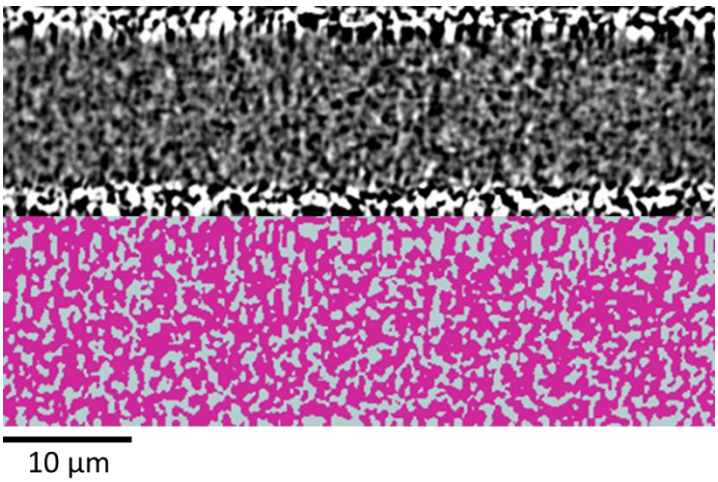

Figure 10-9: Greyscale (top) and corresponding binary slice (bottom) from the *YZ* plane of the MTI ceramic coated separator.

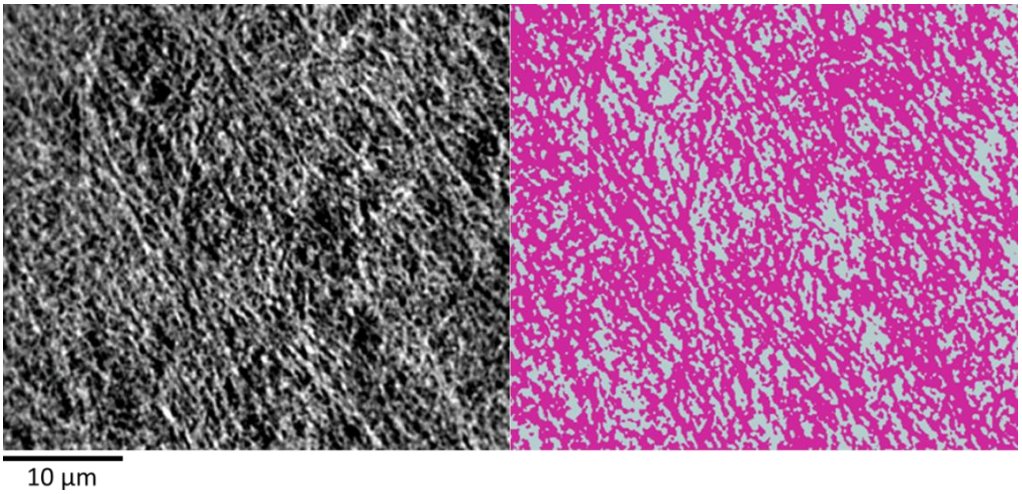

Figure 10-10: Greyscale (left) and corresponding binary slice (right) from the XY plane of the PE layer within the MTI ceramic coated separator.

10.1.2. RVE Analysis of Membrane Porosity

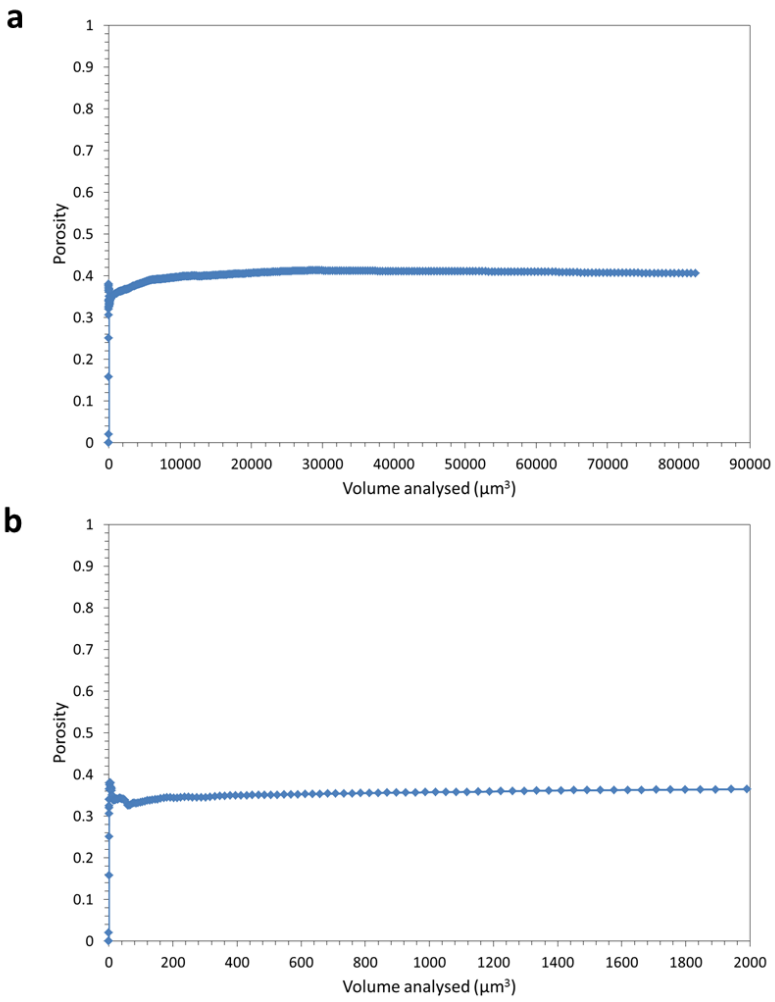

Figure 10-11: Representative volume element analysis of Celgard 2325 showing (a) the RVE for the full volume and (b) a magnified section showing volume required for convergence.

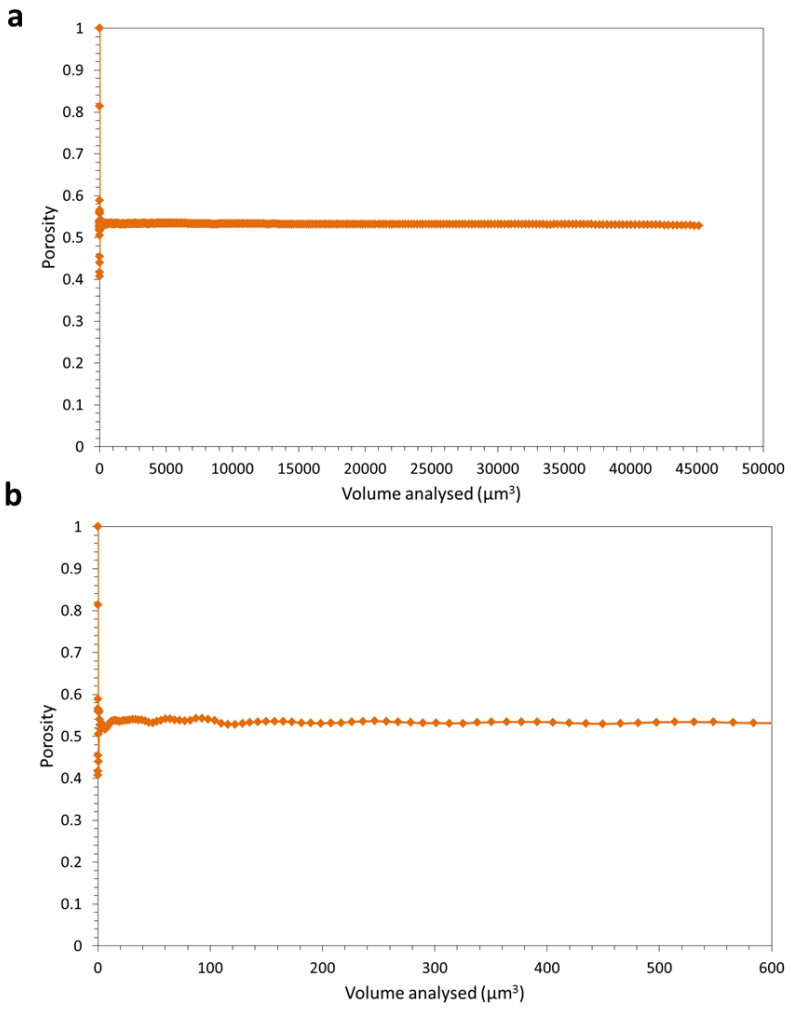

Figure 10-12: Representative volume element analysis of Celgard 2500 showing (a) the RVE for the full volume and (b) a magnified section showing volume required for convergence.

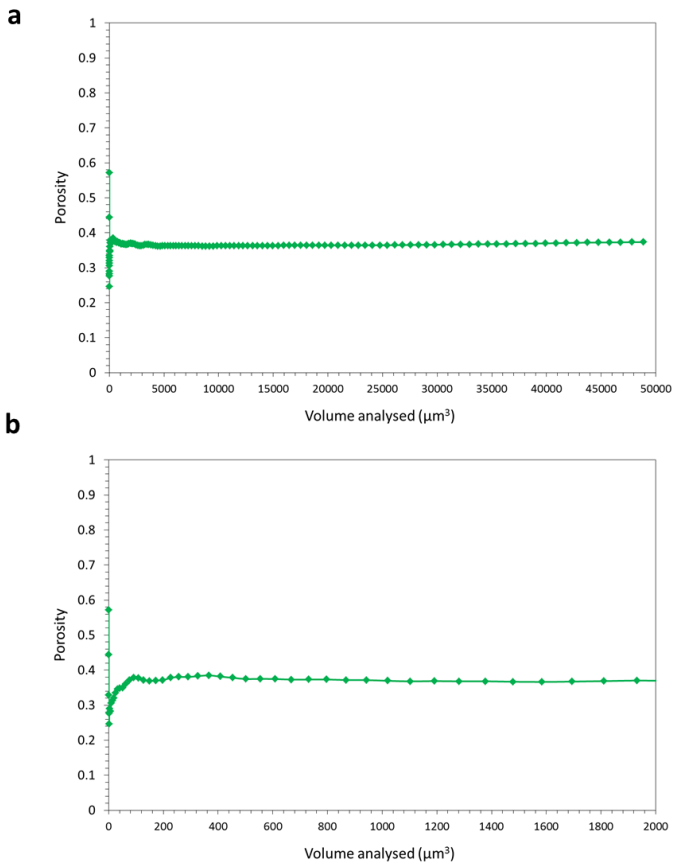

Figure 10-13: Representative volume element analysis of MTI ceramic coated separator showing (a) the RVE for the full volume and (b) a magnified section showing volume required for convergence.

10.1.3. Scanning Electron Micrographs

Scanning electron micrograms of the surface of each of the examined separators are presented in Figure 10-14 to Figure 10-16. Celgard 2325 and Celgard 2500 are uniaxially stretched which caused unidirectional slit-like pores with thin polymer fibres (nano-fibrils) stretching across the pore opening. Upon comparison with the segmented tomograms, it's clear that the imaging technique did not have sufficient resolution to resolve the nano-fibrils.

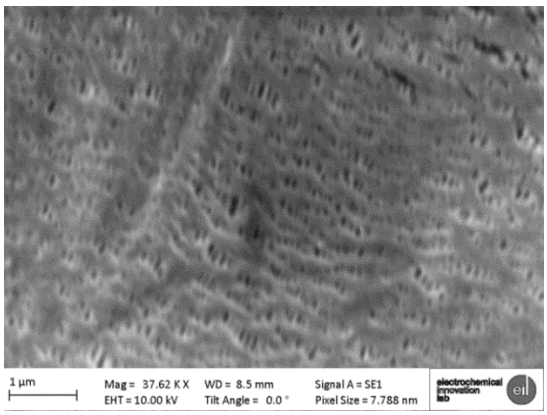

Figure 10-14: Scanning electron micrograph of the surface of Celgard 2325.

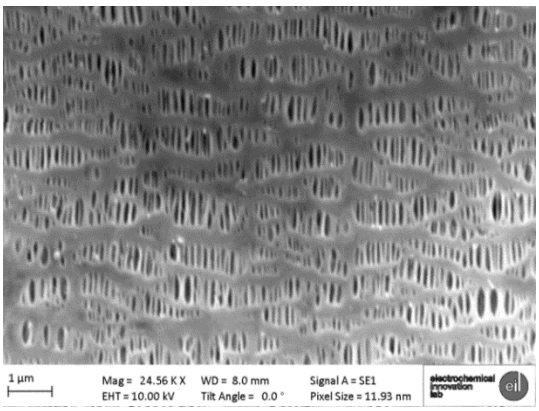

Figure 10-15: Scanning electron micrograph of the surface of Celgard 2500.

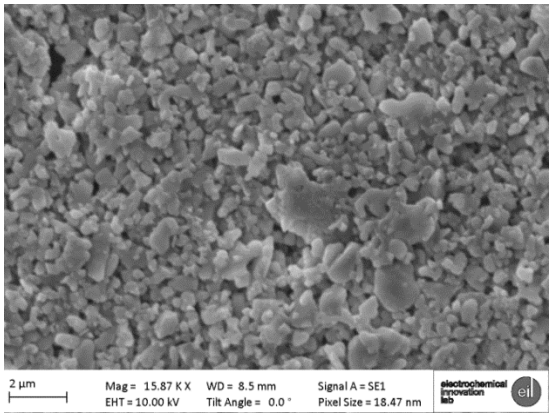

Figure 10-16: Scanning electron micrograph of the surface of the MTI ceramic-coated membrane.

10.2. Chapter 5 Appendix

10.2.1. Correlation coefficients

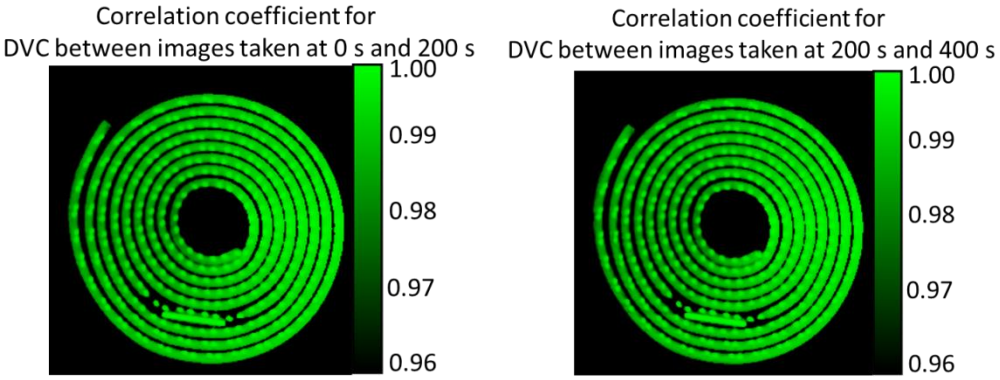

Figure 10-17: XY slice from the correlation coefficient profile for DVC between images taken at 0 s and 200 s, and at 200 s and 400 s.

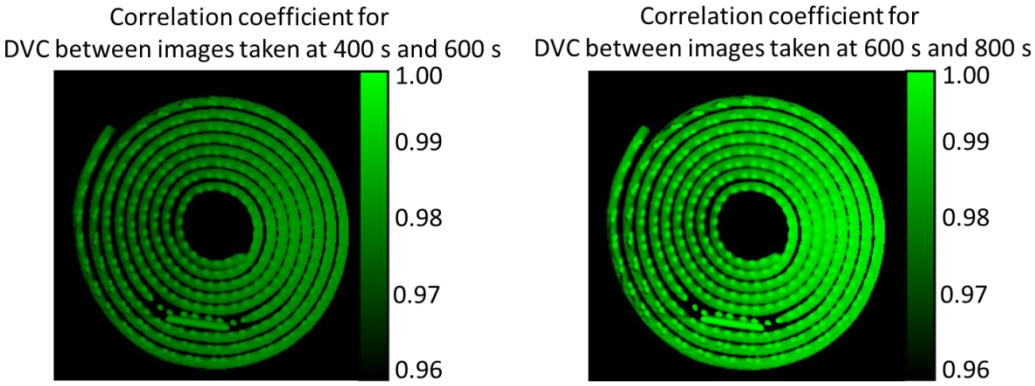

Figure 10-18: XY slice from the correlation coefficient profile for DVC between images taken at 400 s and 600 s, and at 600 s to 800 s.

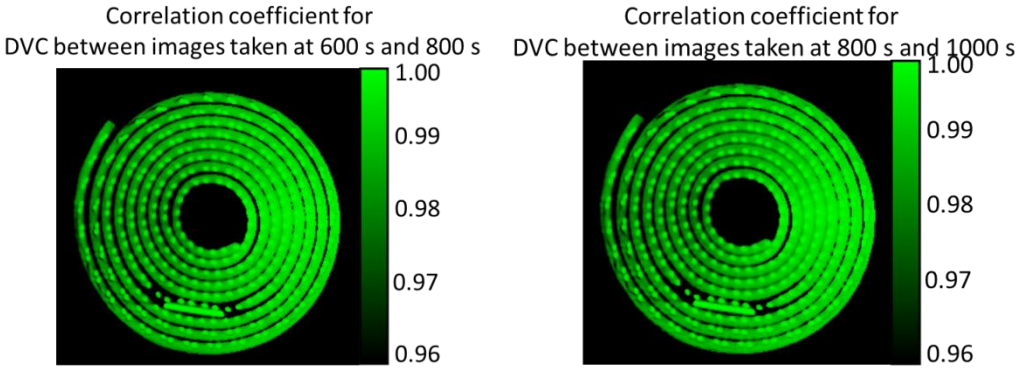

Figure 10-19: XY slice from the correlation coefficient profile for DVC between images taken at 600 s and 800 s, and at 800 s to 1000 s.

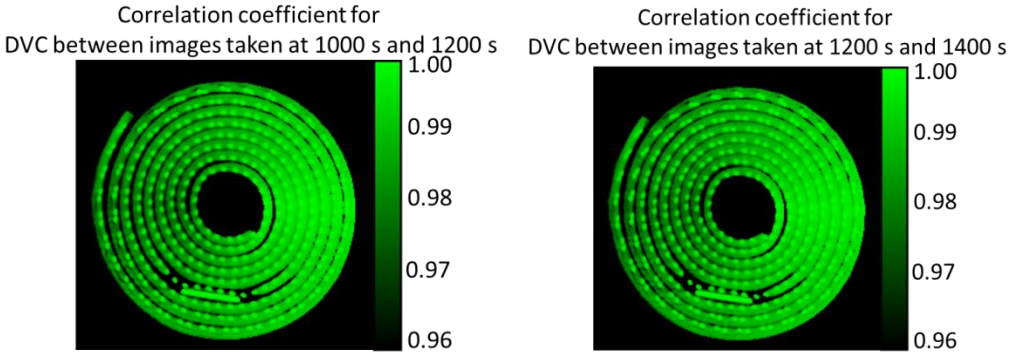

Figure 10-20: XY slice from the correlation coefficient profile for DVC between images taken at 1000 s and 1200 s, and at 1200 s to 1400 s.

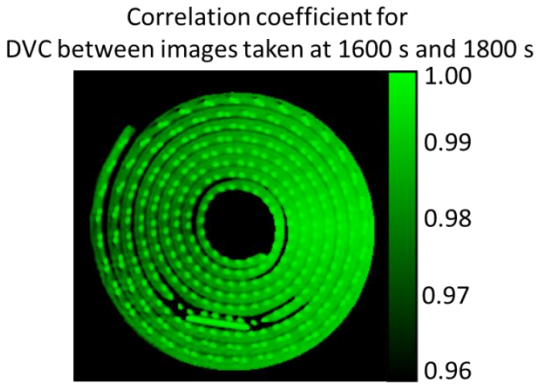

Figure 10-21: XY slice from the correlation coefficient profile for DVC between images taken at 1600 s and 1800 s.

10.3. Chapter 7 Appendix

10.3.1. X-ray Imaging Conditions

10.3.1.1. Zeiss Xradia Versa 520

Full cell tomography: the sample was placed 25 mm from the source and 83 mm from the detector. The accelerating voltage and current were 80 kV and 88 µA respectively. An objective lens giving an optical magnification of 0.4 was used with binning 1 to give an effective pixel size of 7.92 µm. The exposure time was 5 s and the reconstruction consisted of 1601 projections across a 360 ° rotation. Three images taken at different locations along the vertical axis of the battery with a 15 % overlap were stitched together to give the full cell reconstruction shown in the main manuscript.

Fresh $LiCoO_2$ and Al current collector: the sample was placed 16 mm from the source and 9 mm from the detector. The accelerating voltage and current were 60 kV and 84 µA respectively. An objective lens giving an optical magnification of 20 was used with binning 1 to give an effective pixel size of 0.424 µm. The exposure time was 50 s and the reconstruction consisted of 2401 projections across a 360 ° rotation.

Post-mortem $LiCoO_2$ and Al current collector: the sample was placed 14 mm from the source and 12 mm from the detector. The accelerating voltage and current were 30 kV and 66 µA respectively. An objective lens giving an optical magnification of 20 was used with binning 1 to give an effective pixel size of 0.36 µm. The exposure time was 40 s and the reconstruction consisted of 1241 projections across a 360 ° rotation.

10.3.1.2. Zeiss Xradia Ultra 810

Post-mortem scan of $LiCoO_2$ particles showing cracks: Sample was imaged in large field of view (LFoV) in absorption mode. An objective lens giving an optical magnification of 20 was used with 10.3 X-ray magnification with binning 2 × 2 with effective pixel size of 0.1262 µm. The reconstructions consisted of 901 projections with 15 s exposure each.

Post-mortem scan of $LiCoO_2$ particles showing presence of Co: Sample was imaged in large field of view (LFoV) in absorption mode. An objective lens giving an optical magnification of 20 was used with 10.3 X-ray magnification with binning 2 × 2 with effective pixel size of 0.1262 µm. The reconstructions consisted of 1601 projections with 7 s exposure each.

10.3.2. Attenuation Coefficients

The $LiCoO_2$ particles were imaged using the Zeiss Xradia Ultra 810 which uses a 5.4 keV quasi-monochromatic beam. Attenuation coefficients of relevant materials were calculated by using elemental mass attenuation coefficients from the NIST website[201]. Greyscale values in the reconstructed tomograms scale linearly with attenuation coefficients for a monochromatic X-ray beam (5.4 keV). The attenuation coefficient of compounds such as $LiCoO_2$ and CoO can be estimated using equation 10.1.

$$\frac{\mu}{\rho} = \sum w_i \left(\frac{\mu}{\rho}\right)_i \tag{10.1}$$

Where μ is the attenuation coefficient, ρ is the mass density, and w is the fraction of element i in the compound by mass.

Table 10-1: Attenuation coefficients of $LiCoO_2$ and post-thermal runaway compounds.

Material	Mass attenuation coefficient μ/p (cm^2/g) (5.4 keV)	Density ρ (g/cm^3)	Molar mass m_{mol} (g/mol)	Molar volume V_{mol} (cm^3/mol)	Molar attenuation coefficient μ_{mol} (cm^2/mol)	Attenuation coefficient μ (cm^{-1})
Li	1.37	0.53	6.94	13.09	9.48	0.72
Co	130.06	8.90	28.00	3.15	3641.68	1157.53
C	15.85	1.70	12.00	7.06	190.22	26.95
$CoCO_3$	51.16	4.13	88.00	21.31	4501.70	211.27
$LiCoO_2$	61.21	4.90	66.94	13.66	4097.69	299.95
CoO	87.84	6.44	44.00	6.83	3864.94	565.69
Li_2CO_3	11.90	2.11	73.88	35.01	878.98	25.10

As shown in Figure 10-22 the greyscale value in the Co phase is approximately 1.56 times greater than that in the CoO phase in the core of the particle. From the SEM and EDS images included in the main manuscript, it is seen that there is a surface layer of Co on the particles. The compound that most closely matches the difference in the perceived greyscale in Figure 10-22 (and hence attenuation coefficient) is CoO, which is also the most likely material to be present in the core of the particle following thermal runaway. However, the attenuation coefficient differs from that of CoO by a factor of 2.05 (Table 10-1) which is greater than the measured difference in greyscale of 1.56. SEM micrographs appear to show the Co phase to be porous, which would decrease its perceived attenuation coefficient. If the remaining central material were $LiCoO_2$, the greyscale value would differ by a factor of up to 3.9 from Co. Therefore, based on the greyscale values, the most likely material occupying the centre of the particles is CoO.

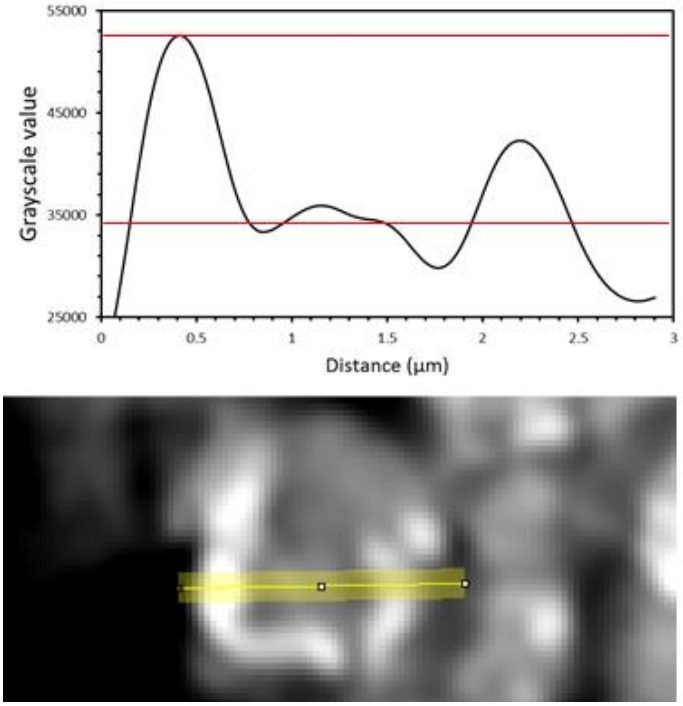

Figure 10-22: (Top) Plot of greyscale values averaged in the vertical direction across the yellow line shown in the tomogram slice of a $LiCoO_2$ particle following thermal runaway (bottom). The maximum greyscale value is found to be 53,000 which corresponds to the Co surface layer, and average greyscale value of the phase in the centre of the particle is 34,000. Hence, the greyscale value of the Co layer is 1.56 times that of the central material.